Observing Galaxy Formation During the First 2 Billion Years

Thesis by

Daniel P. Stark

In Partial Fulfillment of the Requirements

for the Degree of

Doctor of Philosophy

California Institute of Technology

Pasadena, California

2009

(Defended June 24, 2008)

This thesis has benefited from the help of many. First and foremost, I must thank my Ph.D advisor, Richard Ellis. It has been a true pleasure to work with Richard over the past five years. His enthusiasm for astronomy, tireless work ethic, unique vision and ability to grasp the big picture are second to none. I really couldn't have envisioned a better supervisor.

I am very grateful for the guidance and mentoring that I received as an undergraduate at the University of Wisconsin. In particular, I would like to thank Ed Churchwell for taking me in while still a young high school student and guiding me over the years. I also must thank Barb Whitney for teaching me many of the fundamentals of astrophysics research and putting up with the longest ApJ resubmission process ever. I am grateful to Joe Cassinelli for his enthusiastic and insightful approach to teaching. I still find my notes from his courses very useful! In 2001, I had the good fortune to spend a very productive summer working with Debra Shepherd at the VLA. I thank Debra for a wonderful research experience and for opening doors for me at Caltech. I also thank Miller Goss for supporting my research endeavors as a young undergraduate and inviting me back to Socorro numerous times to finish off our project. All of these individuals were always willing to listen to my questions, whether they be about science or picking grad schools, and I am very grateful for all the advice I have received from them over the years.

Caltech has provided a nourishing scientific environment during my Ph.D, and I am thankful to a large number of people that have passed through Caltech during my time there. In my first few years, I was fortunate to interact with a number of postdocs and elder graduate students. In particular, I thank Graham Smith for bringing me into the Ellis group and mentoring me early on. I was fortunate to overlap briefly with Jean-Paul Kneib at Caltech, and I am very appreciative of his help over the years. I am particularly grateful to Dave, Josh, Melissa, and Kevin for always being willing to discuss science and/or provide a fun social outlet during my early years. Perhaps one of the greatest benefits of working with Richard Ellis is the scientific interaction with others in the research group. I gained a great deal from collaboration with Johan Richard throughout my time at Caltech and am very

grateful for all his help! Over the years, I've also been fortunate to interact with Mike Santos, Sean Moran, Chris Conselice, Tom Targett, and James Taylor, each of whom have helped me during my Ph.D. I must also thank George Becker for providing his superb NIRSPEC reduction software. Finally, I'd like to thank Adam, Brian, Larry, and Stuartt for providing great lunchtime diversions over the last several years.

I have also gained a tremendous amount from a number of colleagues outside of Caltech. I learned a great deal from my collaboration with Avi Loeb and am very grateful for his continued support of my research. I thank Mark Swinbank for all his help and expertise dealing with the IFU data which was instrumental in Chapter 6 of this thesis. Tommaso Treu has always been willing to listen to science ideas and career questions which I am very grateful for. I thank Andy Bunker for inviting me to the UK a number of times to work on high redshift galaxies. These trips were instrumental in the papers that are presented in Chapter 2 and 5 of this thesis.

Most of this thesis would not have been possible if it wasn't for the hard work of people at Keck. In particular, I thank Jim Lyke and Grant Hill for all their efforts in keeping NIRSPEC up and running during my first few years at Caltech. Also, Chapter 6 could not have been completed without a properly functioning laser guide star system at Keck, and I thus thank everyone who contributed to getting the system up and running.

I am grealy indebted to Judy McLain for all her hard work during my 5 years at Caltech. I still don't know how Judy does everything she does! It's been a pleasure stopping by her office these past 5 years.

Finally and most importantly, I must thank Marija and my family for all their neverending support and inspiration over the years. I never could have made it through all of these years without their help, and I am truly grateful for it.

Abstract

The universe evolves dramatically in its first two billion years. From the formation of the first stars and protogalaxies, to the reionization of hydrogen and the assembly of massive 10^{11} $M_{\odot}$ galaxies, this era contains some of the most important events in cosmic history. Current observations of this era are limited causing many of these processes to remain unconstrained. This thesis is comprised of five projects, each of which focuses on advancing the observational study of galaxies in this early era.

First, we develop an indirect method of estimating the star formation activity at $z \gtrsim 6$. Motivated by the discovery of galaxies with evolved stellar populations at $z \gtrsim 6$ (Egami et al. 2004, Eyles et al. 2005), we propose that the stellar mass density at $z \simeq 5-6$ can be used to robustly constrain the integrated star formation density at yet earlier times. Given the difficulties in reliably confirming galaxies at $z \gtrsim 6$, we argue that this method may represent one of the most promising means of characterizing the contribution of star forming galaxies to reionization. We compute the stellar masses of a large sample of $z \simeq 5$ rest-UV selected galaxies in the GOODS-South field and derive an estimate of the $z \simeq 5$ stellar mass density. In spite of the fact that this measurement is surely incomplete (only UV luminous galaxies are included), the resulting mass density is very large, requiring significant star formation at higher redshifts. In spite of this indication of earlier activity, no sources have yet been identified with robust spectroscopic confirmation at $z \gtrsim 7$.

Comprehensive searches for galaxies at $z \gtrsim 7$ are thus key to progress. Starting in 2004, we began work on a Keck/NIRSPEC survey for gravitationally lensed Lyman-α emitting galaxies at $z > 8$. The survey yielded six promising candidate LAEs between z=8.7 and z=10.2, suggesting that there may be a large population of feeble

star-forming sources at very early times. If these sources are at $z > 8$, it would indicate that low luminosity galaxies dominate the UV photon budget necessary for reionization, explaining the shortfall found in previous studies of luminous sources (Bunker et al., 2004; Oesch et al., 2008). Follow-up imaging and spectroscopy lends support to the high redshift case, but further work is still required before these objects can be claimed as $z \simeq 10$ sources. We discuss several ongoing efforts to confirm the nature of these candidates.

Noting the rapid observational progress identifying the first candidate galaxies at $z \gtrsim 7$ and hundreds of galaxies at $z \simeq 5 - 6$, we set out to put these observations in the context of a simple analytic star formation model, taking into consideration the evolution in the underlying dark matter halos. We find that the abundance of luminous Lyman break galaxies in the 500 Myr between $z \simeq 6$ and 10 can be naturally explained by the hierarchical assembly of dark matter halos. In contrast, the first estimates of the abundance of less luminous star-forming galaxies at $z \simeq 9 - 10$ are higher than predicted by the simple model and, if verified by further data, may suggest some evolution in the efficiency of star formation or the initial mass function. We also use the simple model to assess the efficiency of future surveys at $z \gtrsim 7$ and conclude that with the development of new instrumentation, dedicated programs should soon allow considerably larger samples ($\simeq 100$) of $z \simeq 7 - 8$ LBGs and LAEs to be detected.

As observations probe closer to the epoch when the first galactic systems emerge, it is thought that star-forming galaxies will begin to appear younger and less massive then their lower-redshift counterparts. While the first glimpse of the stellar populations of high-z has been obtained in recent years (Egami et al. 2004, Eyles et al. 2005) lacking has been a systematic analysis of the evolving stellar masses and ages of a large sample of LBGs uniformly selected in different redshift bins at $z \gtrsim 3$. We present the results of the first such analysis, compiling the stellar populations of a large sample ($\gtrsim 4500$ galaxies) of photometrically selected LBGs spanning $z \simeq 3.5 - 6.5$. While we find considerable variation in the stellar mass as a function of rest-UV luminosity, we find no evidence that the dropouts at $z \simeq 6$ are substantially younger or less

massive than those at $z \simeq 4$. The results are consistent with a picture in which freshly luminous systems are continually emerging over time, consistent with the observed growth in the UV luminosity function (Bouwens et al., 2007). These results also reveal a marked increase in the number density of actively-forming massive 10^{11} $M_{\odot}$ galaxies over $4 \lesssim z \lesssim 6$. Extrapolating this growth to later times, we conclude that a significant fraction of the population of $z \simeq 2-3$ distant red galaxies (van Dokkum et al., 2006; Kriek et al., 2008) may have passed through the LBG phase while assembling their mass.

Most of the progress in our understanding of galaxy formation in the first two billion years has stemmed from measurements of the integrated properties of high redshift galaxies. While such observations have certainly improved our understanding of galaxies at early times, in order to shed light on the physics governing star formation in these galaxies, one must study their internal structure (i.e. dynamical state, distribution of HII regions and molecular gas). The development of integral field spectrographs on 8-10 meter telescopes has led to recent progress on this front (e.g., Forster-Schreiber et al. 2006, Law et al. 2007), but the interpretation of these studies is often ambiguous due to the lack of independent resolution elements. In this thesis, we discuss how progress can be achieved through the study of gravitationally-lensed systems. We present observations of the resolved star formation, dynamics, and gas physics of one of the most highly-magnified LBGs at $z = 3.06$. We find well-ordered rotation and infer that molecular gas is being efficiently converted into stars in a remarkably compact region, suggesting that we are possibly witnessing the early growth of a disk galaxy where the current star formation is rapidly assembling a central bulge. While the results are only based on a single system located at comparitively low-redshift for this thesis, we note that ongoing surveys are now discovering many more strongly-lensed systems out to $z \simeq 7$ (Belukorov et al. 2007, Frye et al. 2007, Richard et al. 2008, Bradley et al. 2008); hence we argue that the method described within this chapter will soon become a commonly-used, effective path toward revealing the nature of the most distant galaxies.

Contents

List of Figures

.

List of Tables

.

Chapter 1

Introduction

Observational cosmologists have long sought to capture the history of the universe, from its origins to the present day. Measurements of the cosmic microwave background radiation (CMB) currently provide our earliest snapshot of the universe, just 400,000 years after the Big Bang ($z \simeq 1100$). At this time, the universe had finally cooled sufficiently to allow electrons and protons to combine to form hydrogen atoms. The next available picture comes almost one billion years later ($z \simeq 6-7$), revealing a decidedly more complex universe containing an abundant population of galaxies and quasars and an ionized intergalactic medium (IGM). The period between these two redshifts represents one of the final uncharted frontiers in cosmology. Buried in this unexplored era are the keys to understanding how the first stars and galaxies came to be and what led to the reionization of intergalactic hydrogen.

The goal of my thesis has been to push back the redshift frontier to yet earlier times, shedding light on the nature of the earliest galaxies, quantifying their contribution to the reionization of hydrogen, and optimizing the methods used to detect them. Before beginning a detailed discussion of the specific projects that make up this thesis, it is worthwhile to consider the developments that have laid the ground for the consideration of these issues. With this goal in mind, in §1.1, I provide a brief historical narrative focused on the events that led to our current observational understanding of cosmic history in the high-redshift universe. Following this section, I discuss more recent developments (§1.2), closing with brief descriptions of each of the projects included in this thesis (§1.3).

1.1 Patching together Cosmic History

We begin our discussion in the early 1920s, a time in which there was still contentious debate focused on whether the universe extended beyond the Milky Way. This debate was ultimately resolved in 1925 through observations of Cepheid stars in spiral nebulae. Using the known relationship between the variability period and stellar luminosity, Edwin Hubble established that the nebulae were located outside of our galaxy. With this discovery, our understanding of the universe was fundamentally altered and moreover the field of extragalactic astronomy was born.

It did not take long for the observational study of distant galaxies to further revolutionize the prevailing cosmological model. Pioneering work by Hubble in the 1920s revealed that distant galaxies were recessing away the Milky Way with a velocity proportional to their distance. Georges Lemaitre claimed that this correlation offered concrete evidence that the universe was expanding, a notion that both he and and Alexander Friedmann had previously proposed. Lemaitre went on to argue that a necessary ramification of the expansion is that the universe began in an "explosion" from what he referred to as a "primeval atom," later coined the big bang by Fred Hoyle.

In the 1940s, work by Gamow and Alpher further developed Lemaitre's theory, working out the sequence of the nucleosynthesis that occurred after the big bang and making one of the fundamental predictions of big bang theory. In their model, the early universe was comprised of a hot plasma of protons, electrons, and photons. The photons coupled to the plasma by their interaction with electrons through Thomson scattering. As the universe expanded, its temperature decreased via adiabatic cooling, eventually reaching 4000 K, whereby the electrons and protons could combine to form neutral hydrogen. At this point, the photons became decoupled from matter and began to travel freely through space, their temperature continuing to decrease as the universe expanded. Gamow predicted this radiation field should be observable at the present day with a temperature of 5 K. Sixteen years later, this prediction was confirmed with the discovery of a 2.7 degree background radiation Penzias & Wilson

(1965), a resounding success for the big bang theory.

The same year that Penzias and Wilson discovered the CMB, astronomers began to realize that the universe must have been reionized at some point after recombination. Two independent papers in 1965 pointed out that if the IGM was still filled with the neutral hydrogen, the resonant interaction between Lyα photons and hydrogen would lead to a very large optical depth to Lyα photons, causing the spectra of extragalactic sources to be strongly absorbed at wavelengths shorter than Lyα (Gunn & Peterson, 1965; Scheuer, 1965). The discovery of a quasar located at a high enough redshift for Lyα to be in the visible (Schmidt, 1965) allowed this "Gunn-Peterson" test to be performed. Remarkably these observations revealed little absorption at frequencies blueward of Lyα implying that the IGM must not contain significant neutral hydrogen. Gunn & Peterson concluded that if current estimates of the mass density of the universe are accurate then the hydrogen making up the IGM must be highly ionized, requiring an additional phase transition at some point after $z \simeq 1100$. What provided the ionizing flux responsible for this reionization was not known, although as we will see in the next several paragraphs, work by Peebles and others would soon predict a tremendous ionizing source at high-redshift likely to play a significant role.

In the mid 1960s, cosmologists began to focus their efforts on explaining the formation of galaxies in the context of an expanding universe. In a series of papers, Peebles layed the groundwork for the field of structure formation, explaining how galaxies could have formed from small-scale fluctuations imprinted on the initial density field. These density perturbations grew more pronounced with time via gravitational attraction, becoming detached from the expansion and forming a bound system once the Jeans instability criterion was satisfied. The collapse of these bound gas clouds subsequently led to the formation of massive protogalaxies (see also Larson 1974).

Throughout the 1960s, observational constraints on these theories were predominantly limited to observations of our own galaxy (e.g. Eggen et al. 1962), which suggested that the halo of our galaxy must have formed in a free-fall time with considerably higher star formation rates in the past than observed at present. In a

seminal paper, Partridge & Peebles (1967) considered the possibility of directly locating galaxies during their initial assembly. Adopting a simple dissipationless model for galaxy formation, they predicted that $\simeq 10^{11}$ $M_\odot$ galaxies would begin forming when the universe was 140 Myr old ($z \simeq 20$). These "primeval galaxies" were predicted to be large ($\simeq 10$ arcsec) low surface brightness systems with bolometric luminosities on order 2.5×10^{45} erg s^{-1}. Detection of rest-UV continuum emission from such protogalaxies was thought difficult given the brightness of the night sky at the wavelengths the galaxy emission was expected to be brightest (1-3 μm). Instead, Partridge & Peebles suggested the most promising method of detecting protogalaxies would be the Lyα emission line, which they predicted might contain up to 6-7% of the bolometric luminosity.

This theoretical exploration led to numerous observational attempts to locate the formation epoch of galaxies. Initial experiments, designed to find diffuse, large ($\theta \lesssim 3$") images on photographic plates (Partridge, 1974) and to find the fluctuation signal expected from such a high-redshift population (Davis & Wilkinson, 1974) met with no success. The advancement of dissipative galaxy formation theories (Larson, 1974; Meier, 1976; Sunyaev et al., 1978) shifted the strategy of primeval galaxy surveys toward more compact, blue systems. With the development of CCD detectors in the late 1970s, such surveys became much more efficient, but the null results continued through the 1980s (see Koo 1986 and references therein).

One of the major barriers impeding progress in the observational pursuit of the primeval galaxies was the tremendous uncertainty in the expected redshift, luminosity, and size distribution of the population. Different assumptions led to widely different predictions which vastly increased the observational parameter space that needed to be probed. Even with the development of galaxy formation scenarios in the context of the now-standard cold dark matter theory of structure formation (White & Rees, 1978; Blumenthal et al., 1984; White & Frenk, 1991), uncertainties in the properties and epoch of the galaxy formation remained significant, due largely to the difficulty in constraining the heating and cooling physics that governs star formation (not to mention the uncertainty in the cosmological model). In general, these hierarchical

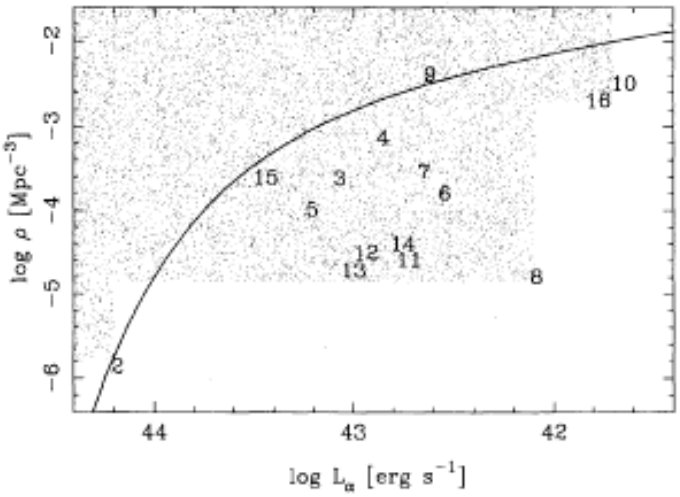

Figure 1.1 Limits on the comoving densities of LAEs at $z \simeq 3$ from the mid 1990s as compiled in Pritchet (1994). The shaded region corresponds to parameter space that had been covered in previous surveys, while the curve represents a simple model of the LAE luminosity function described in Pritchet & Hartwick (1990). The puzzling lack of LAE detections seemed to imply serious flaws in the model.

models predicted a relatively late formation epoch, a conjecture that was given further support by claims that damped Lyα absorbers at $z \simeq 2$ contained sufficient neutral gas to form all the stars seen locally (Wolfe, 1988). However, there was not a complete consensus surrounding the notion of a late formation epoch. Indeed, the discovery of luminous quasars at $z \simeq 4 - 5$ was argued to provide strong evidence that galaxies were primarily formed at $z \gtrsim 5$ (Turner, 1991).

With no clear picture from observations or theory, observers soldiered on in their efforts to locate primeval galaxies, covering new regions of luminosity and redshift parameter space. Deep redshift surveys uncovered a population of faint blue galaxies (Broadhurst et al., 1988; Colless et al., 1990), but these sources were generally found to lie at moderately low-redshifts ($z \lesssim 0.9$). Emission line searches reached increasing levels of sophistication throughout the 1980s and early 1990s using slitless spectroscopy (Crampton et al., 1987), long-slit spectroscopy (Cowie, 1988; Djorgovski & Thompson, 1992; Djorgovski et al., 1993), and narrowband imaging (Cowie, 1988; Pritchet & Hartwick, 1987; Djorgovski & Thompson, 1992; Djorgovski et al., 1993) to

search for primeval galaxies at $z \simeq 2-5$. While these surveys did uncover a number of intriguing candidates, no unambiguous primeval galaxies were identified (Figure 1.1). Knowledge of galaxies in the $z \gtrsim 2$ universe was thus limited to quasars and radio galaxies (Lilly, 1988; Chambers et al., 1990), superluminous infrared objects (Rowan-Robinson et al., 1991), and damped Lyα absorbers (e.g. Wolfe et al. 1992). How these objects related to the sought after primeval galaxies was unclear.

In the mid 1990s, work by Steidel and collaborators identified a population of actively star-forming galaxies at $z \simeq 3$ using color selection techniques (Steidel & Hamilton, 1992, 1993; Steidel et al., 1995). The method targeted star-forming galaxies at $3.0 \lesssim z \lesssim 3.5$ using three custom broadband filters designed to isolate objects with Lyman continuum breaks and flat far-UV continuum slopes ($f_\nu \propto \nu^0$) from the foreground population. Keck spectroscopy soon after confirmed the redshifts of this population of "Lyman break galaxies" (LBGs) and moreover enabled the detailed spectroscopic properties of the population to be studied (Steidel et al. 1996), revealing surpisingly weak Lyα emission and the existence of P-Cygni profiles suggestive of strong winds. The implied star formation rates, velocity dispersions, and morphological properties of the LBGs were argued to be consistent with that expected for the high-redshift precursors to the spheroids of the local universe (Steidel et al., 1996; Giavalisco et al., 1996).

In spite of the success of the LBG surveys, it was realized early on that the galaxies selected using these techniques are biased to the portion of the high-z star-forming population with little dust extinction and strong continuum emission. Indeed some of the most actively star-forming galaxies in the local unvierse are completely enshrouded in dust, emitting most of their luminosity in the far-infrared. With the arrival of sensitive submillimeter observations (via the SCUBA array on the James Clerk Maxwell Telescope) in the mid 1990s, the high- redshift counterparts of these local systems – the submillimeter galaxies (SMGs) – were soon discovered (Smail et al., 1997; Hughes et al., 1998; Barger et al., 1998) suggesting that LBG surveys were missing a substantial amount of star formation at $z \gtrsim 2$. Meanwhile, many continued to pursue emission line searches in hopes of detecting the youngest galaxies at high

redshift. Such objects were thought to have relatively little continuum light making their detection in LBG surveys difficult. In 1996, Hu & McMahon achieved success using this technique, reporting the detection of a pair of Lyα emitting star-forming galaxies (LAEs) at $z = 4.55$. The advent of 10 meter telescopes rapidly made the detection of such high-z LAEs commonplace (Cowie & Hu, 1998; Hu et al., 1998) and soon the galaxy redshift frontier was pushed back nearly to $z \simeq 6$ (Hu et al., 1999). Thus by the late 1990s, after many decades of searching, large numbers of star-forming galaxies were finally being discovered at $z \gtrsim 2$. In the following section, we bring our narrative to the present era, discussing the current challenges facing the field.

1.2 Galaxies in the Reionization Era and Beyond

The motivation for locating primeval galaxies remains twofold. On one hand the goal is to improve our understanding of when and how galaxies formed, but at the same time, we are also interested in patching together the missing pieces of cosmic history in the early universe. With the discovery and characterization of large samples at $z \simeq 2 - 5$, these pursuits diverged. While considerable efforts continue to focus on the physics of galaxy formation at $z \simeq 2 - 3$ (e.g. Shapley et al. 2003, 2005; Förster Schreiber et al. 2006; Erb et al. 2006a,b,c; Law et al. 2007, etc.), those interested in surveying the uncharted eras of cosmic history have begun to focus their efforts on yet earlier times. Their goals have shifted from identifying the high-redshift precursors of the luminous galaxies of the present day to understanding how the IGM was reionized and when the first luminous sources and galactic systems emerged. In this section, I will outline recent progress on this front, laying the framework for the projects that I have conducted in this thesis.

In the last decade, the study of the first generation of stars, the so-called Population III, has emerged as one of the foremost areas of cosmological research. Numerical simulations of the collapse and fragmentation of primordial, metal-free gas have demonstrated that the first stars likely formed $\simeq 150$ Myr after the Big Bang

and were primarily very massive due to the inability of the primordial gas to cool efficiently (Bromm et al., 1999, 2002; Abel et al., 2000, 2002). The exact masses of the Pop III stars and the precise form of the primordial initial mass function remain unknown and are the focus of fervent numerical research (Larson, 1998; Nakamura & Umemura, 2001; Omukai & Yoshii, 2003). Though the details remain controversial and an active area of research (Bromm & Larson 2004 and references within), it is clear that the epoch of Pop III star formation was eventually terminated and replaced by a star-formation mode dominated by lower-mass stars. This important transition is thought to have paved the way for the formation of the first galactic systems and subsequently the reionization of hydrogen in the IGM.

While direct observation of the emergence of the first stars remains out of grasp at the present day, the study of the subsequent reionization era is well within the capabilities of current facilities. The three most fundamental questions that observations are attempting to address are *when* did reionization occur? *How* did it proceed? And *what* were the sources responsible for the transition? Complementary to these questions, observers are seeking to trace the growth of galaxies back to increasingly earlier epochs, in hopes of identifying the era when the first galaxies began to emerge.

Recent observations have narrowed the era during which the bulk of reionization occurred to 6-7$\lesssim z \lesssim$ 20. Studies of the optical depth in Lyman-α absorption probed by high resolution spectra of the most distant quasars show a rapid upward transition in the neutral fraction beyond $z \simeq 5.5$ (Djorgovski et al., 2001; Becker et al., 2001; Fan et al., 2006) suggesting that reionization may have ended at $z \simeq$ 6-7. In contrast, others have argued that the evolution in the Lyα forest between $z \simeq 2$ and 6 can be explained as a result of slowly evolving densities, ionization rates, and temperatures of the IGM, requiring no dramatic transition at $z \simeq 6$ (Becker et al., 2007). Regardless of the interpretation of the quasar absorption spectra, we can be assured that reionization is complete by $z \lesssim 6$ given the presence of significant transmitted flux in the quasar spectra below this redshift. Meanwhile, the optical depth of microwave photons to electron scattering derived from the EE spectrum measured by WMAP (Dunkley et al., 2008) places a valuable upper bound on the reionization

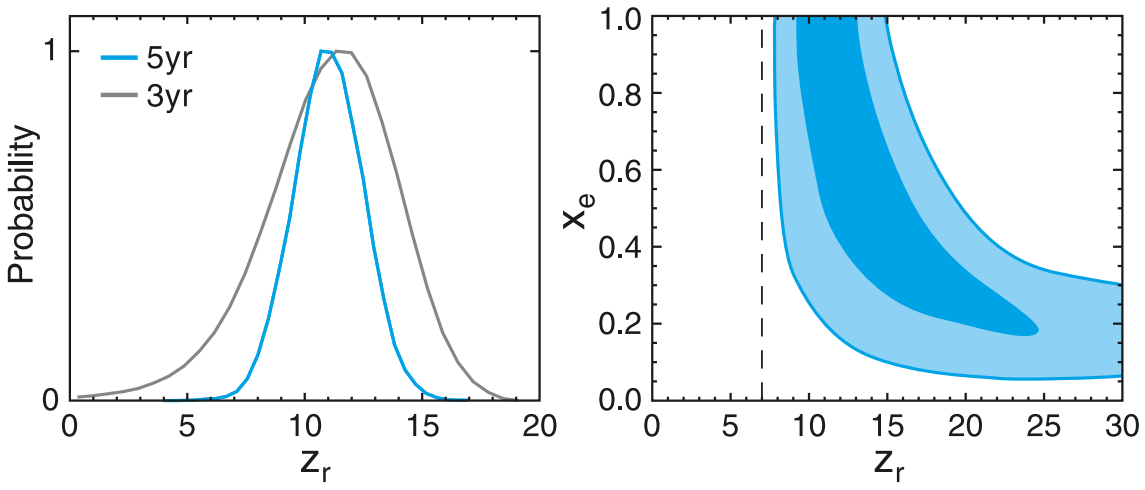

Figure 1.2 Constraints from the five-year WMAP data on the redshift of reionization taken from Dunkley et al. (2008). Assuming a simple instantaneous reionization model (left), the data rule out sudden reionization at z=6 with more than 99.9% confidence. Adopting a two-step reionization model (with reionization proceeding from an ionization fraction x_e at redshift z_r to full ionization at z=7), the WMAP data are consistent with an extended reionization scenario, perhaps beginning as early as $z \simeq 15 - 20$.

process, suggesting that the IGM was significantly ionized by $z \simeq 11$ and excluding an instantaneous reionization at $z = 6$ at the 99.9% confidence level (Figure 1.2). Taken together, the CMB polarization and quasar data are suggestive of a complex and extended ($\Delta z \simeq 5 - 10$) ionization history.

Determining *how* reionization developed is a challenging endeavor with current technology. The basic picture of reionization involves the production and growth of an HII region around each ionizing source with neighboring HII regions eventually overlapping and ultimately terminating the reionization era. Initially it was thought that reionization was limited by recombinations and hence proceeds from low- to high-density regions (Miralda-Escudé et al., 2000; Gnedin, 2000). Recent numerical and analytical work has shown that a different picture emerges if the large- scale clustering of sources is considered (Knox et al., 1998; Sokasian et al., 2003, 2004; Furlanetto et al., 2004). In this picture, a small number of large ionized bubbles form around highly-clustered sources with recombination playing only a secondary role and reionization hence proceeding from high- to low-density regions. Confirming this

picture will require observations of the large-scale distribution of hydrogen throughout the epoch of reionization. Assuming technical challenges (e.g. foreground removal, ionospheric distortions) can be met, new facilities built to observe the redshifted 21-cm transition at high redshift (Morales & Hewitt, 2004) may eventually illuminate how reionization occurred.

Characterizing the ionizing sources responsible for reionization is a more feasible goal for existing observational facilities. The prevailing notion held today is that star-forming galaxies dominate the ionizing photon budget during the end of the reionization era, a conjecture supported by the discovery of evolved galaxies at $z \simeq 6-7$ (Egami et al., 2005; Eyles et al., 2005) and the presence of CIV in the highest redshift quasars sampled (Ryan-Weber et al., 2006), both of which require an earlier ($z \gtrsim 7$) period of vigorous star formation. The emergence of an array of deep fields with extensive multiwavelength coverage has enabled galaxies to be selected to $z \simeq 10$, offering a *direct* probe of the nature of high-redshift galaxies and their contribution to the reionization process. The comoving density of emerging UV photons from luminous galaxies appears to decrease continuously to $z = 8$ (Figure 1.3, Bouwens et al. 2008); simple estimates imply that the luminosity density of these UV-bright sources is insufficient to reionize the universe without invoking non-standard initial mass functions (Stiavelli et al., 2004; Oesch et al., 2008) or very steep faint end-slopes for the luminosity function (Yan & Windhorst, 2004; Richard et al., 2008).

Reconciling the observed decline in the star formation rate density of luminous galaxies with the requirements for reionization has become one of the major driving forces behind the quest to locate the most distant galaxies. According to hierarchical structure formation models, the dominant contribution to reionization comes from low-luminosity galaxies residing in low-mass dark matter halos (e.g., Loeb 2006 and references within), most of which likely lie faintward of the sensitivity limits of current surveys. This notion is supported by measurements of the evolving UV luminosity function of LBGs which show a continuously decreasing characteristic luminosity between $z \simeq 3$ and 8 (Yoshida et al., 2006; Bouwens et al., 2008; McLure et al., 2008), implying that galaxies are becoming increasingly dominated by feeble systems

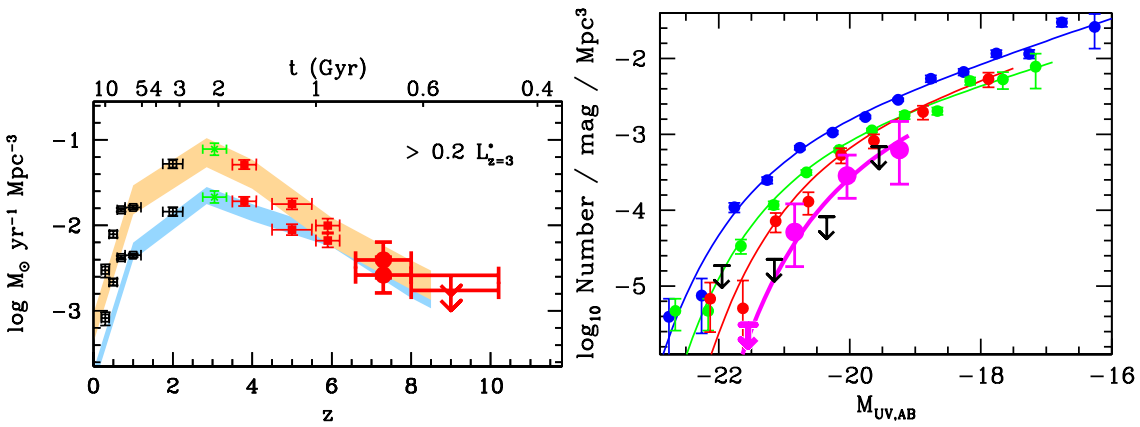

Figure 1.3 *Left:* The evolution of the star formation rate density over cosmic history as taken from Bouwens et al. (2008). The data show a marked decline in luminous UV emitting sources between $z \simeq 3$ and 10, causing tension with the requirements for reionization (e.g., Bunker et al. 2004). *Right:* The evolving UV luminosity functions of B-drops (blue), V-drops (green), i'-drops(red), and z-drops (pink) taken from Bouwens et al. 2008. The decline in density between $z \simeq 4$ and $z \simeq 7.5$ is much larger for the most luminous sources, implying that galaxies are becoming increasingly dominated by low luminosity systems at high-redshift. This suggests that there may be a large population of star-forming galaxies hidden beneath the sensitivity limits of current surveys.

at earlier times (Figure 1.3). While this certainly hints at an important contribution of ionizing photons from low luminosity galaxies, it remains a distinct possibility that feedback suppresses star formation in these dwarf galaxies, negating their contribution to reionization. Characterizing the properties and abundance of this high-redshift population has emerged as one of the most active areas of extragalactic astronomy and plays a central role in my thesis, described in the following section.

1.3 Thesis Overview

My thesis consists of five separate projects, each providing a different means of improving our undersanding of high-redshift galaxies or quantifying their contribution to reionization. Below, I briefly summarize the goals and conclusions of each of these projects.

In Chapter 2 (originally published in Stark et al. 2007, ApJ, 659, 84), we develop

an indirect method of constraining star formation at $z \gtrsim 6$. Motivated by the discovery of galaxies with evolved stellar populations at $z \gtrsim 6$ (Egami et al., 2005; Eyles et al., 2005), we propose that a measurement of the stellar mass density at $z \simeq 5-6$ can be used to robustly constrain the integrated star formation density at yet earlier times. Since it is incredibly challenging for current facilities to unambiguously confirm galaxies at $z \gtrsim 6$, we argue that this method may represent one of the most promising means of characterizing the role that young galaxies play in reionization. Examining the stellar masses of a large sample of $z \simeq 5$ rest-UV selected galaxies in the GOODS-S field, we derive an estimate of the $z \simeq 5$ stellar mass density. In spite of the fact that this measurement is surely incomplete (only UV luminous galaxies are included), the resulting mass density is suprisingly large, requiring significant star formation at yet earlier times.

Such indications of earlier activity strongly motivate attempts to secure a first glimpse of the $z \gtrsim 7$ universe. In Chapter 3, I discuss the results of a Keck/NIRSPEC survey for gravitationally lensed LAEs at $z > 8$ (originally published in Stark et al. 2007, 663, 10). The survey yielded six promising candidate LAEs between z=8.7 and z=10.2, suggesting that there may be a large population of feeble star-forming sources at very early times. If these sources are at $z > 8$, it would indicate that low luminosity galaxies dominate the UV photon budget necessary for reionization, explaining the shortfall found in previous studies of luminous sources. Follow-up imaging and spectroscopy supports the high-redshift case, but the evidence is not yet sufficient to claim these as $z \simeq 10$ sources. Further work is now underway to confirm the nature of the candidates.

Noting the rapid observational progress identifying the first candidate galaxies at $z \gtrsim 7$ and hundreds of galaxies at $z \simeq 5-6$, I set out in Chapter 4 to put these observations in the context of a simple analytic star formation model taking into consideration the evolution in the underlying dark matter halos (originally published in Stark, Loeb, & Ellis 2007, ApJ, 668, 627). We find that the abundance of luminous Lyman break galaxies in the 500 Myr between $z \simeq 6$ and 10 can be naturally explained by the hierarchical assembly of dark matter halos. In contrast, the first estimates of

the abundance of less luminous star-forming galaxies at $z \simeq 9-10$ are higher than predicted by the simple model and, if verified by further data, may suggest a top-heavy stellar mass function at these early epochs. Using the model, we conclude that with the development of new instrumentation, dedicated programs should soon allow considerably larger samples of $z \simeq 7-8$ LBGs and LAEs to be detected.

As observations probe closer to the epoch when the first galactic systems emerge, it is thought that star-forming galaxies will begin to appear younger and less massive then their lower-redshift counterparts. While the first glimpse of the stellar populations of high-z galaxies has been obtained in recent years (Egami et al., 2005; Eyles et al., 2005), lacking has been a systematic analysis of the evolving stellar masses and ages of a large sample of LBGs uniformly selected in different redshift bins at $z \gtrsim 3$. In Chapter 5, we present the first such analysis, compiling the stellar populations of a large sample ($\gtrsim 4500$ galaxies) of photometrically selected LBGs at $z \simeq 3.5-6.5$. While we find considerable variation in the stellar mass as a function of rest-UV luminosity, we find no evidence that the dropouts at $z \simeq 6$ are significantly younger or less massive than those at $z \simeq 4$. The results are consistent with a picture in which the evolving stellar mass and luminosity distributions are being predominantly driven by growth in the underlying dark matter halo mass functions and show no sign of reaching the era when galactic systems are undergoing their initial assembly. These results also have implications for the formation mode of the massive distant red galaxies (DRGs) seen at $z \simeq 2-3$ (e.g., van Dokkum et al. 2006). By computing the density of massive galaxies between $z \simeq 6$ and 4 and comparing to those measured in $z \simeq 2-4$ DRG populations, we conclude that a significant fraction of the $z \simeq 2-3$ DRGs passed through the LBG phase at $z \gtrsim 4$ while assembling their mass.

In the first five chapters, the majority of our discussion has focused on measurements of the integrated properties (i.e., star formation rate, stellar mass) of galaxies at high redshift. While such observations have certainly improved our understanding of star formation at early times, more insight into the physics governing galaxy formation in the high-z universe can be extracted through measurements of the internal properties (i.e. dynamical state, distribution of HII regions and molecular gas)

of high redshift galaxies. Of particular interest is when the angular momentum of galaxies was established. With the development of integral field spectrographs on 8-10 meter telescopes, it is now becoming possible to explore these questions at high redshift for the first time. The first results (e.g., Förster Schreiber et al. 2006; Law et al. 2007) do not yet reveal a complete picture, with the largest galaxies showing evidence of rotation and smaller systems showing more chaotic velocity fields. However, the interpretation of these studies is confused by the lack of independent resolution elements. In Chapter 6, we show how progress can be achieved through the study of gravitationally-lensed systems. We present observations of the resolved star formation, dynamics, and gas physics of one of the most highly-magnified LBGs at $z = 3.07$, concluding that the galaxy is destined to be a bulge-dominated galaxy. While the results are only based on a single system located at comparitively low-redshift for this thesis, we note that ongoing surveys are now discovering many more strongly-lensed systems out to $z \simeq 7$ (Belokurov et al., 2007; Frye et al., 2007; Richard et al., 2008; Bradley et al., 2008); hence we argue that the method described within this chapter will soon become a commonly-used, effective path toward revealing the nature of the most distant galaxies.

In the final chapter, we attempt to synthesize these results. After summarizing the key findings of the thesis and commenting on ongoing work, we revisit the question of whether the ionizing emissivity of the observed $6 \lesssim z \lesssim 10$ galaxy population is sufficient to achieve reionization by $z \gtrsim 6$. We close by proposing several of the most promising routes toward improving our understanding of the early universe. We discuss the prospects of new imaging and spectroscopic campaigns to secure large samples of $z \gtrsim 7$ LBGs and LAEs, to better constrain the formation and quenching of massive galaxies at $z \gtrsim 3$, and to characterize luminosity and redshift trends in the dynamical state of high redshift galaxies.

Chapter 2

A New Measurement of the Stellar Mass Density at $z \simeq 5$: Implications for the Sources of Cosmic Reionization

Abstract

We present a new measurement of the integrated stellar mass per comoving volume at redshift 5 determined via spectral energy fitting drawn from a sample of 214 photometrically-selected galaxies with z'_{850LP} <26.5 in the southern GOODS field. Following procedures introduced by Eyles et al. (2005), we estimate stellar masses for various sub-samples for which reliable and unconfused Spitzer IRAC detections are available. A spectroscopic sample of 14 of the most luminous sources with $\overline{z} = 4.92$ provides a firm lower limit to the stellar mass density of $1 \times 10^6\,\mathrm{M}_\odot$ Mpc^{-3}. Several galaxies in this sub-sample have masses of order $10^{11}\,M_\odot$ implying significant earlier activity occurred in massive systems. We then consider a larger sample whose photometric redshifts in the publicly-available GOODS-MUSIC catalog lie in the range 4.4 $< z <$ 5.6. Before adopting the GOODS-MUSIC photometric redshifts, we check the accuracy of their photometry and explore the possibility of contamination by low-z galaxies and low-mass stars. After excising probable stellar contaminants and using the $z'_{850LP} - J$ color to exclude any remaining foreground red galaxies, we conclude

This chapter has been published previously as Stark et al. 2007, ApJ, 659, 1

that 196 sources are likely to be at $z \simeq 5$. The implied mass density from the unconfused IRAC fraction of this sample, scaled to the total available, is $6 \times 10^6\,M_\odot$ Mpc^{-3}. We discuss the uncertainties as well as the likelihood that we have underestimated the true mass density. Including fainter and quiescent sources the total integrated density could be as high as $1 \times 10^7\,M_\odot$ Mpc^{-3}. Even accounting for 25% cosmic variance within a single GOODS field, such a high mass density only 1.2 Gyr after the Big Bang has interesting consequences for the implied past average star formation during the period when cosmic reionization is now thought to have taken place. Using the currently available (but highly uncertain) rate of decline in the star formation history over $5 < z < 10$, a better fit is obtained for the assembled mass at $z \simeq 5$ if we admit significant dust extinction at early times or extend the luminosity function to very faint limits. An interesting consequence of the latter possibility is an abundant population of low luminosity sources just beyond the detection limits of current surveys. As mass density estimates improve at $z \simeq$ 5-6, our method is likely to provide one of the tightest constraints on the question of whether star forming sources were responsible for reionizing the Universe.

2.1 Introduction

Finding the sources responsible for cosmic reionization is now the active frontier in studies of galaxy formation. A number of independent arguments are focusing efforts on searches for star forming galaxies in the redshift interval $5 < z < 10$. Studies of the optical depth in Lyman α absorption probed by high resolution spectra of the most distant quasars suggest an upward transition in the neutral fraction beyond $z \simeq$ 5.5 (Fan et al., 2006); these data suggest reionization was just ending at $z \simeq 6$. In contrast, the optical depth of microwave photons to electron scattering derived from the angular power spectrum of the WMAP polarization-temperature cross-correlation function (Spergel et al., 2006) places a valuable upper bound on the reionization process corresponding to $z \simeq$ 10-20.

Over the past several years, the quest to observe the most distant galaxies in

the Universe has rapidly expanded to the point where the discovery of $z \simeq 5-6$ star-forming galaxies has now become routine. Deep imaging surveys with the *Hubble Space Telescope (HST)* and 8-10 meter ground based telescopes have uncovered hundreds of galaxies at $z \simeq 5$ (Iwata et al., 2003; Bremer et al., 2004) and $z \simeq 6$ (Bunker et al., 2004; Dickinson et al., 2004; Bouwens et al., 2006) via the Lyman break galaxy (LBG) technique pioneered by Steidel and collaborators to identify star-forming galaxies at $z \approx 3-4$ (Steidel et al., 1996, 1999).

The consensus emerging from these studies, however, is that abundance of *luminous* galaxies is substantially *less* at $z \approx 6$ than at $z \approx 3$ (Stanway et al., 2003; Bunker et al., 2004; Dickinson et al., 2004; Bouwens et al., 2006). If this trend continues to fainter systems and higher redshift, then it may prove challenging to explain the earlier star formation activity necessary to fulfill reionization in the redshift interval $5 < z < 10$ implied by the quasar and WMAP studies (Bunker et al., 2004). However, it has been suggested that the evolution in the galaxy luminosity function between $z = 3$ and $z = 6$ is luminosity dependent: although the entire luminosity function is not yet well-constrained at $z \approx 6$, intrinsically fainter galaxies appear to become more abundant at earlier times (Bouwens et al., 2006). If this is the case, then the bulk of reionizing photons could come from lower luminosity galaxies not yet adequately probed in deep surveys.

As the redshift boundary of cosmic reionization narrows, so it becomes crucial to improve our understanding of the cosmic star formation history in the corresponding time interval. Unfortunately however, confirming even the most luminous sources in the range $7 < z < 10$ is challenging for current facilities. Although some candidate $z \simeq 7-10$ galaxies have been identified in ACS and lensed surveys (Bouwens et al 2004b, Bouwens et al 2005, Richard et al 2006, Stark et al. 2007b), these are generally too faint for spectroscopic study. The situation may not significantly improve for several years.

This paper explores a more practical approach for constraining the amount of star formation prior to $z \simeq$ 5-6, namely the measurement of the integrated stellar mass density at this epoch. Following the idea originally discussed by Stark & Ellis (2006),

the stellar mass density at $z \simeq$ 5-6 must represents the integral of past activity. With adequate precision, such estimates can be used to independently verify the claimed decline in overall star formation to $z \simeq 10$ and to assess whether the past activity is sufficient for cosmic reionization.

The approach is made practical by the remarkable progress recently made in estimating stellar masses at high redshift via the use of the Infrared Array Camera (IRAC, Fazio et al. 2004) onboard the *Spitzer Space Telescope*. Egami et al. (2005) first demonstrated the technique for one of the most distant known sources: a multiply-imaged pair with a photometric redshift of $z \simeq 6.8$. Eyles et al. (2005) later extended the technique for two spectroscopically-confirmed galaxies at $z = 5.8$, demonstrating the presence of massive galaxies ($M_{\rm stellar} > 10^{10}\,M_{\odot}$) with evolved stellar populations of ages $\gg 100\,$Myr.

The IRAC filters at $3.6 - 8.0\,\mu$m probe the rest-frame optical at $z \approx 5-6$, providing a valuable indicator of established stellar populations and, indirectly, hinting at vigorous star formation activity at $z > 6$. Combining these data with deep broadband optical photometry from *HST* and 8-10 meter class ground based telescopes, spectral energy distributions (SEDs) can be compared with population synthesis models to constrain the age, star formation history and stellar masses of galaxies. The initial discovery of massive ($10^{10} M_{\odot}$) galaxies at $z \simeq 6$ presented in Eyles et al. (2005) was subsequently confirmed by the independent analysis of Yan et al. (2005). More recently, Mobasher et al. (2005) identified a galaxy in the Hubble Ultra Deep Field (UDF) with a photometric redshift of $z \simeq 6.5$ (but see also the recent paper by Dunlop et al. 2006). If this high redshift is correct, then the MIPS and IRAC detections imply a very massive system of $M_{\rm stellar} > 10^{11}\,M_{\odot}$, providing further evidence for significant star formation activity at $z > 6$ (Panagia et al., 2005).

The studies of galaxy masses published thus far have focused on only a few individual systems. Although some studies (e.g. Stark & Ellis 2006) have attempted to infer the contribution of past star formation to cosmic reionization, without knowing how typical such massive galaxies are, it is difficult to make precise statements. Clearly what is needed is a *census* of the assembled stellar mass at high redshift. A

comoving *stellar mass density* can be directly compared with various models of earlier star formation.

In a companion paper, we compute the stellar mass density at $z \approx 6$ from the i'-band dropouts in GOODS-South (Eyles et al., 2007). A similar study of i'-drops was conducted in Yan et al. (2006). However, the surface density of i'-band dropout galaxies at $z \approx 6$ with *Spitzer* detections is low. A more statistically-meaningful sample can be found using the $z \approx 5$ v-band dropouts. The age of the Universe at this time is only marginally older (1.2 Gyr c.f. 0.95 Gyr) yet larger, more representative, samples are available. In this paper we will examine the stellar mass density at $z \approx$5 using sources to a limiting magnitude of $z'_{850LP} \approx 26.5$ selected from the Great Observatories Origins Deep Survey (GOODS, Giavalisco et al. 2004a). We present an analysis of various subsamples at $z \approx 5$ drawn from a total of $\simeq$214 v-band dropouts. The goal of the study is to establish whether the assembled stellar mass at $z \simeq 5$ is consistent with current (and admittedly uncertain) estimates of the preceding star formation activity. If not, this might be taken to imply a significant component of star formation is missing, occurring either at lower intrinsic luminosities, obscured by dust, or at uncharted epochs ($z > 10$).

A plan of the paper follows. In §2.2, §2.3, and §2.4, we introduce the various imaging and spectroscopic datasets, the photometric procedures and the selection of various subsamples of $z \simeq 5$ galaxies. We describe the derivation of the stellar masses and comment on the uncertainties in §5.5. In §2.6, we examine the implications for the star formation history at earlier times.

We adopt a cosmology consistent with the initial WMAP data release (**?**): a Λ-dominated, flat universe with $\Omega_\Lambda = 0.7$, $\Omega_M = 0.3$ and $H_0 = 70\,h_{70}\mathrm{km\,s^{-1}\,Mpc^{-1}}$. All magnitudes in this paper are quoted in the AB system (Oke & Gunn, 1983).

2.2 The GOODS-S Dataset

In this paper, we continue our analyses of the Great Observatories Origins Deep Survey (GOODS). GOODS aims to bring together the most powerful space and

ground-based facilities to study the high-redshift universe across a wide range of wavelengths. We focus on the southern GOODS field which has the greatest amount of multi-wavelength data essential for reliable stellar masses. The GOODS-S survey area covers a total of 160 arcmin^2 and is centered on the *Chandra* Deep Field South (CDF-S; Giacconi et al. 2002).

2.2.1 *ACS* Imaging

Deep optical imaging of GOODS-S has been obtained with the Advanced Camera for Surveys (*ACS*, Ford et al. 2003) instrument onboard *HST* as part of a Treasury Program (Giacconi et al., 2002). The Wide Field Camera on ACS has a field of 202×202 arcsec^2 and a pixel scale of 0.″05. The GOODS-South field was observed in the F435W (B-band), F606W (v-band), F775W (SDSS-i') and F850LP (SDSS-z') broad-band filters for 3, 2.5, 2.5 and 5 orbits, respectively over 16 pointings.

Here we present an analysis of $z \simeq 5$ galaxies making use of the publicly-available version-1.0 data-release of the *ACS* GOODS data[1]. The reduced data have been 'drizzled' onto a large grid made up of 18 sections with a pixel scale of 0.″03. Each section comprises an image of 8192 × 8192 pixels in size.

2.2.2 Ground-Based Near-infrared Imaging

Deep near-infrared observations of most of the GOODS-S field were obtained with the ISAAC camera on the Very Large Telescope (VLT) at the ESO Paranal Observatory as part of the ESO Large Programme: LP168.A-0485(A) (PI: C. Cesarsky). The publically available version-1.5 data release includes 24 fully reduced ISAAC/VLT pointings in the J and K_s-bands[2], covering $\approx 160\,\mathrm{arcmin}^2$. Additional details of the observations are to be presented in Vandame et al. (*2006, in prep*). The VLT images have a pixel scale of 0.″15, a factor of five times larger than the drizzled ACS pixels. The median exposure times are 11.3 ksec in J, and 17.9 ksec in K_s.

[1]available from `ftp://archive.stsci.edu/pub/hlsp/goods/`

[2]available from `http://www.eso.org/science/goods/releases/20050930/`

2.2.3 Spectroscopy

We also use publicly-available spectroscopy from the GOODS team to identify confirmed $z \approx 5$ galaxies for futher study. Multi-object spectroscopy was performed on the GOODS-S field with the FORS2 instrument mounted at the Kueyen Unit Telescope of the VLT at ESO's Cerro Paranal Observatory as part of the ESO/GOODS Large Program LP170.A-0788 (PI Cesarsky). Details of the survey are presented in Vanzella et al. (2002, 2005). The primary selection criteria for placing objects on the slitmask was $(i'_{775W} - z'_{850LP}) > 0.6$ and $z'_{850LP} < 25.0$; objects with $0.45 < (i'_{775W} - z'_{850LP}) < 0.6$ were placed on the slitmask with lower priority. We make use of the VLT/FORS2 spectroscopic catalogs from the version-2.0 release which provide 725 unique redshift assignments with quality flags A, B, or C (where A=solid redshift, B=likely redshift, C=potential redshift).

2.2.4 *Spitzer* Imaging

Spitzer images of GOODS-S were obtained with the Infrared Array Camera (IRAC) and Multiband Imaging Photometry for Spitzer (MIPS) cameras on the *Spitzer* Space Telescope as part of the "Super Deep" Legacy programme (PID 169, Dickinson et al. *in prep*, Chary et al., *in prep*). The IRAC camera comprises four channels, each with a 256^2 InSb array imaging a $5.2' \times 5.2'$ field with a pixel size of $\approx 1\farcs22$. Images were taken through four broad-band infrared filters, with central wavelengths at approximately $\lambda_{\rm cent} = 3.6\,\mu$m, $4.5\,\mu$m, $5.6\,\mu$m and $8.0\,\mu$m (channels 1–4), and widths of $\Delta\lambda_{\rm FWHM} = 0.68, 0.87, 1.25, 2.53\,\mu$m respectively. The total exposure time in each channel is $\approx 86\,$ksec, depending on location. The data were taken in two epochs, with the telescope roll angle differing by 180°. In the first epoch, each filter covered a $10.0' \times 10.0'$ area in GOODS-S; however, the area covered by channels 1 and 3 ($3.6\,\mu$m and $5.6\,\mu$m) was offset by 6.7 arcminutes from that covered by channels 2 and 4 ($4.5\,\mu$m and $8.0\,\mu$m). Hence, only a portion of the GOODS-S field was observed in all 4 filters after the first epoch of observations. In the second epoch, the area covered by channels 1 and 3 in the first epoch was observed with channels 2 and 4 and

vice versa. A central overlap region appeared in both epochs, and this deeper area intentionally contains the Hubble Ultra Deep Field (HUDF, Beckwith et al. 2003; Bunker et al. 2004).

We analyze the publicly available *Spitzer* mosaics from the first and second epochs of the observations of GOODS-S [3]. The data reduction pipeline employs a 'multidrizzle' technique similar to that used successfully on *HST*/ACS GOODS data. This provides combined images with a pixel scale of $0\farcs6$. The magnitudes listed in this paper are determined from this 'drizzled' data. We use the updated "Super Deep" epoch 1 images from the third data release (DR3) and the Super Deep epoch 2 images from the second data release (DR2).

2.3 Photometric Samples

The photometry we compute in this section will be used for two independent samples of $z \simeq 5$ objects: a small sample of spectroscopically confirmed galaxies and a larger sample of photometrically selected galaxies. The spectroscopic sample will provide a robust lower limit to the $z \simeq 5$ stellar mass density whereas the photometric sample will provide a more representative estimate of the integrated mass density. To obtain stellar masses of individual galaxies, we must have accurate photometry for both samples as well as photometric redshifts for the photometric sample. The reliability of the photometric redshifts is especially crucial since contamination by low-redshift interlopers could seriously skew our estimates of the total mass.

We obtain photometric redshifts from the GOODS MUSIC photometric catalog of GOODS-S (Grazian et al., 2006). This catalog uses uses 13-band SEDs from *HST* /ACS and *Spitzer*/IRAC photometry along with ground-based U, J, & K_S to derive photometric redshifts. Before adopting the GOODS MUSIC photometric redshifts, we verify the accuracy of the photometry in the GOODS MUSIC catalog (discussed below) and test the reliability of their photometric redshifts which we discuss in §4.1.

[3]available from `http://data.spitzer.caltech.edu/popular/goods`

ACS photometry was obtained from the GOODS team r1.1 catalog [4]. The photometric zeropoints adopted in the catalog on the AB magnitude system are 25.653, 26.493, 25.641, and 24.843 for the B_{435W}-band, v_{606W}-band, i'_{775W} band, and z'_{850LP}-band, respectively. We have corrected for the small amount of foreground Galactic extinction using the *COBE*/DIRBE & *IRAS*/ISSA dust maps of Schlegel et al. (1998); for the GOODS-S field, selective extinction is given by $\mathrm{E}(B-V) = 0.008$ mag. Magnitudes are measured in $0\farcs50$-diameter apertures. Total magnitudes are derived from the aperture magnitudes by correcting for the small amount of light falling outside the aperture: 0.14, 0.15, and 0.20 magin the v_{606W},i'_{775W}, and z'_{850LP}-bands, respectively (Sirianni et al., 2005). We note that GOODS website implies that the SExtractor parameter PHOT_APERTURES measures the *radius* of the photometric aperture, when it in fact measures the *diameter*. The correct interpretation has been applied to our dataset.

Near-infrared photometry was performed with $1''$-diameter apertures using the ground-based near-infrared ISAAC images. The center of the photometric aperture was taken from the centroid of the GOODSr1.1 catalog. The seeing varied across the ISAAC field as different tiles were taken over many nights, so we determined separate aperture corrections from unresolved sources for each tile. For the J- and K_s-band images the seeing is typically good (FWHM $= 0\farcs4 - 0\farcs5$), and the aperture corrections are $\approx 0.3 - 0.5$ mag, determined from bright but unsaturated isolated stars measured in $6''$-diameter apertures. The 3σ limiting AB-magnitudes in a $1''$-diameter aperture are $J \approx 26.4$ and $K_S \approx 25.7$, although these vary over the field because of different exposure times and seeing conditions.

The details of the photometric analysis of the Spitzer images used in this paper are nearly identical to those presented in Eyles et al. (2005). In order to maximize the signal-to-noise ratio (S/N) and minimize possible confusion with other foreground objects, we used a photometric aperture of diameter $\approx 1.5 \times$ FWHM for the IRAC images, appropriate for unresolved objects (our compact souces are essentially unresolved at IRAC resolution, see e.g. Bremer et al. 2004). The aperture diameters were

[4]available from `http://archive.stsci.edu/prepds/goods`

4, 4, 5 & 6 'drizzled' pixels for the 4 channels (3.6, 4.5, 5.6 & 8.0 μm), corresponding to 2.″4, 2.″4, 3.″0, & 3.″7. We used the IRAF `digiphot.phot` package to measure the enclosed flux at the coordinates determined by the ACS GOODS-r1.1 catalogs, taking the residual background from an annulus between 12″ and 24″ radius. We applied aperture corrections to compensate for the flux falling outside the aperture: these were ≈ 0.7 mag for the IRAC data, as determined from bright but unsaturated point sources in the images using large apertures.

The noise for each of the four channels was checked in two different ways. First, we derived an estimate based on a Poisson model using the detector gain, number of frames combined, and the background counts (adding back the zodiacal background estimate subtracted by the pipeline but recorded in the header). Secondly, we measured the standard deviation in background counts of the images. As the mosaicking process introduces correlations between pixels, we also made noise estimates using the individual pipeline basic calibrated data (BCD) images and assuming it decreased as the square root of the number of frames. These estimates lead to 3σ limiting AB magnitudes of 26.5 and 26.1 using 2.″4-diameter apertures in channels 1 and 2, respectively, and 23.8 and 23.5 in 3.″0 and 3.″7-diameter apertures in channels 3 and 4, respectively. There will be additional background fluctuations caused by faint galaxies (i.e. confusion noise), which will increase the noise. Both methods produce consistent estimates.

The low spatial resolution of *Spitzer* results in frequent blending between nearby sources, making accurate photometry of individual objects difficult. We took great effort to ensure that objects in our sample were not contaminated by neighboring bright foreground sources. We approach the IRAC contamination in slightly different ways for the different subsamples of z$\simeq$ 5 objects. Details are provided in §2.4.

We find that our photometry is consistent with that in the GOODS MUSIC cataog. The standard deviation between our photometry and the GOODS MUSIC photometry is 0.13 mags, 0.03 mags, 0.13 mags for the z', J, and K band. This increases to 0.36 mags for the 3.6 micron IRAC photometry.

2.4 Selection of z≃5 Galaxies

2.4.1 The Photometric Sample

We make use of the extensive database of photometric redshifts in the publicly-available GOODS-MUSIC catalog (Grazian et al., 2006) to construct a sample of $z \simeq 5$ candidates. Details of the procedure used to compute the photometric redshifts are discussed in Grazian et al. (2006). As described below, we based our photometric selection on the GOODS-MUSIC catalog rather than upon a more traditional v-band dropout technique (Bremer et al., 2004; Giavalisco et al., 2004a; Yan et al., 2005) on account of the improved performance in various tests. The principle difference is that the former method is based on fitting the entire SED.

First, we consider the fidelity of the GOODS-MUSIC selection of $z \simeq 5$ galaxies with respect to the VLT spectroscopic results of Vanzella et al. (2002, 2005). 21 galaxies within our $z \simeq 5$ spectroscopic sample (see next section) have photometric redshifts in the GOODS-MUSIC catalog. 18 of these (>85%) have photometric redshifts in the $4.4 < z < 5.6$ range with an average absolute scatter of $< |z_{spec} - z_{phot}| >$=0.07. Two of the three objects for which the photometric redshifts fail completely (e.g photometric redshifts of $z \simeq 1 - 2$) have spectroscopic redshift quality grades of C: here it is possible that the photometric redshifts are actually correct. This test suggests the SED-fitting process is reasonably accurate.

A further verification of the reliability of the photometric catalog concerns the implied rest-frame colors. Adopting a magnitude limit of $z'_{850LP} < 26.5$ (the 50% completeness limit for unresolved sources in GOODS Giavalisco et al. 2004a), we find 214 objects with photometric redshifts between $4.4 < z < 5.6$. Their rest-frame UV colors are in uniformly good agreement with those expected from the locus of star-forming galaxies at $z \simeq 5$ (Figure 2.1).

We find that only 42% of the objects in our photometric catalog would have been selected in the traditional Giavalisco et al. (2004a) v-drop method. Examining the redshift tracks, it is clear that the v-drop method misses a significant fraction of $z = 4.5 - 5.5$ star-forming galaxies (Figure 2.1). This region of color-color space

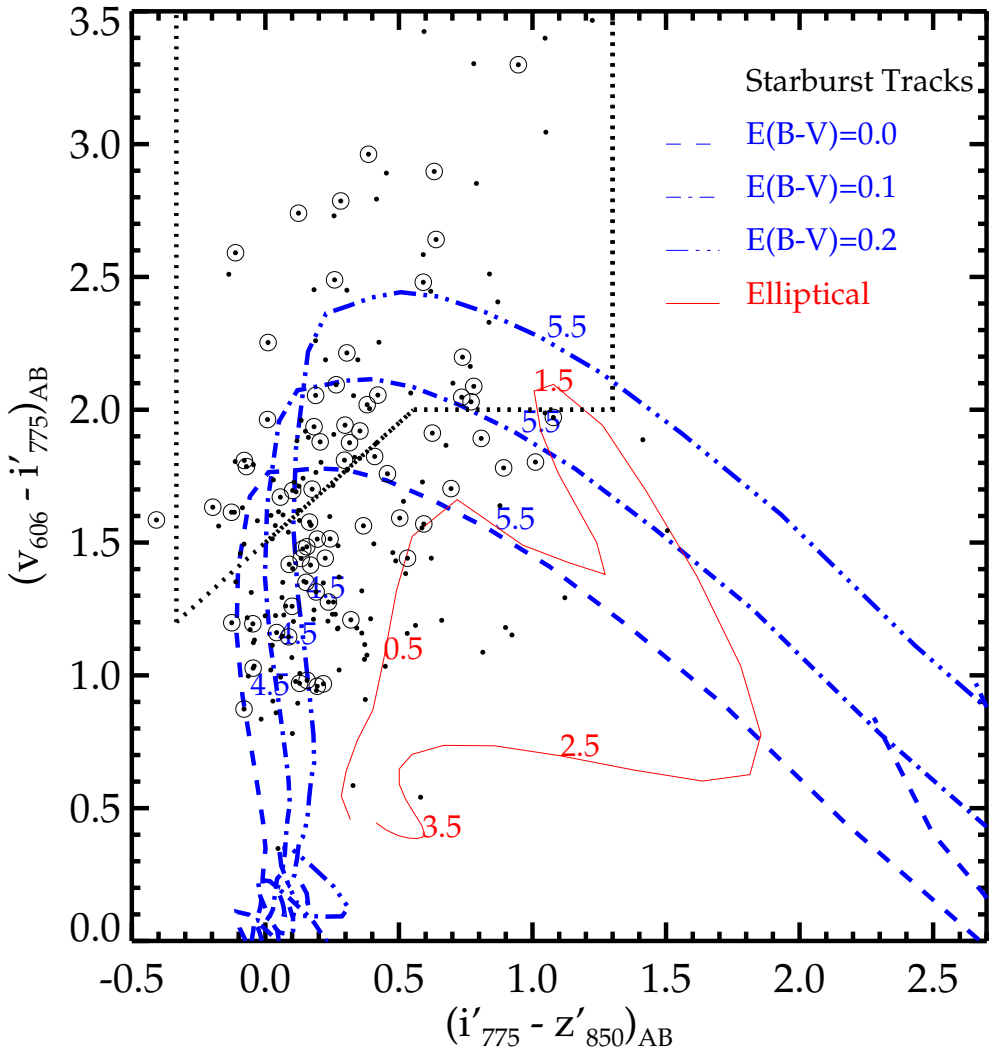

Figure 2.1 ($v_{606W} - i'_{775W}$) vs. ($i'_{775W} - z'_{850LP}$) colors of z≃5 candidates in GOODS-S. We construct a sample of 214 objects with photometric redshifts between 4.4 < z < 5.6 from the GOODS-MUSIC catalog (solid black circles). After removing stellar contaminants, low-z interlopers, and objects blended in Spitzer images, 72 objects with $z'_{850LP} < 26.5$ remain; these objects are marked with an additional circle. Although many objects in the sample fall just outside of the v-band dropout selection window used by Giavalisco et al. (2004a) to select $z \simeq 5$ galaxies (demarcated by dotted line), redshift tracks generated from starburst templates from Bruzual & Charlot (2003) illustrate that their rest-frame UV colors are consistent with the z≃5 interpretation. These tracks assume an age of 100 Myr and a constant star formation rate with E(B−V)=0.0,0.1,0.2 (blue dashed line, dashed-dotted, dashed-triple-dotted, respectively). Redshifting an elliptical galaxy template (Coleman et al., 1980) to z=0-4 (red solid line), we see that old galaxies at z≃1.5 could contaminate our sample.

is not included in the traditional v-drop method to minimize the inclusion of low redshift contaminating galaxies. The GOODS-MUSIC photo-z sample (along with the criteria we impose below) represents an improvement to the traditional v-drop selection criteria as it takes the entire SED into consideration in assessing an object's redshift.

While the GOODS-MUSIC photometric redshifts appear to be an excellent predictor of the true redshift, we remain vigilant to the possibility of a few catastrophic failures. The point is critical as the presence of any residual low redshift or stellar objects that are very bright at *Spitzer* wavelengths could lead to a significant overestimate of the stellar mass density. Recognizing there is a danger of removing true $z \simeq 5$ sources, we conclude it is better to err on the conservative side.

Because of their red colors, low-mass stars are a common contaminant of photometrically-located high redshift galaxy samples. Bright stars can be removed from high-z galaxy samples by selecting unresolved objects in the HST/ACS images. However, this technique begins to fail at fainter magnitudes as extragalactic objects may appear unresolved if observed at low S/N. Alternatively, stellar contaminants can be selected from our sample on the basis of their optical through near-infrared. We fit the SEDs of all objects in the photometric catalog with M, L, and T dwarf stellar templates (Leggett et al., 2002; West et al., 2005; Kraus et al., 2006). We construct a list of stellar contaminants by examining each object well-fit with stellar colors, only including sources without extended emission. Our final list consists of 11 stars (5% of the total sample) with $z'_{850LP} = 24.3 - 26.5$, each of which we remove from our photo-z sample.

Low-redshift galaxies with intrinsically red colors arising from dust extinction or an old stellar population commonly contaminate traditional dropout samples because their (v_{606W}-i'_{775W}) colors are similar to those of $z \simeq 5$ star-forming objects. By considering the shape of the entire SED, low-z interlopers can often be identified and removed from high-redshift dropout samples. Since the GOODS-MUSIC photometric redshifts are computed using the entire SED, we expect the contamination rate from low-z galaxies to be low. Nevertheless, we believe it is important to explore the

possibility that low-redshift galaxies may remain in the GOODS-MUSIC sample and examine the effects that possible contaminants may have on our final results.

A simple way to estimate the contamination rate from low-z galaxies is to measure the rest-frame UV−optical colors of each of the objects in our sample. Unextincted star-forming objects at $z \simeq 5$ typically have spectra that are roughly flat in f_ν (as a function of wavelength) between the Lyman break and rest-frame ≃4000 Å. In contrast, the colors of low-redshift contaminants are red in all filters. To quantify the expected difference in rest-frame UV−optical colors between $z \simeq 5$ sources and possible low-z contaminants, we examined a set of Bruzual & Charlot (2003) population synthesis models. Elliptical galaxies at $z \simeq$1-2 with ages >2 Gyr have $(z'_{850LP} - J)$ colors that vary between 1.4 - 1.6; whereas young (≃ 100 Myr) star-forming galaxies at $z \simeq$5 with E(B−V)=0.0-0.2 have $(z'_{850LP} - J)$ colors ranging between −0.1 and −0.3 Accordingly, to test the low-z contamination rate, we adopt a $(z'_{850LP} - J) > 1.0$ threshold [5] above which we consider galaxies to be possible low-z interlopers. Seven objects in our photo-z sample satisfy this color criterion. Six of the seven objects are relatively faint in the IRAC filters, and thus will hardly contribute to the total stellar mass of the sample. One of the objects (23_18055), however, is very bright in the near and mid-infrared ($m_{3.6\mu m}$=21.1); if at z≃5, its best-fit stellar mass would be 2×10^{12} $M_\odot$. Given that no objects are identified at $z > 4$ with stellar masses above 3×10^{11} $M_\odot$ in the 0.8 sq deg UKIDSS survey (Dunlop et al., 2006), we conclude that it is much more realistic to adopt a low-z interpretation for this object. So as not to bias our total mass estimates we remove the seven objects with $(z'_{850LP} - J)> 1.0$ from our photo-z sample, leaving 196 objects.

The final photometric sample is that for which the *Spitzer* IRAC images reveal a clear, unconfused, detection. Reliable stellar masses cannot otherwise be determined. We examined the *Spitzer* images of each of the 196 $z \simeq$5 candidates, classifying them as either (1) isolated and detected, (2) undetected, (3) confused or (4) hopelessly confused. In the subsequent analysis, we consider only those objects that are detected and isolated. Of the 196 candidates, 72 are sufficiently uncontaminated to allow

[5]The precise value of this color discriminant is not critical in defining the final sample

reliable estimates of the stellar mass.

Table 2.1 lists the measured optical through infrared AB magnitudes (corrected to approximate total magnitudes through an aperture correction), colors, and photometric redshifts for the remaining 72 $z \simeq 5$ objects.

Table 2.1. Photometric catalog of $z \simeq 5$ galaxies in GOODS-S Field

ID	RA (J2000)	Dec (J2000)	v	i'	z'	J	K_s	3.6 μm	4.5 μm	z_{phot}
44_2919	03 32 9.054	-27 43 51.85	27.58±0.16	26.02±0.08	25.65±0.07	25.37±0.26	25.50±0.44	24.01±0.09	24.29±0.14	4.590
42_3601	03 32 10.64	-27 50 29.15	26.83±0.08	25.69±0.06	25.60±0.07	26.04±0.42	25.37±0.37	24.93±0.20	25.41±0.43	4.480
33_4001	03 32 11.44	-27 47 38.63	27.88±0.18	25.95±0.06	25.77±0.07	25.43±0.31	25.46±0.71	24.00±0.09	24.31±0.17	4.720
33_4496	03 32 12.42	-27 47 2.483	27.83±0.20	26.35±0.10	26.21±0.12	26.35±0.59	26.03±0.98	>25.8	>25.4	4.480
33_4687	03 32 12.78	-27 48 2.599	27.47±0.11	26.15±0.07	25.96±0.08	25.48±0.26	25.58±0.62	24.29±0.10	24.95±0.23	4.590
34_4915	03 32 13.25	-27 43 8.289	27.90±0.22	26.32±0.10	26.16±0.11	25.93±0.41	25.85±0.68	25.59±0.41	>25.4	4.680
35_5207	03 32 13.88	-27 41 48.54	29.35±0.83	27.27±0.23	26.49±0.15	29.30±9.44	>25.3	25.88±0.61	>25.4	5.340
33_5533	03 32 14.49	-27 49 32.69	26.67±0.07	25.69±0.06	25.53±0.06	26.21±0.56	25.53±0.48	25.07±0.33	25.85±0.72	4.460
33_5986	03 32 15.35	-27 49 36.08	27.78±0.19	26.15±0.09	26.35±0.13	25.79±0.38	25.40±0.41	25.27±0.58	26.18±0.44	4.610
33_6438	03 32 16.17	-27 46 41.59	28.74±0.47	26.25±0.10	26.00±0.10	26.63±0.75	>25.3	25.16±0.22	26.04±0.64	5.080
33_6440	03 32 16.17	-27 48 19.42	27.83±0.20	26.39±0.11	26.25±0.13	25.71±0.33	25.00±0.38	24.88±0.15	25.28±0.31	4.700
33_6519	03 32 16.34	-27 48 31.99	27.87±0.21	26.06±0.08	26.13±0.11	>26.0	>25.3	25.79±0.31	26.19±0.68	4.490
33_6575	03 32 16.45	-27 46 39.24	29.45±0.89	26.49±0.12	26.11±0.11	25.90±0.39	25.08±0.41	24.22±0.09	25.00±0.25	5.210
32_6854	03 32 16.98	-27 51 23.17	27.41±0.14	25.62±0.05	25.70±0.08	25.97±0.44	24.48±0.19	23.97±0.07	24.44±0.16	4.550
35_6867	03 32 17.00	-27 41 13.71	26.89±0.08	25.38±0.04	25.13±0.04	24.92±0.23	24.37±0.24	23.43±0.04	23.82±0.08	4.590
32_8020	03 32 18.91	-27 53 2.746	27.77±0.19	25.13±0.03	24.49±0.03	24.74±0.13	24.06±0.13	22.73±0.02	22.74±0.03	5.550
31_8593	03 32 19.96	-27 54 58.98	28.64±0.56	26.84±0.21	25.83±0.11	25.50±0.34	25.59±0.45	24.66±0.11	25.23±0.26	5.320
31_9014	03 32 20.70	-27 55 36.14	26.70±0.10	25.67±0.08	25.72±0.10	25.99±0.54	24.99±0.26	24.08±0.07	24.32±0.12	4.520
33_9184	03 32 21.01	-27 49 59.16	27.23±0.12	26.03±0.08	26.16±0.11	26.67±0.63	>25.3	>25.8	>25.4	4.580
33_9338	03 32 21.28	-27 49 59.67	28.54±0.38	26.84±0.16	26.14±0.11	25.85±0.30	26.64±0.92	25.76±0.26	25.35±0.26	5.500
33_9677	03 32 21.82	-27 50 3.346	28.74±0.46	26.49±0.12	26.48±0.15	>26.0	25.48±0.31	25.56±0.28	>25.4	4.800
34_9738	03 32 21.93	-27 45 33.07	28.22±0.29	26.20±0.09	25.82±0.09	26.20±0.51	24.90±0.23	24.31±0.09	24.72±0.18	4.800
33_9812	03 32 22.02	-27 46 42.89	26.76±0.08	25.41±0.05	25.26±0.05	25.94±0.48	24.84±0.25	23.84±0.06	24.05±0.10	4.510
34_9822	03 32 22.03	-27 45 29.31	27.38±0.14	26.41±0.11	26.28±0.13	26.00±0.42	>25.3	25.30±0.22	25.42±0.33	4.570

Table 2.1 (cont'd)

ID	RA (J2000)	Dec (J2000)	v	i'	z'	J	K_s	3.6 μm	4.5 μm	z_{phot}
33_10064	03 32 22.44	-27 47 46.17	28.58±0.40	26.64±0.14	26.34±0.13	26.46±0.77	25.57±0.47	24.86±0.13	25.22±0.27	5.020
32_10232	03 32 22.71	-27 51 54.40	27.90±0.25	26.14±0.10	25.68±0.08	25.58±0.28	25.03±0.24	24.27±0.08	24.82±0.16	5.050
33_10340	03 32 22.88	-27 47 27.56	26.64±0.07	24.94±0.04	24.84±0.04	24.55±0.13	24.59±0.16	23.75±0.05	24.01±0.10	4.440
31_10974	03 32 24.00	-27 54 59.79	27.51±0.16	25.46±0.05	24.73±0.03	24.56±0.16	24.89±0.25	25.39±0.41	25.88±0.66	5.380
32_11635	03 32 25.02	-27 50 24.49	29.10±0.56	27.13±0.18	26.05±0.09	25.61±0.24	25.42±0.30	24.68±0.13	24.67±0.17	5.430
33_13701	03 32 27.94	-27 46 18.57	26.37±0.06	25.18±0.04	25.22±0.05	25.09±0.21	24.44±0.15	24.02±0.10	24.13±0.13	4.480
34_14195	03 32 28.70	-27 42 28.95	28.11±0.21	26.23±0.08	26.03±0.08	26.82±0.84	>25.3	25.67±0.34	>25.4	4.840
23_15316	03 32 30.28	-27 49 22.01	28.04±0.25	26.47±0.12	25.88±0.09	26.30±0.47	>25.3	>25.8	>25.4	5.200
22_15851	03 32 31.07	-27 51 17.85	28.91±0.54	26.17±0.09	26.04±0.10	26.06±0.40	24.89±0.22	24.62±0.17	24.93±0.25	4.820
23_16055	03 32 31.37	-27 48 13.81	28.08±0.26	26.20±0.10	25.89±0.09	25.09±0.20	25.66±0.39	24.94±0.14	25.42±0.32	4.990
22_17535	03 32 33.69	-27 53 21.62	29.06±0.61	27.28±0.24	26.39±0.14	>26.0	>25.3	26.28±0.60	>25.4	5.360
23_17728	03 32 33.98	-27 48 2.043	27.61±0.17	26.10±0.09	25.90±0.09	25.74±0.29	24.52±0.13	24.08±0.07	24.24±0.11	4.470
23_18716	03 32 35.45	-27 49 35.20	29.41±0.60	26.63±0.10	26.35±0.09	25.71±0.28	25.94±0.49	25.12±0.22	25.91±0.56	4.930
22_19011	03 32 35.89	-27 52 44.02	27.78±0.19	26.51±0.12	26.27±0.12	26.92±0.85	>25.3	25.70±0.34	>25.4	4.740
24_19118	03 32 36.08	-27 44 3.942	27.28±0.12	26.07±0.08	25.75±0.08	24.80±0.12	25.22±0.26	24.38±0.13	25.01±0.27	4.550
23_19268	03 32 36.30	-27 49 52.79	27.44±0.14	26.03±0.08	25.86±0.09	25.36±0.21	24.70±0.16	23.96±0.09	24.56±0.18	4.510
24_19435	03 32 36.49	-27 43 53.46	28.52±0.37	26.93±0.17	26.43±0.14	25.83±0.31	25.93±0.55	25.01±0.19	25.59±0.42	4.620
25_19912	03 32 37.25	-27 42 2.570	28.47±0.35	26.42±0.11	26.00±0.10	25.81±0.32	>25.3	25.04±0.18	25.53±0.41	5.180
22_20159	03 32 37.62	-27 50 22.38	>29.5	27.18±0.22	26.24±0.12	25.37±0.20	25.54±0.36	24.64±0.14	24.66±0.17	5.510
22_20304	03 32 37.86	-27 52 59.10	27.43±0.15	26.47±0.12	26.25±0.13	>26.0	>25.3	25.68±0.45	25.92±0.57	4.520
23_20360	03 32 37.95	-27 47 11.05	27.39±0.13	25.80±0.07	26.21±0.12	>26.0	>25.3	24.93±0.19	>25.4	4.690
22_21669	03 32 40.08	-27 50 49.60	27.72±0.18	26.28±0.10	26.05±0.10	25.74±0.30	25.56±0.40	25.45±0.29	26.17±0.64	4.520
24_22091	03 32 40.85	-27 45 46.25	28.03±0.18	26.14±0.07	25.33±0.04	25.12±0.14	25.22±0.32	24.76±0.12	24.45±0.14	5.400
23_22354	03 32 41.34	-27 48 43.13	28.02±0.24	26.31±0.11	26.14±0.11	>26.0	26.02±0.62	24.72±0.13	25.46±0.33	4.530

Table 2.1 (cont'd)

ID	RA (J2000)	Dec (J2000)	v	i'	z'	J	K_s	3.6 μm	4.5 μm	z_{phot}
25_22925	03 32 42.36	-27 41 14.87	27.38±0.21	25.94±0.13	25.41±0.09	26.10±0.62	24.65±0.36	24.12±0.09	24.77±0.21	5.010
24_23215	03 32 42.95	-27 43 39.65	29.16±0.67	26.68±0.14	26.09±0.11	>26.0	>25.3	25.94±0.59	25.84±0.63	5.200
24_23395	03 32 43.30	-27 43 10.59	28.73±0.45	26.14±0.09	26.25±0.12	25.60±0.32	>25.3	24.74±0.16	25.10±0.30	4.780
23_23515	03 32 43.53	-27 49 19.21	27.89±0.21	25.80±0.07	25.53±0.07	26.05±0.34	25.84±0.50	24.89±0.15	25.92±0.49	5.090
22_25323	03 32 47.58	-27 52 28.18	28.49±0.34	26.43±0.11	26.24±0.11	25.43±0.26	>25.3	25.43±0.29	>25.4	4.760
13_25544	03 32 48.14	-27 48 17.69	27.95±0.23	26.04±0.09	25.41±0.06	25.64±0.28	24.89±0.25	24.65±0.12	24.97±0.24	5.170
14_25620	03 32 48.33	-27 45 38.90	27.86±0.21	26.24±0.11	26.37±0.14	26.42±0.49	25.75±0.52	>25.8	>25.4	4.610
12_25696	03 32 48.53	-27 54 25.67	27.44±0.12	26.28±0.08	26.24±0.10	26.49±0.77	>25.3	24.89±0.20	25.63±0.45	4.530
12_25851	03 32 48.89	-27 52 43.17	27.75±0.18	26.49±0.12	26.39±0.14	>26.0	>25.3	>25.8	>25.4	4.540
12_25952	03 32 49.15	-27 50 22.52	28.24±0.29	26.04±0.08	25.30±0.05	25.27±0.19	25.52±0.39	25.20±0.18	25.54±0.33	5.360
12_26198	03 32 49.81	-27 50 22.75	28.23±0.28	26.42±0.10	26.12±0.10	25.58±0.27	25.35±0.35	25.94±0.41	26.22±0.65	5.110
12_26409	03 32 50.44	-27 50 39.64	>29.5	27.01±0.20	26.38±0.14	>26.0	>25.3	26.30±0.57	26.70±0.99	5.460
13_26480	03 32 50.63	-27 49 34.79	>29.5	26.83±0.16	26.36±0.14	>26.0	>25.3	>25.8	>25.4	5.220
13_26492	03 32 50.65	-27 47 15.18	26.80±0.09	25.84±0.08	25.64±0.07	26.26±0.49	>25.3	25.42±0.28	>25.4	4.430
12_26985	03 32 51.94	-27 52 8.494	27.46±0.15	26.04±0.09	25.95±0.09	26.19±0.58	>25.3	>25.8	>25.4	4.580
12_27749	03 32 54.05	-27 51 12.02	29.12±0.68	27.09±0.20	26.32±0.13	>26.0	>25.3	25.82±0.85	>25.4	5.500
12_28370	03 32 56.22	-27 51 51.29	27.81±0.20	26.33±0.10	26.17±0.11	>26.0	>25.3	25.01±0.21	>25.4	4.570
12_28389	03 32 56.29	-27 53 31.53	27.33±0.12	25.66±0.05	25.60±0.07	24.62±0.17	24.83±0.27	24.61±0.15	25.03±0.29	4.690
12_28728	03 32 57.68	-27 53 19.67	28.05±0.25	26.09±0.08	26.08±0.10	25.99±0.59	>25.3	24.99±0.21	25.26±0.32	4.930
12_28859	03 32 58.38	-27 53 39.59	26.41±0.05	25.54±0.04	25.62±0.06	>26.0	26.65±0.88	24.98±0.30	24.92±0.28	4.420
12_28917	03 32 58.66	-27 52 43.69	28.33±0.32	26.11±0.09	25.81±0.08	>26.0	24.98±0.33	25.05±0.20	25.94±0.64	4.840
12_28990	03 32 59.01	-27 53 32.22	27.47±0.13	25.55±0.05	25.20±0.04	25.13±0.21	24.42±0.17	23.39±0.06	24.07±0.13	4.860
12_29097	03 32 59.72	-27 52 2.582	29.20±0.73	26.31±0.10	25.67±0.07	>26.0	>25.3	24.05±0.11	24.66±0.25	5.170
12_29119	03 32 59.89	-27 52 56.42	28.53±0.40	26.70±0.15	26.29±0.13	>26.0	24.91±0.15	23.88±0.08	24.12±0.14	4.890

Table 2.1 (cont'd)

ID	RA (J2000)	Dec (J2000)	v	i'	z'	J	K_s	3.6 μm	4.5 μm	z_{phot}

2.4.2 The Spectroscopic Sample

The FORS2/VLT spectroscopic survey of the GOODS-S field identified 30 unique galaxies in the $4.4 < z < 5.6$ redshift range. The quality flags associated with the redshift assignments range from A (solid) to C (potential). As with the photometric sample, we adopt a magnitude limit of $z'_{850LP} < 26.5$; this requirement excises one object (35_11820) from the sample. Given the possibility of uncertainties in the spectroscopic identification of those sources with C-grade redshifts, we examined their rest-frame ultraviolet colors ($v_{606W} - i'_{775W}$) vs. ($i'_{775W} - z'_{850LP}$) as an additional criterion for selection (Figure 2.2).

Of the 29 remaining FORS2 galaxies with spectroscopic redshifts of $z \simeq 5$, only 17 would be selected as v-drops using the Giavalisco et al. (2004a) selection criteria. An additional 8 of the spectroscopically-confirmed $z \simeq 5$ galaxies fall very near the v-drop selection window in the ($v_{606W} - i'_{775W}$) vs. ($i'_{775W} - z'_{850LP}$) color-color plot. As their colors are consistent with the Bruzual & Charlot redshift tracks (plotted in Figure 2.2) we include them in this sample. Three objects are apparently undetected in the *ACS* images of GOODS-S. Without the availability of rest-frame UV colors, we cannot confirm that the objects are truly located $z \simeq 5$ via the presence of the Lyman break; we presume these were serendipitous detections and exclude them from the final spectroscopic sample. The final object (22_15184) is formally a B-dropout; its relatively blue ($v_{606W} - i'_{775W}$) color is inconsistent with that expected from a v-drop. At the object's purported redshift ($z = 5.08$) Lyα falls in the i'-band, making the intrinsic ($v_{606W} - i'_{775W}$) *bluer* than what is measured. Given the peculiar colors, we exclude it from the spectroscopic catalog.

As before, we examined the *Spitzer* images of each of the 25 spectroscopically-confirmed galaxies for detections and the degree of confusion. These classifications are shown in Table 2.2. Five objects were isolated and detected in the Spitzer images, four sources were hopelessly confused, and the remaining 16 objects were marginally confused. For the 16 partially confused galaxies, we attempted to subtract the contribution from contaminating sources using the 'GALFIT' software package (Peng

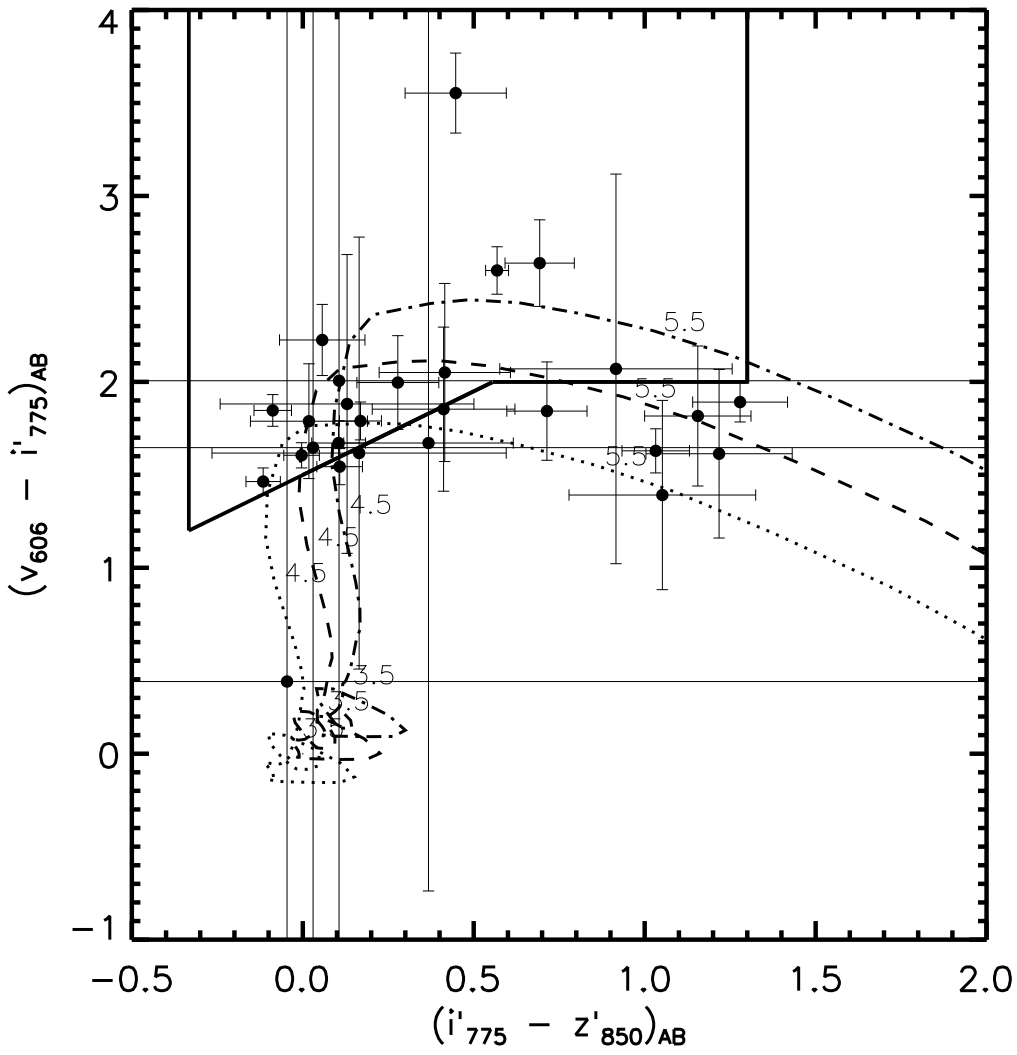

Figure 2.2 ($v_{606W} - i'_{775W}$) vs. ($i'_{775W} - z'_{850LP}$) colors of 30 galaxies with FORS2/VLT spectroscopic redshifts of 4.4 < z < 5.6. The v-drop selection window described in Giavalisco et al. (2004a) is overlaid with a solid line. Starburst redshift tracks are identical to those described in Figure 2.1. Removing objects that either do not satisfy the magnitude limit of z'_{850LP} <26.5 or do not have the rest-frame UV colors expected for a $z \simeq 5$ LBG leaves a sample of 25 objects.

Table 2.2. Spectroscopically-confirmed $z \simeq 5$ galaxies in GOODS-S Field

ID	RA (J2000)	Dec (J2000)	Redshift	$v - i'$	$i' - z'$	Spit. Confusion	z_{spec} Flag	Included?
44_1543	03 32 5.258	-27 43 0.406	4.81	1.85	-0.09	4	A	N
35_4142	03 32 11.71	-27 41 49.59	4.91	1.79	0.17	3	C	Y
35_4244	03 32 11.92	-27 41 57.09	5.57	1.39	1.05	3/4	B	N
35_6626	03 32 16.55	-27 41 3.203	5.25	2.07	0.92	3	C	Y
35_6867	03 32 17.00	-27 41 13.71	4.41	1.54	0.11	1	B	N
33_7471	03 32 17.95	-27 48 17.01	5.40	1.82	1.16	4	C	N
32_8020	03 32 18.91	-27 53 2.746	5.55	2.60	0.57	1	A	Y
35_9350	03 32 21.30	-27 40 51.20	5.29	1.84	0.71	1	A	Y
34_9738	03 32 21.93	-27 45 33.07	4.78	2.00	0.28	3	C	Y
32_10232	03 32 22.71	-27 51 54.40	4.90	2.05	0.42	1	C	Y
33_10340	03 32 22.88	-27 47 27.56	4.44	1.60	0.00	1	B	Y
no_ACS_01	03 32 22.89	-27 45 20.99	5.12	...	...	...	C	N
33_10388	03 32 22.97	-27 46 29.09	4.50	1.65	0.03	3/4	C	N
34_11820	03 32 25.31	-27 45 30.85	4.99	3.55	0.45	2	B	Y
35_14097	03 32 28.56	-27 40 55.71	4.59	1.67	0.37	3	B	Y
35_14303	03 32 28.84	-27 41 32.70	4.80	1.79	0.02	4	B	N
no_ACS_02	03 32 28.93	-27 41 28.19	4.88	...	...	...	B	N
31_14602	03 32 29.29	-27 56 19.46	4.76	1.67	0.10	3	B	Y
22_15184	03 32 30.09	-27 50 57.72	5.08	0.39	-0.05	...	B	N
24_18073	03 32 34.48	-27 44 3.008	4.94	1.46	-0.12	3/4	C	N
22_20159	03 32 37.62	-27 50 22.38	5.51	1.89	1.28	3/4	A	N
22_21502	03 32 39.81	-27 52 58.09	5.54	1.63	1.03	4	C	N
24_21686	03 32 40.11	-27 45 35.49	4.77	1.62	0.16	3/4	B	N
21_23040	03 32 42.62	-27 54 28.95	4.40	1.85	0.41	3	C	Y
23_23051	03 32 42.65	-27 49 38.99	4.84	2.23	0.06	3	C	Y
no_ACS_03	03 32 43.15	-27 50 34.80	4.83	...	...	...	C	N
23_24305	03 32 45.23	-27 49 9.829	5.58	1.61	1.22	3/4	B	N
21_24396	03 32 45.42	-27 54 38.52	5.37	2.64	0.69	3	A	Y
22_25323	03 32 47.58	-27 52 28.18	4.75	2.01	0.11	3	C	Y
12_28085	03 32 55.08	-27 54 14.48	4.71	1.88	0.13	3/4	A	N

Note. — All magnitudes are in AB system. no_ACS_01, no_ACS_02, and no_ACS_03, were not detected with *ACS*. The *Spitzer* confusion classes have the following meanings: 1 = isolated and detected; 2 = isolated but undetected; 3 = confused, but Galfit may help ; 4 = hopelessly confused. Those sources with Spitzer confusion class '3/4' were deemed hopelessly confused after attempting (and failing) to subtract nearby sources with Galfit.

et al., 2002); this was deemed worthy given the need to maximize the information from the limited spectroscopic data.

GALFIT constructs a two-dimensional model of the data according to specified input parameters (e.g., magnitude, position, axis ratio, effective radius), performs a convolution with the instrument point spread function (PSF), and fits the result to the data through an iterative χ^2 minimization process. We determined the PSF for each epoch and channel of the 'drizzled' *Spitzer* images by stacking 4 bright but isolated stars. For each galaxy we assumed a generalized Sérsic surface brightness profile, where $\log I \propto r^{1/n}$, and fit for the shape and index n.

Table 2.3. Photometric Properties of z≃5 spectroscopically-confirmed galaxies.

ID	z_{spec}	v	i'	z'	J	K_s	3.6 μm	4.5 μm
35_4142	4.912	27.22±0.11	25.51±0.05	25.26±0.05	25.19±0.22	25.09±0.35	25.11±0.27	25.65±0.54
35_6626	5.250	29.07±0.62	27.18±0.21	26.35±0.13	···	···	26.19±0.52	>25.4
35_6867	4.416	26.89±0.08	25.38±0.04	25.13±0.04	24.92±0.23	24.37±0.24	23.43±0.04	23.82±0.08
32_8020	5.554	27.77±0.19	25.13±0.03	24.49±0.03	24.74±0.13	24.06±0.13	22.73±0.02	22.74±0.03
35_9350	5.283	28.07±0.32	26.04±0.10	25.41±0.08	···	···	···	25.52±0.60
34_9738	4.788	28.22±0.29	26.20±0.09	25.82±0.09	26.20±0.51	24.90±0.23	24.31±0.09	24.72±0.18
32_10232	4.900	27.90±0.25	26.14±0.10	25.68±0.08	25.58±0.28	25.03±0.24	24.27±0.08	24.82±0.16
33_10340	4.440	26.64±0.07	24.94±0.04	24.84±0.04	24.55±0.13	24.59±0.16	23.75±0.05	24.01±0.10
34_11820	4.992	28.78±0.45	26.95±0.16	26.66±0.16	>26.0	25.63±0.46	>25.8	>25.4
35_14097	4.597	27.72±0.17	25.92±0.07	25.87±0.08	···	···	25.19±0.30	25.16±0.38
31_14602	4.760	26.76±0.09	25.04±0.04	24.88±0.04	···	···	22.64±0.02	22.55±0.02
21_23040	4.400	28.17±0.28	26.12±0.08	25.79±0.08	25.30±0.26	25.49±0.43	24.02±0.06	24.57±0.14
23_23051	4.840	28.31±0.31	26.04±0.08	25.86±0.09	26.19±0.38	25.87±0.50	24.93±0.14	25.12±0.23
21_24396	5.370	28.94±0.55	26.09±0.08	25.30±0.05	24.99±0.22	25.11±0.33	24.80±0.16	24.21±0.11
22_25323	4.758	28.49±0.34	26.43±0.11	26.24±0.11	25.43±0.26	>25.3	25.43±0.29	>25.4

Note. — The VLT mosaic does not cover the entire GOODS field. Those sources that are located off the edge of the VLT images denoted by an ellipsis.

An automated script was developed to run GALFIT three times per source on a $12 \times 12\,\mathrm{arcsec}^2$ region surrounding the contaminated object for the IRAC images. In the first iteration, we held all source parameters fixed in the fitting process except the source magnitude, which was estimated from the SExtractor source detection software version-2.2.1 (Bertin & Arnouts, 1996) . All other input source parameters (e.g. position, axis ratio, position angle, effective radius, Sérsic parameter) were estimated from a fit to the VLT K_s-band image. The higher spatial resolution of the K_s-band allows better deblending and more accurate centroids to be derived for confusing objects in the IRAC images. In the second GALFIT iteration, we again determined input parameters using our fit to the K_s-band image, but this time we allowed all parameters to vary. In the final iteration, we obtained the initial parameters by applying SExtractor to the IRAC channel 1 ($3.6\,\mu$m) image and allowing all parameters to vary. For each source, we selected the most successful of the three GALFIT runs, on the basis of visual inspection of the residual image and the χ^2 value for the fit. Those sources (7 out of 16) for which GALFIT failed to satisfactorily subtract contaminating emission were removed from the sample (see Table 2.2). The photometry of the remaining 14 galaxies are described in Table 2.3.

2.5 Stellar Mass Determination

Although we have removed many sources from the original spectroscopic and photometric samples, it is worth reminding that the degree of confusion in the IRAC images should, on average, be completely independent of the stellar mass of the $z \simeq 5$ galaxy. Confusion in the IRAC images will normally arise from the overlapping isophotes of unrelated sources. Thus, if sources are believed to be at $z \simeq 5$ on the basis of a spectroscopic redshift or the ACS and K-band photometric SED, we can rescue a reasonable estimate of their contribution to the stellar mass density by scaling that determined for the unconfused sample using the relative numbers.

2.5.1 Masses for the Spectroscopic Sample

For those galaxies with confirmed spectroscopic redshifts, we estimate stellar masses by fitting population synthesis models to the observed SEDs. Applying this technique to galaxies for which the redshift is unknown may lead to significant uncertainty in the derived properties (Bundy et al., 2005; Shapley et al., 2005), hence for the photometrically-selected sample, we infer stellar mass by applying the median mass-to-light ratio derived from the spectroscopic sample.

We proceed as Eyles et al. (2005) by fitting the latest Bruzual & Charlot (2003) stellar population synthesis models to the observed SEDs. We use the Padova evolutionary tracks preferred by Bruzual & Charlot (2003). The models utilise 221 age steps from 10^5 to 2×10^{10} yr, approximately logarithmically spaced. For each source, we do not include age steps in excess of the age of the universe at $z \simeq 5$ ($\simeq 1.2$ Gyr). Models with Salpeter (1955) initial mass functions (IMF) were selected; although we also considered the effect of adopting a Chabrier (2003) IMF. There are 6900 wavelength steps, with high resolution (FWHM 3 Å) and 1 Å pixels evenly-spaced over the wavelength range of 3300 Å to 9500 Å (unevenly spaced outside this range). From the full range of metallicities offered by the code, we considered both solar and 0.25 $Z_\odot$ models. From several star formation histories available, a single stellar population (SSP – an instantaneous burst), a constant star formation rate (SFR), and exponen-

tially decaying (τ) SFR models with e-folding decay timescales τ=10, 30, 50, 70, 100, 200, 300, 500, 1000 Myr were used.

For each of the galaxies in our sample, the filters were corrected to their rest-frame wavelengths by the appropriate redshift factor. The measured flux was folded through the filter transmission profiles, and the best-fit age model was computed by minimizing the reduced χ^2, using the measured errors on the magnitudes. The number of degrees of freedom is the number of independent data points (magnitudes in different wavebands) minus the number of parameters that we are fitting. The Bruzual & Charlot spectra are normalized to an initial mass of $1\,M_{\odot}$ for the instantaneous burst (SSP) model, and an SFR of $1\,M_{\odot}\,\mathrm{yr}^{-1}$ for the continuous star formation model. The fitting routine returned the normalisation for the model which was the best-fit to the broad band photometry (i.e., minimized the reduced χ^2). This normalization was then used to calculate the corresponding best-fit total mass using the luminosity distance for the redshift of each source. When considering models other than an SSP (instantaneous burst), it was necessary to correct the total 'mass' values output by the fitting routine. For a constant SFR model, each of these masses needed to be multiplied by the corresponding best-fit age, since the B&C template normalization has the mass grow by 1 $\mathrm{M}_{\odot}\ \mathrm{yr}^{-1}$. For the exponential decay models, the returned mass values were corrected by dividing by $(1-\mathrm{e}^{-t/\tau})$, accounting for the decay timescale and the normalization of the B&C models (where $\mathrm{M} \longrightarrow 1\ \mathrm{M}_{\odot}$ as $\mathrm{t} \longrightarrow \infty$). The fits to the B&C models returned the 'total mass' which is the sum of the mass currently in stars, in stellar remnants, and in gas returned to the interstellar medium by evolved stars. For each best-fit model, we subsequently calculate the mass currently in stars for every galaxy, again using information from the B&C population synthesis code; we use this stellar mass in all future analysis.

Although some of our data points (particularly from the *HST*/ACS imaging) have $S/N > 10$, we set the minimum magnitude error to be $\Delta(\mathrm{mag}) = 0.1$ to account for calibration uncertainties. Futhermore, we do not include data with photometric error above 0.72 mags (1.5 σ).

The presence of a strong spectral line in one of the broadband filters could signifi-

cantly skew the SED fitting. Seven of the 15 galaxies in our spectroscopic sample show powerful Lyα emission. Using the FORS2 spectra, we compute and subtract the Lyα contribution to the broadband flux; corrections range from $0.01 - 0.1$ mags for most sources. Hα contamination could also be a significant issue - Chary et al. (2005) claim to find an excess due to Hα in a z=6.5 galaxy (in the 4.5μm band at that redshift). The sources in our sample are likely to have Hα emission lines as well, which at z$\simeq$5 fall in either the 3.6 μm or 4.5 μm IRAC filter. Indeed many of the SED fits discussed below show an excess at 3.6 μm. Without a direct measure of the Hα line strengths, we cannot robustly remove the line contamination. We estimate that, for most sources, Hα contributes $\simeq$10-20% of the measured broadband flux by converting the inferred rest-frame UV star formation rate to an H-alpha luminosity via empirically-derived relations from Kennicutt (1998) assuming $< SFR_{H\alpha}/SFR_{UV} >$=1.5-3 due to dust extinction in agreement with observations, e.g. Erb et al. (2003). To test the effects that Hα contamination may have on our sources, we re-fit all the objects in the spectroscopic sample, omitting the flux information at 3.6 μm for objects with $z < 5.2$ and at 4.5 μm for objects with $z > 5.2$. We find that this does not significantly change the total stellar mass found in our spectroscopic sample.

The degeneracies associated with the derived best-fit parameters from SED fitting are well known (Shapley et al., 2001; Papovich et al., 2001; Shapley et al., 2005). The uncertainties primarily stem from a poor knowledge of the form of the star formation history, since the best fit age, dust extinction and star formation rate rely on this (Shapley et al., 2005). In most cases, the data do not put strong constraints on the form of the star formation history; hence each fitted parameter typically has a range of values that produce acceptable fits.

The inferred properties also rely on knowledge of the stellar initial mass function (IMF). There is little observational information constraining the IMF at high redshift. The spectrum of the z=2.7 gravitationally-lensed LBG cB58 appears to be inconsistent with IMFs that have steep high-mass slopes or are truncated at high stellar masses (Pettini et al., 2000). Whether this is typical among LBGs is unclear. Papovich et al. (2001) studied the effects that varying the IMF have on the best-

Table 2.4. Modeling Results

Object	Star Formation History	log $M_{stellar}$($M_\odot$)	Age (Myr)	E(B-V)	χ^2
35_4142	csf	9.34	161	0.00	2.11
35_6626	70	9.32	143	0.00	0.26
35_6867	100	10.37	360	0.01	1.77
32_8020	300	11.16	905	0.00	2.90
35_9350	csf	9.33	255	0.00	0.57
34_9738	100	10.13	360	0.00	1.37
32_10232	70	10.06	255	0.01	2.22
33_10340	100	11.28	18	0.24	1.82
35_14097	200	9.93	255	0.05	0.04
31_14602	300	11.10	1015	0.00	1.79
21_23040	burst	8.43	1	0.53	2.24
23_23051	100	9.86	286	0.00	0.47
21_24396	burst	8.40	9	0.17	0.21
22_25323	burst	8.43	3	0.32	0.61

Note. — In the star-formation history column, 'csf' corresponds to constant star formation, while the numbers (e.g 70, 100) correspond to the exponential decay constant (in Myr) for an exponentially-declining star formation history.

fit parameters. Models with IMFs containing steep high-mass slopes (e.g. Scalo, Miller-Scalo) have redder integrated spectra and hence younger derived ages and lower extinction. As with Eyles et al. (2005), we find good agreement between the properties inferred using a Salpeter IMF and a Chabrier IMF: the best-fit ages are nearly the same and the stellar masses are typically 30% lower when the Chabrier IMF is used. Here all masses are quoted for the Salpeter IMF in order to maintain consistency with previous estimates of stellar mass and star formation rates.

In Figure 2.3, we display the best-fit SEDs for each of the galaxies in our spectroscopic sample. The best-fitting model parameters are presented in Table 2.4. The best fitting stellar masses of the galaxies range between 3×10^8 $M_\odot$ and 2×10^{11} $M_\odot$. Derived ages span three orders of magnitude, from 1 Myr to 1.1 Gyr, the age of the Universe at $z \simeq 5$. Interestingly, three of our sources have stellar masses in excess of 10^{11} $M_\odot$, values approaching the high stellar mass for the UDF source located by Mobasher et al (2005). Our results provides support for at least the presence of such galaxies even if their abundance remains uncertain. Moreover, some of the less massive sources can only be fit with remarkably young ages (<20 Myr) reminiscent of the lensed star forming source located by Ellis et al. (2001).

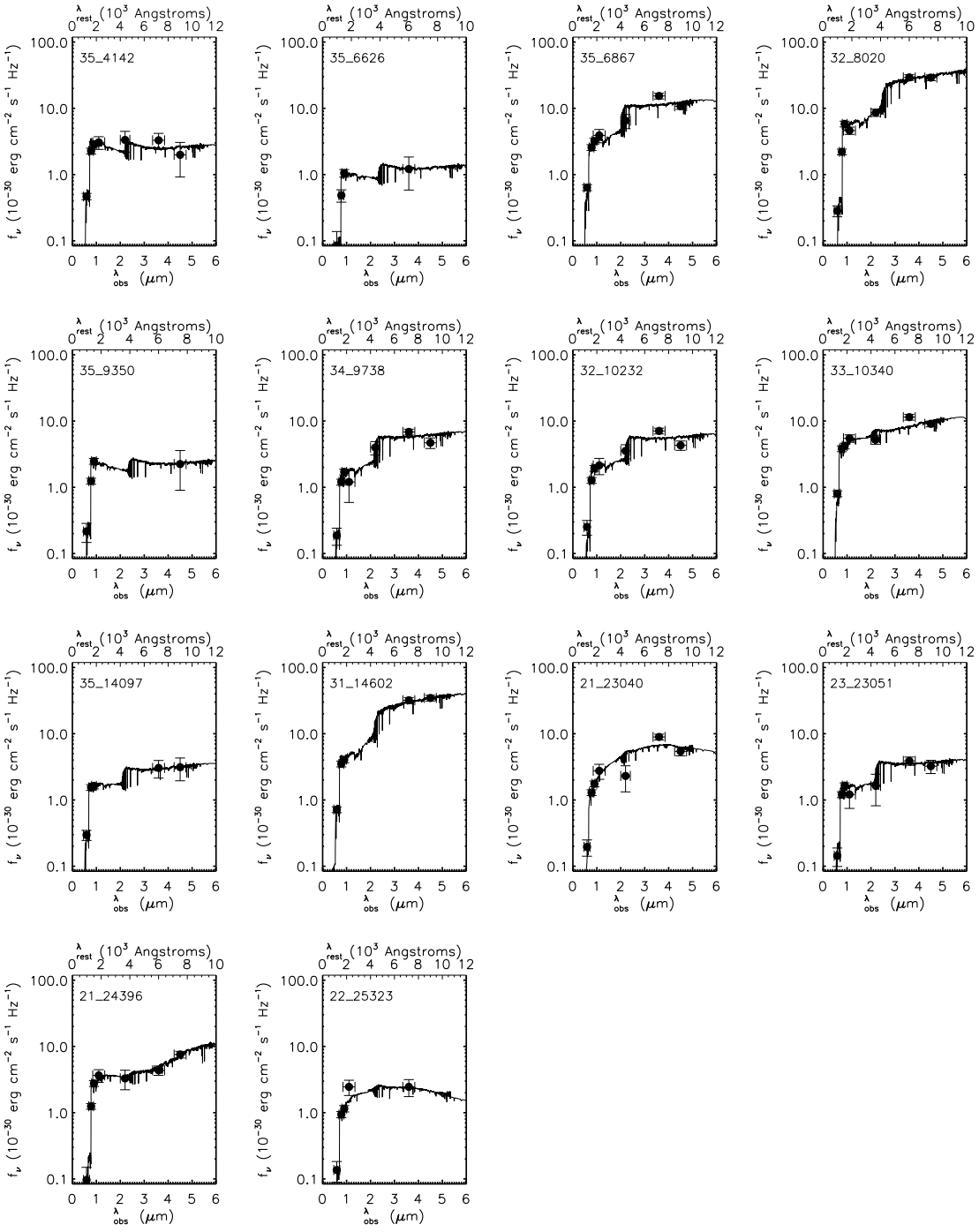

Figure 2.3 Observed and best-fit model Bruzual & Charlot (2003) SEDs of 15 spectroscopically-confirmed $z \simeq 5$ galaxies in GOODS-S.Best-fit model parameters are presented in Table 2.4. Three objects (32_8020, 31_14602, and 33_10340) have inferred stellar masses above 10^{11} $M_{\odot}$, and an additional three objects have inferred stellar masses greater than 10^{10} $M_{\odot}$.

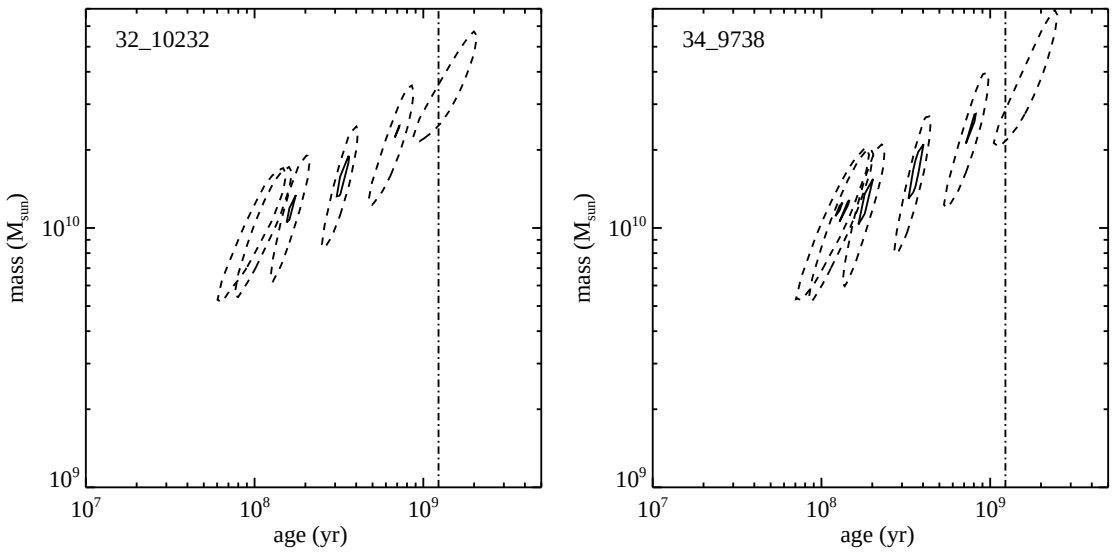

Figure 2.4 Confidence intervals for inferred stellar mass versus age for two objects from the spectroscopically-confirmed z≃5 objects in GOODS-S. The ellipses are different assumed star formation histories, ranging from an initial burst to continuous star formation via a range of exponentially-decaying star formation histories. Contours are 68% confidence (solid line) and 95% confidence (dashed line) corresponding to $\Delta\chi^2_{reduced} = 1$, 4 (respectively), where $\Delta\chi^2_{reduced}=\chi^2_{reduced} - \chi^2_{reduced,min}$. The vertical dashed-dotted line at the right of each plot denotes the age of the universe at the source's redshift. Solutions to the right of this line are ruled out. The typical 68% confidence uncertainties in the stellar mass are are 30-50%.

The total stellar mass of the subsample of spectroscopic galaxies is $5\times\ 10^{11}\,M_{\odot}$. Clearly this estimate is an *unrealistic* lower limit to the total stellar mass since there are nearly twice as many objects known to be at $z \simeq 5$ that certainly have stellar mass.

Uncertainties on this mass arise from two main sources. First, the photometric error for each data-point in the SED translates into an uncertainty in the inferred stellar mass. Second, there is a range in acceptable masses that result from varying the age, extinction, and star formation history. With regard to the latter, we follow the approach outlined in Eyles et al. (2005) where confidence intervals were explored for two sources. We present mass-age confidence intervals for two sources representative of our sample (Figure 2.4). Uncertainties in the inferred stellar mass of individual objects in Table 2.4 range between 30% and 50%. Objects detected at low signal to

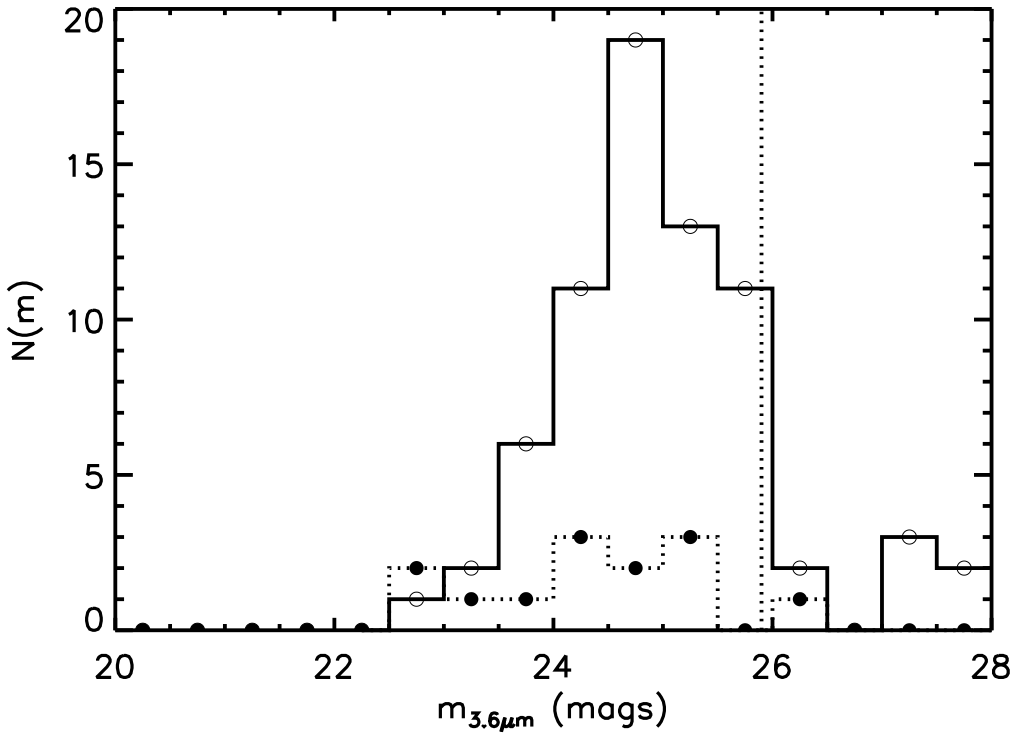

Figure 2.5 Distribution of IRAC 3.6 μm AB magnitudes for 72 photometrically- selected z$\simeq$5 candidates (open circles) and 14 spectroscopically-confirmed z$\simeq$5 galaxies (closed circles). The spectroscopic sample contains a larger relative fraction of Spitzer bright objects.

noise generally have larger uncertainties. Given the range of uncertainties, it seems reasonable to transfer a 50% uncertainty to all of our combined masses.

The FORS2 selection of galaxies was not geared specifically towards constructing a z$\simeq$5 sample; hence it is important to examine how the properties of spectroscopically-confirmed galaxies compares to the photometrically-selected sample. The median rest-frame UV color of the spectroscopic sample, ($< i'_{775W} - z'_{850LP} >$)=0.17, is very similar to the photometrically-selected sample ($< i'_{775W} - z'_{850LP} >$=0.21). The key parameter for determining the stellar mass is the flux in the IRAC filters. The histogram of IRAC 3.6 μm fluxes for the spectroscopic and photometric samples is given in Figure 2.5. The spectroscopic sample does contain a larger fraction of Spitzer-bright (e.g $m_{3.6\mu m} < 23$) objects, but this is reasonable if the overall rest-frame mass/light distribution is fairly similar across the population.

2.5.2 Masses for the Photometric Sample

To estimate stellar masses for the photometric sample we compute the best-fitting rest-frame V-band mass to light ratio of each galaxy that is unconfused in the IRAC images and multiply by the luminosity derived from the IRAC flux.

The best-fitting M/L_V is determined for each galaxy from its $z'_{850LP}-m_{3.6\mu m}$ color (corresponding to the ratio of rest-frame UV and optical fluxes). If we assume the typical galaxy in rest-frame UV selected samples at z$\simeq$5$-$6 has little dust as seems reasonable (see Table 2.4 and Eyles et al. 2006), then the $z'_{850LP}-m_{3.6\mu m}$ color is correlated with the age of the galaxy and hence, for a given IMF and star formation history, its M/L_V ratio.

This is done for a given galaxy in the sample by first computing $z'_{850LP}-m_{3.6\mu m}$ colors for Bruzual-Charlot models (redshifted to the galaxy's photometric redshift) with ages ranging between 0 and 1.2 Gyr (roughly the lookback time at the redshift of the galaxy). We then find the model that produces the $z'_{850LP}-m_{3.6\mu m}$ color closest to that observed for a given galaxy. This model is taken to have the "best-fit" age and M/L_V ratio for this particular galaxy. At $z \simeq 5$, the 3.6μm IRAC filter covers the rest-frame V-band; hence, we convert the 3.6 μm flux to a luminosity (assuming $z = z_{phot}$) and multiply it by the best-fitting M/L_V to compute the stellar mass. For each galaxy, best-fitting stellar masses are computed for the same range of single-component star formation histories used to fit the spectroscopic sample. The stellar mass we assign to each galaxy is taken from the star formation history that produces the best-fitting $z'_{850LP}-m_{3.6\mu m}$ colors. We obtain an estimate of the systematic uncertainty in the mass by considering the range inferred from the different star formation histories and ages that provide a good fit (e.g. $\Delta\chi^2=\chi^2-\chi^2_{min}<1$)to the observed $z'_{850LP}-m_{3.6\mu m}$ color.

We note that the observed 3.6μm luminosity is not equivalent to a rest-frame V-band luminosity for all redshifts. The 3.6μm band shifts between rest-frame 5500-6700 Å for $z = 4.4$-5.5. To test the systematic offsets introduced by relying on M/L_V to derive masses, we compare the mass of the spectroscopic sample derived in the

manner described above to the mass from SED fitting. We find the median offset between the two methods is 40%.

The total stellar mass extracted from the 72 $z \simeq 5$ sources that are uncontaminated in the Spitzer images is $5-9\times10^{11}$ $M_\odot$ with a best-fit value of 7×10^{11} $M_\odot$. The median stellar mass in the sample is 6×10^{9} $M_\odot$. If we make the reasonable assumption that the distribution of stellar masses is independent of IRAC contamination, we can estimate the stellar mass in IRAC contaminated galaxies by multiplying the stellar mass derived from the uncontaminated $z \simeq 5$ galaxies by the ratio of the total number of $z \simeq 5$ sources to the number of uncontaminated $z \simeq 5$ sources. Following this reasoning, the total stellar mass for the photometric sample becomes $2\times10^{12}M_\odot$. Taking the full range of single-component star formation histories into consideration, this total stellar mass could lie between 2 and 3×10^{12} $M_\odot$.

2.5.3 Comoving Mass Densities

To derive the comoving stellar mass densities from the above totals, we need to estimate the redshift-dependent selection function in the 160 arcmin^2 GOODS-S field between $4.4 < z < 5.6$. Although the total possible comoving volume is 5.6×10^5 Mpc^3, the effective volume is less than this value due to sample incompleteness arising as a result of objects being scattered faintward of the magnitude limit or out of the color-selection window.

In order to account for these luminosity and redshift biases, we compute an effective survey volume following the approach of Steidel et al. (1999) using

$$V_{\rm eff}(m) = \int dz\, p(m,z)\, \frac{dV}{dz} \tag{2.1}$$

where $p(m,z)$ is the probability of detecting a galaxy at redshift z and apparent z' magnitude m, and $dz\,\frac{dV}{dz}$ is the comoving volume per unit solid angle in a slice dz at redshift $z = 4.4 - 5.6$.

We compute the probability function $p(m,z)$ by putting thousands of fake galaxies into the GOODS images and recreating a photometric catalog for the new image

using identical selection parameters used in generating the GOODSv1.1 catalogs. The apparent magnitudes of the fake galaxies span $z'_{850LP} = 22 - 27$ in steps of Δm=0.5 and redshifts ranging between $z = 4$ and $z = 6$ in steps of Δz=0.1. The sizes of the fake galaxies are consistent with distriution of half-light radii derived for $z \simeq 5$ galaxies in Ferguson et al. (2004). The colors of the fake galaxies depend on the galaxy redshift and SED. We adopt the SED of a Bruzual-Charlot model with constant star formation history, an age of 100 Myr, and no dust as the intrinsic rest-frame SED of the fake galaxies. Allowing for a selective extinction of E(B-V)=0.1 in the fake galaxies' SEDs decreases the effective volume by roughly 5%, which would not significantly change our final mass density estimates. The colors are then determined for galaxies at each redshift in a manner similar to that which we described in §2.5.1. The probability function, $p(m, z)$ is then given by the fraction of fake galaxies with apparent magnitude, m, and redshift, z, that are brighter than the magnitude limit and satisfy the dropout color selection criteria. Since our selection is based on photometric redshifts, we adopt color-criteria that are appropriate for our photometric sample ($v_{606W} - i'_{775W} > 0.9$ and $i'_{775W} - z'_{850LP} > 1.3$).

The effective volume probed is 5.2×10^5 Mpc^3 at $z'_{850LP} = 23$ and $z = 5$ where we are nearly 100% complete and falls to 1.2×10^5 Mpc^3 at z'_{850LP}=26.5. The stellar mass density inferred from our $z \simeq$5 candidates is thus $5 - 8\times10^6$ M$_\odot$ Mpc^{-3}, with a best-fit value of 6×10^6 M$_\odot$ Mpc^{-3}. The robust lower limit from our spectroscopic sample is 1×10^6 M$_\odot$ Mpc^{-3}.

Our inferred stellar mass density is most likely an underestimate of the total value at $z \simeq 5$ for several reasons. Foremost, the survey is only sensitive to the most luminous and perhaps most massive galaxies since we only included objects with significance above 3σ at 3.6μm.

Second, an additional reservoir of stellar mass may be contained in objects that are not currently forming stars and hence are very faint in the rest-frame ultraviolet. At $z \simeq 3$, LBGs contribute only 17% of the stellar mass density in the most massive sources (van Dokkum et al., 2006); the remaining fraction is likely contained in objects that are not actively forming stars. Although this fraction of quiescent sources

is probably much lower at earlier times, we conservatively estimate the total mass density could rise by a further factor of two.

In summary, therefore, we derive a firm lower limit to the stellar mass density at $z \simeq 5$ of $1{\times}10^6$ $M_\odot$ Mpc^{-3}, a reasonable estimate of the total *observed* population of 5-8$\times10^6$ $M_\odot$ Mpc^{-3} and cannot exclude undetected sources which would increase the total to $1{\times}10^7$ $M_\odot$ Mpc^{-3}. Although the overall estimates span a factor of 2, we emphasize that the spectroscopic sample is clearly a significant underestimate of the observed population.

2.6 Implications for the Previous Star Formation History

In the foregoing we have attempted to put the first bounds on the stellar mass density at $z \simeq 5$, 1.2 Gyr after the Big Bang and about 800 Myr after $z \simeq 10$. We emphasize that there are considerable uncertainties in the various steps in our analysis. First, to derive stellar mass estimates, we had to cull our samples to those with reliable IRAC detections, later scaling on the assumption that they represent a fair subset of the spectroscopic and photometric populations. For our spectroscopic sample, our fitting procedure gives mass estimates that span a wide range depending on the assumed star formation history. Finally, we assumed a median visual mass/light ratio for the photometric sample derived from that for the spectroscopic sample.

Probably the dominant error in deriving the total mass density is not the numerical scaling factors , but rather the intrinsic uncertainty in estimating the masses of individual galaxies. Detailed work at lower redshift (Shapley et al., 2005; Bundy et al., 2005; Papovich et al., 2005) has shown that inferences of the stellar mass from SED fitting yield mass estimates that contain typical uncertainties of $\simeq$30%. The errors certainly increase slightly when considering objects at higher redshift; however, our error estimates (§5.1) suggest that the stellar mass estimates of objects in our spectroscopic sample are typically 50%, possibly more.

Notwithstanding the uncertainties, it is interesting to now consider the implications of our derived mass density. The star formation rate density (SFRD) of bright (> 0.3 $L^{\star}_{z=3}$) star-forming galaxies at $z \simeq 5-10$ appears to decline continuously toward higher redshift (Bunker et al., 2004; Bouwens et al., 2004, 2005). However, current observations may be missing a substantial fraction of star formation either because it is enshrouded in dust, too faint to be detected with current facilities, or located at redshifts uncharted by current telescopes ($z > 10$). Comparing the comoving density of assembled stellar mass at $z \simeq 5$ with estimates derived from models of the previous star formation history enables us to test these possiblities, thereby providing constraints beyond direct reach of current facilities.

Taking data on the SFRD from the recent literature (Giavalisco et al., 2004a; Bouwens et al., 2004; Stanway, 2004; Bouwens et al., 2005, 2006), we fit the redshift dependence with a simple functional form over $z \simeq 5-10$. In cases where the SFRD was not evaluated down to the adopted fiducial luminosity limit ($0.1L^{\star}$ at z=3), we compute the additional contribution by integrating the luminosity function assuming the Schechter function parameters derived in each paper. Since the data at $z > 7$ do not allow for the robust derivation of the form of the luminosity function, we assume the shape of the luminosity function remains constant before $z \simeq 6$.

As Bouwens et al. (2006) discuss, at $z \simeq$6 there is some disagreement in the value of the SFRD. The disagreement stems primarily from whether the shape of the luminosity function is evolving. Bouwens et al argue for a decrease in the characteristic luminosity and an increase in the faint end slope prior to z$\simeq$3, so we adopt the redshift-dependent LF parameters derived in Bouwens et al. (2006) and Stanway (2005) and integrate accordingly. We find that the SFRD (integrated down to 0.1 $L^{\star}_{z=3}$) can be fit reasonably well by $\rho \propto (1+\mathrm{z})^{-3.3}$ between z=5-10 (Figure 2.6).

The stellar mass density obtained by integrating this function over time between z$\simeq$10 and $z \simeq 5$ is lower than that derived from the photometric sample of $z \simeq 5$ objects in this paper (Figure 2.7). We note that the integral of the star formation rate density as a function of redshift overestimates the mass density. This is because we do not account for the mass that is returned to the interstellar medium in stellar winds

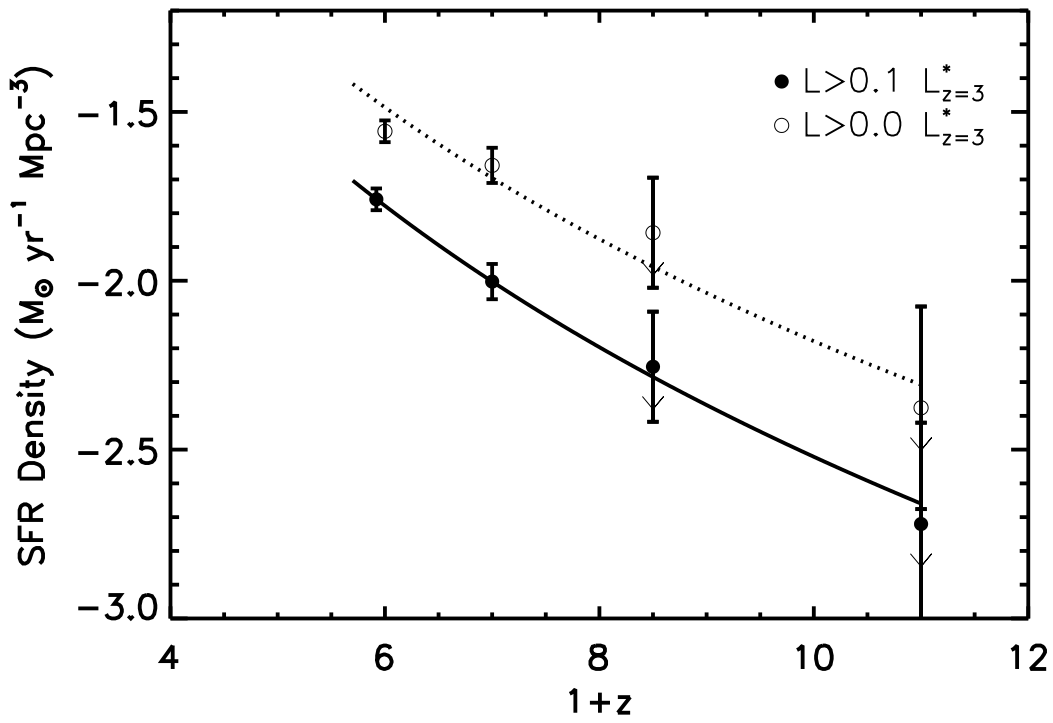

Figure 2.6 Comoving star formation rate density as a function of redshift, assuming no extinction. The star formation rate densities are derived from Giavalisco et al. (2004) at $z = 5$, Stanway (2005) and Bouwens et al. (2006) at $z = 6$, Bouwens et al. (2005) at $z = 7.5$, and Bouwens et al. (2005) at $z = 10$. The solid circles represent the star formation rate densities achieved by integrating the derived luminosity function down to 0.1 $L^\star_{z=3}$. Integrating the luminosity function down to zero luminosity (open circles) assuming a faint-end slope of $\alpha = -1.73$ adds an additional factor of 2.3 to the star formation rate density. The evolution of the star formation rate density with redshift is well fit by a $(1 + z)^{-3.3}$ parameterization over $5 < z < 10$.

and stellar deaths. This can be quantified using the Bruzual & Charlot (2003) software (we do this to compute stellar masses, see §2.5.1), but it is a complicated function of the average star formation history and age, which are not well-constrained. We find that this effect could *reduce* the stellar masses inferred from integrating the observed star formation rate densities by up to ≃30% (assuming a 1 Gyr instantaneous burst). Given the uncertainties, we do not adjust the curves in Figure 2.7 by this factor, but we note that this effect further enhances the discrepancy between the observed stellar mass density at z≃ 5 and that which can be accounted for by previous star formation. Therefore, the observed stellar mass of the $z \simeq 5$ galaxies in GOODS-S either implies a significant amount of dust extinction or that not all star formation at z>5 has been observed in current surveys.

To examine the amount of star-formation that may be hidden in low-luminosity systems, we integrate the luminosity functions to zero luminosity utilizing faint-end slopes of $\alpha = -1.73$ (as measured at z≃6 in Bouwens et al. 2006) and $\alpha = -1.9$ (as suggested by Yan & Windhorst 2004) and integrate the luminosity function to zero luminosity.

Star formation is unlikely to occur at very low luminosities because of radiative feedback processes and (after reionization) a photoionized IGM which raises the cosmological Jeans mass. We nonetheless take this extreme approach to place an upper limit on the amount of unextincted star formation. Assuming no evolution in the shape of the LF between $z \simeq 5$ and $z \simeq 11$, this increases the predicted stellar mass at $z \simeq 5$ by an extra factor of 2.3 for faint end slopes of $\alpha = -1.73$; if we instead consider an extreme faint-end slope of $\alpha = -1.9$, the star formation rate density increases by a factor of 6.8. This gives a better account of the assembled mass and if correct has interesting consequences for higher redshift surveys probing to low luminosities Stark et al. (2007b).

A significant amount of star formation may also be enshrouded by dust. However, recent observations have shown that the rest-frame UV slope of $z \simeq 6$ galaxies is actually somewhat *bluer* than that at $z \simeq 3$ suggesting that the mean dust extinction declines between $z \simeq 3$-6 (Stanway et al., 2005; Yan et al., 2005; Bouwens et al., 2006).

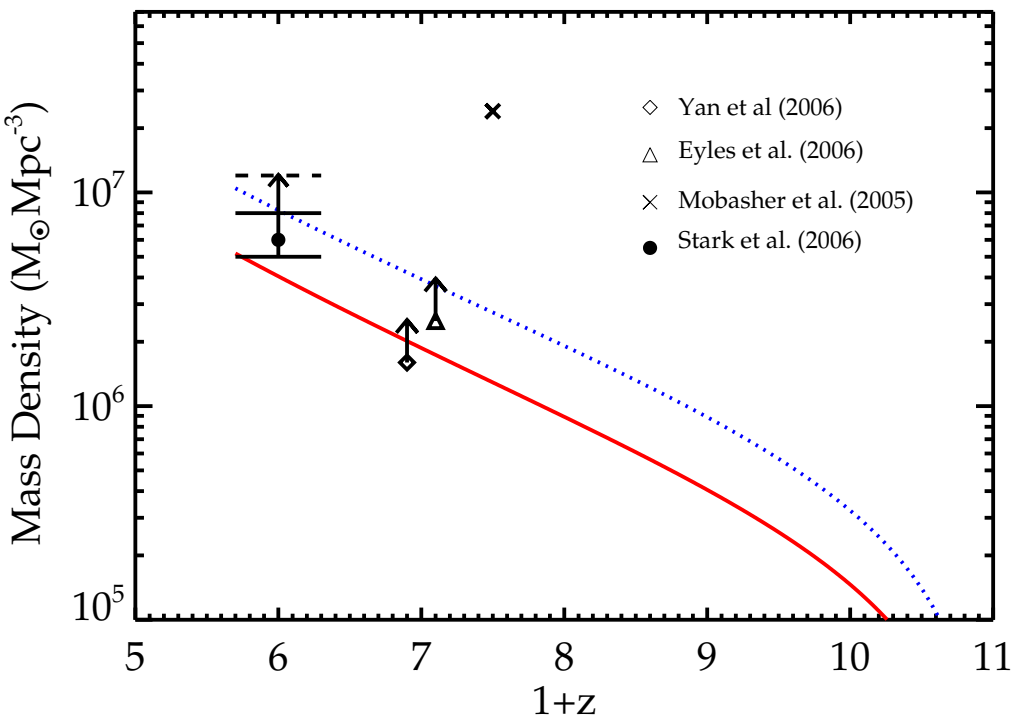

Figure 2.7 Comparison of stellar mass density at $z \simeq$5-10 derived from spectral energy distributions of galaxies in GOODS-S with that derived from integrating the observed star formation rate density at z$\simeq 5-10$ integrated down to 0.1 $L^{\star}_{z=3}$ (solid line) and zero luminosity (dotted line) assuming a faint-end slope of $\alpha = -1.73$. The filled solid circle with the upward arrow corresponds to the stellar mass density derived from spectroscopically-confirmed galaxies in GOODS-S (1×10^6 $M_{\odot}$) whereas the solid filled circle corresponds to the stellar mass density from the photometric sample (6×10^6 $M_{\odot}$). We estimate that the stellar mass density may be as high as 1×10^7 $M_{\odot}$ Mpc^{-3} (solid horizontal line) depending on the contribution from undetected sources. We also include previous estimates of the stellar mass density at $z > 5$ from Yan et al. (2006) (diamonds), Eyles et al. (2006) (triangle), and Mobasher et al. (2005) (cross). The Yan et al. (2006) and Eyles et al. (2006) symbols are offset slightly from $z = 6$ for clarity. The large stellar mass density at $z \simeq$5 inferred from this study suggests that a significant amount of star formation is hidden by dust or has yet to be located, perhaps lying at higher redshift or in intrinsically faint systems.

Taking the empirically derived fit relating the extinction at 1600 Å (A_{1600}) to the UV slope β, A_{1600}=4.43 + 1.99β (Meurer et al., 1999) yields an overall attenuation factor of $\times$ $\simeq$1-1.5 at z $\simeq$6 for two different estimates of the UV continuum slope at $z \simeq 6$ ($\beta = -2.2$ from Stanway et al. 2005 and $\beta = -2.0$ from Bouwens et al. 2006).

Hence, the expected extinction correction to the SFR density at $z \simeq 5 - 10$ could in principle account for the stellar mass contained in the photometric sample in this paper if the Bouwens et al. (2006) estimate of the UV continuum slope is correct. If there exists either a significant population of quiescent massive galaxies or low-mass galaxies below the 3σ 3.6 μm flux limit imposed on the data, a significant amount of low-luminosity star-forming galaxies would be required to assemble the stellar mass. Future studies will test this hypothesis.

2.7 Conclusions

We have argued that the assembled stellar mass density at high redshift provides a valuable constraint on the past star formation history and, with improved precision, may ultimately indicate whether there was sufficient star formation in the previous $\simeq$500-900 Myr to reionize the intergalactic medium.

We have demonstrated both the promise and limitations of this method by computing the comoving stellar mass density at $z \simeq 5$. Following the ideas discussed in Stark & Ellis (2006), we use the stellar mass density to constrain the amount of star formation at earlier times.

We detail our findings below.

1. We construct a sample of 25 spectroscopically confirmed z $\simeq$5 objects in GOODS-S (14 of which are uncontaminated in the *Spitzer* data) to place a robust lower limit on the comoving stellar mass density. Fitting the SEDs of these objects to templates from Bruzual & Charlot (2003) populations synthesis models, we infer a total comoving stellar mass density of 1×10^6 $M_\odot$ Mpc^{-3}.

2. We construct a sample of $z \simeq 5$ galaxies using the photometric redshifts of the GOODS-MUSIC catalog. After removing likely stellar and low-z contaminants, 196

objects remain in the sample. Computing the stellar mass from the 72 objects that are uncontaminated by nearby sources in the Spitzer data, we estimate a stellar mass density of 6×10^6 $M_\odot$ Mpc^{-3}. Systematic uncertainty in the star formation history causes this value to be uncertain at the 30% level.

3. The total comoving stellar mass density (6×10^6 $M_\odot$ Mpc^{-3}) represents a lower limit for several reasons. First, robust stellar mass estimates are only attainable for reasonably massive galaxies; hence the estimates presented in this paper do not include the contribution from low-mass systems. Second, we require objects to be bright in the rest-frame UV (and hence actively forming stars) for selection into our sample. If there is a large population of quiescent galaxies at $z \simeq 5$, the total stellar mass density may be significantly higher than estimated. We estimate that the stellar mass density of massive galaxies is unlikely to exceed 1×10^7 $M_\odot$ Mpc^{-3}.

4. The estimated comoving stellar mass density at $z \simeq 5$ suggests that current observations may be missing some star formation at z > 5. The missing star formation could, however, be accomodated by extincted star formation in LBGs currently seen at $z \simeq$ 6-10 or in low-luminosity star-forming systems below the detection threshold of current observations. In the latter case, our results have important implications for searches for low luminsoity SF systems at high redshift.

Acknowledgements

D.P.S. is grateful for the hospitality of the School of Physics at the University of Exeter, where most of this work was completed. We thank Peter Capak, Johan Richard, Kevin Bundy, Adam Kraus, Elizabeth Stanway, Kuenley Chiu and Richard McMahon for enlightening conversations. We thank our anonymous referee for very insightful comments. This paper is based on observations made with the NASA/ESA Hubble Space Telescope, obtained from the Data Archive at the Space Telescope Science Institute, which is operated by the Association of Universities for Research in Astronomy, Inc., under NASA contract NAS 5-26555. The *HST/ACS* observations are associated with proposals #9425 & 9583 (the GOODS public imaging survey).

Spitzer VLT/FORS2 VLT/ISAAC We are grateful to the GOODS team for making their reduced images public – a very useful resource.

Chapter 3

A Keck Survey for Gravitationally-Lensed Lyman-α Emitters in at $8.5 \lesssim z \lesssim 10$

Abstract

We discuss new observational constraints on the abundance of faint high redshift Lyman-α emitters secured from a deep Keck near-infrared spectroscopic survey which utilizes the strong magnification provided by lensing galaxy clusters at intermediate redshift ($z = 0.2 - 0.5$). In each of 9 clusters we have undertaken a systematic 'blind' search for line emission with NIRSPEC in the J-band within carefully-selected regions which offer very high magnifications ($\gtrsim \times$10-50) for background sources with redshifts $z \simeq 10$. The high magnification enables the detection of emission at unprecedented flux limits (10^{41} - 10^{42} erg s^{-1}), much fainter than those of conventional narrow band imaging and other spectroscopic searches. As the comoving volumes probed are small, our survey is designed to address the important question of whether intrinsically feeble star forming galaxies could provide the dominant ionizing flux at $z \sim 10$. Our survey has yielded six promising ($> 5\sigma$) candidate Lyman-α emitters which lie between $z = 8.7$ and $z = 10.2$. We carefully discuss the validity of our detections in the light of earlier, apparently false, claims. We then focus on the likelihood that the detected line is Lyman-α from a distant lensed-source. All but one of the candidates

This chapter has been published previously as Stark et al. 2007, ApJ, 663, 10

remain undetected in deep HST optical images and lower redshift line interpretations can be excluded, with reasonable assumptions, through the non-detection of secondary emission in further spectroscopy undertaken with LRIS and NIRSPEC. We demonstrate that rigorous confirmation of the Lyman-α hypothesis for all of our candidates will be a challenge with current facilities. Nonetheless, as a result of our tests, we argue that at least two of our candidates are likely to be at $z \simeq 10$. Given the small survey volume, this suggests there is a large abundance of low luminosity star-forming sources occupying the era when the reionization process is thought, from independent evidence, to be ongoing. While the predicted reionization photon budget depends upon a large number of physical assumptions, our first glimpse at the $z \simeq 10$ Universe suggests that low luminosity star-forming galaxies contribute a significant proportion of the UV photons necessary for cosmic reionization.

3.1 Introduction

After the epoch of recombination at z$\simeq$1000, neutral hydrogen permeated the universe. The earliest observable structure dates back to the beginning of this era at the surface of last scattering traced by the cosmic microwave background (CMB). The next most distant observable represent the populations of galaxies, gamma-ray bursts, and quasars at $z \simeq 6.2 - 7.0$ (Hu et al., 2002; Iye et al., 2006; Totani et al., 2006; Kashikawa et al., 2006; Fan et al., 2006; Bouwens & Illingworth, 2006). The interval between $z \simeq 1000$ and $z \simeq 6.5$ contains many landmark events: the formation of the first stars, the assembly of first galaxies, the growth of the first supermassive black holes that power quasars, and the reionization of neutral hydrogen in the intergalactic medium. One of the primary driving forces in observational cosmology today is to illuminate the growth of these first structures in this important, but poorly understood, era.

Recently, important constraints have emerged on the extent of star formation activity that occurred in the latter part of this era. The WMAP temperature-polarization cross correlation signal on large angular scales (Spergel et al., 2006)

implies scattering of microwave photons by free electrons from ionizing sources at $z \simeq 10 - 12$, suggesting an early period of efficient star formation. Meanwhile, Hubble Space Telescope (HST) and Spitzer observations have uncovered a population of very massive ($M_{stellar} \sim 10^{10}$ - 10^{11} $M_{\odot}$) galaxies at z$\simeq$6 with well-established (>100 Myr) stellar populations (Egami et al., 2005; Eyles et al., 2005; Mobasher et al., 2005; Yan et al., 2005; Stark et al., 2007a; Eyles et al., 2007; Yan et al., 2006). The assembly of such massive galaxies by these redshifts requires significant star formation at yet earlier times. Observations of z-dropouts and J-dropouts with HST indicate a decline in the star formation activity of luminous Lyman-break galaxies out to $z \simeq 7 - 10$ (Bouwens et al., 2005; Bouwens & Illingworth, 2006); if there is significant star formation activity in this redshift interval, these observations indicate it likely occurred in lower-luminosity systems.

Despite these indications of early activity, current facilities are poorly-equipped to undertake conventional searches for star-forming sources beyond $z \simeq 7$. Even with HST and 8 meter class telescopes, continuum ('drop-out') and narrow-band imaging Lyman-α searches probe only the most luminous, rare, sources at these redshifts; the contribution to the reionization flux from these sources may well be small. While narrowband surveys have had significant success at detecting Lyman-α emitters at $z \simeq 6$ (Hu et al., 1998, 2002, 2004; Malhotra & Rhoads, 2004; Hu et al., 2005; Stern et al., 2005; Kashikawa et al., 2006; Shimasaku et al., 2006) only one Lyman-α emitter has been convincingly detected at $z \simeq 7$ (Iye et al., 2006). At $z \simeq 9$, narrowband surveys for relatively luminous Lyman-α emitters ($\gtrsim 10^{42.5}$ erg s^{-1}) have yet to find any sources (Willis & Courbin, 2005; Cuby et al., 2006). While a few candidate Lyman-break galaxies beyond $z \simeq 7$ have been suggested from photometric data (Bouwens et al., 2005; Labbé et al., 2006; Richard et al., 2006; Bouwens & Illingworth, 2006; Henry et al., 2007), none has yet been spectroscopically confirmed, due largely to the difficulties inherent to observing in the near-infrared.

Recent observations of the faint end slope of the star-forming luminosity function at $z \simeq 6$ (Yan & Windhorst, 2004; Bouwens et al., 2006) support the suggestion that the bulk of the integrated star formation at high redshift may arise from very low

luminosity sources, as expected theoretically (Barkana & Loeb, 2001; Wyithe & Loeb, 2006). However, forming stars in low mass halos is complicated by a number of feedback effects, any of which could significantly decrease the star formation efficiency. Clarifying whether low luminosity systems are abundant at early times requires observations probing well below the sensitivity limits obtainable with current facilities using conventional methods.

The study of lower luminosity sources rendered visible by the strong gravitational lensing induced by foreground clusters is the only current means to advance this quest before the next generation of telescopes is available. Although a typical lensing cluster magnifies sources by $\times$5-10 over 1 arcmin^2 for sources at $z > 7$, faint signals can be boosted $> \times 15$ on the so-called *critical line* - the location of the lensing caustic in the image plane. Spectroscopy and detailed studies become feasible at otherwise impossible (unlensed) limits. For several objects recently located via this technique (Ellis et al., 2001; Kneib et al., 2004; Santos et al., 2004; Egami et al., 2005), stellar continuum slopes, Lyman-α profiles and star formation rates have been determined for sources whose intrinsic flux is close to the faintest direct imaging limits so far reached, $I_{AB} \simeq 30$ (Beckwith et al., 2006). Until the availability of more powerful ground and space-based facilities, scanning the critical lines of massive clusters provides possibly the only reliable means of estimating the abundance of low luminosity star forming sources in the $7< z <12$ interval over which cosmic reionization is thought to take place.

This paper presents the results of a spectroscopic survey for strongly-lensed Lyman-α emitters at $8.5<z<10.4$ using the NIRSPEC near-infrared spectrograph on the Keck II telescope. The survey follows logically from a very similar, successful one undertaken at $z \simeq 4-6$ using the LRIS optical spectrograph on the Keck I telescope (Santos et al., 2004) to which the reader is referred.

A plan of the paper follows. We contrast our lensing search technique with other, more conventional probes of early star forming sources in §3.2. The NIRSPEC observations and reduction methods are presented in §3.3. Here we describe the candidate selection criteria and derive the survey sensitivity function. A set of 6 promising

candidate $z \simeq 10$ Lyman-α emitters are presented in §3.4. Here we discuss in detail both the reality of the line detections and the likelihood that the line identifications represent high redshift Lyman-α. Noting the likelihood that a significant fraction of our sources may lie at $z \simeq 10$, we infer the abundance of high redshift low luminosity sources and compare these with other constraints in §3.5. In §3.6 we discuss whether the abundance so derived might represent a significant fraction of that necessary to complete cosmic reionization. We present our conclusions in §3.7.

Throughout the paper, we have assumed a flat universe and $(\Omega_m, \Omega_\Lambda)$=(0.27,0.73) following the results presented in the initial WMAP data release (Spergel et al., 2003).

3.2 Gravitational Lensing and Survey Strategies - A Critique

Strong gravitational lensing by intermediate redshift galaxy clusters offers the capability of extending the current generation of high redshift galaxy surveys so that lower luminosity sources can be brought into view. This added boost in sensitivity is particularly effective at the highest source redshifts ($z \gtrsim 7$) where the bulk of star formation activity may be taking place in low mass dark matter halos (Barkana & Loeb, 2001).

Lensing increases the apparent area of a background source while conserving the surface brightness; thus the gain in sensitivity is the magnification factor, $\mathcal{M}$. Rich clusters of galaxies at intermediate redshifts (e.g. $z \simeq 0.2 - 0.5$) amplify high redshift sources by factors of typically $\mathcal{M} \simeq 3-5$ over areas of a few arcmin^2. However, boosts of $\mathcal{M} \simeq 10 - 50$ are possible near the *critical line* - the theoretical locus of points in the image plane corresponding to the caustic of infinite magnification. Clusters are usually characterized by both an inner and an outer critical line, the location of which varies as a function of source (background) redshift.

The accurate location on the sky of these critical lines can only be determined in the case of clusters for which detailed mass models are available. Such a mass model is

primarily constrained by the positions and redshifts of lensed features (Kneib et al., 1996). A mass model can be validated, for example, by securing spectrosopy of lensed features whose redshifts were predicted by the mass model using an 'inversion' technique (Ebbels et al., 1998). Currently, such high quality mass models are only available for $\simeq$20 clusters; however this should increase in the future with additional surveys (Ebeling et al., 2001).

However, the gain in sensitivity afforded by strong lensing comes with a loss in survey area, compared to an equivalent unlensed survey, by a factor of $\mathcal{M}$. This is an important point as the area of high magnification (say $\mathcal{M}$ >10) is already quite small ($\simeq$ 0.1 arcmin^2). Provided, as seems reasonable (§3.1), that the slope of the faint-end slope of the luminosity function is very steep, then strong lensing surveys should be a very effective way to characterize the amount of star formation at $z > 7$.

Observers are considering several ways to conduct surveys for z >7 Lyman-α emitters. Before describing the present survey, we therefore consider it instructive to examine the benefits and drawbacks of the different strategies.

The primary survey techniques used thus far are narrowband imaging (Hu et al., 2002, 2004) and spectroscopy (Martin et al., 2006). Neither technique has yet been routinely used in the near-infrared spectral region appropriate for z >7 and both methods can, in principle, be combined with strong lensing by focusing on fields containing rich clusters. At optical wavelengths, unlensed narrow-band imaging techniques typically reach flux limits of 2×10^{-17} ergs cm^{-2} s^{-1}, whereas spectroscopic techniques probe to 5×10^{-18} ergs cm^{-2} s^{-1} (Santos et al., 2004).

In the near-IR, a longslit spectrograph such as NIRSPEC offers a $\sim$8 Å resolution over a moderate redshift interval (Δz=2). Although bright atmospheric emission lines restrict visibility for 50% of the redshift range in the J-band, for a resolving power R$\simeq$1500, the gain in redshift coverage is still a factor of 10-100 over the narrow band technique (Δz=0.01-0.1). Per exposure, there is however a very small field of view ($\simeq$30 arcsec^2) c.f. narrowband imaging ($\simeq$ 10 arcmin^2 for a cluster but much larger for panoramic field surveys).

Assuming the characteristics for current instrumentation and their detectors, we

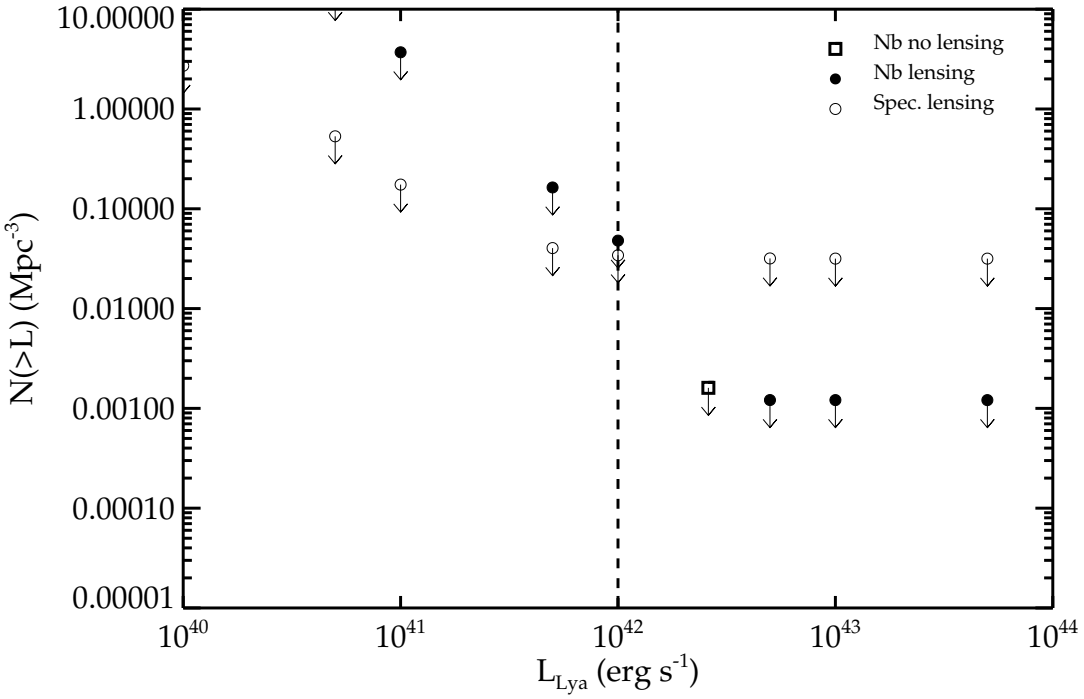

Figure 3.1 Comparison of different survey strategies for locating Lyman-α emitters with current instrumentation in seeing-limited conditions. Solid circles represent the minimum source abundance that a 60 hour spectroscopic lensing observing campaign (over 10 clusters) could constrain (at 5σ); while open circles correspond to the minimum source abundance that a narrowband imaging lensing survey could constrain in the same exposure time. Both survey techniques probe orders of magnitude fainter than a conventional narrowband survey (open square), albeit over much smaller volumes. At luminosities to the left of the dashed vertical line, the spectroscopic approach covers a larger volume, and thus it is significantly more efficient than narrowband imaging in constraining the abundance of the faintest ($\lesssim 1$ M$_\odot$ yr^{-1}) Lyman-α emitters.

compare the efficiencies of the two methods in the lensing case in Figure 3.1. Details of the computation are given in the Appendix. Both lensed survey techniques probe at least an order of magnitude deeper than conventional near-IR Lyman-α narrowband surveys. Of the two lensing methods, long-slit spectroscopy is better suited for detecting the faintest Lyman-α emitters for detectors 1024×1024 pixels in size. This can be explained as follows. While a narrowband imager covers a larger area on the sky, only a very small fraction of this area is highly magnified (e.g. $>10\times$). The small gain in the highly-magnified survey area is insufficient to compensate for the significantly smaller redshift coverage. Moreover, the $\simeq$100 Å bandwidth typical for many narrowband filters results in significantly poorer sensitivity limits. Taking the various factors into consideration, a long slit spectroscopic survey represents the more efficient technique for detecting sources with star formation rates below 10^{42} erg s^{-1}, and hence is the optimal strategy for determining whether reionization was predominantly caused by large numbers of feeble sources.

3.3 NIRSPEC Critical Line Survey

3.3.1 Cluster Sample

Our goal is to constrain the abundance of sources up to an order of magnitude below current survey sensitivity limits. Accordingly, following the discussion above, we have conducted a spectroscopic survey for Lyman-α emission along the critical lines of 9 clusters at $z \simeq 0.2 - 0.5$. We limited our observations to those clusters with mass models that are well-constrained by the combination of HST imaging and ground-based spectroscopy of multiply imaged systems. The list of survey clusters and the associated mass models are summarized in Table 1.

Many criteria entered into the final selection of our 9 clusters. An essential criteria was the availability of deep HST imaging for constructing samples of multiply-imaged systems (Kneib et al., 1996; Broadhurst et al., 2005). The most well-understood clusters in our sample contain 10-30 multiply-imaged systems, a signification fraction

Table 3.1. Clusters surveyed

Cluster	Redshift	RA[a]	Dec[b]	Lens Model Reference
Cl 0024	0.39	00 26 35.5	+17 09 50.7	(1)
Abell 68	0.255	00 37 06.8	+09 09 23.4	(2)
Abell 370	0.375	02 39 53.1	-01 34 54.8	(3)
MS 0451	0.55	04 54 10.6	-03 00 50.7	(4)
Abell 963	0.206	10 17 03.7	+39 02 49.2	(2)
Abell 1689	0.183	13 11 29.4	-01 20 28.7	(5)
Abell 2218	0.176	16 35 49.3	+66 12 43.5	(6)
Abell 2219	0.226	16 40 19.8	+46 42 41.9	(2)
Abell 2390	0.228	21 53 36.9	+17 41 43.4	(7)

[a]units of HH MM SS

[b]units of +DD MM

References. — (1) Kneib et al. (2003); (2) Smith et al. (2005) (3) Bézecourt et al. (1999); (4) Borys et al. (2004), (5) Limousin et al. *in prep*; (6) Kneib et al. (2004); (7) Swinbank et al. (2006)

of which have spectroscopic redshift (e.g. Abell 1689 has 33 such systems of which 21 are spectroscopically-confirmed, Richard et al, in prep). This data is necessary to astrometrically pinpoint the location of the critical line along which the NIRSPEC slit is oriented.

Deep HST optical imaging is also essential for verifying, via the absence of any detectable continuum, that any lensed emitters are genuinely at high redshift. Due to neutral hydrogen absorption we would not expect any of our $z \simeq 10$ emitters to be seen at optical wavelengths and HST provides the deepest verification.

A final consideration is the availability of deep optical *spectroscopy* which is helpful in order to check for associated emission lines that might arise if any NIRSPEC line detection arises from a lower redshift source. Given the comprehensive critical line survey undertaken by (Santos et al., 2004) using LRIS, where possible we chose the same clusters and explored the same critical line regions.

In practice, telescope scheduling and weather losses compromised a perfect adoption of the latter criteria. However, for each of the 9 clusters, the mass model, the critical line location and associated magnification properties are well understood.

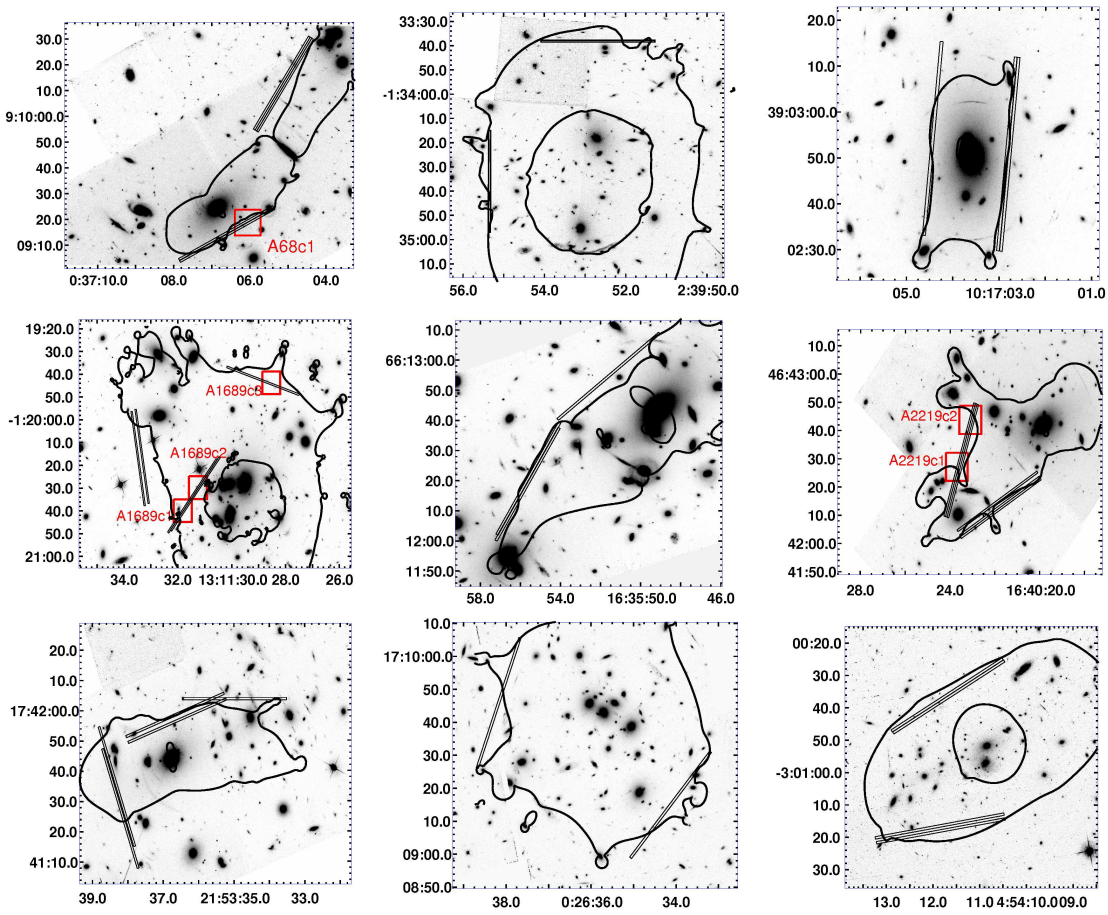

Figure 3.2 Survey clusters, with survey area and lensing critical curves. For each cluster, superposed on the *HST*/WFPC2 image are slit positions observed with NIRSPEC and the critical lines for a source at $z = 8$ (dotted lines). The solid curves bound areas where the magnification provided to $z = 8$ background sources exceeds a factor of 10. From left to right and top to bottom are Abell 68, Abell 370, Abell 963, Abell 1689, Abell 2218, Abell 2219, Abell 2390, CL 0024, MS 0451.

3.3.2 Observations and Data Reduction

We utilized the Near Infrared Spectrometer (NIRSPEC, McLean et al. 1998) mounted on the Keck II 10 m telescope at Mauna Kea to perform our survey. Observations were performed in the J-band (1.143-1.375 μm) with a slit 42″ long and 0.″76 wide. We used the low-resolution mode of NIRSPEC with the 75 line mm^{-1} grating which offers a net resolving power of R$\simeq$1500 and a spectral resolution of $\simeq$8 Å. At the wavelengths sampled within the NIRSPEC J-band filter, any detected Lyman-α emission would correspond to sources with redshifts between $z = 8.5$ and $z = 10.4$.

Table 3.2. NIRSPEC Survey Observations

Date	Cluster	Position Angle[a]	Integration time[b]
Aug 2004	Abell 2390 1	117	12.0
	Abell 2219 1	119.2	9.6
	Abell 68 1	330.	13.2
Jan 2005	MS 0451 1	120.9	11.4
	Abell 963 1	177.2	10.8
	Abell 963 2	175.0	5.4
	Abell 1689 1	73	5.4
June 2005	Abell 1689 1	73	3.6
	Abell 1689 2	205	10.8
	Abell 1689 3	139.1	10.8
	Abell 2218 1	153	10.8
	Abell 2218 2	134	5.4
	Abell 2219 1	119.2	5.4
	Abell 2219 2	160	16.2
	Abell 2390 2	109	10.2
	Abell 2390 3	20.0	6
Oct 2005	Abell 68 2	300	10.8
	Cl 0024 1	139.7	5.4
	Cl 0024 2	160.2	4.8
	MS 0451 2	100.1	7.2
	Abell 2390 3	20.0	5.4
	Abell 2390 4	90.0	4.8
	Abell 2219 2	160	2.4

[a]in degrees North through East

[b]in ksec

Figure 3.2 shows how the targeted slit positions match the predicted location of the $z \simeq 9$ critical lines for each of the 9 clusters in our survey. To maximize efficiency, where a choice was available we selected regions where the critical line is straight enough to provide high magnification across the entire slit.

Typically, 2-5 slit positions were observed per cluster. For each slit position, we took 6-10 ten minute exposures using a three point dither pattern in which the telescope was offset $\pm 3''$ along the slit. Table 2 summarizes the details of our NIRSPEC observations. In four observing runs, we observed 35 slit positions corresponding to a total sky area of 0.3 arcmin^2.

Spectra were flat-fielded and sky-subtracted using IDL scripts written by G. Becker (2004, private communication). Following techniques described in Kelson (2003), the two-dimensional spectra were *not* straightened prior to sky subtraction, thus ensuring sub-pixel sampling of atmospheric emission lines which, in turn, led to a significantly improved removal of the sky background.

The camera distortion and spectral curvature were computed by fitting standard star traces along the slit and atmospheric emission lines across the dispersion axis. Knowledge of the distortion and spectral curvature was used to construct arrays that provide proxies to the slit position and wavelength for each exposed pixel on the NIRSPEC detector. Using this information, sky background modeling was performed using a two-dimensional b-spline fit, where a low-order polynomial is fit to the slit illumination and a b-spline is fit along the dispersion axis. The wavelength calibration is subsequently computed using atmospheric emission lines. For each exposure, we also compute 2D-variance arrays by summing the contribution from the dark current, flat-field, read noise, sky background, and source counts to the variance.

Following techniques introduced by Santos et al (2004), we determined the astrometric position of each spectral exposure by registering images from the NIRSPEC slit-viewing camera (SCAM) to HST images of the same field. WCS coordinates were computed for each exposed pixel on the detector using the slit position grid described above. Since these are galaxy cluster fields, many bright objects appear in the 46×46 arcsec^2 field of view, enabling accurate registration on to the WCS of the HST images with a typical rms of $0\farcs15$ (less than 25% of the slit width). Offsets between exposures of a given slit position are calculated from the registered SCAM images, and the 2D-spectra and their associated 2D-variance arrays are subsequently shifted and combined. To remove cosmic rays and bad pixels, we median combine the data rejecting the brightest and faintest frame at each pixel.

Our ability to detect faint emission lines is strongly dependent upon the accuracy with which the offsets between the different exposures of a slit position are known. If a bright emission line from a foreground galaxy lies serendipitously on the slit, the accuracy of the offsets can be determined by comparing the shifts derived from the SCAM images to the offsets between the centroid of the emission line. Suitable emission lines are present in several of our slit positions and applying the aforementioned test, we find the offsets determined from the SCAM images are typically good to $0\farcs1$. At less than 15% of the slit width, this uncertainty does not compromise the S/N of faint emission features.

One additional concern in dealing with faint emission line objects is the possible transverse drift of the object across the slit from frame to frame when the seeing is less than a slit width (Pelló et al., 2004; Weatherley et al., 2004). This would cause the centroid of the emission line to drift in the *dispersion* direction of the spectrun. Uncorrected, this would increase the area over which the emission line flux is spread, thereby reducing the observed S/N of the emission line in the final stacked spectrum. We quantify the magnitude of the transverse drift by measuring the frame-to-frame centroid of a very bright [OIII] emission line in NIRSPEC observations taken with exceptional seeing ($0\farcs45$). We find that the standard deviation in the centroid position over 9 frames is 0.8 pixels, or $0\farcs2$. Adding this measured tranverse drift in quadrature to the seeing FWHM only increases the FWHM of the line by 5%. Given that the seeing was never better than the value quoted above, it is clear that the drift has a negligible effect on the detectability of emission lines.

3.3.3 Survey Sensitivity

We now determine our survey sensitivity function. We first discuss the limiting line flux as a function of wavelength and source redshift. Converting this flux to a limiting source luminosity requires knowledge of the magnification across the NIRSPEC slit. In practice, we will quote our limit in terms of that line flux we can expect to detect, at 5σ confidence, for an unresolved emitter whose rest-frame line width is typical of a faint, but very well-studied, $z \simeq 5.7$ system (Ellis et al., 2001).

To accomplish this, we computed the total noise as a function of dispersion and slit position using the variance arrays obtained in the data reduction (§3.1). This comprises the sum of the variance from the sky background, read noise, flat-fielding, dark count as well as the source counts. Flux calibration of the variance arrays was performed using observations of spectroscopic standard stars. The 5σ limiting Lyman-α line flux was then computed as a function of slit position and wavelength by calculating the signal that is 5 times the root of the variance in an aperture whose spatial dimension is twice the measured seeing disk (typically $0\farcs7$) and whose spectral

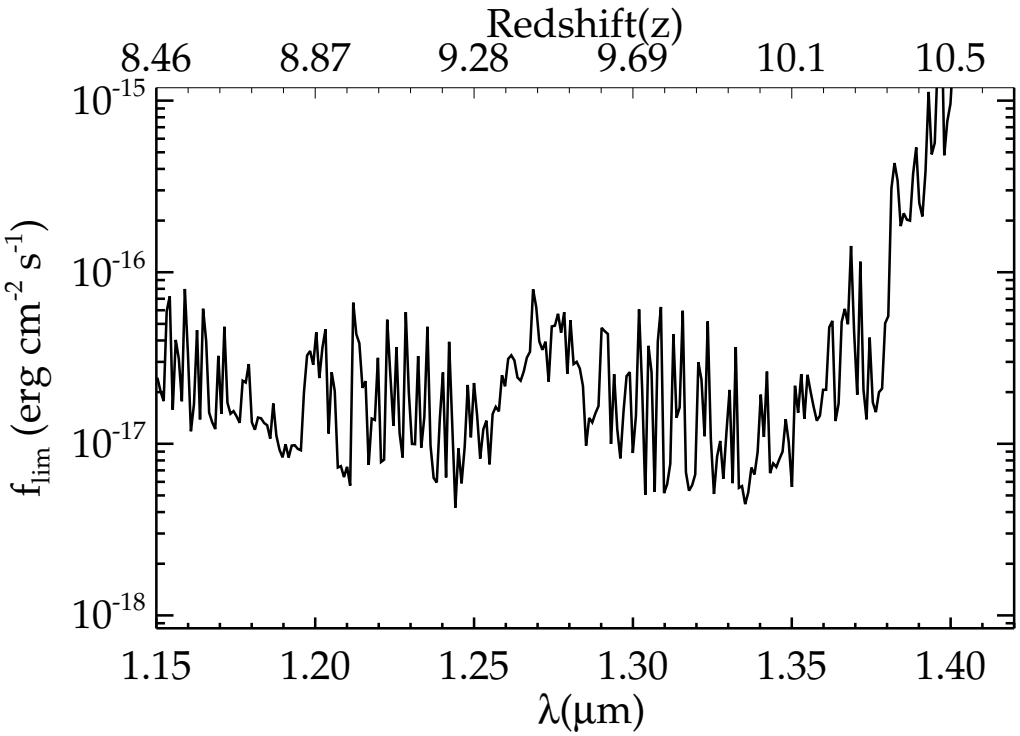

Figure 3.3 Limiting flux for detection of 5σ Lyman-α emission line for a typical NIRSPEC J band exposure. The top axis denotes the redshift corresponding to observed Lyman-α at the wavelength along the bottom axis. OH bands lie throughout the J-band spectrum, signficantly increasing the limiting flux at those wavelengths. The widest band occurs in the middle of the spectrum at $\simeq 1.26 - 1.28\mu m$.

dimension equals the Lyman-α line width, $\sim$300 km s^{-1} of the lensed system studied with high precision by Ellis et al. (2001).

We find the median 5σ limiting line flux across a typical slit position with 1.5 hours of integration is $2\times$ 10^{-17} erg cm^{-2} s^{-1} (see Figure 3.3); the sensitivity varies between 0.9-3 $\times$ 10^{-17} erg cm^{-2} s^{-1} depending on the proximity to atmospheric OH lines. This flux limit is similar to that reached in the $z = 8.8$ narrowband survey of GOODS-S discussed in Cuby et al. (2006) (1.3×10^{-17} erg cm^{-2} s^{-1}) and slightly less sensitive than the $z = 8.8$ narrowband survey presented in Willis & Courbin (2005) (3.3×10^{-18} erg cm^{-2} s^{-1}); however the lensing magnification enables the detection of sources that are significantly less luminous than those detectable in either conventional narrowband survey.

3.3.4 Cluster Magnification

As discussed in our precursor optical paper (Santos et al., 2004), the cluster mass models listed in Table 1 provide a 2-D map of magnifications for any given source redshift. The details by which these magnifications are realized follow techniques described in detail by (Kneib et al., 1996). Further discussion of the code, LENSTOOL, used to create the mass models for systems for which rich detail is available Jullo et al, (*in prep* and Smith et al. (2005). From each mass model, the magnification can be computed as a function of source redshift and position.

In practice, for each position and wavelength, the mass models produce a matrix of the convergence and shear. The magnification is then determined from the convergence κ and shear γ using the following equation:

$$\mathcal{M}(\mathbf{\Omega}, z) = \frac{1}{[1 - \kappa(\mathbf{\Omega}, z)]^2 - \gamma(\mathbf{\Omega}, z)^2} \tag{3.1}$$

where $\mathbf{\Omega}$ is the position on the sky and z is the source redshift.

A key question that often arises in the consideration of critical line surveys is the accuracy with which the location of the line can be pinpointed and also that of the associated magnification map. To address this question, we have used a Markov chain Monte Carlo sampling algorithm within LENSTOOL (Jullo et al., in prep) to map the probability density in the mass model parameter space for each cluster. We then generated a magnification map for each model and in turn computed the mode of the distribution at each pixel as well as the range of magnification factors which bracket the mode by $\pm 34\%$. This we take as the uncertainty in the magnification. The errors derived for each cluster are applied in the determination of both the candidate luminosities (§3.5) and the survey volume (§3.6.1).

Taking each exposed pixel on the NIRSPEC detector as an element of solid angle, the convergence and shear is computed as a function of position via interpolation between the NIRSPEC coordinate grid and that of the convergence and shear maps. For each NIRSPEC pixel, the associated redshift at which a Lyman-α emitter would be located is calculated using the wavelength solution described above. The convergence,

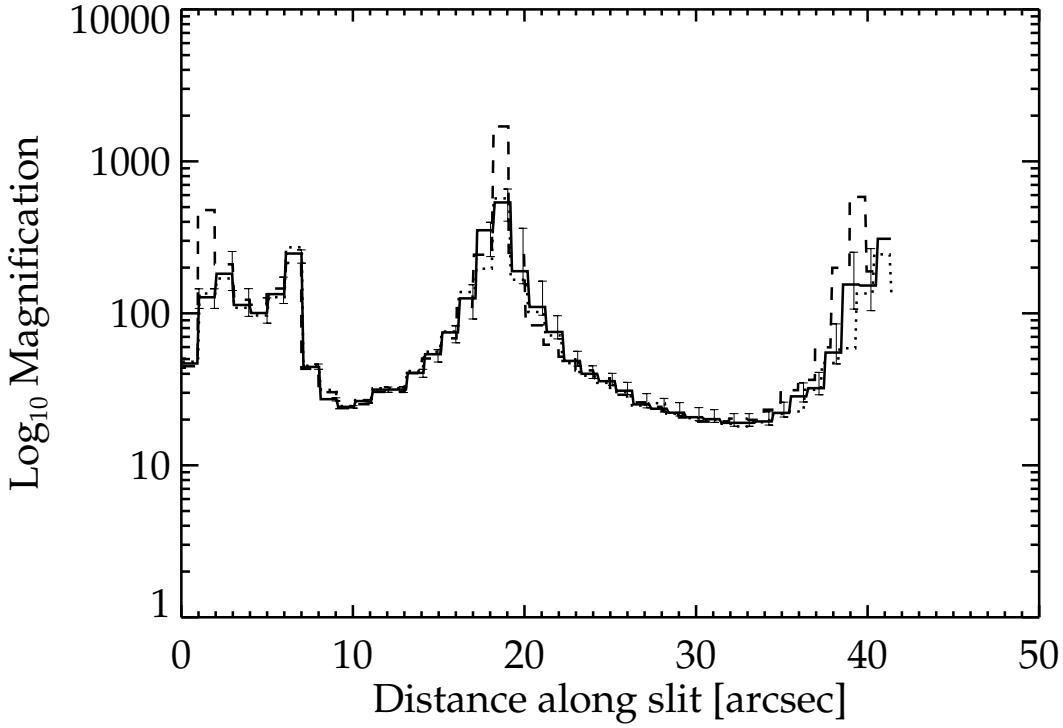

Figure 3.4 Lensing magnification provided to background sources as a function of NIRSPEC slit position and redshift. This figure shows the amplification at one of the slit positions along the critical line of Abell 2219. The solid line corresponds to the amplification provided to background sources at z=9 whereas the dotted and dashed line denotes that provided to sources at z=8.5 and 10.0, respectively. The error in lensing magnification is plotted as a function of NIRSPEC slit position for sources at z=9. The error does not vary significantly as a function of source redshift. Even allowing for uncertainty in the mass model, the magnification is still very high across the entire slit.

shear and Lyman-α redshift is then inserted into equation 1 and the magnification $\mathcal{M}$ at each pixel determined. Likewise, the magnification uncertainty map is interpolated onto the NIRSPEC coordinate grid enabling the computation of the error as a function of slit position. Both the magnification and associated error maps were smoothed using a $1\farcs0$ median box filter to ensure that our results are not corrupted by sharp high peaks in the magnification distribution. The change in the magnification error with redshift is negligible; hence we adopt the uncertainity at $z = 9$ to be the magnification error for all Lyman-α redshifts probed by our survey.

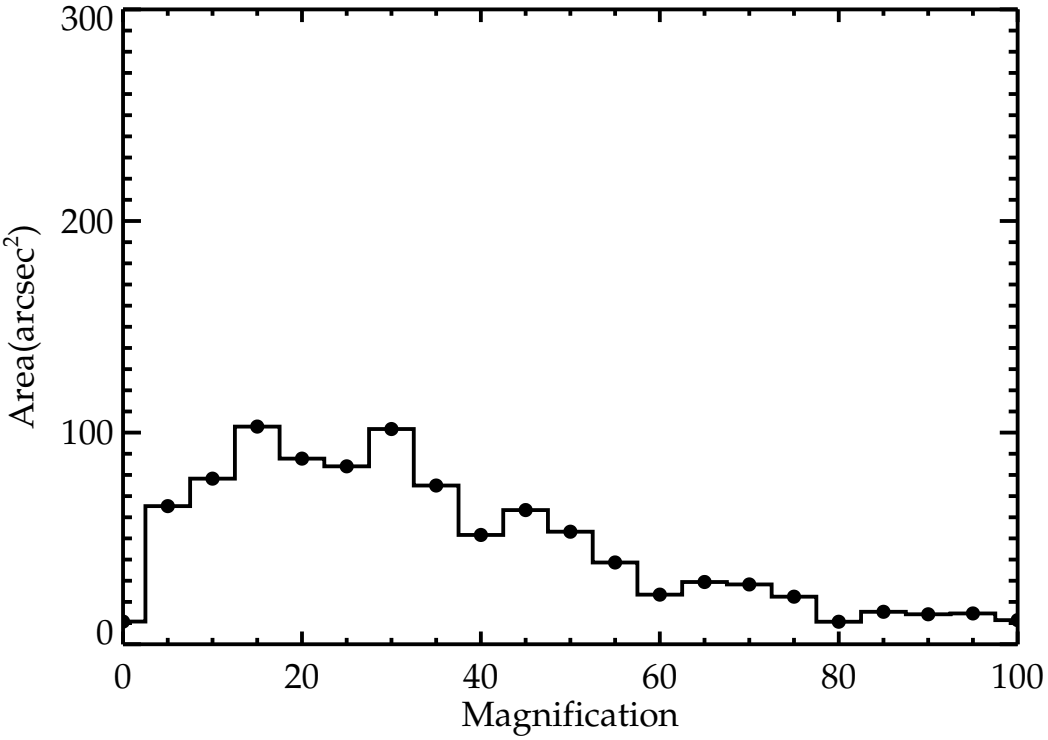

Figure 3.5 Distribution of lensing magnfication across our total survey area. The median magnification across our survey area is $\simeq$20, about a factor of 2 larger than in a similar optical spectroscopic lensing survey (Santos et al., 2004) (see §3.3.4 for explanation). A non-negligible fraction of each slit is magnified by larger than this factor.

As an example of the magnifications sampled, the wavelength-independent magnification along one of our survey slit positions is displayed in Figure 3.4 for three different redshifts. The magnification is $> \times 20$ over nearly the entire slit and fairly constant with redshift. We also plot the associated 1σ uncertainty as a function of position along the slit at one of the redshifts. Even allowing for the uncertainty in the lensing model, the magnification is still expected to be uniformly high across the entire slit. This is largely a result of the fact that we only select clusters with well-defined mass models. Furthermore, in regions where the location of the critical line is known less precisely, there is generally a region $\simeq 2\farcs$ in width around the critical line where the magnification factor is greater than fifteen, so the positioning of the NIRSPEC slit is always in a region of high magnification.

Figure 3.5 presents a histogram of the magnification in our survey. Throughout the entire survey area, the median magnification provided to background sources is $\simeq \times 20$, a factor of two larger than in the optical survey conducted by Santos et al. (2004). The increased magnification is due to several factors. First, ultra-high magnification regions ($\times$15-30 throughout the slit-area) were preferably selected to allow very low-luminosity systems ($\lesssim 10^{42} ergs^{-1}$) to be probed. Second, since the NIRSPEC longslit covers a factor of three smaller angular extent on the sky than the LRIS longslit used in Santos et al. (2004), we were able to avoid regions where the critical line curved off the slit, resulting in high magnification uniformly across the slit.

3.3.5 Limiting Lyman-α Luminosity

Given our knowledge of the limiting Lyman-α flux (§3.3.2) and the spatially-dependent magnification (§3.3.3), we are now in a position to calculate the limiting source Lyman-α luminosity, $L_{\rm lim}(\mathbf{\Omega}, z)$. This we define as the least luminous source detectable (with 5σ confidence) in a given volume element, allowing for the cluster magnification $\mathcal{M}$.

Allowing each NIRSPEC pixel to correspond to a volume element, we can calculate the limiting luminosity across each slit in the survey according to the following:

$$L_{\rm lim}(\mathbf{\Omega}, z) = \frac{4\pi(1+z)^2 D_{\rm c}^2(z)}{T(\mathbf{\Omega})} \frac{f_{\rm lim}(z)}{\mathcal{M}(\mathbf{\Omega}, z)}. \tag{3.2}$$

where $\rm D_c(z)$ is the comoving distance of the volume element and $T(\mathbf{\Omega})$ is the slit transmission.

In the absence of the lensing magnification, the typical limiting Lyman-α luminosity is $2\times\ 10^{43}$erg s^{-1} in between atmospheric OH lines. However, more than 50% of the survey area is magnified by $> \times 30$, enabling the detectability of sources as faint as $7\times\ 10^{41}$erg s^{-1} over $\simeq$0.15 arcmin^2 in the image plane. Conventional narrowband Lyman-α surveys at $z > 6$ typically reach limiting luminosities between 10^{42} and 10^{43} erg s^{-1}. Our NIRSPEC survey probes over an order of magnitude fainter and thus

can clearly provide constraints on star forming sources that are otherwise out of reach of traditional methods, at least with current facilities.

3.4 Identification and Reality of the Candidate Lyman-α Emitters

At the faint limits now being probed, we have found the reliable identification and verification of distant Lyman-α emitters to be a very challenging endeavor, even with the most powerful facilities available to us. The burden of proof that a detected line is (a) real and (b) truly arises from a highly-redshifted Lyman-α emission line is very great given earlier controversies (Pelló et al., 2004; Bremer et al., 2004; Smith et al., 2006). So far as the identification process is concerned, the key issue is to ensure candidate emission features are not spurious and do not arise from detector artefacts Weatherley et al. (2004). Concerning the redshift verification, a new set of challenges emerge at $z \simeq$10 since additional (confirmatory) emission lines are not available from ground-based facilities (see §3.5).

Beginning with the identification process, each of the sky-subtracted 2-D spectra were independently inspected for Lyman-α candidates by three of the authors (D.P.S, R.S.E, and J.R.). We demanded that any candidate feature be both extended over multiple pixels (in order to differentiate a signal from bad pixels and other detector artifacts) and located away from contaminating OH airglow lines. The three lists of line candidates each contained $\simeq$ 25 possible features with many being in common between two of the three lists. A final catalog of six promising candidates was constructed by selecting those features with the highest significance common to all three observers. These are displayed in Figure 3.6. The S/N ratios of these candidate emission lines, defined as in §3.3.2, varies between 5 and 8 (see Table 3).

A spurious feature could arise if the reduction process does not adequately remove a cosmic ray or bad pixel. Obviously dithering the telescope so the candidates move up and down the slit eliminates most detector anomalies. However artefacts can

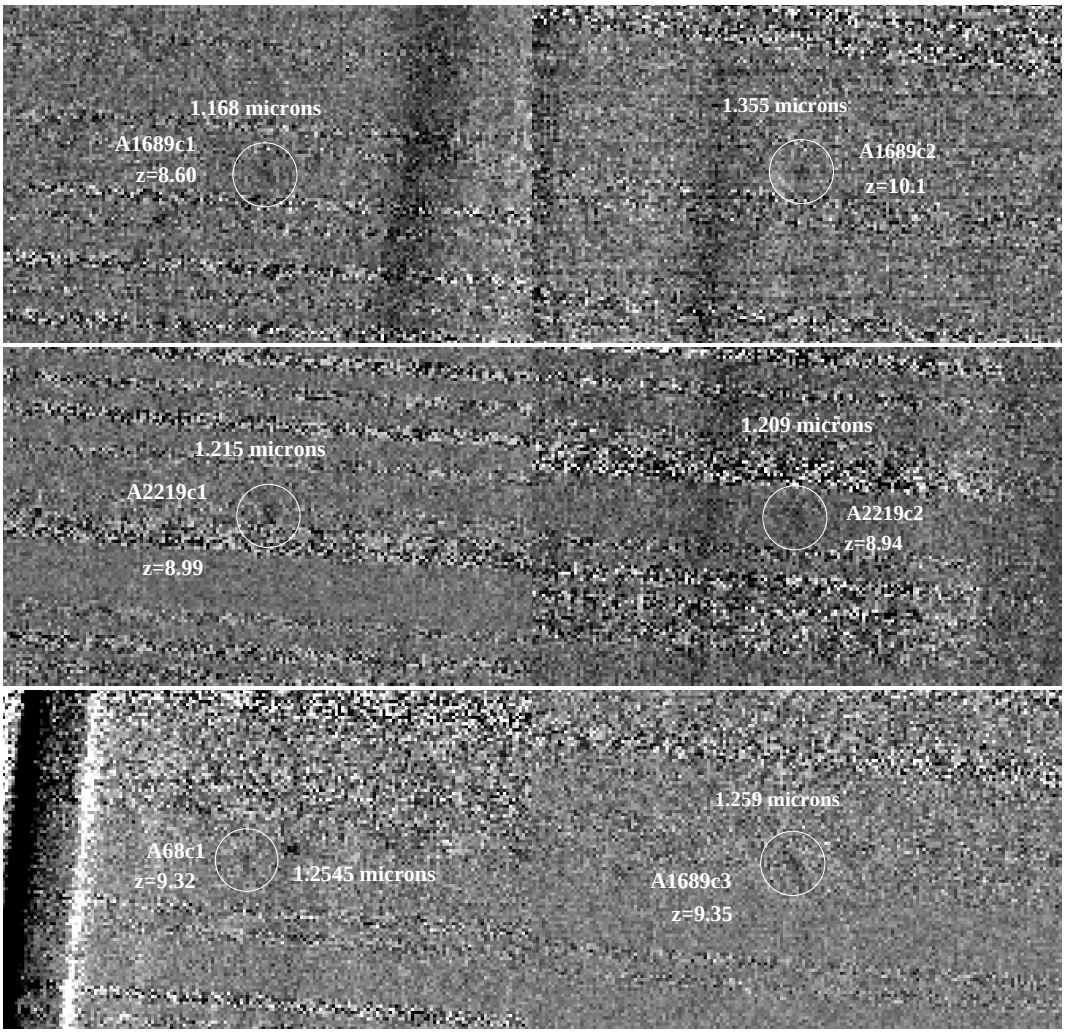

Figure 3.6 Candidate Lyman-α emitters, each undetected in deep optical HST data. If Lyman-α, the emission line redshifts range between $z = 8.7$ and $z = 10.2$. Line fluxes range between $2 - 5{\times}10^{-17}$ erg cm^{-2} s^{-1} implying intrinsic (unlensed) star formation rates of 0.2-5 M$_\odot$ yr^{-1}, for nominal source assumptions.

Table 3.3. NIRSPEC Lyman α Candidates

Candidate	RA(J2000)	DEC(J2000)	flux (erg s^{-1} cm^{-2})	λ (μm)	z $_{Ly\alpha}$	Log$_{10}$ L $_{Ly\alpha}$ (erg s^{-1})	Log$_{10}$ Mag
A68c1	00 37 06.10	+09 09 18.7	$2.2{\pm}0.3{\times}10^{-17}$	1.254	9.32	$41.2^{+0.1}_{-0.7}$	$2.2^{+0.7}_{-0.1}$
A1689c1	13 11 31.85	−01 20 40.0	$2.3{\pm}0.3{\times}10^{-17}$	1.366	10.23	$42.3^{+0.02}_{-0.01}$	$1.2^{+0.01}_{-0.02}$
A1689c2	13 11 31.26	−01 20 29.8	$4.0{\pm}0.7{\times}10^{-17}$	1.173	8.65	$42.7^{+0.07}_{-0.08}$	$0.8^{+0.01}_{-0.03}$
A1689c3	13 11 28.43	−01 19 44.5	$4.1{\pm}0.6{\times}10^{-17}$	1.259	9.35	$42.1^{+0.06}_{-0.08}$	$1.5^{+0.04}_{-0.03}$
A2219c1	16 40 23.64	+46 42 26.5	$4.8{\pm}0.6{\times}10^{-17}$	1.215	8.99	$41.8^{+0.09}_{-0.07}$	$1.9^{+0.04}_{-0.07}$
A2219c2	16 40 23.04	+46 42 43.2	$2.1{\pm}0.3{\times}10^{-17}$	1.209	8.94	$42.0^{+0.06}_{-0.09}$	$1.3^{+0.06}_{-0.03}$

remain if the spectra are rebinned during the wavelength calibration; in this case, such bad pixels would be smoothed out and appear similar to emission lines (Weatherley et al., 2004). Fortunately, we do not face this problem in our Keck dataset since our reduction technique altogether avoids rebinning the spectra (see §3.3). Nevertheless, one may still worry that the measured emission line flux originates from one or two frames with overlapping cosmic rays or bad pixels. We have tested this possibility by median combination of all of the exposures of slit positions containing our candidates and rejecting the three highest pixels. We also median combined half of the exposures (chosen randomly) for each candidate. In both tests, all six candidates are still clearly visible (albeit at lower S/N for the latter test), suggesting that our emission features do not arise from flux in only one or two frames.

Finally, it is conceivable that the noise distribution of the spectral data is such that 5σ noise features are much more common than would be expected under Gaussian statistics. Such a curious situation might arise if there was some unforeseen property of the NIRSPEC detector. In this case our candidate emission features might simply be peaks in the noise distribution. We investigated this possibility by computing the flux in apertures centered at random positions in areas of the spectra where the sky-subtraction is clean. The aperture size was matched to the expected size of a Lyman-α feature at high redshift: the spatial FWHM was taken to be the size of a typical seeing disk, $0\farcs6$ and spectral FWHM corresponding to typical line width of Lyman-α emitters, 300 km s^{-1})

A normalized histogram of the distribution of summed aperture fluxes is presented in Figure 3.7. The frequency with which a feature with S/N = 5 appears in our spectra is $\simeq$0.02%, which corresponds to just under a 4σ detection for a Gaussian distribution. Though the frequency of features with fluxes comparable to our candidates may be slightly higher than indicated by Gaussian statistics, the test clearly illustrates that features of prominence similar to those of our candidates are extremely rare in clean regions of the spectra.

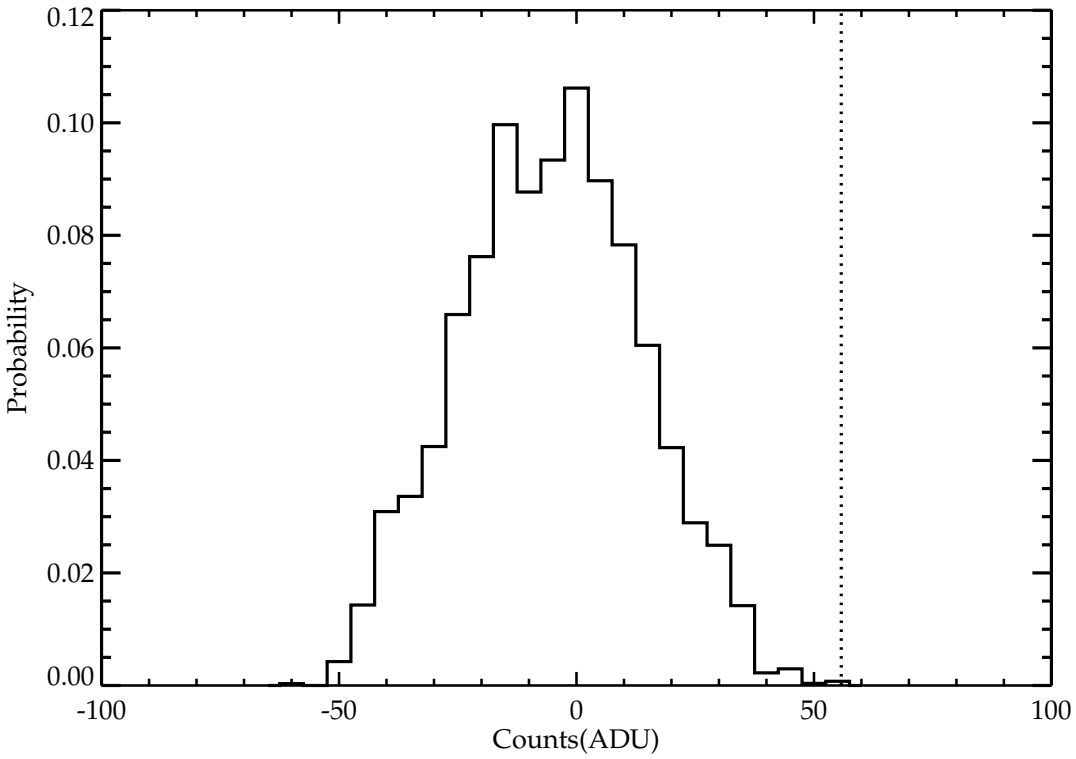

Figure 3.7 Normalized histogram of summed flux in randomly placed apertures in clean regions of sky-subtracted spectra. The dotted line represents value of a typical candidate Lyman-α emitter. The frequency of features with fluxes on par with the candidates is 0.02%, consistent with a $\simeq 4\sigma$ detection assuming a Gaussian distribution of noise.

3.5 Verifying the Candidate Redshifts

If the emission features discussed above are Lyman-α , then the source redshifts for our 6 candidates range between $z = 8.7$ and $z = 10.2$ and the observed fluxes span 2-5$\times10^{-17}$ erg cm^{-2} s^{-1}. Converting these observed fluxes into intrinsic luminosities is complicated by uncertainties in the fraction of emitted Lyman-α photons that reach the observer. We can compute a lower limit to the unlensed Lyman-α luminosity by converting the fluxes to luminosities and dividing by the magnification factor. With these assumptions, the derived unlensed luminosities range from 1.6-50$\times10^{41}$ erg s^{-1}.

We convert these Lyman-α luminosities to star formation rates assuming case B recombination: $L_\alpha = \frac{2}{3} h\nu_{Ly\alpha}(1 - f_{esc})Q(H)\dot{M}_\star$ where $h\nu_\alpha$ is the energy of a Lyman-α photon, Q(H) is the Hydrogen ionizing photon flux per unit of star formation, and f_{esc} is the fraction of ionizing photons that escape from the galaxy (and hence are not emitted in recombination emission lines). Assuming a Salpeter initial mass function, 1/20th solar metallicity, and a minimum and maximum stellar mass of 1 and 20 $M_\odot$, respectively, the hydrogen ionizing photon flux is 4×10^{53} s^{-1} (Schaerer, 2003) for galaxy forming stars continuously at a rate of 1 $M_\odot$ yr^{-1}. For $f_{esc} \ll 1$ (e.g. Shapley et al. 2006), this results in a conversion factor of 1 $M_\odot$ yr^{-1} = 4.2×10^{42} erg s^{-1}. With these assumptions, the star formation rates range from 0.038 to 1.2 $M_\odot$ yr^{-1}. If a Scalo IMF was adopted instead, the star formation rates would be a factor of three greater (Loeb et al., 2005).

We note that these star formation rates are uncertain for several reasons. If dust in the galaxy absorbs any Lyman-α photons, then the intrinsic luminosities and corresponding star formation rates will be larger. Likewise, if only a fraction of the Lyman-α line is transmitted through the IGM due to the presence of neutral hydrogen, then Lyman-α luminosity and star formation rates will again be underestimated. On the other hand, if the stellar IMF at these early times is more top-heavy than a Salpeter or Scalo IMF, more ionizing photons are predicted per unit of star formation. Similarly, if the metallicity of these galaxies is less than what is assumed above, the efficiency of ionizing photon production (and hence Lyman-α luminosity) is increased

(Tumlinson & Shull, 2000; Tumlinson et al., 2001; Schaerer, 2003). Hence, in these cases, the star formation rates tabulated will be overestimates.

But how can we be sure, with a single emission line, that we have truly detecteda Lyman-α emitter? Normally, for a narrow-band imaging survey (Hu et al., 2002, 2004; Malhotra & Rhoads, 2004; Shimasaku et al., 2006; Kashikawa et al., 2006) or an unlensed spectroscopic survey (Martin et al., 2006), contamination from foreground [O II] and Hα emitters can be significant. However, it is worth pointing out that such foreground contamination is likely to be much reduced for a critical-line survey designed to probe faint emitters since, for lensing clusters at $z \simeq$0.2-0.5, *all contaminating emitters will also be lensed and thus their respective most-likely location in the image plane will be spatially offset with respect to that for a source at $z \simeq 2$.* The degree to which this benefits a lensed survey with respect to a blank field survey will depend on the relative magnifications at each redshift and the shape of the faint end of the respective line emitting luminosity functions.

A redshift that the general community normally accepts is usually one in which at least two, preferably more, features are reliably identified. Single line identifications are quite naturally questioned as unreliable. As we probe to $z \simeq 10$ with ground-based telescopes, however, we reach the situation where multiple-line identifications are simply not practical. With Lyman-α in the J-band no additional feature is visible in the full practical spectroscopic range from the UV limit to the beginning of the thermally-dominated background at 2μm. The Infrared Spectrograph (*IRS*) on Spitzer in principle offers the possiblity of detecting Hα emission from $z \simeq 10$ objects. However, sensitivity calculations (Lacy et al., in prep.) suggest that the Hα/Lyman-α flux ratio would have to be significantly greater than that expected for case B recombination (perhaps due to Lyman-α suppression from resonant scattering and absorption) in order for this to be an effective verification.

A second-best verification of Lyman-α that might be convincing would be the identification of an associated Lyman break in broadband imaging of the continuum distribution (Stanway et al., 2004) or the presence of an asymmetric line profile (Ellis et al., 2001; Hu et al., 2002). The Lyman break is due to intergalactic absorption of

flux shortward of the Lyman-α line and causes all $z > 7$ sources to be undetected at optical wavelengths. However, the lack of an optical broad-band detection need not necessarily rule out a lower redshift source, for example those with very strong emission line spectra and weak continuum emission.

Asymmetric line profiles are expected because of resonant scattering by neutral hydrogen within the host galaxy and in the IGM. This leads to absorption on the blue side of the line as the light redshifts into resonance, leaving a sharp cutoff on the blue side of the line and an extended red damping wing. Unfortunately, the detection of an asymmetric line profile requires very long integrations and high spectral resolution in order to detect the damping wing.

A key factor in our consideration of how to verify the Lyman-α label for our 6 candidates is the importance of exquisite conditions to see such faint emitters. The required seeing and transparency occur only 40-50% of the time even on an excellent site such as Mauna Kea. Conservatively, we estimated that to measure the Lyman-α profile of any one of our 6 candidates with adequate signal/noise would take 8-10 hours of integration on Keck II. Allowing for weather, to follow-up all 6 candidates in this fashion would take 24 nights; clearly this is not a practical proposition!

One might conclude we have reached new territory where we may never quite know with certainty whether an object is at $z \simeq 10$. In practice, however, there is a way forward although it is less definitive and more statistical in nature. The approach we will adopt is to search spectroscopically in various passbands for lines associated with alternative, lower redshift explanations for the detected J-band emission line. In ruling out a particular alternative identification, we must make some assumptions about the likely emission line spectrum of the interloper. As such this is then a statistical process since we cannot cover all possible emission line ratios. While this method will never confirm the Lyman-α interpretation with 100% certainty, it is clearly an essential pre-requisite to spending 2 nights per candidate measuring the line profiles.

In the following subsections, we proceed to apply the tests discussed above to our candidates in order to constrain their redshifts. In §3.5.1, we examine the stacked line

profiles of the six candidates to see if we can collectively assess the likelihood the bulk represent Lyman-α emission; in §3.5.2, we test for the presence of a Lyman break in deep broadband photometry; finally in §3.5.3, we discuss our follow-up spectroscopic program to test for low-redshift interlopers.

3.5.1 Stacked Line Profile of Candidates

Asymmetric line profiles cannot be discerned in the individual emission features, because of the low spectral signal/noise. As discussed, much longer integrations (8-10 hrs) would be needed to characterize the emission line profiles and this seems pointless until lower redshift interlopers have been rigorously tested.

Nonetheless, one can ask whether statistically as a combined set, the combined line profile of all 6 candidates reveals an asymmetric profile suggestive of a Lyman-α origin. The practicality of such an exercise is limited by a number of factors. First the resolution of NIRSPEC is only moderate; $R \simeq$1500 c.f. $R \simeq$15,000 for the ESI spectrum obtained at z=5.7 (Ellis et al., 2001). Second, stacking assumes that all 6 lines are Lyman-α with similar profiles and, most importantly, requires an accurate registration using the central wavelength within each low signal/noise profile. Finally, as the adjacent OH sky lines are distributed differently for each emitter, wavelength regions that are clean in one candidate become averaged with noisy regions in another so the contrast of the stacked line does not increase as $\sqrt{N}$. Even with weighted addition, we did not find the test to be very conclusive.

3.5.2 Searching for Lensed Pairs

In several of the lensed emitters and drop-outs we have published in the past (Ellis et al., 2001; Kneib et al., 2004), the location of a second or third counter-image has been a particularly convincing demonstration of both the lensed hypothesis and, via the mass model, the approximate redshift. Indeed, the accurate recovery of the third image for the $z \simeq 6.8$ drop-out source in Abell 2218 (Kneib et al., 2004) was one of the major arguments justifying its location beyond $z \simeq$6.

Generally speaking, image pairs are expected in strong lensing configurations depending on the degree of alignment between the background source and the cluster caustics, the physical size of the source and, in this case, the ground-based seeing. The key feature which led to the satisfactory recovery of image pairs in our earlier studies was a broad-band detection with HST. As an example, in the case of the $z = 5.7$ pair discussed by Ellis et al (2001), only a single emitter was recovered by LRIS. The location of the second image required a detection by HST. Indeed, pairs were not detected for any of the other lensed sources in the subsequent LRIS survey (Santos et al., 2004).

Some true pairs may simply not be resolved in our ground-based spectra and, quite possibly, the second image lies outside our NIRSPEC slit coverage. For the most well-constrained mass model, the location of a counter-image can usually be predicted with an uncertainty of $0\farcs5$-$1\farcs$, i.e. to within 1-2 NIRSPEC slit widths. Although it is practical to consider chasing the second images, this could still be fairly time-consuming and we concluded that priority should be given in eliminating low-redshift interlopers from our catalog of candidates.

3.5.3 Broadband Photometry of Candidates

The next test is to determine whether optical continuum emission is visible for any of our candidates. Such a detection would clearly rule out a high z interpretation although non-detection does not imply the opposite. Deep ACS/WFPC-2 (Kneib et al., 2004; Smith et al., 2002) images are available for all 9 clusters so we have examined these images at the precise locations of each of our 6 emitters.

No definitive broadband optical detection is seen at the location of any of the candidates to R$\simeq$27.5 (3σ, Figure 3.8). One of the candidates (Abell 2219 c2) is very marginally detected in the z'_{F850LP}-band; if this flux is associated with the J-band emission feature, then the high redshift interpretation would seem unlikely. Although 3 of the candidates (Abell 2219 c1, Abell 1689 c1, c2) are located within $2\farcs$õf brighter objects, in all cases, our registration sufficiently accurate to rule out the possibility

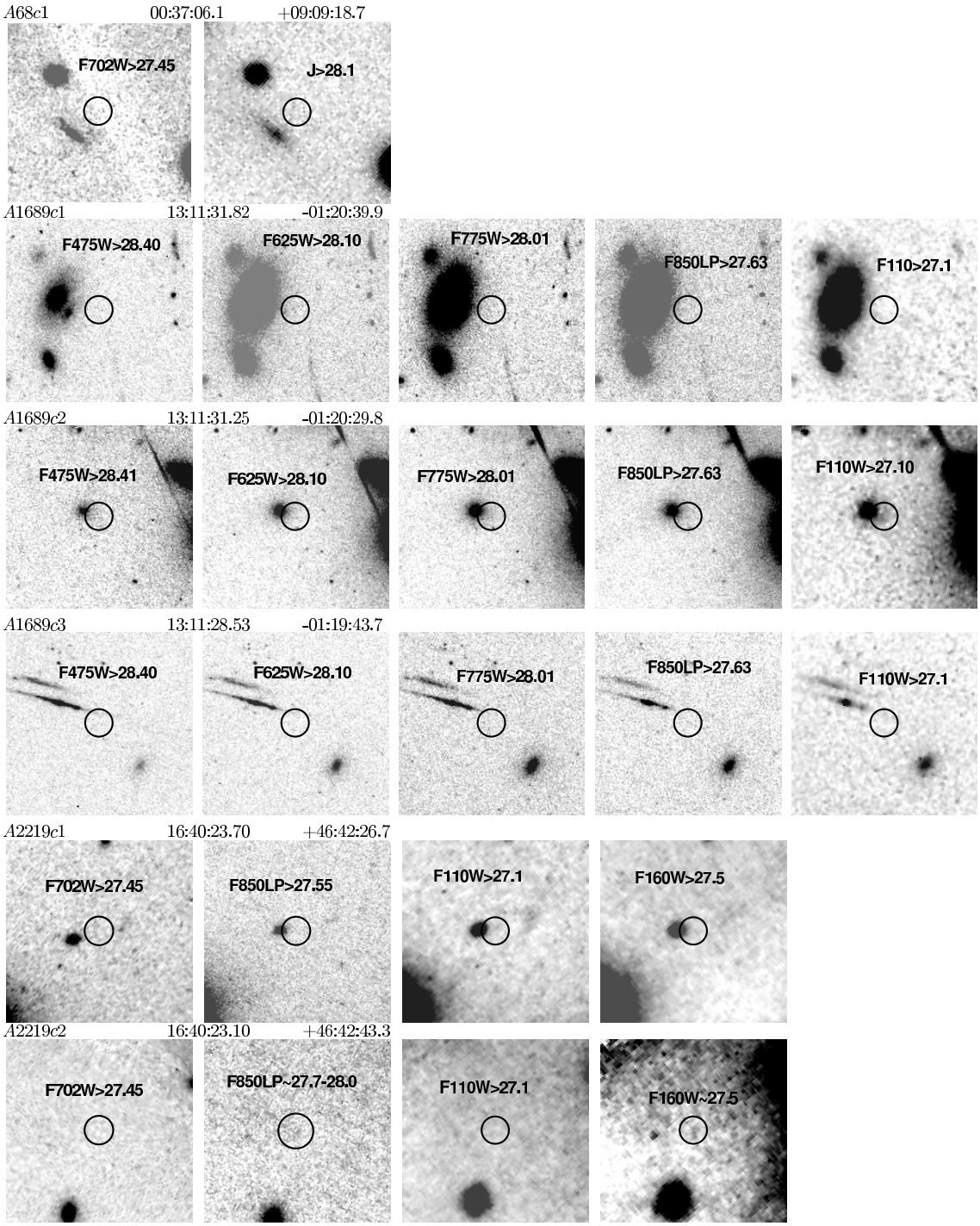

Figure 3.8 Deep broadband images of the locations of the candidate J-band emission features. None of the candidates have *definitive* detections in the optical; although A2219c2 is very marginally detected in the z'_{F850LP} and H_{F160W} bands. Three of the candidates are located within several arcseconds of brighter objects (A2219c1, A1689c1, and A1689c2); however in both cases, our registration is known to sufficient precision to rule out the possibility that the J-band emission features emanate from the bright objects. The lack of detection in very deep near-IR images suggests that if these candidates are at $z \simeq 9$, then their rest-frame UV continuum emission is very faint.

that the J-band emission emanates from the bright objects.

A detection in deep near-infrared imaging would be more interesting. Coupled with the optical non-detections discussed above, this might hint at the presence of a Lyman break, lending credence to a $z \simeq 10$ interpretation. In fact, none of the candidates is detected at or above the 5σ level ($\simeq$27 AB mag) in deep broadband HST J_{110W}, H_{160W} and Keck J-band imaging. Abell 2219 c2 is marginally detected at $\sim 2\sigma$ in the H_{160W}-band.

In fact the lack of definitive near-infrared detections for our Lyman- α candidates is not at all surprising if they are at high-z. If the equivalent width distribution of Lyman-α emitters at $z \simeq 10$ is comparable to that at $z \simeq$4-6, then we would need to reach $H_{160W} = 27.7$ (1 magnitude below our sensitivity limit) to detect our candidates, if they are indeed Lyman-α emitters (Malhotra & Rhoads, 2004; Shimasaku et al., 2006).

Thus, we can conclude that our deep imaging adds a further important component in the case for the hypothesis that bulk of our emission line sources lie at $z \simeq 10$.

3.5.4 Spectroscopically Testing Low Redshift Scenarios

Aside from Lyman-α, the most likely alternative identifications for the J-band emission features include Hα, [OIII], Hβ, and [OII], in which case the features would correspond to lensed sources at $z = 0.5 - 2.5$. Sources located at these redshifts would almost certainly have additional, associated emission lines bright enough to be seen in the optical and near-infrared spectral regions (see Table 4). We have constrained each of these lower redshift hypotheses by undertaking further spectroscopy, placing stringent limits on the presence of lines.

This technique has value so long as the expected line spectrum of the foreground interlopers is known. In practice selective extinction and excitation differences make the relevant line ratios somewhat uncertain. The best we can do is to approach the problem statistically, assuming a typical HII region spectrum (Figure 3.9) allowing some leeway in the line ratios.

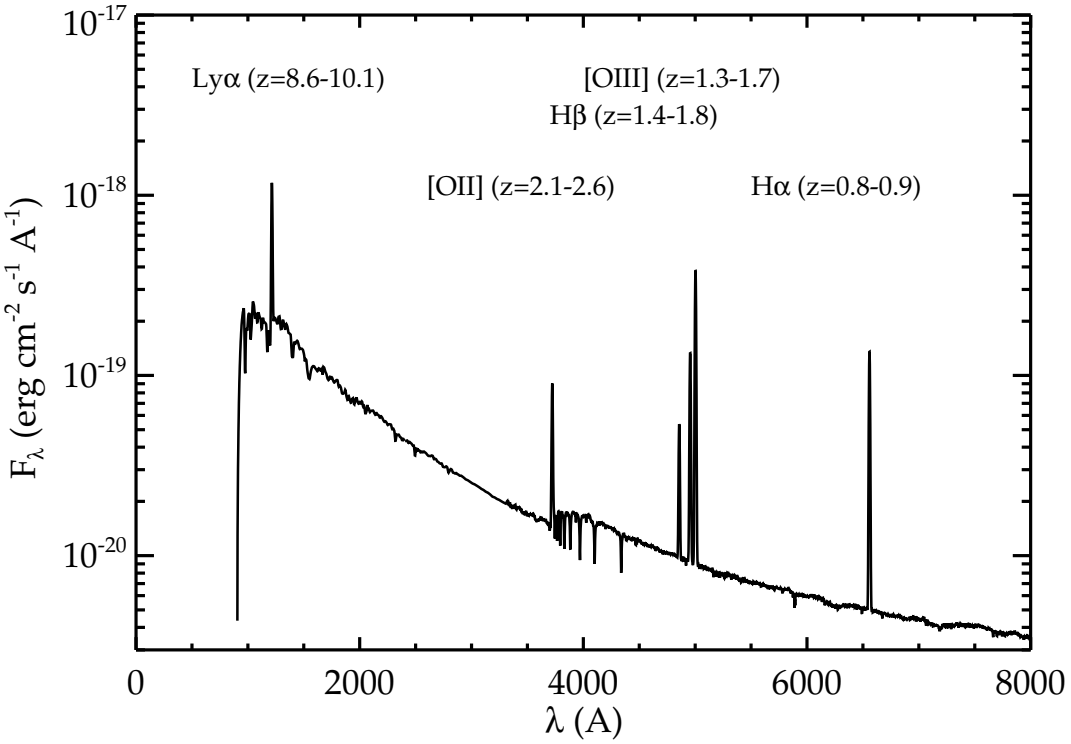

Figure 3.9 Most likely emission features and corresponding redshifts of the J-band emission features. If the line lies in the rest-frame optical ([OII], Hβ, [OIII], Hα), then additional emission features should be present in optical or near-infrared spectroscopy. If, on the other hand, the line is Lyman-α at z=8.5-10, then additional powerful emission lines will have been redshifted into the mid-infrared, making confirmation very difficult.

Table 3.4. Wavelengths of Additional Emission Lines for Low-z Scenarios

Line	z	λ Lyα (μm)	λ [OII] (μm)	λ Hβ (μm)	λ [OIII] (μm)	λ Hα (μm)
Hα	0.85	0.2253	0.6905[a]	0.9007	0.9188/0.9277	1.2160
[OIII]	1.43[b]	0.2953	0.9051	1.1805	1.2043/1.2160	1.5939
	1.45[c]	0.2982	0.9139	1.1920	1.2160/1.2278	1.6093
Hβ	1.50	0.3042	0.9323	1.2160	1.2405/1.2525	1.6418
[OII]	2.26	0.3967	1.2160	1.5860	1.6180/1.6336	2.1413
Lyα	9.0	1.2160	3.7270	4.8610	4.9590/5.0070	6.5630

[a]Throughout the table, we take the luminosity-weighted value of [OII], λ=3727 Å, for conciseness.

[b]λ=5007 Å

[c]λ=4959 Å

We generate the HII region spectrum by computing flux ratios of bright recombination lines (Lyman-α, Hα, and Hβ) assuming Case B recombination and accounting for the possibility that a signficant fraction of Lyman-α photons are absorbed by dust thereby reducing its flux by up to a factor of three. With these assumptions, we adopt the following emission line ratios for hydrogen recombination lines: Lyman-α : Hα : Hβ = 7.4-22 : 2.8 : 1.0. Flux ratios involving the forbidden oxygen lines ([OII] and [OIII]) can be determined from observations of low- and high-metallicity galaxies (Pilyugin et al. 2000, 2001). Here we adopt a ratio of [OIII]λ5007 : [OIII]λ4959 : [OII] : Hβ = 0.8-7 : 0.3-2 : 0.8-3 : 1. Using these ratios and the conversion between Lyman-α luminosity and star formation rate (§3.5), we generate a template spectrum (Figure 3.9); the continuum flux spectrum is determined for a given star formation rate via a Bruzual & Charlot (2003) model with identical stellar properties to those assumed in §3.5.

There are certainly a number of shortcomings in such an approach. Predicting the flux of Lyman-α is always difficult due to the resonant nature of the transition. While we allow for a factor of three suppression in the Lyman-α flux, it is possible that a larger fraction of Lyman-α photons could be absorbed. Furthermore, the flux ratios, especially those involving the forbidden oxygen lines, are dependant on the metallicity and the effective temperature of the ionizing stars. However, as we will show below, our observational flux limits are often sufficiently tight to rule out low-redshift hypotheses for a wide variety of metal abundance and stellar effective temperature assumptions.

Following the above logic, after completion of the blind scanning survey, we set out to secure additional optical and H-band spectroscopy for all 6 candidates to apply this interloper-rejection method. Sadly, after two seasons of observing, weather and other observing vagaries mean that exhaustive consideration of all interloper possibilities is only available for 3 of our candidates. For the other 3 candidates, only partial coverage is in place.

Table 4 summarizes the various hypotheses for the J–band emission and lists, for each case, which additional lines would be expected and at what wavelengths. Optical

spectroscopy is very efficient at constraining the likelihood that our J-band emission arises from either $H\alpha$ (z$\simeq$0.9) or [O III] ($z \simeq$1.5) since, in these cases, the LRIS data probes very deep in the associated wavelength regions where [O II] would be seen (at 7100 Å and 9300 Å respectively). In some cases, the survey J-band NIRSPEC data can also be used to constrain the hypothesis that the primary detection is $H\beta$ or [O III] where we would expect to locate one or both of the [OIII] λ4959,5007 pair and Hβ. In practice, this is complicated by the fact that lines can be obscured by the OH night sky or seen at very low significance (e.g. 2σ). We found that such cases can be more effectively dispensed with using H-band spectroscopy to search for Hα which should be easily observable if it lies in between the sky lines.

3.5.5 Best Candidates: Abell 68 c1 and Abell 2219 c1

The most convincing elimination of foreground interloper status has been achieved for the two candidates Abell 68 c1 and Abell 2219 c1. In our subsequent analysis we will assume these emitters are Lyman-α and so we describe these spectroscopic constraints in some detail.

In addition to the null broad-band detections discussed earlier, deep optical LRIS and H-band NIRSPEC spectroscopy was secured in good conditions for both candidates and no definitive features are seen in either case. We summarize the predicted fluxes and limiting sensitivities for each low-redshift interloper case in Table 5.

Table 3.5. Constraints on Low-redshift Interpretations of Candidates

Line	z	f $_{Ly\alpha}$ (10^{-17} erg cm^{-2} s^{-1})	f $_{[OII]}$ (10^{-17} erg cm^{-2} s^{-1})	f $_{H\beta}$ (10^{-17} erg cm^{-2} s^{-1})	f $_{[OIII]_1}$/ f $_{[OIII]_2}$ (10^{-17} erg cm^{-2} s^{-1})	f $_{H\alpha}$ (10^{-17} erg cm^{-2} s^{-1})
			Abell 68 c1			
Hα	0.91	N/A	0.63-2.4 (0.07)	0.79 (0.07)	N/A / N/A	N/A
[OIII]$_2$	1.51	N/A	N/A	0.31-2.8 (1)	0.73 (0.9)/ NA	0.4-13(2)
[OIII]$_1$	1.53	N/A	N/A	1.1-7.7 (6)	NA / 6.9 (5)	3.1-21 (2)
Hβ	1.58	N/A	N/A	NA	0.66-4.4 (5) / 1.8-15 (3)	6.2 (2)
[OII]	2.37	31 (0.02)	N/A	1.4 (5)	0.22-7.3 (7) / 2.2-5.1 (5)	N/A
			Abell 1689 c1			
Hα	1.06	N/A	N/A	N/A	N/A / N/A	N/A
[OIII]$_2$	1.71	N/A	N/A	0.33-2.9(6)	0.77(1) / N/A	N/A
[OIII]$_1$	1.72	N/A	N/A	1.2-7.7(0.9)	N/A / 6.9(4)	N/A
Hβ	1.79	N/A	N/A	N/A	0.69-4.6(20) / 1.8-16(100)	N/A
[OII]	2.64	N/A	N/A	N/A	N/A / N/A	N/A
			Abell 1689 c2			
Hα	0.78	N/A	N/A	N/A	N/A / N/A	N/A
[OIII]$_2$	1.33	N/A	N/A	N/A	1.3 (5) / N/A	N/A
[OIII]$_1$	1.36	N/A	N/A	N/A	N/A / 12(3)	N/A
Hβ	1.40	N/A	N/A	N/A	1.2-8.0(1) / 3.2-38(4)	N/A

Table 3.5 (cont'd)

Line	z	f $_{Ly\alpha}$ (10^{-17} erg cm^{-2} s^{-1})	f $_{[OII]}$ (10^{-17} erg cm^{-2} s^{-1})	f $_{H\beta}$ (10^{-17} erg cm^{-2} s^{-1})	f $_{[OIII]_1}$/ f $_{[OIII]_2}$ (10^{-17} erg cm^{-2} s^{-1})	f $_{H\alpha}$ (10^{-17} erg cm^{-2} s^{-1})
[OII]	2.13	N/A	N/A	N/A	N/A / N/A	N/A
			Abell 1689 c3			
Hα	0.94	N/A	N/A	N/A	N/A / N/A	N/A
[OIII]$_2$	1.54	N/A	N/A	0.59-5.1 (8)	1.4 (2) / N/A	N/A
[OIII]$_1$	1.57	N/A	N/A	6.2-11 (2)	N/A / 12 (5)	N/A
Hβ	1.62	N/A	N/A	N/A	1.2-8.2 (3) / 3.3-29 (1)	N/A
[OII]	2.42	N/A	N/A	N/A	N/A / N/A	N/A
			Abell 2219 c1			
Hα	0.85	N/A	1.4-5.1 (0.3)	1.7 (1)	0.51-3.4 (0.4) / N/A	N/A
[OIII]$_2$	1.43	N/A	N/A	0.69-6.0(2)	1.6 (5) / N/A	1.9-17(2)
[OIII]$_1$	1.45	N/A	N/A	2.4-16(0.9)	N/A / 14(1)	6.7-45 (7)
Hβ	1.50	N/A	N/A	N/A	1.4-96 (2) / 3.8-34(0.9)	13 (3)
[OII]	2.26	35-130 (0.4)	N/A	1.6-6.0 (8)	1.8-3.2 (2) / 4.8-11 (5)	N/A
			Abell 2219 c2			
Hα	0.84	N/A	0.6-2.3 (0.4)	0.75 (1)	0.23-1.5(0.4) / 0.60-5.3 (0.5)	N/A
[OIII]$_2$	1.41	N/A	N/A	0.30-2.7 (2)	0.7 (3) / N/A	0.84-7.3 (10)
[OIII]$_1$	1.44	N/A	N/A	0.40−13 (1)	N/A / 6.3 (2)	0.4-13 (1)

Table 3.5 (cont'd)

Line	z	f $_{Ly\alpha}$ (10^{-17} erg cm^{-2} s^{-1})	f $_{[OII]}$ (10^{-17} erg cm^{-2} s^{-1})	f $_{H\beta}$ (10^{-17} erg cm^{-2} s^{-1})	f $_{[OIII]_1}$ / f $_{[OIII]_2}$ (10^{-17} erg cm^{-2} s^{-1})	f $_{H\alpha}$ (10^{-17} erg cm^{-2} s^{-1})
Hβ	1.49	N/A	N/A	N/A	0.63-4.2(3) / 1.7-15(0.8)	5.9(4)
[OII]	2.24	15-58 (0.4)	N/A	0.70-2.6 (2)	0.79-2.4(4) / 2.1-4.9 (5)	N/A

Note. — The fluxes are predictions given the flux of the J-band feature and typical flux ratios for HII regions. The value in paranthesis is the limiting line flux at the corresponding wavelength (see §3.2 for details on how the limiting flux is computed). $[OIII]_1$ is λ4959Åand $[OIII]_2$ is λ5007Å

In the case of Abell 68, if the J-band line was Hα, for our adopted template H II region spectra, [OII] and Hβ would have been recovered with $> 45\sigma$ in the LRIS spectrum.

If the J-band feature was [OII], then Lyman-α would have been seen with ease in the blue LRIS spectrum. While the resonant nature of the transition makes it difficult to predict the Lyman-α flux , if even 0.1% of the photons can escape, a $\simeq 5\sigma$ detection would still have resulted. Since Lyman-α emission is often not seen in distant Lyman break galaxies (Shapley et al., 2003), we can secure additional constraints from the non-detection of Hβ and the two [OIII] lines in the H-band spectrum. Although some of the relevant regions are affected by OH emission, [OIII] 5007 Å would be strong enough to be detected at $>5\sigma$ under some cases.

If the line were [OIII]λ5007Å , then Hβ, [OIII]λ4959Å , and Hα would all fall in the spectral region covered by the H-band spectroscopy. Hβ and Hα would each be seen at >5 σ for most of the range of emission line ratios.

One seemingly unlikely hypothesis deserves attention. The candidate is quite close (1.8 arcsec) to a z=1.58 galaxy with Hβ and [OIII] revealed in the J-band discovery spectrum (Richard et al. 2006, in preparation). If the candidate line were Hβ, the rest-frame velocity separation between the two sources would only be 400 km s^{-1}. The likelihood of an association thus seems high. However, it turns out the combined J+H spectra of the two sources are very different. Hα is seen from the foreground galaxy in the H-band but the same line can be rejected for the candidate with 15σ confidence for a Case B Balmer line ratio. Likewise the limiting sensitivity at the location of [OIII] emission line for the foreground hypothesis is sufficiently deep such that we would have expected to see a line for nearly all reasonable line ratio assumptions. In combination, therefore, the non-detection of Hα and [OIII]λ 5007 Å strongly rule out any association of the candidate with the z=1.58 galaxy.

Similarly, in the case of Abell 2219 c1 if the J-band line were Hα, [OII], Hβ and [O III] 4959Å would have been seen in the LRIS spectra at 23-85, 8.5, and 6.4-43 σ respectively.

If the line was Hβ, Hα would have been detected at 22σ in the H-band spec-

trum.and [OIII] λ4959Å and λ5007Å at 3.5-24 and 21-190 σ respectively in the J-band.

If the line were [OII], then, as before strong Lyman-α would be expected in the blue LRIS spectrum, even if only a small fraction of photons escaped. And [OIII]λ4959Å and λ5007Å would have been seen at up to 4.5-8.0 and 4.8-11σ respectively in the H-band spectrum.

Finally, if the line were [OIII] λ5007Å , then Hβ would be detected at $1.7-15\sigma$, depending on the oxygen abundance. and Hα would been seen in a clean area of the H-band with $4.8-43\sigma$.

All cases described above assume an HII region template spectrum. Assuming the emission lines are instead generated by a harder ionization source such as an AGN, the CIV $\lambda\lambda$ 1548, 1550 line may be prominent in the rest-frame UV spectrum. If Lyman-α is suppressed via resonant scattering and absorption by dust, narrow-line AGN can exhibit line ratios of $1 \lesssim$ CIV/Lyα $\lesssim 1.4$ (Dey et al., 1995; De Breuck et al., 2001; Dawson et al., 2003). If these sources are indeed Lyman-α emitters at $z \simeq 10$, then the CIV line may also be observable in the H-band. For both Abell 68 c1 and Abell 2219 c1, CIV would lie in clean regions (1.60 μm and 1.55 μm, respectively); however, neither emission line is seen, suggesting that if the candidates are at $z \simeq 10$, they have CIV/Ly$\alpha < 1$.

3.5.6 Other Candidates

Comprehensive optical and H-band spectroscopy is also available for Abell 2219 c2 and in fact the constraints we discuss above for Abell 2219 c1 are just as convincing here making it a very promising source. However, we prefer not to elevate it into the status of the two most promising sources because of the potential broad-band ACS detection (§3.5.2). In this sense it represents a source of status intermediate between our top two candidates and those discussed below for which, due to weather and other problems, our spectroscopy is currently incomplete.

For A1689c1, c2 and c3, we have no optical or H-band spectroscopy and so major

interloper hypotheses such as $H\alpha$ and [O II] cannot yet be excluded.

In summary, we can conclude that at least two (and quite possibly three) of our six candidates cannot be accounted for as lines from lower redshift emitters. Moreover, there is no reason to denigrate the status of the other 3 candidates either since, so far, every additional spectrum we have taken has continued to support the Lyman-α hypothesis. Our low contamination ratio is not that surprising when one considers all of the considered interloper hypotheses would still represent lensed systems and thus, if highly magnified, not be seen at the location of the $z \simeq$10 critical line.

On the other hand, it is clear that our tests make necessary assumptions about the line ratios expected from $0.85 < z < 2.26$ galaxies. It is conceivable that these assumptions are invalid and that the sources have anomalous line ratios (although it would seem surprising that this is the case in several systems). Given the wavelength ranges accessible to ground-based spectrographs, we believe we have undertaken all possible tests.

3.6 Implications

Noting that at least two of our six candidates may indeed lie at $z \simeq$10, we now address the goal of the survey: what is the volume density of high z emitters? However, noting their identification could still be considered tentative, we will also explore the implications if *none* of our candidates is real. After making simple assumptions about the effect of dust and resonant scattering on escaping Lyman-α photons, we will use the derived abundance to constrain the star formation rate density. We then attempt to understand whether the derived abundance represents a significant contribution to the ionizing photon budget at $z \simeq 10$.

3.6.1 Volume Density of z>8 Lyman-α Emitters

In a blank-field survey, the surface density of sources brighter than a given limiting line flux can be computed by dividing the number of detected sources by the area observed. The calculation is more complex in this case because of the varying amplification of

the source flux over the survey volume and the distortion, by lensing, of the survey area.

The differential comoving volume element at ($\mathbf{\Omega}$,z) along one of the NIRSPEC slit positions is

$$\mathrm{d}V_\mathrm{c}(\mathbf{\Omega}, z) = \frac{1}{\mathcal{M}(\mathbf{\Omega}, z)} \left[\frac{\mathrm{d}l_\mathrm{c}(z)}{\mathrm{d}z}\mathrm{d}z\right] \times \left[D_\mathrm{c}^2(z)\mathrm{d}\mathbf{\Omega}\right]. \tag{3.3}$$

where $\mathrm{d}l_\mathrm{c}$ is the comoving length of the volume element along the line of sight. We also compute the uncertainty associated with each volume element due to the error in the magnification (§3.3.4).

The total survey volume over which sources with Lyman-α line luminosity greater than L is the integral over all volume elements with limiting Lyman-α luminosity below L,

$$V_\mathrm{c}(L) = \int_{\mathbf{\Omega}}\int_{z} \mathrm{d}V_\mathrm{c}(\mathbf{\Omega}, z)\ H[L - L_\mathrm{lim}(\mathbf{\Omega}, z)], \tag{3.4}$$

where H[L-$L_\mathrm{lim}(\mathbf{\Omega}, z)$] is a step function equal to 1 when L$\geq L_\mathrm{lim}(\mathbf{\Omega}, z)$ and equal to 0 when L$< L_\mathrm{lim}(\mathbf{\Omega}, z)$.

The uncertainty in the magnification introduces error into the derived comoving volume. We quantify this error by computing the distribution of comoving volume for all acceptable cluster mass models (see § 3.3.4). The range of comoving volume that spans ±34% of the total samples is taken to be the uncertainty in the volume.

The survey volume and associated errors are plotted as a function of Lyman-α luminosity in Figure 3.10. The comoving volume decreases from $\simeq$30 Mpc^3 at L=3$\times10^{42}$ erg s^{-1} to $\simeq$3 Mpc^3 at L=3$\times10^{41}$ erg s^{-1}. The 'one-sigma' error bars in the volume are small enough that they do not extend outside the datapoints. In Figure 3.11, we plot the number density of $z \simeq$9 Lyman-α emitters as a function of Lyman-α luminosity assuming that (i) none of our candidates is at $z \simeq$8-10 (left) and (ii) two of our candidates are Lyman-α emitters (middle) and (iii) all six of our candidates are real (right).

In the case where two of the candidates are real, the Poisson errors are 100%. This

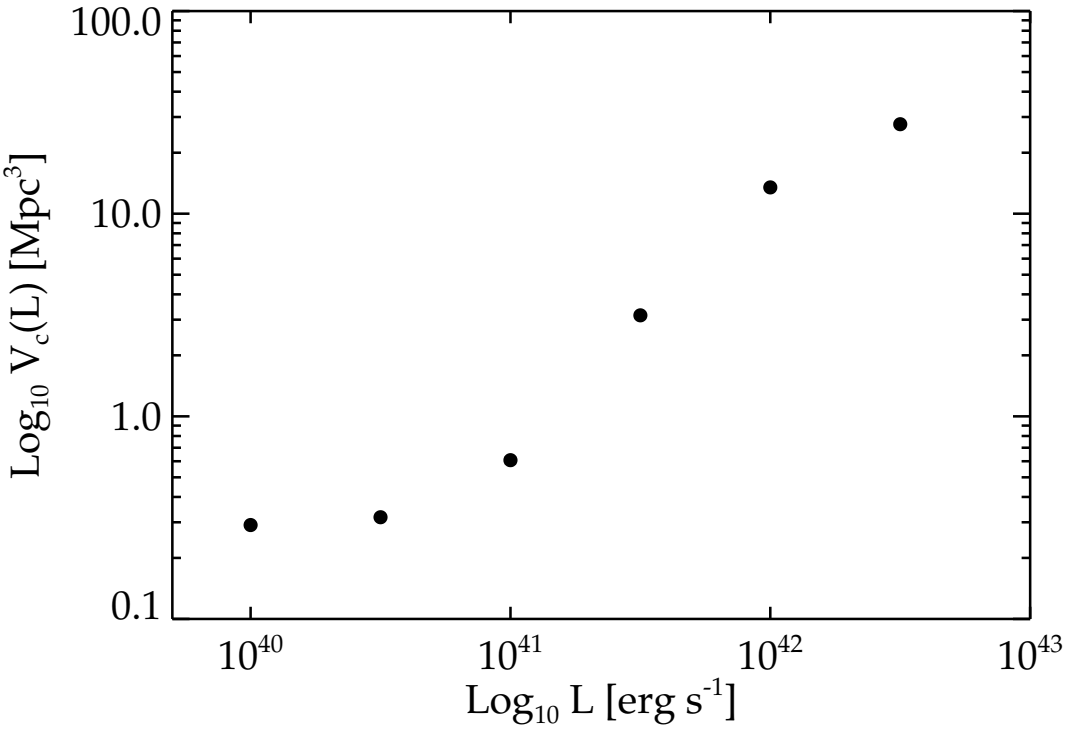

Figure 3.10 Survey volume (comoving) sensitive to sources with Lyman-α luminosity L. The volumes observed are very small as a result of the small area of the spectroscopic slit and the decrease in survey area resulting from gravitational lensing.

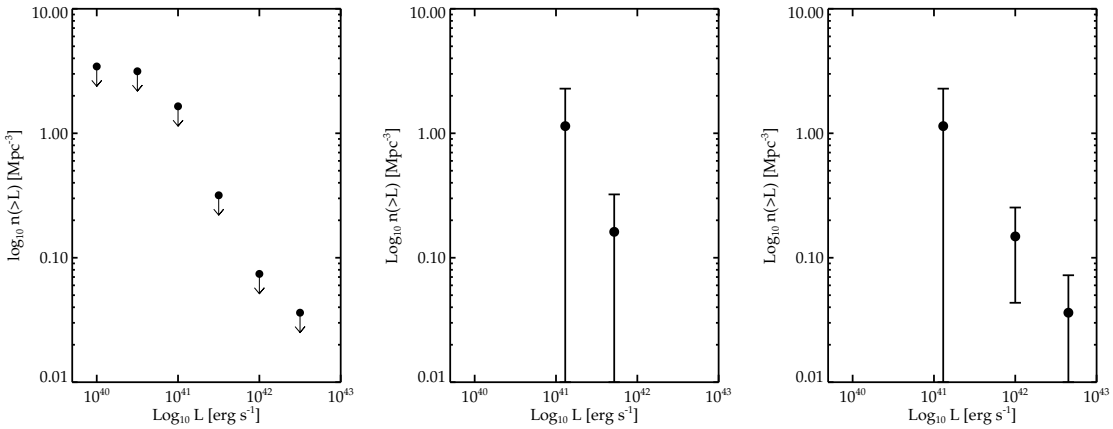

Figure 3.11 Constraints on number density of 8.5<z<10.2 sources with Lyman-α luminosity brighter than L. Left: The 5σ upper limit to the abundance of low luminosity Lyman-α emitters is presented assuming none of our candidate Lyman-α emitters is real. Middle: The cumulative abundance of Lyman-α emitters if two of the candidates (A68c1 and A2219c1) are real. Right: The cumulative abundance of Lyman-α emitters assuming each of the six candidates is a Lyman-α emitter. If even one candidate is real, the inferred abundance of low luminosity Lyman-α emitters at $z \simeq 9$ would be very high.

arises because galaxies need not only be brighter than the survey limiting luminosity but must also lie within the area covered by the survey. In lensing experiments, in order for inclusion associated with some limiting luminosity, the 5σ limiting luminosity at the location of the object must be lower than the limiting luminosity of the survey. The net result is that objects with fluxes close to the sensitivity limits only are included in "surveys" with a small range of limiting luminosities. If two candidates are real, as considered here, the luminosity ranges over which the objects would be detected do not overlap; hence no bin contains more than one object.

To place the inferred abundances in context, we compare our results with other surveys that have been conducted, particularly at z$\simeq$6 where the luminosity function of Lyman-α emitters is more firmly established.

The first observational constraint on the abundance of Lyman-α emitters at z>8 was presented by (Willis & Courbin, 2005). These authors conducted a narrow-band imaging survey in the J-band toward the Hubble Deep Field South and found no $z = 8.8$ sources with Lyman-α luminosity greater than $10^{42.5}$ erg s^{-1} over a volume of

approximately 990 Mpc^{-3}. More recently, Cuby et al. (2006) reported a null detection of $z = 8.8$ Lyman-α emitters brighter than 10^{43} erg s^{-1} over a comoving volume of $\simeq 4200 Mpc^3$. Given the large error bars, the upper limits from Willis & Courbin (2005) and Cuby et al. (2006) are consistent with the case in which only two of the candidates are real. If all six of the candidates are Lyman-α emitters, it becomes slightly more difficult to explain the lack of Lyman-α emitters in the two narrowband surveys without resorting to luminosity dependent evolution. Hence, in this case, the observations could suggest that the decline in luminous Lyman-α emitters relative to fainter sources observed at $z \simeq 6-7$ (Shimasaku et al., 2006; Kashikawa et al., 2006; Iye et al., 2006) continues to $z \simeq 10$.

A second question is whether our density is higher or lower than the Lyman-α luminosity function which is now fairly well-established at $z = 5.7$, at least at the bright end (Santos et al., 2004; Malhotra & Rhoads, 2004; Shimasaku et al., 2006). It is worth remembering that despite the fact that over 100 Lyman-α emitters are now catalogued at this redshift, the degree of spectroscopic confirmation is still quite limited. The extant data are well-fit by a Schechter function with $\phi^\star$=1.6$\times$10^{-4} Mpc^{-3} and L*=1.6$\times$10^{43} erg s^{-1} where, for the purposes of discussion, we have adopted the steepest likely faint-end slope of $\alpha = -2$ so as to provide the most optimisitc no-evolution scenario. Assuming, naively, no evolution between z=5.7 and z=10, it is unlikely that we would find a source brighter than 10^{40} erg s^{-1}. At face value, therefore, our detection of at least two promising cases would suggest an upwards evolution in the abundance of faint emitters with redshift.

The likely evolution of the Lyman-α luminosity function between z=5.7 and z$\simeq$10 is a complicated function of the star formation efficiency, stellar initial mass function, relative geometry and kinematics of HII and HI gas, and dust content of the host galaxy, as well as the ionization state of the IGM. If, for example, the dust content of galaxies decreases toward higher redshifts, the percentage of Lyman-α photons that escape the host galaxy may increase. On the other hand, as the IGM becomes increasingly neutral, observed Lyman-α counts are expected to decline (Malhotra & Rhoads, 2004; Haiman & Cen, 2005), although the presence of large HII regions

around clustered star-forming sources may slightly offset the magnitude of this decline (Furlanetto et al., 2004). Clearly, it is very difficult to predict exactly *how* the Lyman-α luminosity function will evolve over this $\simeq$500 Myr time interval.

Bearing these uncertainties in mind, our detection of two promising candidates clearly implies a steep faint-end slope and hence a large abundance of intrinisically faint sources. If more of our candidates are at $z \simeq 10$, it would almost certainly imply that low-luminosity star-forming systems are *more* abundant at $z = 9$ than at $z = 5.7$. This may be a result of evolution in galaxy properties (as discussed), or the effect of a predominantly neutral IGM which increases star formation efficiency in low-mass halos due to the decrease in the Jeans mass (Barkana & Loeb, 2001). Determining which of these factors is primarily responsible for the possible upturn in counts is difficult with the available data.

If none of our candidates is real, a number of explanations are possible. First the faint-end slope may not be as steep as required for us to detect sources in our observed volume. There are a number of feedback processes (galactic winds, supernova explosiona, etc.) that could significantly reduce star formation efficiency in low-mass halos, thereby resulting in a relatively shallow faint-end slope. Alternatively, if the IGM is significantly neutral, it is possible that faint-end slope is very steep, but the neutral IGM is blocks our view of these systems. We defer a detailed discussion of the implications of our survey in terms of what is now known at $z \simeq$5-6 to a later paper (Stark, Loeb & Ellis, 2007).

3.6.2 Contribution of Low Luminosity Galaxies to Reionization

Several methods have been adopted for considering the contribution of star-forming sources to cosmic reionization. One approach is to compare the inferred ionizing photon production rate from star-forming galaxies of all luminosities to that required to reionize neutral hydrogen in the IGM (Madau et al., 1999; Stiavelli et al., 2004). Since the abundance of Lyman-α emitters at $z \simeq 10$ is very uncertain, comparing the

total ionizing photon output is highly dependent upon assumptions about the luminosity function. In this initial study, we ask a more basic question: do low luminosity Lyman-α emitters provide a significant contribution to reionization? Following this approach, we therefore only tabulate the ionizing photon production arising from low luminosity (i.e. 10^{41} - 10^{42} erg s^{-1}) sources that our survey is designed to probe.

The contribution of low luminosity star-forming sources to reionization can be parameterized in simple terms by comparing their ionizing photon production rate to that required for reionization:

$$n_{gal} = 2 \left(\frac{B}{10}\right)\left(\frac{f_{esc}}{0.05}\right)^{-1}\left(\frac{\dot{M}_\star}{0.1\ M_\odot\ yr^{-1}}\right)^{-1}\left(\frac{\Delta t}{575\ Myr}\right)^{-1} Mpc^{-3} \quad (3.5)$$

assuming the space density of sources is constant during the reionization epoch. Here, B is the number of ionizing photons required to keep a single hydrogen atom ionized, n_H is the comoving number density of hydrogen at the redshift of interest, Δt is the period over which reionization occurs, f_{esc} is the escape fraction of ionizing photons, $\dot{M}_\star$ is the time-averaged star formation rate of galaxies in units of $M_\odot$ yr^{-1}.

In both cases, we fix the comoving number density of hydrogen at n_H=1.9 $\times$ 10^{-7} cm^{-3}, appropriate for the comoving hydrogen number density adopting the best-fit WMAP cosmological parameters (Spergel et al., 2006). We have also assumed an IMF with Salpeter slope with stellar masses ranging from 1 $M_\odot$ to 100 $M_\odot$ and metallicity of of Z=0.001 (1/20th solar) (Schaerer, 2003). If the IMF is weighted more toward massive stars or is substantially more metal-poor, the ionizing photon output for a given star formation rate will be greater, and less galaxies will be required for reionization.

The escape fraction of ionizing photons is not well-constrained observationally; we allow this quantity to vary between 0.02 and 0.5 (Steidel et al., 2001; **?**; Shapley et al., 2006). We assume the escape fraction is constant with luminosity; however, models of high-redshift galaxies suggest that it should increase toward the low-luminosity end of the luminosity function (Ricotti & Shull, 2000). If this is the case, then contribution of low-mass galaxies to reionization will be even greater than what is shown below.

The recombination rate increases with the local hydrogen number density, hence the number of ionizations required per atom for reionization depends strongly on the clumpiness of the IGM (C=$\frac{<n_e^2>}{<n_e>^2}$). Simulations generally predict clumpiness factors of C$\sim$6-30 (Gnedin, 2000; Kohler et al., 2005) for z$\sim$6-7. Following the interpolation formulae in (Stiavelli et al., 2004), this results in $\simeq$3-10 ionizations per hydrogen atom depending on the timescale of reionization.

Substituting the range of parameter values into equation 5, we find that for galaxies with star formation rates of 0.1 $M_\odot$ yr^{-1} to dominate the reionization process, they should have comoving number densities in excess of 0.1 - 2 Mpc^{-3} (Figure 3.12). If two or more of the candidates are at z$\simeq$10, then it would appear that low luminosity galaxies contribute significantly to the reionization process.

While there is currently not enough data at $z \simeq 10$ to estimate the integrated ionizing photon output from Lyman-α emitters, we can attempt to constrain this quantity by assuming that the luminosity function evolves only in normalization (hence maintaining the same shape) between $z = 6.5$ and $z = 10$. In the most optimistic case where six candidates are at high-redshift, we take the characteristic luminosity, $L^\star$ derived for the $z = 6.5$ Lyman-α emitters by Kashikawa et al. (2006) with a diverging faint-end slope of $\alpha = -2$. Integrating the luminosity function down to the survey limit ($\simeq$0.01 $M_\odot$ yr^{-1}), we find that the total ionizing photon production rate would be sufficient for reionization for nearly the full range of assumptions considered in Figure 3.12.

3.7 Summary

Low luminosity star-forming galaxies are often predicted to produce a large supply of ionizing photons during the reionization era (Barkana & Loeb, 2001). However, feedback processes from supernova explosions or galaxy winds may significantly decrease star formation efficiency in the low-mass dark matter halos that are thought to house the majority of low-luminosity star forming sources. Tentative observational evidence hints at a very large abundance of low luminosity sources (Yan & Wind-

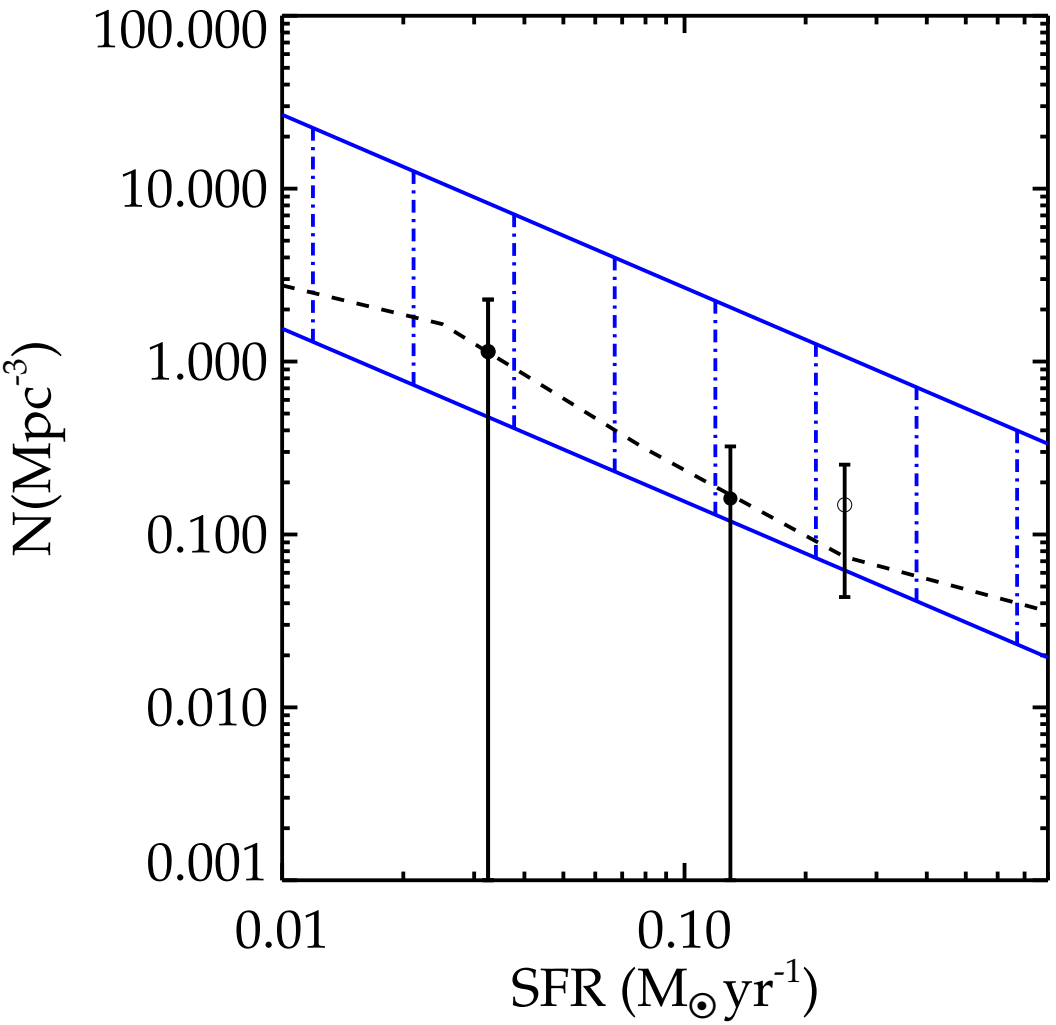

Figure 3.12 Abundance of sources required for reionization assuming a single population of star-forming galaxies dominates the process (blue swath) compared the observed abundances (a) if all the candidates are real (open circles), (b) two of the candidates are real (solid circles), or (c) if none of the candidates are real (dotted line). The abundance constraints for case a and case b are identical for the two lowest luminosity bins plotted in the figure. The range for the abundance of sources required for reionization is determined assuming f_c=0.5, Δt_{reion}=575 Myr, and B=10 for the lower locus of points and f_c=0.02, Δt_{reion}=250 Myr, and B=3 for the upper locus of points. If two or more of the candidates are real, then it appears that intrinsically faint galaxies may play a dominant role in the reionization of neutral hydrogen.

horst, 2004; Bouwens et al., 2006) suggesting that these feedback processes may not significantly affect star formation in low-mass halos. Until the construction of JWST and 20-40 meter class ground-based telescopes, gravitational lensing surveys offer one of the most efficient means of spectroscopically verifying the presence of an abundant population of low-luminosity ($\lesssim 10^{43}$ergs^{-1}) sources. With this as our goal, we have conducted a spectroscopic survey for gravitationally lensed Lyman-α emitters over the redshift interval $8.5< z <10.4$. We summarize our results below.

1. The critical lines of 9 well-understood lensing clusters were scanned spectroscopically in the J-band for lensed Lyman-α emission from galaxies at z=8.5 to 10.4. The new observations are sensitive to star-forming sources with intrinsic (unlensed) Lyman-α luminosities of $10^{41.5}$ erg s^{-1} over a significant fraction of the survey area. This limit is over an order of magnitude fainter than the corresponding sensitivity limits of conventional surveys for Lyman-α emitters at $z > 6$.

2. Six promising candidate Lyman-α emitters were identified whose reality we justify noting the possibility of instrumental and detector artifacts. The emission features have fluxes that range from 2-5$\times10^{-17}$ erg cm^{-2} s^{-1} and significances between 5-8σ. The Lyman-α luminosities of the sources range from 10^{41} to 5×10^{42} erg s^{-1}.

3. We attempt to verify that our lines arise from $z \simeq$10 Lyman αvia several tests. No convincing broadband optical counterparts were seen in deep HST images (R$\simeq$27) except in one marginal case. For 3 out of the 6 cases, we conduct exhaustive additional spectroscopy to explore the likelihood that low-redshift interloper lines may explain the J-band emission. In no case do we find such an example, and, overall we conclude that at least 2 of our 6 candidates probably lie at $z \simeq$10. We briefly discuss the considerable challenges of making further progress in confirming any or all of our candidates given the limited rest-wavelength range available with large ground-based telescopes.

4. Assuming two or more of our Lyman-α emitter candidates are real, then the cumulative abundance of low luminosity galaxies (defined as those with L>$10^{41.5}$ erg s^{-1}) is at least 0.3 Mpc^{-3}. Such a large abundance of low luminosity Lyman-α emitters supports the contention of a steep faint end slope for the star-forming

luminosity function at z$\simeq$10.

5. Assuming a single population of galaxies dominates the reionization process the number density of galaxies forming stars at a rate of 0.1 $M_\odot$ yr^{-1} must exceed 0.1-4 Mpc^{-3} to reionize neutral hydrogen. Our inferred abundance is consistent with being within this range indicating that intrinsically faint Lyman-α emitters may well produce a substantial supply of ionizing photons during the reionization era.

6. However, if none of our candidates are at high-redshift, then there are several likely explanations. If the IGM is significantly neutral, low luminosity star forming systems may be very abundant but may not be observed due to resonant absorption of Lyman-α photons by hydrogen in the IGM. Alternatively, it is possible that the faint-end slope is not as steep as predicted by Yan & Windhorst (2004); hence larger volumes would be needed to detect a representative sample.

Notwithstanding the uncertainties and speculation, our survey demonstrates the practicality, over the next few years, of providing a valuable glimpse at the nature of the $z \simeq$10 Universe ahead of the commissioning of future large facilities such as the Thirty Meter Telescope and the James Webb Space Telescope.

Acknowledgments

We thank our anonymous referee and Avi Loeb for very helpful comments. We are indebted to George Becker for providing his spectroscopy reduction software and Tom Broadhurst for providing mass models for several of our survey clusters. We thank Mark Sullivan for observing and reducing data on the candidate Abell 68 c1 with LRIS. G.P.S. acknowledges support from a Royal Society University Research Fellowship. Faint object near-infrared spectroscopy at Keck is possible thanks to the dedicated efforts of instrumentalists and the Keck support staff; we thank Ian McLean, Jim Lyke, and Grant Hill for making this project possible.

The authors recognize and acknowledge the very significant cultural role and reverance that the summit of Mauna Kea has always had within the indigenous Hawaiian community. We are most fortunate to have the opportunity to conduct observations from this mountain.

APPENDIX

The observing sequence for narrowband surveys often involves alternating between two narrowband filters (e.g. A and B) with slightly different central wavelengths. In each filter, the observations are divided into subexposures with integration times that are comparable to the variability timescale of the sky background (typically 5-10 minutes). A composite image is made of all of the subexposures in each filter, resulting in two "subsurveys" slightly offset in redshift space. Subtracting the two composite images removes continuum soures, thereby allowing line emitters to be identified. Alternatively, instead of a second narrowband filter, a broadband filter can be used to identify line emitters (Willis & Courbin, 2005). Using either approach, if integration time t_{int} is devoted to a narrowband survey, then the total integration devoted to each individual "subsurvey" is only $(t_{int}/2)$ in length. In the following calculations, we assume a total integration time of 60 hours.

The field of view of the survey camera is one of the key parameters in determining the survey sensitivity. For a single exposure, the field of view is limited by the size of the detector and the plate scale of the detector. The plate scale is typically set such that each pixel samples 1/4 of a spatial resolution element. Assuming seeing-limited observations with a $0\farcs6$ seeing disk, this corresponds to 0.1-0.2 arcseconds per pixel. Until very recently, only 1024×1024 pixel detectors were available on 8-10 meter telescopes in the near-infrared; given typical plate scales, this allows fields of view between 3 and 12 arcmin^2. Recently, larger format cameras have become available (e.g. MOIRCS on Subaru) allowing fields of view of $\simeq$30 arcmin^2 to be observed in single exposures. In the signal to noise calculations that follow, we consider both a detector with a field of view of 4 arcmin^2 (similar to that of NIRI on Gemini) as well as one with a field of view of 30 arcmin^2.

In the near-infrared, the noise is dominated by bright atmospheric emission lines from OH molecules; hence the background in a given exposure is dependent on the central wavelength and bandwidth of the narrowband filter. The central wavelength is chosen to lie in >50Å gaps between bright OH lines, where the atmospheric

transmission is near 100%. We assume a central wavelength of 11905 Å for our predictions. The signal to noise in a single exposure is minimized when the filter bandwidth is matched to the FWHM of the emission line, which is typically 5-10 Å for Lyman-α emitters at high redshift (Shimasaku et al. 2006); hence, we adopt 10Å as the FWHM for our calculations. We also consider a filter with a FWHM of 100 Å; while the noise in a single exposure is larger for this filter, the redshift range covered is ten times larger (Δz=0.1 vs. Δz=0.01).

The received signal from the science source is estimated as follows,

$$S_{source} = \int f_{\lambda,source}\tau(\lambda)\, d\lambda\ A_{tel}\eta_{tel}\eta_{inst}\eta_{QE}\eta_{atm}(t_{int}/2) \qquad \text{(A-1)}$$

where $f_{\lambda,source}$ is the spectrum of the source in units of photons s^{-1} cm^{-2} $Å^{-1}$, $\tau(\lambda)$ is the filter transmission profile (assumed gaussian with FWHM defined above), η_{tel} is the telescope optics throughput, η_{inst} is the throughput of the instrument, η_{QE} is the quantum efficiency of the detector, η_{atm} is the atmospheric transmision, A_{tel} is the collecting area of the telescope. As discussed in §3.5.1, we expect the line profile of high-redshift Lyman-α emitters to be asymmetric with the blue side of the line absorbed. Along these lines, we assume the line profile is a half-Gaussian with no flux shortward of the central wavelength. While this profile is perhaps oversimplified, the S/N calculations do not change signficantly if the profile is altered. We adopt throughput and quantum efficiency values that are consistent with those expected for DAzLE (η_{tel}=0.6, η_{inst}=0.5, η_{QE}=0.7), a near infrared narrowband imager designed to find $z > 7$ Lyman-α emitters Horton et al. (2004). The atmospheric transmission, η_{atm}, is computed following models presented in Lord (1992) assuming an air mass of 1.5 and a 1.0 mm water vapour column [1] and is near unity for the OH window considered. We assume a telescope collecting area of 7.9×10^5 cm^2 corresponding to the size of Keck. The photometric aperture is matched to the area subtended under reasonably good seeing conditions ($\simeq 0\farcs6$ diameter seeing disk). The integration time is only ($t_{int}/2$) because the total integration time is split between two different

[1] available from `http://www.gemini.edu/sciops/ObsProcess/obsConstraints/atm-models/trans_10_15.dat`

narrowband filters, as described above.

The noise in an exposure of time t_{int} is a function of the integrated source counts, sky background, detector dark current, and detector read noise. Formally, the noise is defined as

$$N = \sqrt{N_{sky} + N_{source} + N_{DC} + RN^2} \tag{A-2}$$

where N_{sky}, N_{source}, N_{DC} are the number of electrons from the sky background, science source, and dark current, and RN is the read noise.

We compute the expected background count rate utilizing the Gemini model for the near-infrared sky background spectrum[2]. The model inludes the contribution from atmospheric OH emission lines, zodiacal emission (from a 5800 K blackbody), and thermal emission from the atmosphere (from a 250 K blackbody). The total counts from the sky background in a photometric aperture of area a_{phot} in the composite image, is given by

$$N_{sky} = \int f_{\lambda,sky}\ \tau(\lambda)\, d\lambda\ \eta_{tel}\eta_{inst}\eta_{QE}\ A_{tel}\ a_{phot}\ (t_{int}/2) \tag{A-3}$$

where $f_{\lambda,sky}$ is the sky background in photons s^{-1} cm^{-2} $Å^{-1}$ $arcsec^{-2}$, τ is the filter transmission profile (assumed gaussian with FWHM defined above), a_{phot} has units of $arcsec^2$, and all other parameters are the same as defined above.

The total counts associated with the dark current is given by

$$N_{DC} = n_{pix} dc (t_{int}/2) \tag{A-4}$$

where n_{pix} is the number of pixels in the photometric aperture area and dc is the dark current in units of electrons per second per pixel. The number of pixels in the aperture is derived assuming a plate scale of $0\farcs15$. The typical dark current for near-IR imagers on 8-10 meter telescopes is 0.25 electrons s^{-1} $pixel^{-1}$; hence we adopt this value in our calculations.

The read noise contribution to the total noise is computed assuming Fowler sam-

[2]available from `http://www.gemini.edu/sciops/ObsProcess/obsConstraints/atm-models/nearIR_skybg_16_`

pling is used, which reduces the read noise by a factor of $\sqrt{4}/n_{read}$ where n_{read} is the number of reads at the beginning and end of each exposure. The total read noise in an aperture of size n_{pix} in the composite images is thus given by

$$RN = rn\sqrt{\frac{4\ n_{pix}n_{exp}}{n_{read}}} \tag{A-5}$$

where rn is the detector read noise (for single readout) in units of electrons per pixel and n_{exp} is the number of exposures in the composite frame. We adopt a read noise of 10 electrons per pixel (Horton et al., 2004) for a single readout and assume the detector is read out 16 times per exposure.

The 5σ limiting flux is defined as the line flux for which the signal from the science source is a factor of five greater than the noise. For the instrument properties assumed, the 5σ limiting flux in a 10 hour narrowband survey is 3-9$\times10^{-18}$ erg cm^{-2} s^{-1} for a 10Å and 100Å narrowband filter, respectively. At z=9, this corresponds to a Lyman-α luminosity of 0.6-2$\times10^{42}$ erg s^{-1} assuming a magnification of $\times5$. The survey volume is computed following equations 3 and 4 presented in §3.6.1 and assuming a magnification distribution for one of the most well-studied clusters, Abell 1689.

We also compute the efficiency of a conventional narrowband survey. The survey parameters are identical to those assumed for the lensing survey. The only difference is that in computing the limiting luminosity and survey volume, we do not fold in the magnification due to the lensing cluster.

The parameters chosen for the spectroscopic survey correspond to the properties of NIRSPEC on Keck. The limiting sensitivity in a spectroscopic survey is computed in the same way as for the narrowband survey. The spectroscopic survey strategy is described in §3.3.2. We divide the total integration time into many 1.5 hour observations; each 1.5 hour integration is further divided into nine 10 minute exposures. One key difference between the spectroscopic and narrowband survey is that the entire integration time is devoted to a single survey; hence, the ($t_{int}/2$) in the equations above become t_{int} for spectroscopic surveys.

Most of the parameters used in the spectroscopic S/N computation are identical to those used above. The read noise in each ten minute exposure is 25 electrons pixel^{-1} assuming 16 total reads; while slightly higher than in the narrowband survey described above, the noise is still sky-background dominated.

The median 5σ limiting flux for the spectroscopic survey is 8×10^{-18} erg cm^{-2} s^{-1}. We assume the longslit is placed along the critical lines of the lensing clusters listed in Table 1, which results in a significantly higher median magnification than in the narrowband survey. For a magnification of $\times25$, this corresponds to a limiting Lyman-α luminosity of 4×10^{41} erg s^{-1}.

Chapter 4

An Empirically-Calibrated Model For Interpreting the Evolution of Galaxies During the Reionization Era

Abstract

We develop a simple star formation model whose goal is to interpret the emerging body of observational data on star-forming galaxies at $z \gtrsim 6$. The efficiency and duty cycle of the star formation activity within dark matter halos are determined by fitting the luminosity functions of Lyα emitter and Lyman-break galaxies at redshifts $z \simeq 5-6$. Our error budget takes proper account of the uncertainty arising from both the spatial clustering of galaxies and the commonly-used Poisson contribution. For a given survey geometry, we find a cross-over luminosity below which clustering provides the dominant contribution to this variance. Using our model parameters we predict the likely abundance of star forming galaxies at earlier epochs and compare these to the emerging data in the redshift interval $7 < z < 10$. We find that the abundance of luminous Lyman-break galaxies in the 500 Myr between $z \simeq 6$ and 10 can be naturally explained by the hierarchical assembly of dark matter haloes; there is only marginal evidence for strong physical evolution. In contrast, the first estimates of the abundance of less luminous star forming galaxies at $z = 9-10$ are

This chapter has been published previously as Stark et al. 2007, ApJ, 668, 627

higher than predicted and, if verified by further data, may suggest a top-heavy stellar mass function at these early epochs. Although these abundances remain uncertain because of the difficulty of spectroscopic confirmation and cosmic variance, even a modest improvement in survey capability with present or upcoming facilities should yield great progress. In this context, we use our model to consider those observational techniques that hold the most promise and make predictions for specific surveys that are, or will soon be, underway. We conclude that narrowband Lyα emitter surveys should be efficient on searches at $z \simeq 7-8$; however, such conventional surveys are unlikely to detect sufficient galaxies at $z \simeq 10$ to provide useful constraints. For this reason, gravitational lensing offers the best prospect for probing the $z \simeq 10$ universe prior to JWST.

4.1 Introduction

The recent discovery of star-forming galaxies at high redshifts, $z > 6$, represents an emerging frontier in our understanding of the early stages of galaxy formation. Such studies aim to determine the role that young galaxies may play in completing cosmic reionization, as well as to define more clearly how feedback and other poorly-understood processes shape the early distribution of galaxy luminosities and sizes from which later systems evolve (see reviews by Loeb 2006; Ellis 2008).

Considerable observational progress is being made through ambitious campaigns undertaken with the Hubble and Spitzer Space Telescopes and large ground-based telescopes. As a result, luminosity functions and stellar mass distributions are now available for various star-forming populations observed at $z \simeq 5-6$. These include the continuum 'drop-outs' or Lyman break galaxies (LBGs,Bouwens et al. 2006; Yan et al. 2006; Eyles et al. 2007; Stark et al. 2007a), and the Lyman-alpha emitters (LAEs, Santos et al. 2004; Malhotra & Rhoads 2004; Hu et al. 2004; Shimasaku et al. 2006; Kashikawa et al. 2006), located either spectroscopically or via narrow band imaging. Alongside these achievements, the first constraints are now emerging on the abundance of equivalent systems at $7 < z < 10$ (Richard et al., 2006; Willis &

Courbin, 2005; Bouwens & Illingworth, 2006; Iye et al., 2006; Cuby et al., 2006; Stark et al., 2007b).

Several questions arise as observers continue to make progress. First, what is the physical relationship between the Lyman Break Galaxy (LBG) and Lyman-alpha emitter (LAE) populations? This is important in interpreting the quite significant differences that have been observed between the properties of the two classes. Second, what redshift trends are expected for these populations? Some authors (e.g. Kashikawa et al. 2006; Bouwens & Illingworth 2006) have claimed strong evolution in the abundances with redshift. However, in the absence of any theoretical framework it is difficult to assess the significance of these claims. Finally, given the abundance of star forming galaxies at $z \simeq 5-6$, what is expected at $z \simeq 7-10$, the current observational target? And what is the optimum observational strategy for finding those sources which will be valuable in constraining the epoch of cosmic reionization and the properties of young galaxies?

The present paper is motivated by the need to answer these questions given the improving observational situation at $z \simeq$5–6. As the time interval between z=6 and z=10 is short by cosmic standards ($\simeq$470 Myr in the WMAP3 cosmology, Spergel et al. 2006), the growth of the halo mass function over this redshift range is well understood. Accordingly, it is practical to fit the $z \simeq 5-6$ observations in the context of a simple star-formation model, thereby deducing the likely differences between the LBG and LAE populations, and to then use such an empirically calibrated model to predict their likely abundances at $z \simeq 10$.

The model we adopt assumes all early star-forming galaxies observed during this relatively short period are primarily triggered into action by halo mergers. The key parameters governing their visibility are thus the efficiency of star formation and the duty cycle of its activity. An observed luminosity function at $z \simeq 5-6$ thus provides a joint constraint on the star formation efficiency (which determines the rate at which baryons are converted into stars) and the duty cycle of activity (which determines the fraction of halos occupied by visible galaxies). We consider such a simple model to be complementary and perhaps more intuitive than full *ab initio* numerical simulations

which must also assume sub-grid presriptions for star formation (e.g Nagamine et al. 2005; Finlator et al. 2006). The goal is to infer the likely redshift trends in the context of emerging data and to use the model to evaluate the future observational prospects, particularly in the optimal design of surveys to locate sources at $z \simeq 10$ or so.

Several authors have already made good progress with such semi-analytic models. Le Delliou et al. (2005) and Dijkstra et al. (2006) have attempted to fit the luminosity distribution of LAEs. Dijkstra et al. argue that the evolution observed by Kashikawa et al. (2006) between z =5.7 and z=6.5, claimed as arising from changes in the intergalactic medium, may be understood instead through simple growth in the halo mass function. Mao et al. (2006) have extended the method to contrast the properties of LAEs and LBGs; they find LBGs reside in a wide range of halo masses (10^{10} to 10^{12} $M_\odot$), whereas LAEs reside within a narrower range ($\simeq 10^{11} M_\odot$). A key inference from their model is the short duty cycle of activity in the most luminous sources. Samui et al. (2006) have argued that the evolution observed at $6 \lesssim z \lesssim 10$ in the Hubble Ultra Deep Field (UDF) can be attributed to evolution in the underlying dark matter halo number density without requiring a dramatic change in the nature of star formation; in contrast, they find that the large abundance of $z \simeq 9$ LBGs discovered in the gravitational lensing survey of Richard et al. (2006) requires significant evolution in the stellar initial mass function, the reddening correction, and the mode of the star formation.

The present paper continues the earlier work. We focus not only on explaining the growing body of data at $z \simeq 5 - 6$ but will also include the emerging data at higher redshift to see how it agrees with our model predictions. A crucial ingredient in finding the model parameters that best fit the observational data is the error budget on that data. The commonly-used scatter due to Poisson fluctuations must be supplemented by the spatial clustering of galaxy halos within the volume of each survey. Here we will provide new error bars for existing data and show that the cosmic variance due to clustering dominates over Poisson fluctuations below a particular galaxy luminosity for a given survey geometry. This understanding can be used to optimize the flux sensitivity and strategies of future high-z surveys.

The plan of the paper is as follows. In §4.2 we introduce the basic ingredients of our model for star forming galaxies at high-redshifts. In §3 we calculate the error budget for observations of LBGs and LAEs at high redshift. The model is calibrated against existing data for LBGs and LAEs at $z \simeq$5–6 in §4.4 and used to discuss the emerging data at earlier epochs in §4.5. In §4.6 we discuss the implications of our model for further observational campaigns with current and projected facilities. In §4.7, we summarize our conclusions.

Throughout the paper, we have assumed a flat universe and $(\Omega_m, \Omega_\Lambda)$=(0.24,0.76) following results in Spergel et al. (2006). All magnitudes are given in the AB system.

4.2 A Physical Model for High Redshift Star Forming Galaxies

The rationale of this paper is to empirically-calibrate, using the data now available at $z \simeq 5-6$, the parameters of a simple model that describes the evolving luminosity function of star-forming galaxies (both LBGs and LAEs) over the quite short time interval corresponding to the redshift range $5< z <10$. Such a model can then be used to make predictions for the upcoming $z \simeq 7-10$ surveys.

The model assumes star formation at these early epochs is primarily triggered by the well-understood rate at which dark matter halos coalesce. We assume that the ratio of baryons to total mass in halos above some minimum mass (Wyithe & Loeb, 2006) follows the universal value Ω_b/Ω_m. Baryons are subsequently converted to stars with an efficiency given by $f_\star$. Following Loeb et al. (2005) and Wyithe & Loeb (2006), we define the star formation timescale, t_{LT}, as the product of the star formation duty cycle, ϵ_{DC}, and the cosmic time, $t_H \equiv 2/3H$ at that redshift. Using these ingredients, the star formation rate $\dot{M}_\star$ is related to halo mass M_{halo} as follows

$$\dot{M}_\star(M_{halo}) = \frac{f_\star \times (\Omega_b/\Omega_m) \times M_{halo}}{t_{LT}}. \quad \text{(A-1)}$$

One simplification of this model is that it assumes that the mean age of stars

is independent of halo mass. In hierarchical structure formation, the progenitors of a massive halo would have, on average, crossed above the cooling threshold and begun star formation at an earlier time than the progenitor of a less massive halo; hence the star formation timescale, t_{LT}, should increase with halo mass. We tested whether incorporating this improves the fits to the observations by allowing the star formation timescale to vary as $t_{LT} = \epsilon_{DC} t_H (M_{halo}/M_{c,age})^{\alpha}$, where $M_{c,age}$ and α are free parameters. Under the simple model we have assumed, the duty cycle for star formation must also be multiplied by the factor $(M_{halo}/M_{c,age})^{\alpha}$. We do not find better model fits to the observations by including this factor, so we hold the star formation lifetime fixed with halo mass in our analysis.

For comparison to LBG samples, the star formation rate defined above is converted to the luminosity per unit frequency at 1500 Å following the prescription presented in Madau et al. (1998): $L_{1500\mathring{A}} = 8.0 \times 10^{27} (\dot{M}_{\star}/M_{\odot}\ \mathrm{yr}^{-1})$ erg $\mathrm{s}^{-1}\mathrm{Hz}^{-1}$. This conversion factor assumes a Salpeter initial mass function (IMF) of stars; if the IMF is more top-heavy than the Salpeter IMF, the far-ultraviolet luminosity will be greater for a given $\dot{M}_{\star}$.

Comparison to LAE samples requires converting the star formation rates derived above to a Lyα luminosity. We do this assuming that two-thirds of all recombining photons result in the emission of a Lyα photon (case B recombination). The ionizing photon production rate is calculated from the star formation rate for a given IMF and metallicity. We fix the metallicity at 1/20 solar and assume a Salpeter IMF which yields $N_{\gamma} = 4 \times 10^{53}$ ionizing photons per second per star formation rate in $M_{\odot}$/yr (Schaerer, 2003). An extreme top-heavy Population III IMF would produce $3{\times}10^{54}$ ionizing photons (Bromm et al., 2001; Schaerer, 2003), and we will consider such an IMF in later sections. Since the Lyα photons are assumed to be produced via recombinations, only the fraction of ionizing photons which do not escape into the intergalactic medium, $(1 - f_{ip})$, produce Lyα photons. Furthermore, only a fraction, $T_{Ly\alpha}$, of the emitted Lyα photons escape the galaxy and are transmitted through the intergalactic medium (IGM). With this prescription the Lyα luminosity is related to

the halo mass as follows:

$$L_{\mathrm{Ly}\alpha} = \frac{2}{3} h \nu_{Ly\alpha} N_{\gamma} T_{\mathrm{Ly}\alpha} (1 - f_{\mathrm{ip}}) \dot{M}_{\star}. \tag{A-2}$$

A substantial change in the IGM transmission parameter $T_{\mathrm{Ly}\alpha}$ is expected to signal the end of reionization.

We also consider a more advanced model, incorporating the effects of supernova feedback on the luminosity function of star-forming galaxies. Since supernova feedback can significantly reduce the efficiency of star formation in low-luminosity galaxies, it is particularly important to consider when predicting the efficiency of future surveys for high-redshift galaxies aimed at detecting intrinsically fainter systems, rather than the luminous and rare objects that have been detected thus far, Following the scaling relations presented in Dekel & Woo (2003), we assume there is a critical halo mass at each redshift below which the star formation efficiency begins to decrease due to feedback. The star formation efficiency (which we now call $\eta(M)$) is a function of halo mass,

$$\eta(M_{halo}) = \begin{cases} \mathrm{f}_{\star} \left(\frac{\mathrm{M_{halo}}}{\mathrm{M_{halo,crit}}} \right)^{2/3} & \mathrm{M_{halo}} < \mathrm{M_{halo,crit}} \\ f_{\star} & \mathrm{M_{halo}} > \mathrm{M_{halo,crit}} \end{cases} \tag{A-3}$$

where $\mathrm{M_{halo,crit}}$ represents the critical value. At a given redshift, the critical halo mass can be related to a critical halo velocity. In the local universe, observations suggest a critical halo velocity of ~ 100 km s^{-1} (Dekel & Woo, 2003); we adopt this for our high-redshift models, assuming that the physics of supernova feedback depends only on the depth of the gravitational potential well of the halos. If the initial mass function is top-heavy at early times, then the ratio of supernova explosions to halo mass will be greater than implied locally, and hence the critical halo mass will likely shift to a lower value. Since we calibrate our data using initial mass functions consistent with stellar populations in the local universe, we choose not to include the effects of the IMF on the star formation efficiency.

Finally, in §4.6 we also consider the expected evolution of galaxy sizes. This is

particularly important for gauging the efficiency of future surveys utilizing adaptive optics in detecting galaxies at $z \gtrsim 7-20$. If a galaxy is resolved in a particular observation, the signal-to-noise ratio for the detection increases as the size of galaxy decreases since a smaller aperture (with less noise) is required to encircle its flux. Next-generation adaptive optics systems on thirty-meter class ground-based telescopes will offer a resolution of $\gtrsim$9 milliarcseconds at 1.1μm, corresponding to $\simeq$50 pc at $z \simeq$7. With such exquisite angular resolution, the size of early galaxies is likely to be a limiting factor in their detection.

We assume that the extent of the stellar region of a galaxy at a particular epoch is a constant fraction of the size of the host dark matter halo. The virial radius of a halo is given by

$$r_{vir} = \left[\frac{GM_{vir}}{100H^2(z)}\right]^{1/3} \tag{A-4}$$

where M_{vir} is the halo virial mass and $H(z) = H_0[\Omega_{\Lambda,0} + (1-\Omega_{\Lambda,0}-\Omega_0)(1+z)^2 + \Omega_0(1+z)^3]^{1/2}$ is the Hubble canstant at redshift z. At very high redshift, the halo virial radius scales as $(1+z)^{-1}$ for fixed halo mass. Following the parameterization presented in Barkana & Loeb (2000), a typical galaxy brighter than 1 nJy between $5 \lesssim z \lesssim 10$ will have a disk radius of 0.″1-0.″2, with the range depending on the efficiency with which baryons are converted to stars.

Observations lend support to this simple scaling of disk radius with redshift: $z \simeq 2-6$ dropouts in the UDF and Hubble Ultra Deep Field Parallels (UDF-P) are best fit by a $(1+z)^{-1}$ power law for a fixed luminosity (Bouwens et al., 2004). The mean half-light radius of 0.3-1.0 $L_{\star,z=3}$ LBGs at $z \simeq 6$ is 0.8 kpc, corresponding to 0.″1 at $z \simeq 6$, consistent with the model presented in Barkana & Loeb (2000). To make predictions for future observations in §4.6, we thus assume the mean size of galaxies of similar luminosity scales as $0.''1(1+z/7)^{-1}$.

4.3 The Effect of Variance in Deep Surveys

Interpreting and planning observations of galaxies in the reionization era requires an accurate understanding of uncertainties arising from both Poisson errors and fluctuations in the large-scale distribution of galaxies. For example, one of the main motivations for galaxy surveys at $z \simeq$7–10 is the question of whether the imprint of reionization can be seen in the evolution of LAEs (Malhotra & Rhoads, 2006; Dijkstra et al., 2006) or dwarf galaxies (Barkana & Loeb, 2006; Babich & Loeb, 2006). However, to answer these questions, it is important to ensure that the variance is less than the claimed evolution. In this section, we develop the formalism necessary to compute the variance for narrowband, dropout, and spectroscopic lensing surveys, and we then apply this formalism to recent surveys. An analysis of clustering variance was presented in Somerville et al. (2004). We improve upon two simplifications made in that work, both of which we discuss below.

The variance due to Poisson errors is given by $\mathcal{N}_i$, where $\mathcal{N}_i$ is the number of galaxies in luminosity bin i. To compute this we determine the number density of galaxies (either LBGs or LAEs) as a function of luminosity using the best-fitting models described in §4.4, from which we can determine the predicted counts for a given survey volume. When characterizing the variance at redshifts where data is sparse ($z \gtrsim 7$), we assume no evolution in the model parameters from $z \simeq 6$. This method clearly has its limitations when probing new parameter space (e.g. low luminosities or high redshifts) where the abundance of galaxies is not well-known. However, given the lack of data, we consider it to be the simplest approach.

The clustering of galaxies in overdense regions causes fluctuations in galaxy counts, often referred to as cosmic variance. Determining this variance requires knowledge of the mass of the dark matter haloes that host the observed galaxies. If the correlation function of the galaxy population is known the clustering variance can be predicted for a given field of view. Moreover, if the data set is sufficiently large, the correlation function can be derived separately for bright and faint galaxies, thereby showing how the dark matter halo mass (and hence the clustering variance) varies with galaxy

luminosity. A detailed spatial correlation function analysis is very challenging for current observations at $z \gtrsim 6$; hence an alternative method is needed for deriving the clustering variance.

Using the LBG and LAE model described in §4.2, the halo mass can be determined as a function of galaxy luminosity. The clustering variance can then be calculated for a given halo mass by taking the product of the variance of dark matter in the survey volume and the bias factor associated with halos of a given mass M. With this method, we compute the clustering variance as a function of galaxy luminosity for narrowband, dropout, and spectroscopic lensing surveys, taking into consideration the survey geometry specific to each survey.

First, we compute the variance of dark matter in a given smoothing window as follows:

$$\sigma^2(r) = \int P(k)\tilde{W}^2(\mathbf{k})\, d^3\mathbf{k} \tag{A-5}$$

where $P(k)$ is the power spectrum of density fluctuations extrapolated to z=0 as a function of wavenumber k and $\tilde{W}^2(\mathbf{k})$ is the Fourier transform of the window function in real space. The form of window function depends on the survey geometry; in the following subsections, we detail the window functions adopted in our analysis. Non-linear corrections to the power spectrum and probability distribution become important if the variance is larger than unity. In computing the variance, we adopt the non-linear power spectra using the halo model fitting functions presented in Smith et al. (2003). While fluctuations are in the linear regime, their probability distribution is Gaussian. However, in the non-linear regime, the probability distribution function appears to be well-described by a log-normal distribution (Kayo et al., 2001). Confidence intervals are thus determined via the geometric mean and standard deviation; the one-sigma upper and lower bound are given by $\exp(\mu+\sigma)$ and $\exp(\mu-\sigma)$, respectively, where μ and σ are the mean and standard deviation of the logarithm of a given density fluction, $\ln\,\delta$. If the standard deviation of the log-normal distribution is much less than one, $\sigma_{LN} \ll 1$, the probaility distribution function reduces to Gaussian with confidence intervals given by $\mu \pm \sigma$.

The clustering variance in the distribution of *galaxies* is then estimated by multiplying the variance in dark matter by the halo bias, which is defined as the ratio of the rms fluctuations of haloes to that of dark matter. We adopt the halo bias formula derived for the ellipsoidal collapse model by Sheth et al. (2001).

A key assumption in the clustering variance formalism described above is that there is not more than one galaxy per halo. More complex occupation numbers are possible, but since cooling is efficient at such high redshifts, the simplest case is that with one galaxy per halo.

Now we introduce two key differences between our approach and that of Somerville et al. (2004). First, the survey geometry was assumed to be spherical in Somerville et al. (2004). However, different survey geometries may have substantially different power spectra (Kaiser & Peacock, 1991). This is a particular concern for strong lensing surveys that utilize longslit spectroscopy (Santos et al., 2004; Stark et al., 2007b). Second, the observed number density of the population was assumed to be equivalent to the number density of the underlying dark matter halos (Somerville et al., 2004). This assumption could be in error if the star formation duty cycle, $\epsilon_{\rm DC}$, is significantly smaller than unity. In this case, the observed number density of galaxies would be less than that of their host dark matter haloes by a factor of $\epsilon_{\rm DC}$. Depending on the slope of the mass function, this would overestimate or underestimate the cosmic variance.

In the following subsections, we apply the formalism described above to recent surveys for LBGs and LAEs. For each survey, we compute the typical amplitude of clustering and Poisson fluctuations in the relevant observational regime. In addition, we determine the cross-over luminosity, $\rm L_c$, defined as the luminosity above which the Poisson error dominates that from clustering fluctuations.

4.3.1 Variance in Narrowband Surveys

The geometry of a narrowband LAE can be approximated as a rectangular parallelepiped with a comoving volume of $a_x a_y a_z$, where a_x and a_y are the comoving

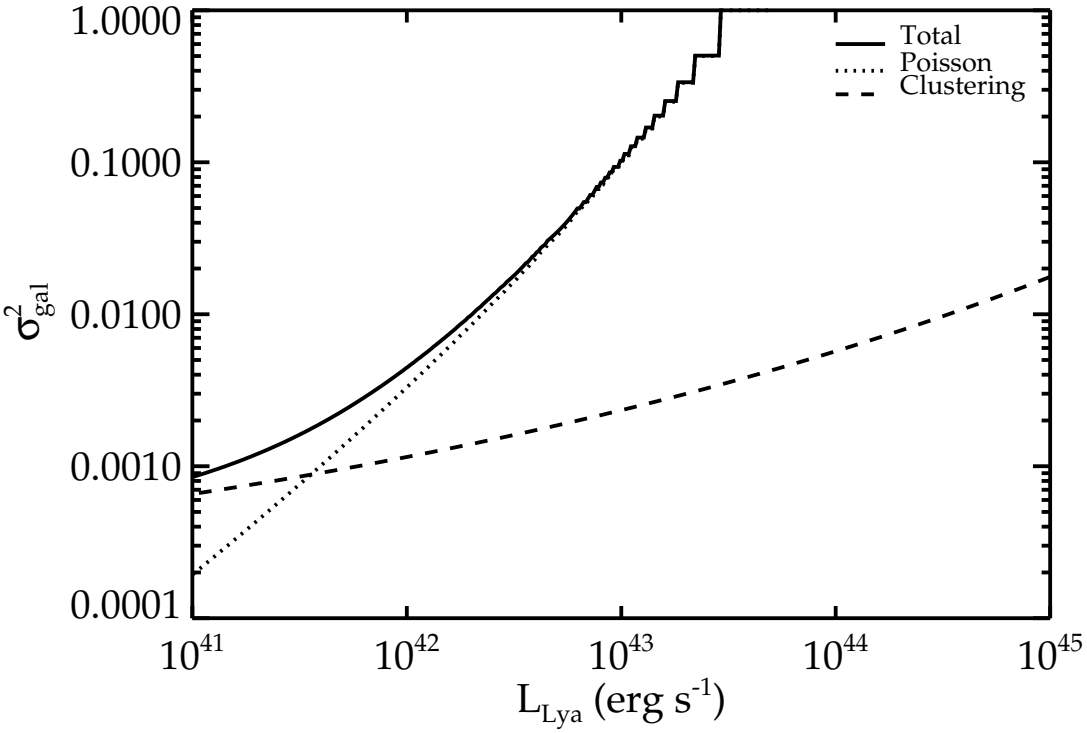

Figure 4.1 Variance in a narrowband Lyα survey. The total variance (solid line) is the sum of the variance from Poisson noise (dotted line) and clustering fluctuations (dashed line). The survey specifications adopted in the left panel are equivalent to Subaru survey for Lyα emitters at $z = 5.7$ (Shimasaku et al., 2006). The clustering fluctuations in such a narrowband survey are very small (less than 6%) in the luminosity range over which Lya emitters are detectable.

distances corresponding to the areal field of view of the survey and a_z is the comoving line-of-sight distance of the survey. The window function in k-space is simply the Fourier transform of a rectangular top-hat with dimensions corresponding to the survey geometry:

$$\tilde{W}(k_x, k_y, k_z) = \frac{\sin(k_x a_x/2)}{(k_x a_x/2)} \frac{\sin(k_y a_y/2)}{(k_y a_y/2)} \frac{\sin(k_z a_z/2)}{(k_z a_z/2)}. \quad \text{(A-6)}$$

Using the window function defined above, we evaluate the expected variance in narrowband surveys for LAEs at $z \simeq 6$. We focus our analysis on the narrowband surveys conducted at $z = 5.7$ and $z = 6.5$ in the Subaru Deep Field (SDF). Using the wide-format, Suprime-Cam (Miyazaki et al., 2002) on the Subaru Telescope, the observations sample an area of $34' \times 27'$ in the NB816 and NB921 narrowband filters. The central wavelength and FWHM of the NB816 and NB921 filters are (8150 Å, 120 Å) and (9196 Å, 132 Å) respectively.

In Figure 4.1, we plot the variance in the $z = 5.7$ narrowband survey of the SDF. The Lyα luminosities probed in the Subaru survey range from $\simeq 10^{42} - 10^{43}$ erg s^{-1}. The clustering variance is less than $\simeq$0.01 over this luminosity range, resulting in less than 10% uncertainty in the observed counts. Poisson errors dominate the clustering errors for sources brighter than the cross-over luminosity of $10^{41.7}$ erg s^{-1} (Table 4.1). Since this is intrinsically fainter than the luminosity limit of the SDF, this survey is dominated by Poisson errors.

Table 4.1. Variance in High-z Galaxy Surveys

Field	Type	Field of View (arcmin^2)	z	$L_{Lya,c}$ (erg s^{-1})	L_{1500} (erg s^{-1} Hz^{-1})	$\sigma^2_{F2F}(L_c)$
GOODS	dropout	160	6	N/A	$10^{28.0}$	0.002
UDF	dropout	11	6	N/A	$10^{28.2}$	0.03
SDF	narrowband	1295	5.7	$10^{41.7}$	N/A	0.001
Cluster	spec. lensing	0.13	8.5-10.4	N/A	N/A	N/A

Note. — The field of view for the spectroscopic lensing survey is in the source plane, assuming a median magnification of 10. The crossover luminosity is listed as "N/A" for the lensing survey because the clustering fluctuations are greater than the Poisson noise for all luminosities over which our model predicts sources should be detected.

4.3.2 Variance in Lyman-break Surveys

We focus our dropout survey analysis on the two $16' \times 10'$ Great Observatories Origins Deep Surveys (GOODS) of the Hubble Deep Field North (HDF-N) and Chandra Deep Field South (CDF-S) and the $3.4' \times 3.4'$ Hubble Ultra Deep Field (UDF). The redshift distribution of dropouts depends on the filters and color-cuts used in their selection. While the typical color-selection criteria for $i-drops$ select galaxies between $z = 5.5$ and $z = 7.0$ (Bunker et al., 2004), the effective distance sampled along the line-of-sight is less than the total comoving radial distance in this redshift interval because of incompleteness arising from objects being scattered faintward of the magnitude limit or out of the color-selection window. This incompleteness has been quantified in both GOODS and the UDF (Bunker et al., 2004; Bouwens & Illingworth, 2006), allowing an effective volume to be derived for each survey. We approximate the geometry of the LBG survey as a rectangular parallelepiped with a characteristic line-of-sight distance equal to the ratio of the effective volume and the survey area and with dimensions in the plane of sky corresponding to the field-of-view of the survey.

The variance of the GOODS and UDF surveys for $z \simeq 6$ LBGs is presented in Figure 4.2. The GOODS survey is sensitive to sources brighter than 5×10^{28} erg s^{-1} Hz^{-1} (corresponding to a 10σ limit of z'_{AB}=26.5). At this limit, the clustering variance is only 0.003, and the total variance is dominated by the Poisson term. The clustering fluctuations are slightly lower than those estimated in Somerville et al. (2004), due largely to the more realistic source geometry. In the UDF, both the clustering and Poisson error are larger due to the smaller survey volume. The 8σ limiting far UV luminosity in the UDF is 8×10^{27} erg s^{-1} Hz^{-1} (Bunker et al., 2004). The total variance near this limit is dominated by clustering fluctuations, which contribute an uncertainty of $\sim$15-20% to the observed densities.

The field-to-field fluctuations of $z \simeq 6$ LBGs have been measured in Bouwens et al. (2006) by degrading the depth of the UDF to that of the two UDF-parallel fields and subsequently comparing the number of i-dropouts in each field. The density of i-dropouts selected in the (degraded) UDF is similar to that in the first parallel (50.2

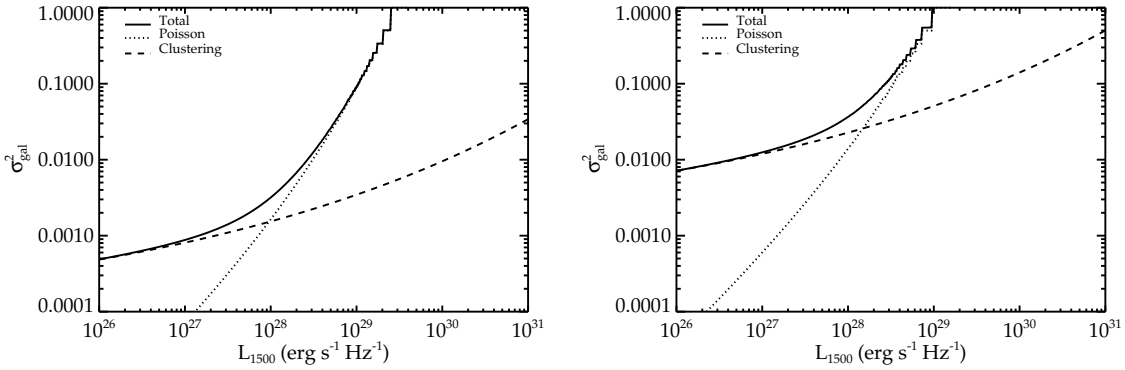

Figure 4.2 Variance in dropout LBG survey. The total variance (solid line) is the sum of the variance from Poisson noise (dotted line) and clustering fluctuations (dashed line). In the case of a survey such as the HST-GOODS observations of the CDF-S and HDF-N (limiting luminosity of 5×10^{28}ergs^{-1}Hz^{-1}), the clustering fluctuations of $z \simeq 6$ LBGs are greater than $\simeq$6% (top panel). In the Hubble Ultra Deep field (limiting luminosity of 8×10^{27}ergs^{-1}Hz^{-1}), clustering fluctuations result in a slightly higher uncertainty of $\gtrsim$15-20% (bottom panel).

and 42.6, respectively) but is significantly greater than that in the second parallel (27.8 vs. 11.4). The latter comparison implies field-to-field variations on 7 arcmin^2 at the magnitude limit ($z_{850} = 28.6$ at 8σ) of the second UDF parallel are $\simeq$ 40%. The observed field-to-field variations result from both Poisson (19% for the degraded UDF and 30% for the second UDF parallel) and clustering fluctuations (19-26% over 7 arcmin^2). When these uncertainties are accounted for, the two measurements are consistent at the 1.3σ level.

4.3.3 Variance in Lensed Longslit Spectroscopic Surveys

The geometry of a longslit spectroscopic survey can be approximated as a rectangular parallelepiped. However, in the case of a strong lensing longslit spectroscopic survey, the geometry is potentially slightly more complex. For a lensing survey, the slit geometry only corresponds to the *image* plane; however, we are interested in the geometry of the survey in the *source* plane, which can be calculated accurately via ray tracing if a reliable mass model is available. While the source plane geometry depends on the location of the longslit relative to the critical line, for typical clusters

studied in Stark et al. (2007b) it is well-approximated by a rectangular-parallelepiped (J. Richard 2006, private communication). The source plane area is reduced by a factor of the lensing magnification, $\mathcal{M}$; further, the magnification is not isotropic and is strongest perpendicular to the cluster critical line. Hence, assuming the longslit is oriented along the cluster critical line, the slit-width is compressed more than the slit-length. For the computations that follow, we assume the source plane slit width, a_x, is related to the image plane slit width, a'_x by $a_x{=}a'_x/\sqrt{2\mathcal{M}}$, and likewise, the source plane slit width is given by $a_y{=}a'_y\sqrt{2/\mathcal{M}}$, in agreement with typical slit positions from Stark et al. (2007b).

As with the narrowband survey, the appropriate window function is a three-dimentional rectangular top-hat in real space, which in k-space corresponds to the product of three sinc functions (see Equation A-6).

A typical near-infrared spectrometer has dimensions of $0.76''\times\ 42''$(Stark et al., 2007b), which at $z \simeq 9$ corresponds to a comoving distance of 6 kpc$\times$610 kpc, assuming a median magnification factor of $\mathcal{M}{=}20$. In each cluster, an area is mapped out around the critical line; assuming six slit positions are observed, this results in a total survey area of 0.02 Mpc^2 per cluster. If observations are conducted in the J-band between $z = 8.5$ and $z = 10.4$, the comoving line-of-sight distance spanned is 479 Mpc. We compute the clustering variance expected over the total survey volume for a fifteen cluster survey. In the near future, significantly more clusters will become available for strong lensing surveys (Ebeling et al., 2003).

The clustering fluctuations are significantly larger in the spectroscopic lensing survey than in either the traditional narrowband or dropout surveys due to the much smaller survey volumes. While such surveys may offer the only prospect of detecting galaxies at $z \simeq 10$, clearly there will still be large uncertainties in their abundance due to cosmic variance. The development of larger and more sensitive near-infrared spectrometers is necessary to increase the survey volume obtainable in a reasonable time allocation.

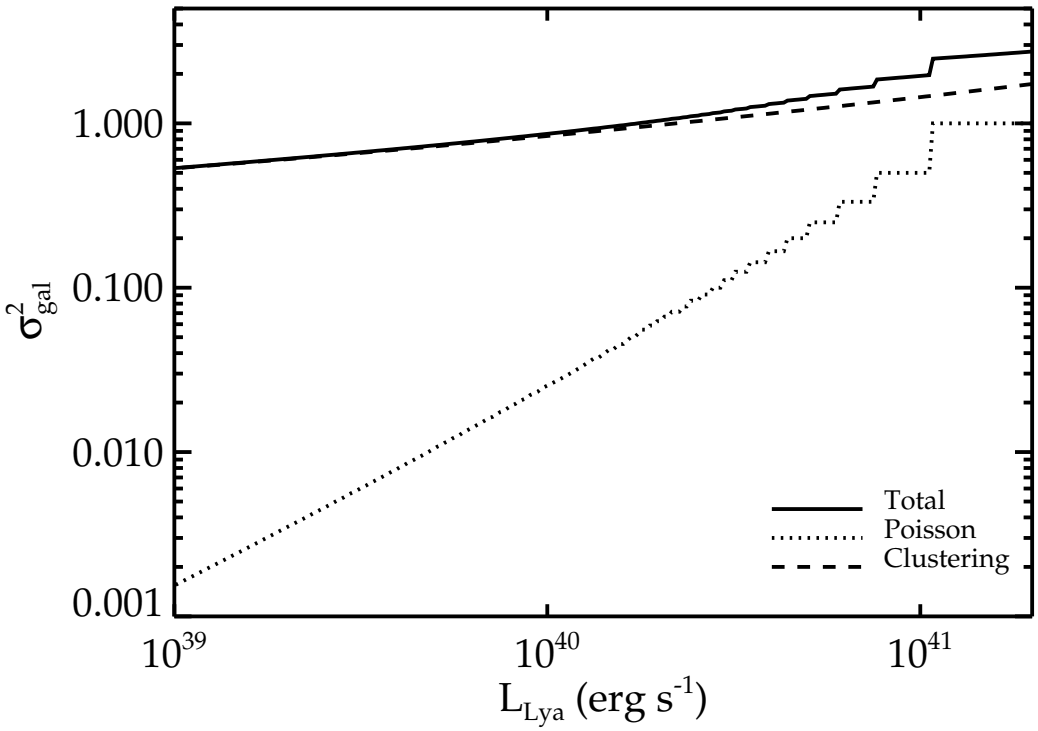

Figure 4.3 Variance in a $z = 10$ lensed longslit spectroscopic survey. The total variance (solid line) is the sum of the variance from Poisson noise (dotted line) and clustering fluctuations (dashed line). The uncertainty from clustering fluctuations is significantly greater than the Poisson noise for all luminosities and is nearly 100% for sources with Lyα luminosities of 10^{40}-10^{41} and erg s^{-1}.

4.4 Model Calibration Using $z \simeq 5-6$ Observations

We are now in a position to use our model and our improved understanding of the effects of cosmic variance to constrain its parameters using observations of the luminosity functions at $z \simeq 5-6$. By doing this independently for LBGs and LAEs we will hopefully gain valuable insight into the physical differences between these two star-forming populations.

4.4.1 Lyman-Break Galaxies

Lyman-break galaxies are perhaps more straightforward to model than Lyα emitters because of the complex resonant interaction of Lyα photons with neutral hydrogen which occurs in the latter population. In our model of LBGs described in §4.2, there are two free-parameters: the star formation efficiency $f_\star$ and the duty cycle $\epsilon_{\rm DC}$. First we determine these parameters by reproducing the observations at $z \simeq 6$. We later use this model to consider whether the emerging data at $z \simeq 7-10$ requires any adjustment. Significant evolution in the model parameters between the two redshifts might signify some external phenomenon, such as the reionization of the intergalactic neutral hydrogen. Alternatively it could cast doubt on the reliability of the observations.

We compute a grid of LBG luminosity functions by varying $f_\star$ and $\epsilon_{\rm DC}$. The comoving number density of galaxies predicted by the models, $n_{\rm mod}$, is compared to the observed value, $n_{\rm obs}$ (with corresponding uncertainty $\sigma_{{\rm obs},i}$), in each of the N luminosity bins, and a likelihood of a given set of parameters is defined such that $\mathcal{L}({\rm f}_\star, \epsilon_{\rm DC}) = \exp[-0.5\chi^2]$, where $\chi^2 = \Sigma_{\rm i=1}^{\rm N}([{\rm n_{obs,i}} - {\rm n_{mod,i}}]^2/\sigma_{\rm obs,i}^2)$. The 1-sigma uncertainty in the observed densities ($\sigma_{{\rm obs},i}$) include the contribution from cosmic variance (see §4.3) in addition to that from Poisson noise. In the following, we present the peak likelihood for each set of parameters we fit against the data and also provide the range of parameters that have likelihoods within 64% and 26% of the peak-likelihood (corresponding to 1- and 2-σ for a Gaussian distribution.

We first apply our model to the observed abundance of LBGs at $z \simeq 6$, as compiled

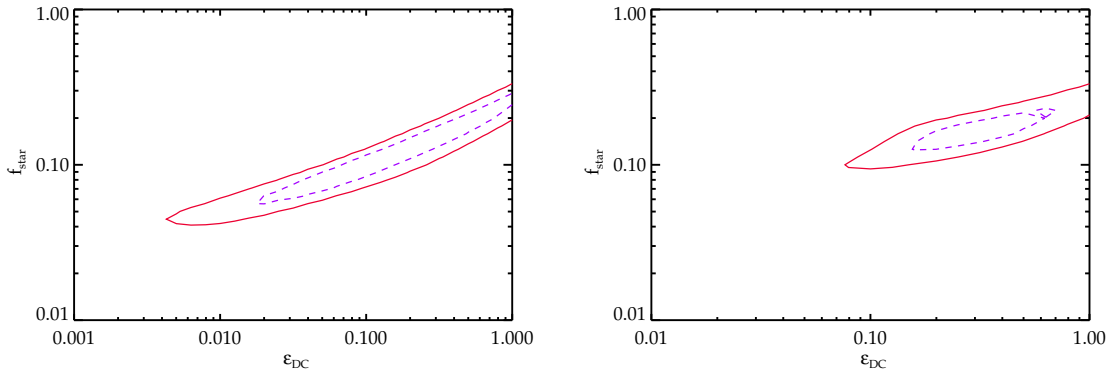

Figure 4.4 *Top:* Confidence intervals on star formation efficiency $f_\star$ and duty cycle $\epsilon_{\rm DC}$ in a simple theoretical model for the observed abundances of LBGs at z=6. The likelihood contours are 64% (blue dashed line) and 26% (red solid line) of the peak likelihood ($\mathcal{L}(\mathrm{f}_\star, \epsilon_{\rm DC}) = 0.33$). *Bottom:* Same as above except with supernova feedback included in model. The peak likelihood increases by almost a factor of two ($\mathcal{L}(\mathrm{f}_\star, \epsilon_{\rm DC})$ =0.58)

by Bouwens et al. (2006). In Figure 4.4, we show the likelihood contours at 64% and 26% of the peak likelihood. The maximum likelihood ($\mathcal{L}(\mathrm{f}_\star, \epsilon_{\rm DC}) = 0.33$) and 1-$\sigma$ confidence intervals are $(f_\star, \epsilon_{\rm DC}) = [0.13^{+0.15}_{-0.07}, 0.20^{+0.80}_{-0.18}]$, in reasonable agreement with a similar fit to these observations in Wyithe & Loeb (2006). When supernova feedback is allowed to decrease the star formation efficiency in low-mass halos (see §4.2 for details), the best-fit parameters change slightly: $(f_\star, \epsilon_{\rm DC}) = [0.16^{+0.06}_{-0.03}, 0.25^{+0.38}_{-0.09}]$ and the peak likelihood increases by almost a factor of two ($\mathcal{L}(\mathrm{f}_\star, \epsilon_{\rm DC}) = 0.58$). The strong degeneracy between the duty cycle and the star formation efficiency arises because an increase in the star formation efficiency requires a longer star formation timescale (and hence larger star formation duty cycle) to produce the same far-UV luminosity for a given halo mass.

Although there is some degeneracy between the best-fitting star formation efficiency and duty cycle at $z \simeq 6$, the range of values can be physically understood. A duty cycle of 20% at $z \simeq 6$ corresponds to a star formation lifetime of $\simeq 200$ Myr which is only slightly larger than the dynamical time of virialized halos (or the duration of equal-mass mergers) at that redshift. Our simple model thus suggests that at $z \simeq 6$, star formation is proceeding on roughly the same timescale it takes virialized

baryons to settle to the center of the galaxy. A star formation efficiency of $\sim 13\%$ is reassuringly similar to the ratio between the global mass density in stars and baryons in the present-day Universe (Fukugita et al., 1998).

An independent check on the inferred duty cycle could conceivably be obtained if the spectral energy distribution was known for a large sample of $z \simeq 5-6$ LBGs. Fitting these with a grid of population synthesis models Bruzual & Charlot (2003) allows, in principle, the estimation of the stellar mass, dust extinction, and luminosity-weighted age of representative galaxies. Unfortunately, the ages inferred via this technique have large systematic uncertainties due to the inability of the population synthesis models to constrain the past star formation history (Eyles et al., 2007; Shapley et al., 2005). Taking the star formation histories that minimize the χ^2 fit to the SEDs of LBGs at $z \simeq 6$, Eyles et al. (2007) find a median age of 500 Myr for those objects detected in the rest-frame optical with Spitzer (and hence the most massive objects). A stacking analysis of the least massive LBGs in their survey indicates that these objects have ages of $\simeq$60 Myr. Recalling that the duty cycle is equal to the star formation timescale divided by the cosmic time, these inferences suggest that the duty cycle lies in the range 6-50% and perhaps increases with the mass of the galaxy.

A further check is provided by limited data on the clustering of LBGs. The halo masses probed in the Bouwens et al. (2006) compilation in the GOODS and UDF surveys are 7×10^9 $M_\odot$–3×10^{11} $M_\odot$ according to the simple model we have adopted. These values are consistent with clustering analysis of $z \simeq 6$ LBGs in GOODS, which suggest that the hosting dark matter haloes are $\sim 10^{11}$ $M_\odot$ (Overzier et al., 2006). Reionization would be accompanied by a dramatic increase in the cosmological Jeans mass and and therefore in the minimum galaxy mass (Wyithe & Loeb, 2006). A direct detection of this effect requires finding galaxies in dark matter haloes over an order of magnitude less massive than those probed in current surveys (Barkana & Loeb, 2006).

One important implication of our best-fit duty cycle is that $\simeq$80% of dark matter halos of a given mass are not traced by LBGs. The "missing" dark matter halos may have gone through bursts of star formation at earlier times and may be currently

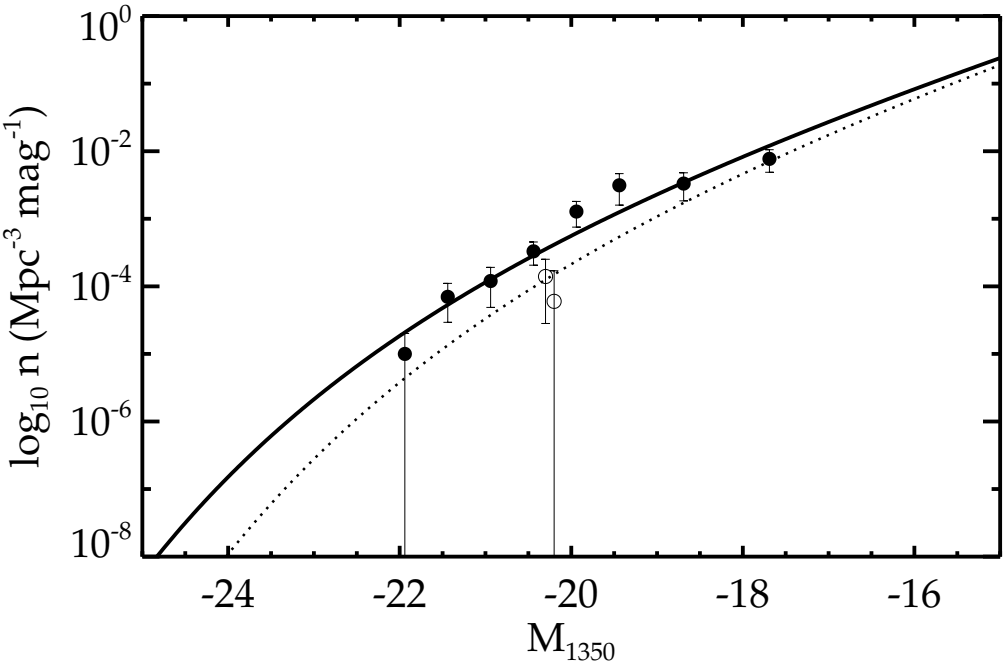

Figure 4.5 The LBG luminosity function at z=6 (solid line) and z=7.6 (dotted line) obtained using the model parameters that maximize the likelihood at z=6. The solid and open circles correspond to observed LBG abundances at z=6 (Bouwens et al., 2006) and z=7.6 (Bouwens & Illingworth, 2006). The two datapoints at z=7.6 (offset horizontally for clarity) correspond to more and less conservative selections of z-drops in Bouwens & Illingworth (2006). While there is not yet much data at z=7.6, the existing data at these two redshifts can be fit without any evolution in the fit parameters $f_\star$ and $\epsilon_{\rm DC}$.

quiescent. However, this does not mean that 80% of the stellar mass is missing from observations at $z \simeq 6$. Rather, the gas in the "missing" dark matter halos may not have cooled sufficiently to be forming stars rapidly enough to be selected as LBGs and thus may not be significant repositories of stellar mass. The first option suggests that there may have been a significant amount of star formation at earlier times. This is evidenced by observations of LBGs at $z \simeq 6$ with stellar masses as great as a few $\times 10^{10} M_{\odot}$ and ages of 200-700 Myr (Eyles et al., 2005; Eyles et al., 2007). Given the current observed star formation rate of these galaxies, the past star formation rate had to have been higher at earlier times. Taken together, these observations and the 20% duty cycle inferred from the luminosity function of the LBGs suggest that the purported deficity of ionizing photons compared to taht required for reionization (Bunker et al., 2004; Bouwens et al., 2006) at $z \simeq 6$ could be accounted for by earlier star formation.

4.4.2 Lyα emitters

We now use a procedure similar to that described for the LBGs to model the LAEs. The key difference is that we must also consider the fraction of Lyα photons that escape from the galaxy and IGM, T_{α}. We generate a grid of models at $z = 5.7$ and $z = 6.5$ with the duty cycle, $\epsilon_{\rm DC}$ ranging from 10^{-3} and 1 and the product of the star formation efficiency and Lyα escape fraction, $f_{\star}T_{\alpha}$ spanning between 10^{-3} and 1. Each model is compared to the observed abundances, and the likelihood is then determined for each model in an identical fashion to that discussed for the LBGs (see §4.4.1 for definition of likelihood parameter). We first perform this procedure for our simple model and then examine it in the context of a model including supernova feedback.

Likelihood contours are presented in the top panel of Figure 4.6 for $z = 5.7$ (solid contours) and $z = 6.5$ (dotted contours). As with the fit to the LBGs, there exists a strong degeneracy between $\epsilon_{\rm DC}$ and $f_{\star}T_{\alpha}$. The maximum likelihood is $\mathcal{L}(f_{\star}T_{\alpha}, \epsilon_{\rm DC})$ =0.20 at z=5.7 and 0.06 at z=6.5. The best-fitting parameters

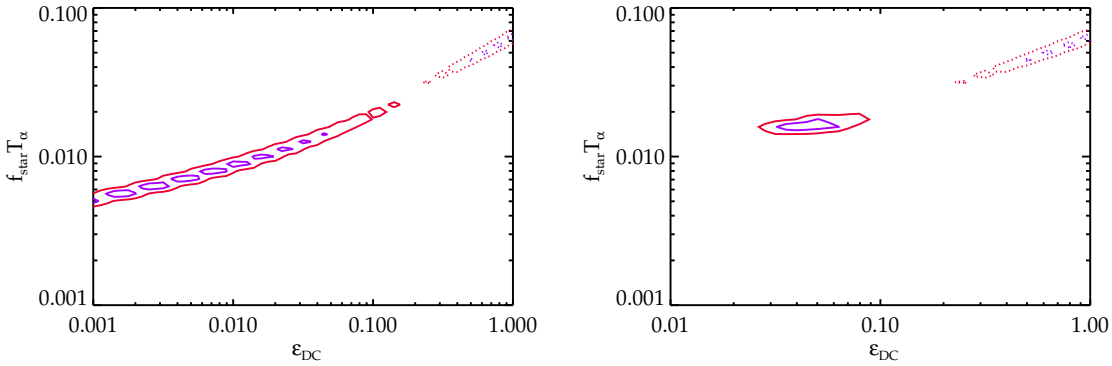

Figure 4.6 *Top:* Confidence intervals on free parameters in analytic fit of observed LAE abundances at z=5.7 (solid lines) and z=6.5 (dotted lines). The peak likelihood for the simple model at $z = 5.7$ and $z = 6.5$ is given by 0.20 and 0.06, respectively. The likelihood contours are 64% (blue) and 26% (red) of the peak likelihood. The parameters that maximize the likelihood are $(\epsilon_{DC}, f_{star}T_\alpha)$=(0.0016,0.0056) at z=5.7 and $(\epsilon_{DC}, f_{star}T_\alpha)$=(1.0,0.063) at z=6.5. *Bottom:* Same as Figure 4.6a with the addition of a simple prescription for supernova feedback. The peak likelihood improves at z=5.7 (0.44) but remains the same at z=6.5 (0.06).

corresponding to the peak likelihood (with associated one-sigma uncertainties) are $(\epsilon_{\rm DC}, {\rm f}_\star {\rm T}_\alpha) = (0.0016^{+0.0431}_{-0.0006}, 0.0056^{+0.0085}_{-0.0006})$ at $z = 5.7$ and $(\mathcal{L}\epsilon_{\rm DC}, {\rm f}_\star {\rm T}_\alpha) = (1.0^{+0.0}_{-0.5}, 0.063^{+0.004}_{-0.018})$ at $z = 6.5$. The $z = 5.7$ data are significantly better fit ($\mathcal{L}({\rm f}_\star {\rm T}_\alpha, \epsilon_{\rm DC}) = 0.44$) by the advanced model including supernova feedback (bottom panel of Figure 4.6). The best-fitting parameters at $z = 6.5$ remain unchanged, while those at $z = 5.7$ change slightly: $(\epsilon_{\rm DC}, {\rm f}_\star {\rm T}_\alpha) = (0.040^{+0.023}_{-0.004}, 0.016^{+0.0019}_{-0.0017})$. Since the model with supernova feedback provides a better fit to the $z = 5.7$ data, we focus our discussion on the model parameters derived in this fit, rather than the most simple model, in our discussion below.

The best-fitting luminosity functions are plotted over the observed abundances in the top panel of Figure 4.7 (simple model) and in the bottom panel of Figure 4.7 (advanced model with supernova feedback). The error bars in these plots include both Poisson and clustering variance. Examining the confidence intervals and luminosity functions, it seems that the data suggest some evolution in the best-fitting model parameters between z=5.7 and z=6.5. It is unlikely that the evolution is associated with a change in the neutral fraction of the IGM because the parameter that is pro-

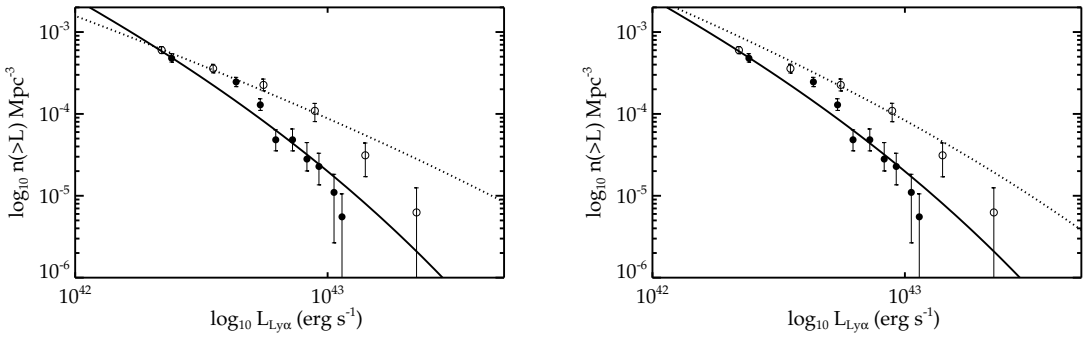

Figure 4.7 *Top:* The Lyα luminosity function at z=5.7 (dotted line) and z=6.5 (solid line) obtained using the model parameters that maximize the likelihood. Open and solid circles are observed abundances at $z = 5.7$ from Shimasaku et al. (2006) and at $z = 6.5$ from Kashikawa et al. (2006). *Bottom:* Same as above but for best-fitting parameters to model that now includes a simple prescription for supernova feedback.

portional to the transmission of Lyα photons, $f_\star T_{Ly\alpha}$, increases between z=5.7 and z=6.5, contrary to what would be expected if the neutral fraction increased. Taken at face value, the evolution in the model parameters suggests that the star formation efficiency and lifetime in LAEs increases between $z = 5.7$ and $z = 6.5$. However, uncertainties in the observations make these conclusions tentative. The LAE luminosity function adopted in this paper is based on a photometric sample of objects selected with a narrowband filter. While many of the most luminous photometrically-selected objects have been confirmed spectroscopically, at lower luminosities the completeness is still low. It is possible that there is significant contamination from low-redshift line emitters, and hence that the densities at these low luminosities are overestimated. If the error bars at low luminosities are enlarged to reflect this uncertainty, then Dijkstra et al. (2006) claim the model parameters are consistent with no evolution between $z = 5.7$ and $z = 6.5$ except in the underlying halos. Additional spectroscopic observations of the lowest luminosity LAEs are clearly necessary to resolve whether the physical parameters of LAEs evolve between z=5.7 and z=6.5.

We now examine the consistency of our best-fit model parameters in the context of additional observations of $z \gtrsim 5$ LAEs. Recently, observations have shown that many luminous LAEs at $z \simeq 5$ have relatively low stellar masses. In Pirzkal et al.

(2006), LAEs at $z \simeq 5$ with $L_{Lya} \simeq 10^{42} - 10^{43} ergs^{-1}$ have $M_{stellar} \simeq 10^6 - 10^8$ $M_\odot$. Assuming the ratio of baryons to total mass follows the unversal value Ω_b/Ω_m and a star formation efficiency of $\simeq 10\%$, the observed stellar masses suggest halo masses of $0.06 - 6 \times 10^9$ $M_\odot$. According to our best-fit models, the halo masses probed by the Subaru observations are signficantly greater: at $z = 5.7$ halo masses range from 10^{10} to $10^{11} M_\odot$, while at $z = 6.5$, the halo masses range between 4×10^{10} and 4×10^{11} $M_\odot$.

Given the low stellar masses observed for these objects, it seems that one of our assumptions must be incorrect. Under our simple model, the stellar mass is given by $M_{stellar} = f_\star[\Omega_b/\Omega_m]M_{halo}$; in order to decrease the stellar mass for a given halo mass, the star formation efficiency must be lower than the 10% value we have assumed above. However, the star formation efficiency must also satisfy the relation between Lyα luminosity and halo mass (equation 2) which is constrained via the observed abundance of LAEs as a function of luminosity. Hence, if the star formation efficiency decreases, either the Lyα transmission factor or the ionizing photon rate must increase to satisfy equation A-2. The latter could occur if the IMF of stars was more top-heavy than the standard Salpeter form. While a top-heavy IMF would reduce the stellar mass predicted by our model, it would also decrease the observationally inferred LAE stellar masses. These masses have been inferred via population synthesis models assuming a Salpeter IMF. Top-heavy IMFs have a lower rest-frame optical stellar mass-to-light ratios then the Salpeter IMF does; hence, for a given luminosity, the inferred mass in stars is lower than for a Salpeter IMF. Therefore, the stellar masses inferred from observations remain at odds with those predicted from our models. Alternatively, if the Lyα transmission fraction, $T_{Ly\alpha}$, is enhanced to account for the lower star formation efficiency, the models achieve much better agreement with the observations. At z = 5.7, our best-fitting models have $f_\star T_{Ly\alpha} \simeq 0.04$. If the Ly$\alpha$ transmission factor is near unity, then the star formation efficiency is roughly 4%. In this scenario, the stellar masses predicted by the models are $\simeq 10^7 - 10^8$ $M_\odot$ at $z = 5.7$, in much closer agreement with the observations.

The low star formation efficiency and large Lyα transmission factor of LAEs can

be understood physically. In addition to showing that the brightest LAEs have low stellar masses, observations have also shown that the most luminous LAEs are a young population with ages of a few $\times 10^6$ years (Pirzkal et al., 2006; Finkelstein et al., 2006), comparable to the lifetime of massive stars before they may explode as supernovae. Hence, these galaxies are observed at such a young stage that they have not had sufficient time to convert more than roughly 4% of their baryons to stars. Moreover, they likely have not had enough time to produce a significant amount of dust. This conjecture is corroborated by population synthesis modeling of the observed SEDs of $z \simeq 3$ LAEs (Gawiser et al., 2006). Without dust to absorb the resonantly scattered Lyα photons, the fraction of Lyα photons escaping the galaxy may increase substantially, explaining the very large Lyα transmission factor needed to fit the observed stellar masses. However, the Lyα transmission factor is also dependent on intergalactic absorption. The typical flux decrement encountered by Lyα photons in the intergalactic medium (Fan et al., 2006) may be substantially reduced in the vicinity of LAEs if they reside in groups of galaxies which significantly ionize their surroundings, allowing the Lyα photons to escape out of resonance before encountering neutral hydrogen in the IGM (Wyithe & Loeb, 2005; Furlanetto et al., 2006).

4.4.3 Comparison of LAEs and LBGs

Recent observations at $z \simeq 5$ suggest that LAEs may differ from LBGs in their typical stellar mass and ages. Observations presented in Eyles et al. (2007) have shown that $z \simeq 6$ LBGs are a composite population of galaxies, some with low stellar masses ($\simeq 10^8$ $M_\odot$) and some with high stellar masses ($\simeq 10^{10}$ $M_\odot$). These stellar masses emerge from our model given the best-fit star formation efficiency and halo masses probed by the observations. While the uncertainties are still significant, there appears to be a weak correlation between the stellar mass and age of $z \simeq 6$ LBGs (Eyles et al., 2007); the most massive galaxies appear to have a significant population of old stars (ages up to $\simeq$ 700Myr), while the less massive objects appear to be much younger

(ages of $\simeq 60$ Myr). The model considered in this paper fixes the star formation duty cycle to be constant with halo mass and hence cannot confirm this observational inference. The best-fitting duty cycle for LBGs suggests an age of 200 Myr, which is roughly in the middle of the range of lifetimes expected of the LBGs.

LAEs at $z \simeq 5$ also appear to be a composite population spanning a range of masses and ages, but it appears that their typical ages and stellar masses are systematically lower than LBGs. A correlation exists between the equivalent width (EW) of the Lyα line and the galaxy age and stellar mass (Finkelstein et al., 2006). The highest EW lines exhibit the lowest ages (few million years) and stellar masses ($10^6 - 10^7$ M$_\odot$); these objects are very faint continuum emitters and hence are not selected in LBG surveys (Finkelstein et al., 2006; Pirzkal et al., 2006). LAEs with lower EWs have larger inferred ages (40-200 Myr) with stellar masses up to $\simeq 10^{10}$ M$_\odot$ (Finkelstein et al., 2006; Lai et al., 2007); however, these ages and masses do not reach the values as large as those seen in LBG surveys at these redshifts. Finally, the SEDs of the young LAEs at $z \simeq 5$ suggest that there is little exinction from dust in these galaxies (Pirzkal et al., 2006). As explained in the §4.4.2, in order for our model to fit the observations described above, the star formation efficiency of the high EW LAEs must be low (due to their extreme youth) and transmission of Lyα photons through the host galaxy and IGM must be very high.

It is intriguing to consider the fate of the high EW LAEs. In one possible scenario, star formation continues, depleting the gas content and increasing the total stellar mass of the galaxy. The dust content of the galaxy begins to increase. The dust absorbs the resonantly-scattered Lyα photons, although the Lyα EW might be enhanced depending on geometric details (Neufeld, 1991; Hansen & Oh, 2006), If the star formation rate remains high, these objects could continue to be observed as LBGs. As more of the gas is converted to stars, the star formation efficiency will increase. Within our model we indeed inferred that the average star formation efficiencies of the $z \simeq 6$ LBGs is on order 10%.

Alternatively, the high EW LAEs could eject their gas via feedback from supernovae explosions or quasar activity. As soon as the gas density is significantly

diluted, the recombination rate decreases and there is little emission of Lyα photons. The galaxies would continue to be selected as LBGs as long as massive stars remain; however, without gas, star formation eventually ceases, leaving the galaxies quiescent and with a low stellar mass. Such objects would no longer be detected as either LBGs or LAEs.

4.5 Interpretations of Observations at $z \simeq 7 - 10$

We now use our model fits, keeping in mind the uncertainties and simplicity of the model, to make predictions for both LBGs and LAEs observed at $z >$7. We will assume no evolution in the model parameters to determine what redshift trends are expected solely from the natural growth of dark matter halos over the era $5 < z < 10$. A modest amount of observational data is available for the $z > 7$ universe and we will address this to see if it is consistent with no evolution. Necessarily this discussion will be tentative given the considerable uncertainty about the validity of the observations. Most of the sources claimed to lie beyond $z \simeq 7$ have no convincing spectroscopic identification.

4.5.1 Lyman-Break Galaxies

Preliminary constraints are now available on the abundance of LBGs at $z > 7$ (Bouwens et al., 2005; Bouwens & Illingworth, 2006; Richard et al., 2006). LBGs selected as z-band dropouts are considered to have a mean redshift $z \simeq 7.4$. The most recent compilation from fields with deep HST-NICMOS data (e.g. GOODS, UDF, UDF-P) includes one candidate in the most conservative selection and 4 candidates in a more aggressive selection (Bouwens & Illingworth, 2006). After comparing the observed abundance of candidate $z \simeq 7.4$ LBGs to those at $z \simeq 6$, Bouwens & Illingworth (2006) suggest that there is a rapid assembly of the most luminous star forming systems between $z \simeq 6$ and $z \simeq 7.4$.

By extrapolating our star-formation model to $z \simeq 7.4$ and holding the parameters fixed at their best-fit $z \simeq 6$ values, we can estimate whether the claimed rapid assem-

bly of luminous galaxies requires evolution in the star formation efficiency or duty cycle. If all four candidate z-dropouts identified in Bouwens & Illingworth (2006) are at $z \simeq 7.4$, then the observed evolution in the abundance of luminous galaxies seemingly can be explained simply by evolution of the host dark matter haloes (Figure 4.4). However, if only one of the candidate z-dropouts is at $z \simeq 7.4$, then our simple model does permit some evolution in either the star formation efficiency or duty cycle in the 200 million years between $z \simeq 7.4$ and $z \simeq 6$. Such evolution could be triggered, for example, by the photo-ionization heating of the intergalactic medium at the end of reionization and the corresponding change in its accretion rate onto galaxies.

At $z \simeq 10$, several candidate LBGs (selected as J-band dropouts) have been identified in the UDF (Bouwens et al., 2005) and in cluster lensing fields (Richard et al., 2006). With the addition of deeper optical data, two of the three candidate $z \simeq 10$ LBGs from Bouwens et al. (2005) are now known to be at lower-redshift (R.J. Bouwens 2006, private communication). In this case, the abundance implied if the remaining one candidate is at $z \simeq 10$ is consistent with hierarchical growth (Figure 4.8).

In contrast, the abundance of less luminous $z \simeq 9$ candidates located in Richard et al. (2006) is significantly larger than expected (Figure 4.8). However, if clustering fluctuations are included in the uncertainties, then the abundances derived are formally consistent with the lower density implied by Bouwens et al. (2005). We note that the 1-sigma error bars on the Richard et al. (2006) data include a large contribution (typically a factor of 3) from the uncertainty in the completeness correction. This uncertainty is difficult to determine accurately; if overestimated by as little as $\simeq 20\%$, the one-sigma uncertainties on the Richard et al. (2006) datapoints would no longer be consistent with the Bouwens et al. (2005) observations. More clusters must be studied to verify the large density of lensed $z \simeq 9$ candidate LBGs. If the large abundances are representative, the Richard et al. (2006) observations require either significant evolution in the parameters of the simple model we have adopted or a top-heavy stellar IMF. Holding the duty cycle fixed at its $z \simeq 6$ value, an implausible star formation efficiency of 100% is required to explain the observed abundance (Figure

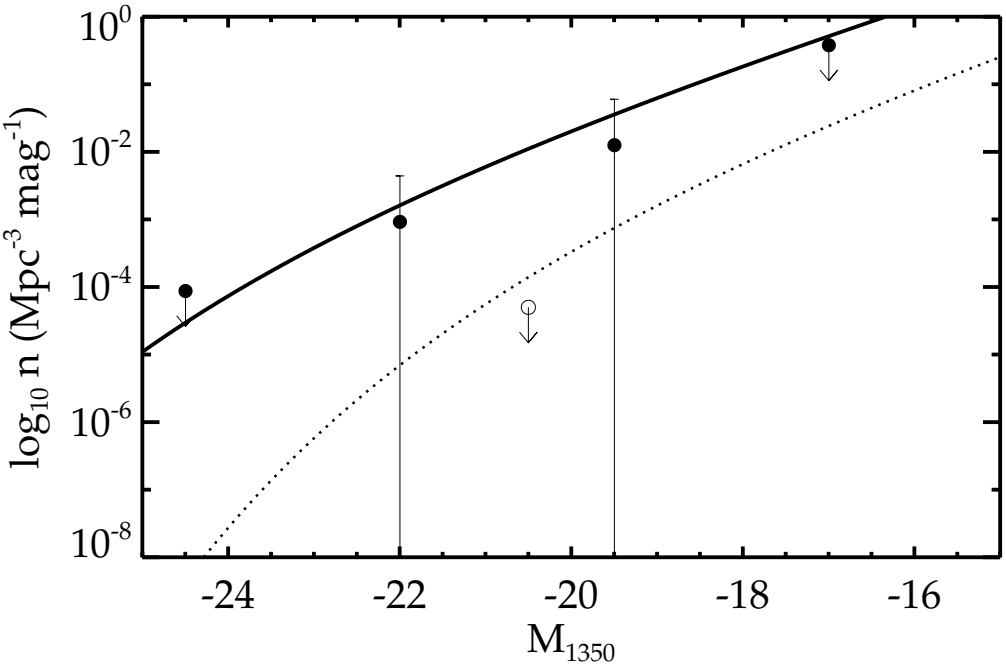

Figure 4.8 Comparison of model $z = 9$ LBG luminosity function with constraints from observations. The observed abundance of LBGs presented in the cluster lensing survey of Richard et al. (2006), denoted by solid circles, is greater than the upper limit found in the Hubble Ultra Deep Field (open circle), as presented in Bouwens et al. (2006). The error bars on the Richard et al. (2006) data are large but may overestimate the true uncertainty (see §4.5.1). The luminosity function obtained by assuming the duty cycle and star formation efficiency remain constant between $z = 6$ and $z = 9$ (dotted line) is underpredicts the large abundances observed in Richard et al. (2006). Reconciling these data points with our models without resorting to more top-heavy IMFs require a star formation efficiency near 100% (solid line).

4.8).

The emerging physical picture describing the evolution of LBGs at $z \simeq 7-10$ is still somewhat tentative. Nonetheless, results from the UDF suggest that evolution in the abundance of *luminous* LBGs in the 500 Myr between $z \simeq 6$–10 can be largely explained by the hierarchical assembly, i.e. without any evolution in the star formation efficiency or duty cycle. In contrast, the high abundance of *less luminous* $z \simeq 10$ candidates suggested by Richard et al. (2006) may require significant evolution in either the stellar IMF or the star formation efficiency. Similar conclusions are reached using semi-analytic models in Samui et al. (2006). Additional observations are required to confirm the large density observed in Richard et al. (2006) is robust and to reconcile these potentially differing pictures. In §4.6, we will use our model to predict the ability of future surveys to detect starburst galaxies at $z \simeq 7-10$.

4.5.2 Lyα Emitters

The first results are also now available from Lyα surveys at $z \simeq 9$. As with the LBGs, the high redshift results are seemingly contradictory. Willis et al. (2005) and Cuby et al. (2006) find no Lyα emitters in narrowband surveys centered at $z = 8.8$ with the Very Large Telescope (VLT). However, both surveys are only sensitive to the brightest LAEs ($> 3 \times 10^{42}$ erg s^{-1} in Willis & Courbin 2005 and $>10^{43}$ erg s^{-1} in Cuby et al. 2006) over modest comoving volumes (870 Mpc^3 and 5000 Mpc^3, respectively).

Stark et al. (2007b) conducted a cluster lensing survey for LAEs at $z = 8.5-10.4$. The magnification provided by the clusters allows significantly less luminous LAEs to be detected ($\gtrsim 10^{41}$ erg s^{-1}), albeit over a much smaller comoving volume ($\simeq 30$ Mpc^3). Six candidate LAEs were identified with unlensed luminosities spanning 2–50×10^{41} erg s^{-1}; at least two of the six candidates are considered likely to be at $z \simeq 9$ following additional spectroscopy which casts doubt on alternative low-redshift explanations for the J-band emission features.

In Figure 4.9, we use our model to compute luminosity functions of LAEs at $z \simeq 9$ assuming the duty cycle, star formation efficiency, and Lyα escape fraction remain

fixed at either their best-fit $z = 5.7$ or $z = 6.5$ values. As the narrowband observations refer to a single redshift, we use the mass function at $z = 8.8$ to compute the luminosity function. For the cluster lensing survey presented by Stark et al. (2007b), as the halo mass function evolves significantly over the redshift range sampled, we compute the average halo mass function between $z = 8.5$ and $z = 10.4$, weighting mass by the relevant sensitivity function. We generated luminosity functions using both mass functions. While the resulting luminosity functions are marginally different, the net results described do not change; hence, for the sake of clarity, in Figure 4.9 we only overlay the luminosity function from the $z = 8.8$ mass function on the data points from the three surveys described above.

The results suggest that, for *luminous* LAEs, current surveys do not yet have the combined sensitivity and depth to detect any sources at $z \simeq 9$. Although the upper limits presented in Willis & Courbin (2005) and Cuby et al. (2006) are consistent with our expectations, those surveys only rule out the possibility that the density of luminous LAEs decreases in the time interval between $z \simeq 9$ and $z \simeq 6$. On the other hand, for *less luminous LAEs*, if all six of the candidates in Stark et al. (2007b) are at high-redshift and the inferred abundances are representative, significant evolution is implied in the model parameters. As with the lensed LBGs at $z \simeq 9$, either a high ($\simeq 100\%$) star formation efficiency (for a fixed duty cycle) or a top-heavy IMF of stars (Figure 4.9) would be required. An important caveat is the uncertainty caused by cosmic variance, which we do not include in the error bars in Figure 4.9. Even for a significantly more ambitious spectroscopic lensing survey, the fluctuations expected from large-scale structure are $\gtrsim 100\%$ (Figure 4.3); hence, it is possible that the candidate LAEs discovered in Stark et al. (2007b) may trace an extreme overdensity in the underlying mass distribution, in which case the derived densities may be larger than the cosmic average at that epoch. Clearly, more clusters must be observed. If only the two prime LAE candidates are at high redshift[1], the derived abundances

[1]The fact that the Poisson errors are 100% for the two datapoints in Figure 4.9 corresponding to the case that two candidates from Stark et al. (2007b) are at $z \simeq 10$ may seem counterintuitive given that there are two sources; however this arises from strongly-varying limiting (detectable) source luminosity over the field of view due to the cluster magnification. For details, see Stark et

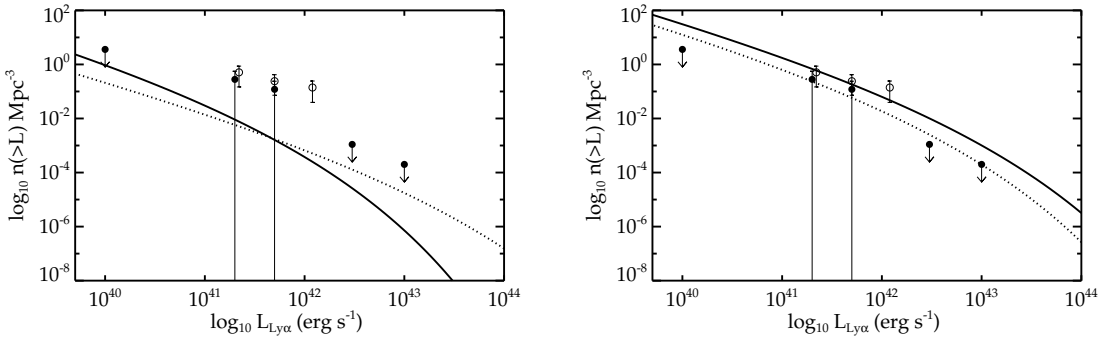

Figure 4.9 Comparison of model $z \simeq 9$ LAE luminosity function with constraints from observations. Solid circles assume two of the six LAE candidates from Stark et al. (2007b) are at $z \simeq 9$; open circles assume all are at $z \simeq 9$. *Top:* If all the $z \simeq 9$ LAE candidates in Stark et al. (2007b) are at high-redshift, then the best-fit model parameters at $z = 5.7$ (dotted line) and $z = 6.5$ (solid line) are inconsistent with their values at $z = 9$. *Bottom:* Model luminosity functions assuming an extreme top-heavy IMF characteristic of Pop-III stars with model parameters fixed at their $z = 6.5$ (dotted line) and a star formation efficiency of 100% (with duty cycle fixed at its best-fit z=6.5 value, solid line) overlaid upon observational constraints.

are formally consistent with the predicted $z \simeq 9$ luminosity function due to the large Poisson fluctuations.

4.6 Implications for Future Surveys

Although in this paper, we have defined a new semi-empirical method for understanding the physical implications of the growing body of data at redshifts $z \simeq 5 - 7$, it is clear from the limited statistics (particularly at the higher redshifts) and the simplicity of the model that unambiguous conclusions cannot yet be drawn with great confidence. However, as the datasets improve, we argue that the framework of our model can help provide the basis for designing future searches for earlier sources.

Over the next few years, several new instruments will be placed on current ground-based telescopes and Hubble Space Telescope motivated in part by extending the search for $z > 7$ sources. These surveys offer the exciting possibility of characterizing

al. (2007b).

the assembly of the first galactic sources through the era of reionization. With our model, calibrated by the data available at $z \simeq 6$, we can estimate the optimal volume and depth necessary for detecting star-forming sources of various luminosities to $z \simeq 10 - 20$. Thus it is hoped our model can assist in guiding the design of future instruments and surveys.

In the following subsections, we will evaluate several benchmark imaging and spectroscopic surveys. We consider a large, blank-field, narrowband survey for LAEs at $z \simeq 8$ and $z \simeq 10$ in §4.6.1, and discuss two different surveys for dropouts at $z \simeq 7.5$ and $z \simeq 10$ in §4.6.2. Finally, in §4.6.3, we examine the efficiency of a variety of lensing surveys for LAEs and LBGs. Since some of these proposed surveys reach to significantly lower luminosities than the current surveys discussed in §4.4 and §4.5, we examine the effects of feedback on the predicted counts, as well as the gains of adaptive optics given our predicted sizes for faint LAEs.

4.6.1 The Dark Ages z Lyman-alpha Exlorer: LAEs at $z \simeq 7 - 10$

The Dark Ages z Lyman-alpha Explorer (DAzLE) is a narrowband imager on the VLT which aims to detect Lyα emitters at $6.5 < z < 12$ (Horton et al., 2004). DAzLE has recently observed two pointings of GOODS-South in two filters corresponding to Lyα redshfits of $\simeq 7.7$ and $\simeq 8.0$ (R. McMahon 2006, private communication). The observing sequence for DAzLE involves alternating between two narrowband filters with slightly different central wavelengths. A composite image is made of all of the subexposures in each filter, resulting in two "subsurveys" slightly offset in redshift space. Subtracting the two composite images removes continuum soures, thereby allowing candidate LAEs to be identified.

In ten hours of integration, DAzLE is expected to reach a 3σ sensitivity of 2×10^{-18} erg cm^{-2} s^{-1} in the differenced image (Horton et al., 2004). At $z = 7.7$, this corresponds to a limiting LAE luminosity of 1.5×10^{42} erg s^{-1}. As a benchmark survey with this instrument, we consider a four position mosaic (i.e. $4\times$ 6.′83×6.′83).

The total comoving volume sampled in four pointings of the two filters at $z = 7.7$ is $\simeq 6900$ Mpc^3. A simple extrapolation of our model suggests that a comoving volume of 1100 Mpc^3 is necessary to detect one LAE at $z = 7.7$. Thus, in this proposed survey, 6-7 LAEs would be detected with DAzLE assuming no rapid evolution in the star formation efficiency, duty cycle or IGM transmission between $z \simeq 6.5$ and $z \simeq 7.7$.

However, although a promising survey in terms of likely detections, the uncertainties are considerable. Clustering fluctuations are 40-50% (for the best-fit z=5.7 and 6.5 model parameters, respectively) at the limiting luminosity of 1.5×10^{42} erg s^{-1}. The Poisson fluctuations expected for a 7200 Mpc^3 survey are similar ($\simeq 40\%$). It is prudent to consider what effects such large fluctuations would have on attempts at using the DAzLE results to constrain the progress of reionization via the evolution of the LAE luminosity function (Malhotra & Rhoads, 2004, 2006; Dijkstra et al., 2006). While our model predicts that 6-7 sources should be detected assuming only evolution in the underlying halos, the large ($\simeq 60\%$) expected field-to-field variations imply that the source counts could vary significantly from the predicted value. Ignoring additional complications on the tranmission of Lyα photons through the IGM from galaxy groups (Wyithe & Loeb, 2005; Furlanetto et al., 2004, 2006) and peculiar velocities (Dijkstra & Loeb 2006, in preparation), if between two and ten LAEs are detected with DAzLE in GOODS-S, little information can be reliably deduced on the evolution of IGM. Holding the duty cycle and star formation efficiency fixed, it would require a $\gtrsim$60% decrease in the Lyα transmission factor, T_α, for only one $z = 7.7$ LAE to be detected towards GOODS-S. Hence, these results suggest that, with currently feasible survey geometries and instruments, this method of constraining reionization will only be effective if the IGM evolves rapidly ($\gtrsim$60%) over a short redshift interval.

DAzLE is able to search for LAEs out to $z \simeq 10$. There is a large gap in the atmospheric OH forest between 1.3325 μm and 1.3401 μm, corresponding to a LAE redshift window of Δz=0.06 centered at $z = 9.99$. A similar window is located at $z = 9.91$. A single DAzLE pointing at this redshift (assuming a filter width of $\simeq$ 10Å) samples a comoving volume of $\simeq 1250$ Mpc^3 summed over both filters. Extrapolating the model

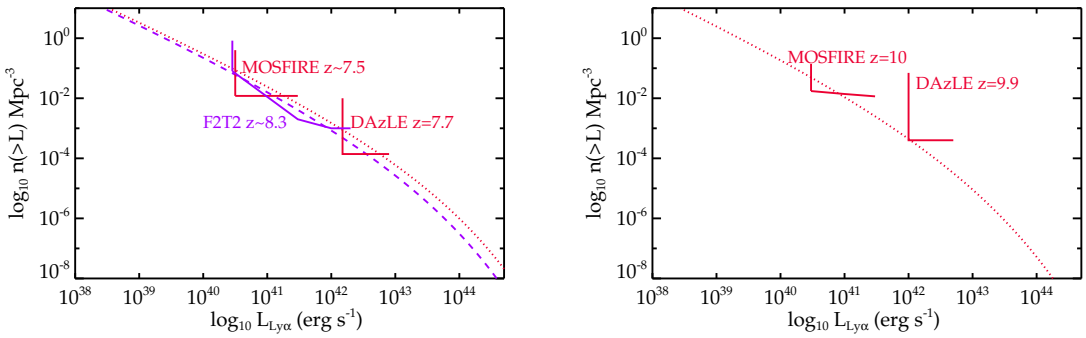

Figure 4.10 *Top:* Extrapolation of Lyα luminosity function to $z \simeq 7.7$ (dotted red curve) and 8.3 (dashed purple curve) fixing star formation model parameters at their best-fit $z = 6.5$ values (§4.4). The predicted luminosity function suggests that DAzLE should detect 6-7 $z \simeq 7.7$ sources in a four pointing mosaic with total integration time of $\simeq 40$ hours. A lensing survey utitlizing F2T2 could detect up to 8 $z \simeq 8.3$ sources in $\simeq 200$ hours of observations. *Bottom:* Extrapolation of Lyα luminosity function to $z \simeq 10$ fixing star formation model parameters at their best-fit $z = 6.5$ values. Almost 200 hours are required to detect a single $z \simeq 10$ source with DAzLE under these assumptions. The estimated performance of lensing surveys with a multi-object spectrograph such as MOSFIRE or a tunable narrowband filter (F2T2) suggest that lensing is an efficient means of detecting LAEs at $z \simeq 7-10$, but supernova feedback could drastically reduce the number of LAEs detected.

luminosity function to this redshift with the parameters fixed at their best-fit $z = 5.7$ values, it would take just over a volume of 2500 Mpc^3 (two pointings) to detect one LAE brighter than 10^{42} erg s^{-1}. At $z = 9.99$, this luminosity limit corresponds to a limiting flux of 8×10^{-19} erg cm^{-2} s^{-1}. Reaching this sensitivity would require 70–80 hours for each pointing (adjusting for the expected atmospheric transparancy in the wavelength interval of the observations); hence almost 200 hours would be required to detect a single $z \simeq 10$ source. Alternatively, if the LAE candidates identified by Stark et al. (2007b) are at high-redshift and not probing an overdensity, then $\gtrsim 100$ LAEs brighter than 10^{42} erg s^{-1} would be expected in the single 70-80 hour DAzLE pointing.

In summary, DAzLE may well detect many z=7.7 sources but spectroscopic confirmation will be a challenge. However, even in the most ambitious surveys we can currently contemplate, the contribution of these sources to reionization will be seriously limited by the expected clustering fluctuations. Surveys at higher redshift will be much more demanding. Few sources are expected within reasonable exposure times at $z \simeq 9$–10 unless there is significant evolution in the LAE model parameters between $6 < z < 10$, as may be possible only if all of the fainter lensed LAEs detected by Stark et al. (2007b) are at high redshift.

4.6.2 Imaging Surveys for LBGs at $z \simeq 7 - 10$

Selection of $z \gtrsim 7$ LBGs will be greatly aided by dedicated programs on telescopes using the new generation of large-format near-infrared detectors. The Visible and Infrared Survey Telescope for Astronomy (VISTA) is projected to be available in late 2007 and will offer near-infrared imaging with a mosaiced 1.6 deg^2 field of view [2]. In 2008, the Wide Field Camera 3 (WFC3) is scheduled to be installed on HST; this near-IR camera will offer imaging in a $127'' \times 137''$ field of view. We thus consider the efficiency of likely surveys with VISTA and WFC3.

The vast majority of VISTA time (75%) will be available for large public surveys.

[2] http://www.vista.ac.uk/

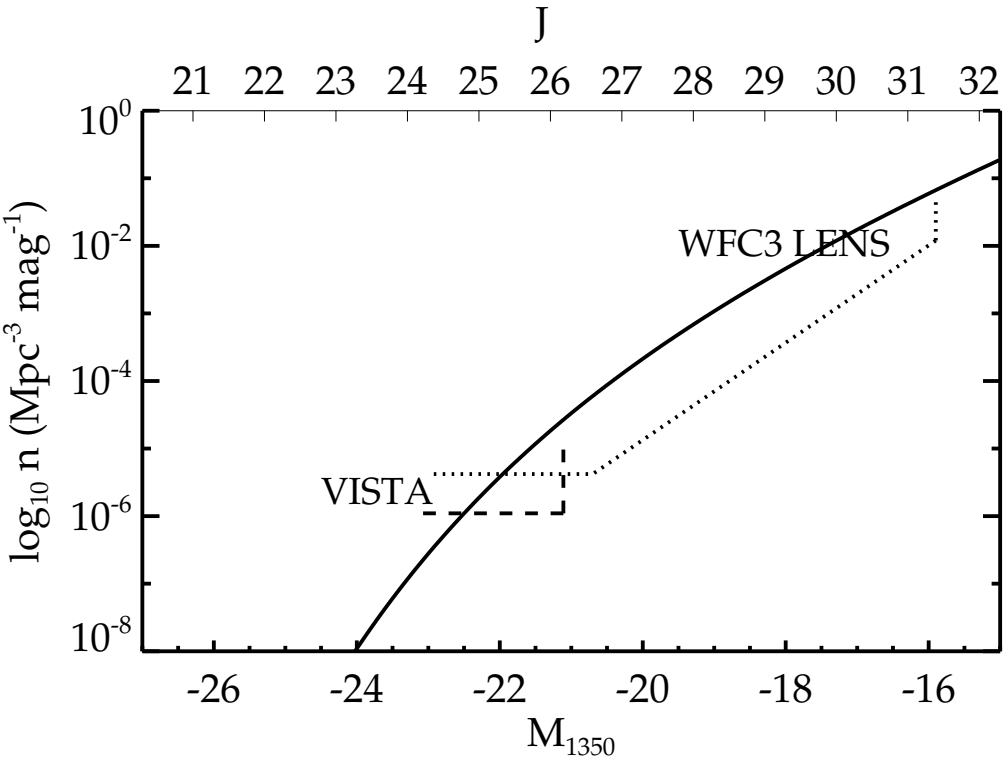

Figure 4.11 Predicted LBG luminosity function at $z \simeq 7.5$ assuming star formation model parameters are fixed at their best-fit $z \simeq 6$ values (§4.4). The absolute magnitude at 1350Å is plotted horizontally along the bottom of the plot, and the corresponding J-band apparent magnitude is plotted along the top of the plot, assuming $z = 7.5$. The efficiency of several mock surveys for $z \simeq 7.5$ sources is overplotted.

We consider a hypothetical survey with VISTA where a central $\simeq$0.9 deg^2 area is imaged down to 5σ limiting (AB) magnitudes of z=27.0, J=26.6, and H=26.1. We adopt selection criteria for z-drops ($z - J >$0.8, Bouwens & Illingworth 2006) and J-drops (J-H>1.8, Bouwens et al. 2005) and estimate how many sources each survey is likely to detect. With these selection criteria, the 5σ limiting J- and H-band limits (J=26.2 and H=24.8) correspond to limiting star formation rates of 13 and 70 $M_\odot yr^{-1}$ at $z \simeq 7.5$ and 10, respectively.

The hypothetical survey field of view samples a comoving area of 4390 Mpc^2 at $z \simeq 7.5$ and 6130 Mpc^2 at $z \simeq 10$. We assume the redshift probability distribution of z-drops and J-drops is a Gaussian with a standard deviation of σ_z=0.5 and a mean of μ_z=7.5 and 10 for z-drops and J-drops, respectively. We normalize the probability

distribution so that the maximum completeness is 50% at the mean redshift of the survey. While the completeness is certainly higher for objects that are much brighter than the sensitivity limit of the survey, monte carlo simulations suggest that 50% is a reasonable average for entire population which is dominated by the faintest objects (Stark et al., 2007a). We compute the effective radial distance sampled by the surveys by integrating the normalized redshift probability distribution over a distance spanning Δz=2 in redshift and centered at μ_z. This corresponds to a total comoving volume of $9{\times}10^5$ Mpc^3 at $z \simeq 7.5$ and $1{\times}10^6$ Mpc^3 at $z \simeq 10$.

In Figures 4.11 and 4.12, we extrapolate the best-fit luminosity function from $z \simeq 6$ to $z \simeq 7.5$ and $z \simeq 10$ allowing only for evolution in the dark matter mass function. The comoving number density of detected LBGs at the sensitivity limit of the survey is 2.8×10^{-5} Mpc^{-3} mag^{-1} at $z \simeq 7.5$ and 4×10^{-9} Mpc^{-3} mag^{-1} at $z \simeq 10$. Integrating over the entire magnitude range, 9 sources would be detected brighter than J=26.2 at $z \simeq 7.5$ and no sources would be detected brighter than H=24.8 at $z \simeq 10$.

As with the VISTA observations, the mock WFC3 observations require deep z, J, and H-band coverage to select z- and J-band dropouts. WFC3 offers a significant improvement in both throughput and areal coverage with respect to NICMOS, so the camera is ideal for selecting J-drops. By contrast, WFC3 is *not* more efficient than ACS in the z-band. Therefore, WFC3 is not particularly well-suited for conducting a new z-drop survey that is significantly deeper than UDF. We thus consider its efficiency at detecting J-dropouts.

We adopt limiting magnitudes that are $\sim$1 and $\sim$2 magnitudes deeper than the UDF in H_{160} and J_{110}, respectively, corresponding to 5σ sensitivities of J_{110}=31.3 and H_{160}=29.5 for point sources (assuming an $0\farcs4$ diameter aperture). With a J-band 5σ sensitivity of 31.3, J-drops can be selected as faint as H_{160}=29.5, using the selection criteria of Bouwens et al. (2005). The estimated star formation rate for $z \simeq 10$ LBGs with H_{160}=29.5 is 0.9 $M_\odot$yr^{-1}. Based on the anticipated WFC3 performance, reaching such sensitivities in a single pointing would take 301 hours in J_{110} and 48 hours in

H_{160} resulting in 349 hours of total integration [3]. Since K-band observations are not practical with WFC3, we rely only on an H-band detection for J-drop selection. Each WFC3 field of view covers a comoving area of 6.0 Mpc $\times$ 6.5 Mpc at $z \simeq 10$. Assuming a redshift probability distribution identical to that described above for z-drops and J-drops with VISTA, we find that the single WFC3 pointing will sample a comoving volume of 5410 Mpc^3 at $z \simeq 10$.

The predicted comoving number density of detected J-drop LBGs at the sensitivity limit of the single deep WFC3 pointing is 7.2×10^{-4} Mpc^{-3} mag^{-1} at $z \simeq 10$, assuming no-evolution in the star formation efficiency and duty cycle. Integrating over the entire magnitude range, 1-2 sources would be detected at $z \simeq 10$.

In summary, it appears that dedicated surveys using ground based telescopes equipped with large field-of-view imagers (e.g. VISTA) should be able to detect $\simeq 10$ LBGs at $z \simeq 7.5$; however detecting sources at $z \simeq 10$ may be difficult with sensitivity limits typically obtained from the ground. Even from space (using WFC3 on HST), detecting LBGs at $z \simeq 7-10$ will not be trivial, requiring hundreds of hours to detect a single LBG at $z \simeq 10$.

4.6.3 Lensing Surveys for Star-forming Galaxies at $z \simeq 7-10$

Currently, strong lensing surveys for high-redshift galaxies could be contemplated for about 20 galaxy clusters for which there are well-defined mass models; these mass models are essential in accurately defining the spatial distribution of magnification. However, ongoing HST surveys will significantly increase the number of suitable galaxy clusters (e.g. Ebeling et al. 2003). Here, we examine the efficiency of surveys for lensed LBGs and LAEs assuming a larger sample of clusters and more efficient instruments that will soon become available. We consider both an extension of the longslit spectroscopic survey discussed in (Stark et al., 2007b) and as well as an imaging campaign to identify lensed z-drops and J-drops.

In the next several years, a number of near-IR multi-object spectrometers will be

[3]Estimated sensitivies for WFC3 are listed at `http://www.stsci.edu/hst/wfc3/documents/handbook/cycle16/wfc3_cyc166.html`

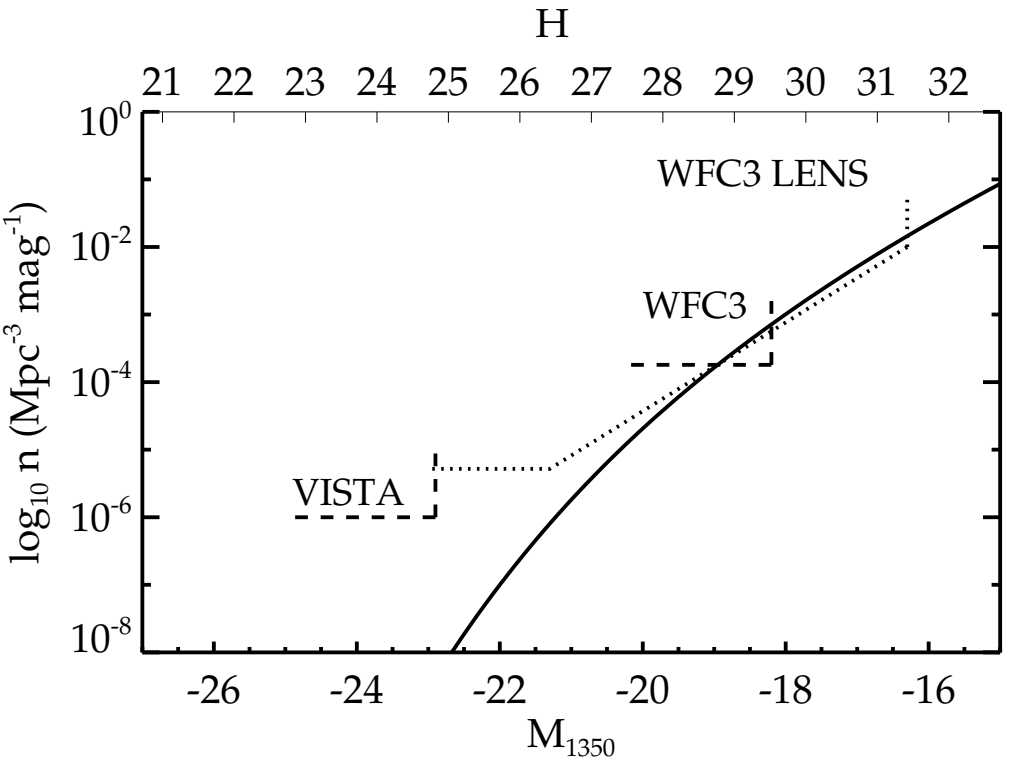

Figure 4.12 Predicted LBG luminosity function at $z \simeq 10$ assuming star formation model parameters are fixed at their best-fit $z \simeq 6$ values (§4.4). The absolute magnitude at 1350 Å is plotted horizontally along the bottom of the plot, and the corresponding H-band apparent magnitude is plotted along the top of the plot, assuming $z = 10$. The efficiency of several mock surveys for $z \simeq 10$ sources is overplotted.

installed on 8-10 meter class telescopes, offering significant gains in sensitivity and field-of-view over current near-IR instruments. One such instrument is the Multi-Object Spectrograph For Infra-Red Exploration (MOSFIRE, PI: I. McLean & C. Steidel) on Keck I. MOSFIRE will utilize a configurable slit unit allowing up to 45 slits, each 7.″3 in length, within the 6.′14×6.′14 field of view. While tilted and curved slits are not possible with MOSFIRE, the configurable slit unit will still allow for more areal coverage of high magnification regions than with NIRSPEC. In addition, MOSFIRE will be more sensitive than NIRSPEC, reaching 5σ line flux sensitivities of 1×10^{-18} erg cm^{-2} s^{-1} in 4 hours, assuming an unresolved line with R=3270 [4]. Given the specifications of MOSFIRE, it is optimal to concentrate observations to clusters with vary large and well-determined critical lines (e.g. Abell 1689, Abell 1703, Abell 2218). While the exact magnification distribution provided to background sources may very slightly from cluster to cluster, it is reasonable to expect 80% of the MOSFIRE survey area to be at a magnification of 20, 15% of the area to have a magnification of 10, and 5% of the area to be magnified by only a factor of 5 (Stark et al., 2007b).

We consider a MOSFIRE *spectroscopic* lensing survey for LAEs both at $z = 7.0 - 8.3$ (Y-band) and at $z = 8.5 - 10.3$ (J-band). Assuming $\simeq 15\%$ of the line-of-sight distance is lost due to bright OH lines, this corresponds to comoving radial distances of 353 and 334 Mpc, respectively. Assuming 10 clusters are observed for 8 hours each in the Y-band, the resulting survey volume is $\simeq 73$ Mpc^3 for LAEs brighter than $10^{40.5}$ergs^{-1}. For the mock J-band survey, we assume longer integration times (20 hours) over eight clusters, giving an identical integration time to the mock DAzLE $z = 9.9$ survey considered previously. This results in the coverage of $\simeq 58$ Mpc^3 for $z \simeq 10$ LAEs brighter than $10^{40.5}$ergs^{-1}. Extrapolating our LAE model to $z = 7.5$ and to $z = 10$ holding the model parameters fixed at their $z = 5.7$ values, we predict that the MOSFIRE survey should detect 9 sources brighter than $10^{40.5}$ergs^{-1} at $z = 7.5$ and 4 sources brighter than this limit at $z \simeq 10$. If supernova feedback decreases the star

[4]Sensitivities and additional specifications of the spectrograph are provided in the Preliminary Design Report located at `http://www.astro.ucla.edu/ irlab/ mosfire/MOSFIRE%20PDR%20Report%20v4.pdf`

formation efficiency in a manner described in §4.2, then the predicted number of LAEs would drop drastically. The $z \simeq 7.5$ survey would potentially detect 1-2 LAE brighter than $10^{40.5}$ergs^{-1} while the $z \simeq 10$ survey would not detect any sources. Hence, the success of the mock lensing survey depends strongly on whether supernova feedback decreases the efficiency of star formation in low-mass dark matter halos. Given the possible efficiency with which the lensing survey could detect $z \simeq 7-10$ galaxies, it is of the utmost importance to observationally constrain the effects of supernova feedback on the LAE luminosity function at lower redshifts ($z \simeq 3-6$).

Gravitational lensing can also be very valuable for *imaging* surveys for LBGs that are intrinsically fainter than those detected in conventional deep surveys (e.g. GOODS, UDF). One such survey is currently being conducted toward six galaxy clusters with NICMOS on HST (Stark & Ellis 2006, Richard et al. 2007, in preparation). With WFC3, such a survey could potentially be conducted much more efficiently, allowing many more clusters to be observed. We examine the feasibility of a hypothetical WFC3 lensing survey of galaxy clusters for z- and J-dropout galaxies. The primary benefit of a WFC3 survey for $z \gtrsim 7$ LBGs is the added throughput and field of view in the J_{110} and H_{160}-bands compared to what is available with NICMOS. For each cluster, we assume 5-σ point-source sensitivities (in an aperture with $0\farcs4$ diameter) of z_{850}=27.4, J_{110}=28.2, and H_{160}=27.4, requiring $\simeq$ 8, 1, and 1 hour(s) per cluster, respectively. These limits allow z-drops to be selected down to J_{110}=26.6 and J-drops to be selected down to H_{160}=26.4 (without considering the effects of lensing). If we allot 350 hours to this observing program (an identical time allocation to the traditional survey discussed in the previous subsection), 35 clusters can be observed. The total area surveyed would be more than a factor of fifteen greater than previous lensing surveys for $z \gtrsim 7.5$ LBGs (Richard et al. 2007, in preparation).

Both the survey volume and limiting source luminosity are modified by the magnification provided by the foreground galaxy cluster (see Santos et al. 2004 or Stark et al. 2007b for a description). A typical cluster provides a magnification boost of $\times$2,5,10, and 30 over 92%, 46%, 29%, and 12% of the entire WFC3 field of view. Adopting this magnification distribution for each of the 20 clusters, at $z \simeq 7.5$,

the survey is sensitive to a volume of 2.4×10^5 Mpc^3, 7.6×10^4 Mpc^3, 1.5×10^4 Mpc^3, 3.1×10^3 Mpc^3, and 580 Mpc^3 for sources brighter than J_{110} = 26.6, 27.6, 28.6, 29.6, and 30.6 respectively[5]. At $z \simeq 10$, the survey probes a comoving volume of 1.9×10^5 Mpc^3, 6.0×10^4 Mpc^3, 1.1×10^4 Mpc^3, 2.4×10^3 Mpc^3 and 460 Mpc^3 for sources brighter than H_{160}=26.4, 27.4, 28.4, 29.4, and 30.4, respectively. Over 35 clusters, if the star formation efficiency and duty cycle remain fixed, then such a survey should detect 82 $z \simeq 7.5$ LBGs brighter than J_{110}=31.6 (corresponding to a star formation rate of 0.09 $M_\odot yr^{-1}$ at $z \simeq 7.5$ for the source assumptions discussed in §4.2, Figure 4.11) and 6 $z \simeq 10$ LBGs brighter than H_{160}=31.4 (corresponding to a star formation rate of 0.2 $M_\odot yr^{-1}$ at $z \simeq 10$, Figure 4.12).

Adaptive optics (AO) provides the possibility of diffraction-limited observations from the ground. If the projected size of the target objects is small enough, such observations are more efficient than non-AO observations because the photometric aperture can be decreased, thereby allowing significantly less noise for nearly the same amount of flux[6]. One planned survey that aims to take advantage of AO is the Gemini Genesis Survey (GGS). This survey will use a tunable Fabry-Perot etalon (F2T2, Scott et al. 2006) on Gemini with resolution of R=800 to detect lensed LAEs at $z \simeq 8-10$. If the projected angular size of the sources is less than $\simeq$0.03 arcsec^2, then GGS should be able to reach a 5σ sensitivity of $3-6\times10^{-18}$erg cm^{-2} s^{-1} in 10 minutes (R. Abraham 2006, personal communication). Following the scaling relation derived in §4.2, galaxies at $z \simeq 10$ should have typical sizes of 0.01 arcsec^2, small enough to significantly benefit from AO. The field of view of F2T2 is $45''\times45''$, ideally suited to imaging the most highly magnified regions of galaxy clusters.

We consider a mock GGS survey of 60 clusters; we assume each cluster is observed for 5 minutes in 40 different wavelength positions between 1.1μm and 1.3μm, allowing the detection of LAEs at $z = 8.1$ to $z = 9.7$. This should take $\simeq$ 200 hours of integration. A typical cluster provides a magnification gain of $\times5, 10,$ and 30 over 80%,

[5]The quoted magnitudes correspond to the apparent magnitude that a source would be observed with if it was not magnified.

[6]The validity of this statement depends on the strehl ratio, which is the ratio of the peak brightness of the stellar image to that produced by an ideal optical system. If the strehl is very low, then the amount of flux in the diffraction-limited aperture will be greatly reduced.

69%, and 33% of the F2T2 field of view (Richard et al., 2006). Taking this as the magnification distribution for each of the clusters, the total survey volume sensitive to LAEs brighter than 10^{41} erg s^{-1} is 30-86 Mpc^3. The $z \simeq 8 - 8.5$ LAE luminosity function (assuming fixed model parameters from $z = 5.7$) suggests that 3-7 sources would be detected at $z \simeq 8 - 8.5$. If the effects of supernova feedback are parameterized as in §4.2 and §4.4, the number density of low luminosity sources is drastically reduced; in this case, no sources would be detected in the survey. Alternatively, if all six candidate LAEs in Stark et al. (2007b) are at high-redshift and not probing an overdensity, then GGS should detect over 30 $z \simeq 8 - 10$ sources.

It appears that lensing surveys offer one of the more efficient means of identifying galaxies at $z \simeq 7 - 10$ since they are able to reach sensitivity limits where objects are expected to be much more abundant. However, supernova feedback may drastically reduce the number of sources detected in these surveys. Regardless, spectroscopic confirmation of these sources will continue to remain challenging until JWST and 20-30 meter ground-based telescopes become available.

4.7 Conclusions

We have attempted to empirically calibrate the parameters of a simple star formation model using observations of star-forming galaxies (both LBGs and LAEs) at $z \simeq 6$. The error budget used in fitting the data takes proper account of both the Poisson and clustering variance. We use the calibrated model to characterize the physical properties of LBGs and LAEs at $z \simeq 6$ and extrapolate it to higher redshifts to make predictions for upcoming surveys for galaxies at $z \simeq 7 - 10$. Our primary conclusions are as follows:

1. We have derived accurate formulae for the field-to-field variance expected in broad-band surveys for LBGs, narrowband surveys for LAEs, and lensing surveys for LAEs. For each survey geometry, there exists a cross-over luminosity L_c below which the clustering variance dominates over commonly-used Poisson variance. In total, the clustering variance accounts for less than 6% error in narrowband surveys for LAEs

in the Subaru Deep Field and 15-20% error in the $z \simeq 6$ surveys for LBGs in UDF. The clustering fluctuations are significantly higher for spectroscopic lensing surveys reaching up to 100%.

2. LBGs at $z \simeq 6$ are best-fit by a model with a star formation efficiency of 13% and a duty cycle of 0.2. Taken at face value, the star formation efficiency suggests that, on average, 87% of the baryonic mass of $z \simeq 6$ LBGs still remains in the gas-phase. The duty cycle, if taken at face value, would indicate that the current burst of star formation has a lifetime of 200 Myr, roughly equivalent to the dynamical time of virialized halos at $z \simeq 6$. The duty cycle also implies that 80% of dark matter halos of a given mass are not traced by LBGs. If this is indeed true, the missing halos could have yet to form many stars (due perhaps to inefficient cooling) or could be quiescent after experiencing a burst of star formation at earlier times. This result could suggest that the claimed deficit in ionizing photons from luminous LBGs at $z \simeq 6$ relative to what is required for reionization may be explained by star formation at higher redshift.

3. The best-fitting model parameters for LAEs show some evidence for evolution between $z = 5.7$ and $z = 6.5$. However, most likely the evolution is not due to a change in the neutral fraction of the IGM since the parameter that is proportional to the transmission of Lyα photons through the IGM *increases* between $z = 5.7$ and $z = 6.5$. Thus, we consider the evolution to be tentative because of the large uncertainties in the density of the lowest luminosity LAEs. Additional spectroscopic efforts are needed to improve the spectroscopic completeness at low-luminosities.

4. The star formation efficiency of LAEs must be very low ($\simeq 1\%$) in order to reproduce the low stellar masses inferred from observations of LAEs at $z \simeq 5$. Such a low star formation efficiency is only possible in the context of the models if the Lyα transmission factor is near unity. This not only requires a large escape fraction of Lyα photons from the galaxy, but also requires that the photons are not substantially absorbed in their path through the IGM. The emerging physical picture is that the LAEs with large EWs are young objects (10-20 Myr) that have only converted on order 1% of their baryons to stars (and hence remain gas-rich) and have not yet pro-

duced much dust, allowing a large escape fraction for Lyα photons. The intergalactic absorption decrement in Lyα may be reduced if the ionizing luminosity of the LAEs or the galaxy groups in which they reside is sufficiently large so as to strongly ionize the IGM in their vicinity.

5. We have attempted to fit preliminary data at $z \simeq 7-10$ by extrapolating our model to higher redshifts assuming model parameters are fixed at their calibrated $z \simeq 6$ values. The observed evolution of LBGs between $z \simeq 6$ and $z \simeq 7.5$ can be explained largely by changes in the host dark matter halos. At $z \simeq 10$ the picture is more complicated. Constraints on the presence of $z \simeq 10$ LBGs in the Hubble UDF (Bouwens et al., 2005) are explained by the hierarchical growth of dark matter halos. In contrast, the large abundance of $z \simeq 9$ LBGs claimed in the lensing survey of Richard et al. (2006) is difficult to explain in the context of our simple model without resorting to a top-heavy IMF or large field-to-field fluctuations. The situation is similar for the lensed LAEs. Two traditional surveys at $z = 8.8$ are consistent with no-evolution in the model parameters from $z = 5.7$, while the abundances inferred from candidate LAEs in a spectroscopic lensing survey (Stark et al., 2007b) are only explicable if the IMF is top-heavy or if the observations are probing an overdensity in the underlying mass distribution.

6. New instruments that will become available on ground-based telescopes and HST in the next 2-3 years should greatly increase the efficiency with which $z \simeq 7-8$ LAEs and LBGs are detected. However, unless there is significant upward evolution in the luminosity function from $z \simeq 6$, detecting $z \simeq 10$ galaxies via conventional methods will only be feasible if heroic efforts are undertaken. With current telescopes, lensing surveys are potentially better suited to detecting $z \simeq 10$ sources depending on supernova feedback. JWST and thirty-meter class ground-based telescopes are most likely necessary to detect a substantial population of objects at $z \simeq 10$.

7. Constraining reionization at $z \simeq 6-7$ via the evolution in the LAE luminosity function as probed by future narrowband surveys will be complicated by clustering and Poisson variance. Given the large fluctuations ($\gtrsim 60\%$ for feasible survey geometries and sensitivities) and small number of sources expected to be detected ($\simeq 7$

assuming no evolution from z=5.7), this technique will only be effective if the neutral fraction in the IGM evolves very rapidly in the redshift interval between $z = 6.5$ and $z = 7.7$.

Acknowledgements

D.P.S is grateful for the hospitality of the Institute of Theory and Computation (ITC) at the Harvard-Smithsonian CfA where this work was initiated. We thank Johan Richard and Rychard Bouwens for providing us with the luminosity function from their surveys and Joey Munoz for helpful comments on the paper.

Chapter 5

The Evolutionary History of Lyman Break Galaxies Between Redshift 4 and 6: Observing Successive Generations of Massive Galaxies in Formation

Abstract

We present new measurements of the evolution in the Lyman break galaxy (LBG) population between $z \simeq 4$ and $z \simeq 6$. By utilizing the extensive multiwavelength datasets available in the GOODS fields, we identify 2443 B, 506 V, and 137 i'-band dropout galaxies likely to be at high redshift. For the subset of dropouts for which reliable *Spitzer* IRAC photometry is feasible (roughly 35% of the sample), we estimate luminosity-weighted ages and stellar masses. With the goal of understanding the duration of typical star formation episodes in galaxies at $z \gtrsim 4$, we examine the distribution of stellar masses and ages as a function of cosmic time. We find that at a fixed rest-UV luminosity, the average stellar masses and ages of galaxies do not increase significantly between $z \simeq 6$ and 4. In order to maintain this near equilibrium in the average properties of high redshift LBGs, we argue that there must be a steady flux of young, newly-luminous objects at each successive redshift. When considered along with the short duty cycles inferred from clustering measurements, these results

may suggest that galaxies are undergoing star formation episodes lasting only several hundred million years. In contrast to the unchanging relationship between the average stellar mass and rest-UV luminosity, we find that the number density of massive galaxies increases considerably with time over $4 \lesssim z \lesssim 6$. Given this rapid increase of UV luminous massive galaxies, we explore the possibility that a significant fraction of massive (10^{11} $M_{\odot}$) $z \simeq 2-3$ distant red galaxies (DRGs) were in part assembled in an LBG phase at earlier times. Integrating the growth in the stellar mass function of actively forming LBGs over $4 \lesssim z \lesssim 6$ down to $z \simeq 2$, we find that $z \gtrsim 3$ LBGs could have contributed significantly to the quiescent DRG population, indicating that the intense star-forming systems probed by sub-millimeter observations are not the only route toward the assembly of DRGs at $z \simeq 2$.

5.1 Introduction

The detailed study of various classes of distant galaxies has enabled great progress in understanding the star formation and mass assembly history of normal field galaxies (for recent reviews see Hopkins & Beacom 2006; Ellis 2008; Wilkins et al. 2008). Multi-wavelength probes have been particularly effective in revealing the co-existence of diverse categories of galaxies with redshifts $z \simeq$ 2-3. These include the relatively unobscured star-forming 'Lyman break' galaxies (LBGs, Steidel et al. 1996; Shapley et al. 2005), the infrared-selected massive 'distant red' galaxies (DRGs, Franx et al. 2003; van Dokkum et al. 2006) and heavily obscured sub-mm galaxies which contain both intensely star-forming and active components (SMGs, Smail et al. 1998; Chapman et al. 2005). The collective study of these populations has revealed that the redshift range $1 < z < 3$ is a formative one when the bulk of the stars in present-day massive galaxies was produced (Hopkins & Beacom, 2006).

Understanding the inter-relationship between these various sources is an important goal and intense efforts are now underway to address this issue (van Dokkum et al., 2006; Reddy et al., 2008). A relevant aspect of this discussion concerns the assembly history of objects observed during the redshift interval $4 < z < 6$, corresponding to a

period only 1 Gyr earlier. Such data may provide valuable insight into the connection between actively star-forming and passive populations as well as define the mode of star formation in typical massive galaxies.

Over the last five years, deep multiwavelength surveys have resulted in the discovery of large samples of LBGs at $z \simeq 4-6$ (Bouwens et al., 2007). Despite early controversies (Bunker et al., 2004; Giavalisco et al., 2004b; Beckwith et al., 2006), it now seems clear that the star formation density declines with redshift beyond $z \simeq 3$. Recent evidence also suggests the characteristic luminosity is also fading (Yoshida et al., 2006; Bouwens et al., 2007; McLure et al., 2008). Bouwens et al. (2007) attribute this evolutionary pattern to the simple hierarchical assembly of galaxies. Unfortunately, because of the transient nature of star formation probed by the rest-frame UV luminosity function, these studies alone provide only an approximate measure of the evolutionary processes occurring during $3 < z < 6$. Key to testing the mode of assembly of galaxies in this early period is additional information on the physical properties, such as the associated stellar mass and the inferred age of the stellar populations. The availability of deep IRAC data for many of the HST fields enables such an approach (Egami et al., 2005; Eyles et al., 2005; Yan et al., 2005).

In this paper, we aim to improve our understanding of galaxy evolution during the first 2 Gyr by systematically tracking the evolving stellar content of star-forming galaxies in uniformly-selected samples spanning three separate redshift intervals between $z \simeq 4$ and 6. By adding the additional physical parameters of stellar mass and luminosity-weighted ages, we can break degeneracies associated with studies that rely only on the UV luminosity function.

An important issue is how and when the quiescent subset of DRGs seen at $z \simeq 2-3$ (van Dokkum et al., 2006; Kriek et al., 2006) assembled their mass. Contemporary models of galaxy formation suggest that the number density of massive galaxies increases continuously with cosmic time over $2 \lesssim z \lesssim 5$ (Bower et al., 2006), a picture supported by the relatively young ages of massive DRGs at $z \simeq 2$ (Kriek et al., 2006). Alternatively, it is potentially feasible that the bulk of the most massive systems at $z \simeq 2$ formed their mass at much earlier times (e.g., $z \gtrsim 5$) which in turn would

imply little evolution in the number density of massive galaxies over $3 \lesssim z \lesssim 6$. We seek to constrain the formation epoch of quiescent DRGs by studying the evolving stellar mass function of star-forming galaxies over $4 \lesssim z \lesssim 6$. Moreover, we wish to understand whether most DRGs were assembled entirely in intense, dust-enshrouded star formation episodes (probed by higher redshift SMGs), or if a significant fraction were formed in less vigorous star-forming systems traced by higher redshift LBGs. By determining the number density of massive galaxies in the LBG phase at each redshift interval, we hope to estimate the fraction of DRGs whose progenitors formed a significant component of their mass in relatively unobscured systems with moderate star formation rates (SFR) typical of the LBG population (Shapley et al., 2001, 2005).

A further question of significance in characterizing the mode of early galaxy assembly is understanding the duration of star formation episodes in high redshift galaxies. In the context of models in which gas accretion dominates galaxy growth at high redshift (e.g., Birnboim & Dekel 2003; Kereš et al. 2005; Finlator et al. 2007) leading to rapid and steady star formation, one might imagine that the LBGs seen at $z \simeq 4$ have evolved relatively smoothly since their formation at an earlier epoch, creating stars at a near constant rate. If their assembly timescales are long enough, we would thus expect similarly luminous $z \simeq 5$ and 6 LBGs to be less evolved versions than their $z \simeq 4$ descendants with lower stellar masses, less dust extinction, and younger ages. Alternatively, it is conceivable that this era witnesses a rapid increase in the intensity of star formation in individual galaxies, as has been predicted for the early stages of galaxy growth (Kereš et al., 2005; Finlator et al., 2007). In this case, galaxies would grow along a locus of points (or "main sequence") in the $M_\star$-SFR plane. Thus, if viewed at fixed UV luminosity, the observed stellar populations would not vary significantly from one redshift to another. Finally, in contrast to these "sustained" star formation histories, we may expect star formation episodes to occur on much shorter timescales. If the past duration of star formation is sufficiently short ($\lesssim 300$ Myr), then each dropout sample would be dominated by newly emerged systems, and we would not necessarily expect to see significant growth in the $M_\star$-SFR plane over

the redshift range studied.

Earlier work in this direction has been promising but the datasets have been limited. Drory et al. (2005) traced the mass assembly of galaxies to high redshift using K-band selected samples. However since their study did not include IRAC data, reliable stellar masses could only be derived to $z \simeq 4.5$. Verma et al. (2007) used HST and IRAC data to compare the stellar mass and age distribution of a small, robust sample of $z \simeq 5$ LBGs to those derived by Shapley et al. (2001) at $z \simeq 3$. Most recently, McLure et al. (2008) computed the stellar mass function of LBGs at $z \simeq 5$ and 6 by scaling the UV luminosity function by the average mass/light ratio of the LBG population at high redshift. While these efforts have improved our understanding of the stellar content of high-redshift galaxies, none has yet systematically traced the evolving stellar populations of galaxies over the full redshift range, using large and uniformly selected samples with no scaling assumptions.

A plan of the paper follows. In §5.2, we describe the GOODS data used in our analysis. In §5.3, we discuss the color selection used to identify dropouts, and criteria used to remove contaminants from our sample. We close the section by assessing the evolving surface densities and rest-UV slopes of the dropouts. In §5.4, we consider the mid-infrared properties of the dropouts and in §5.5, we discuss the population synthesis models used to infer stellar masses and ages and comment on the uncertainties in the derived properties. In §5.6, we examine the redshift evolution in the stellar masses and ages of dropouts at a fixed UV luminosity. Using this information, we discuss the implications for the star formation histories of galaxies at high redshift. Finally, in §5.7, we study the evolving stellar mass functions of LBGs over $4 \lesssim z \lesssim 6$ and estimate the fraction of LBGs that evolve into quiescent massive galaxies at $z \simeq 2-3$.

Throughout the paper, we adopt a Λ-dominated, flat universe with $\Omega_\Lambda = 0.7$, $\Omega_M = 0.3$ and $H_0 = 70\,\mathrm{h_{70}km\,s^{-1}\,Mpc^{-1}}$. All magnitudes in this paper are quoted in the AB system (Oke & Gunn, 1983).

5.2 Data

5.2.1 The GOODS Fields

We focus our analysis on the data from the Great Observatories Origins Deep Survey (GOODS). Detailed descriptions of the datasets are available in the literature (Giavalisco et al., 2004a), so we only provide a brief description here. The GOODS-S and GOODS-N survey areas each cover roughly 160 arcmin^2 and are centered on the *Chandra* Deep Field South (CDF-S; Giacconi et al. 2002) and the *Hubble* Deep Field North. Extensive multiwavelength observations have been conducted in each of these fields. In this paper, we utilize optical imaging from the Advanced Camera for Surveys (ACS) onboard the Hubble Space Telescope (HST). Observations with ACS were conducted in F435W, F606W, F775W, and F850LP (hereafter B_{435}, V_{606}, i'_{775}, z'_{850}) toward GOODS-S and GOODS-N (Giavalisco et al., 2004a). The 5σ limiting magnitudes in the GOODS ACS data are B_{435}=29.5, V_{606}=29.5, i'_{775}=28.5, and z'_{850}=27.5. We also make use of U-band observations of GOODS-N taken with the Kitt Peak National Observatory 4, telescope with the MOSAIC prime focus camera (Capak et al., 2004) and of GOODS-S taken with the Wide-Field Imager mounted on the 2.2m MPG/ESO telescope (Arnouts et al., 2001).

In the near-infrared, we utilize publicly available deep J and K-band observations of GOODS-S (PI: C. Cesarsky) using the ISAAC camera on the Very Large Telescope (VLT). The sensitivities vary across the field depending on the effective integration time and seeing FWHM. Average 5σ magnitude limits are J$\simeq$26.4 and $K_s \simeq 25.7$. Toward GOODS-N, we make use of a new Subaru K-band mosaic of the field (Bundy et al., 2008) using the MOIRCS camera (Ichikawa et al., 2006). The specifics of the observations are described in detail in Bundy et al. (2008). The 5σ limiting magnitude varies between K_s=23.9 and 24.1 across the mosaic.

Deep *Spitzer* imaging is available toward both GOODS fields with the Infrared Array Camera (IRAC) as part of the "Super Deep" Legacy program (Dickinson et al. *in prep*, Chary et al. *in prep*). Details of the observations have been described in detail elsewhere (Eyles et al., 2005; Yan et al., 2005; Stark et al., 2007a) so we do

not discuss them further here. The 3σ limiting magnitudes of the IRAC imaging are 26.5 at 3.6μm and 26.1 at 4.5μm (using $2\farcs4$ diameter apertures).

In a later section (§5.3.3), we will revisit the sensitivity limits of the GOODS datasets, utilizing completeness simulations to determine magnitude limits for our survey.

5.2.2 Optical Photometry

ACS photometry was obtained from the GOODS team r1.1 catalog [1]. The photometric zeropoints adopted in the catalog are 25.653, 26.493, 25.641, and 24.843 for the B_{435}-band, v_{606}-band, i'_{775} band, and z'_{850}-band, respectively. We have corrected for the small amount of foreground Galactic extinction using the *COBE*/DIRBE & *IRAS*/ISSA dust maps of Schlegel et al. (1998); for the GOODS-S field, selective extinction is given by $\mathrm{E}(B-V) = 0.008$ mag. Colors are computed using magnitudes measured $0\farcs50$-diameter apertures. As detailed further in §5.3.1, total magnitudes are computed using a combination of the aperture colors and MAG_AUTO SExtractor parameter.

5.2.3 Near- and mid-infared Photometry

Near-infrared fluxes were computed on each of the sources in the GOODS r1.1 catalog. We utilized $1''$-diameter apertures centered on the source positions in the *ACS* images. The seeing varied across the GOODS-S and GOODS-N fields as different tiles were taken over many nights, so we determined separate aperture corrections from unresolved sources for each tile. For the J- and K_s-band ISAAC images the seeing is typically good (FWHM $= 0\farcs4 - 0\farcs5$), and the aperture corrections are $\approx 0.3 - 0.5$ mag, determined from bright but unsaturated isolated stars measured in $6''$-diameter apertures. Likewise, the MOIRCS GOODS-N K_s-band seeing was fairly constant at FWHM=$0\farcs5$ and the aperture corrections are typically 0.3-0.7 mag.

For the GOODS IRAC images, magnitudes are measured in relatively small aper-

[1] available from `http://archive.stsci.edu/prepds/goods`

tures ($\approx 1.5 \times$ FWHM) to maximize the signal-to-noise ratio (S/N). We applied aperture corrections to compensate for the flux falling outside the aperture: these were ≈ 0.7 mag for the IRAC 3.6 and 4.5 μm data, as determined from bright but unsaturated point sources in the images using large apertures. The PSF of IRAC leads to frequent blending with nearby sources, so care must be taken to ensure that the photometry is robust. We discuss our strategy for dealing with this in §5.4.

5.3 Selection of High-Redshift Galaxies

The goal of this section is to compile a robust sample of dropouts at $z \simeq 4$, 5, and 6. In §5.3.1, we identify B, V, and i'-dropouts using standard selection criteria (e.g., Giavalisco et al. 2004b; Beckwith et al. 2006; Bouwens et al. 2007). We excise low-redshift and stellar contaminants from these samples using a combination of photometric, spectroscopic, and morphological techniques (§5.3.2). In §5.3.3, we compute the completeness limits of our data and determine the surface density of our samples. Finally, we briefly discuss the evolution of the rest-UV slopes of the dropouts in §5.3.4.

5.3.1 Dropout Selection

Galaxies at $z \simeq 4$, 5, and 6 are selected via the presence of the Lyman-break as it is redshifted through the B_{435}, V_{606}, and i'_{775} bandpasses, respectively. We detail our color-selection and S/N limit criteria for selecting dropouts below.

Conditions for selection as B_{435}-drop :

$$B_{435} - V_{606} > (1.1 + V_{606} - z_{850}) \quad \text{(A-1)}$$

$$B_{435} - V_{606} > 1.1 \quad \text{(A-2)}$$

$$V_{606} - z_{850} < 1.6 \quad \text{(A-3)}$$

$$S/N(V_{606}) > 5 \quad \text{(A-4)}$$

$$S/N(i_{775}) > 3 \quad \text{(A-5)}$$

Conditions for selection as V_{606}-drop:

$$\begin{aligned} V_{606} - i_{775} &> 1.47 + 0.89(i_{775} - z_{850}) \\ &\text{or } 2 \end{aligned} \tag{A-6}$$

$$V_{606} - i_{775} > 1.2 \tag{A-7}$$

$$i_{775} - z_{850} < 1.3 \tag{A-8}$$

$$S/N(z_{850}) > 5 \tag{A-9}$$

$$S/N(B_{435}) < 2 \tag{A-10}$$

Conditions for selection as i'_{775}-drop:

$$i_{775} - z_{850} > 1.3 \tag{A-11}$$

$$S/N(z_{850}) > 5 \tag{A-12}$$

$$S/N(V_{606}) < 2 \tag{A-13}$$

In order to utilize these dropout criteria, we must compute accurate colors and total magnitudes for each source in the GOODS catalogs. The colors are computed using the aperture magnitudes discussed in §5.2.2. We adopt the i'_{775}-band MAG_AUTO magnitude as the total i'_{775}-band magnitude for the B_{435}-drops. Total magnitudes are subsequently computed in the B_{435}, V_{606}, and z_{850}-bands using the $B_{435} - i'_{775}$, $V_{606} - i'_{775}$, $z'_{850} - i'_{775}$ colors measured using aperture magnitudes. Similarly, total magnitudes are computed for the V_{606} and i'_{775}-drops taking the z_{850}-band MAG_AUTO magnitude and $B_{435} - z'_{850}$, $V_{606} - z'_{850}$, $i'_{775} - z'_{850}$ colors.

We examine each source in the dropout catalogs, removing diffraction spikes from bright stars, image artifacts, and spurious features (primarily along the edges of the GOODS mosaic), leaving a sample of 2819 B-drops, 615 V-drops, and 166 i'-drops. A histogram of the measured optical magnitudes for the three dropout samples is presented in Figure 5.1. In the next section, we seek to further refine these samples, identifying and removing stellar and low-redshift interlopers.

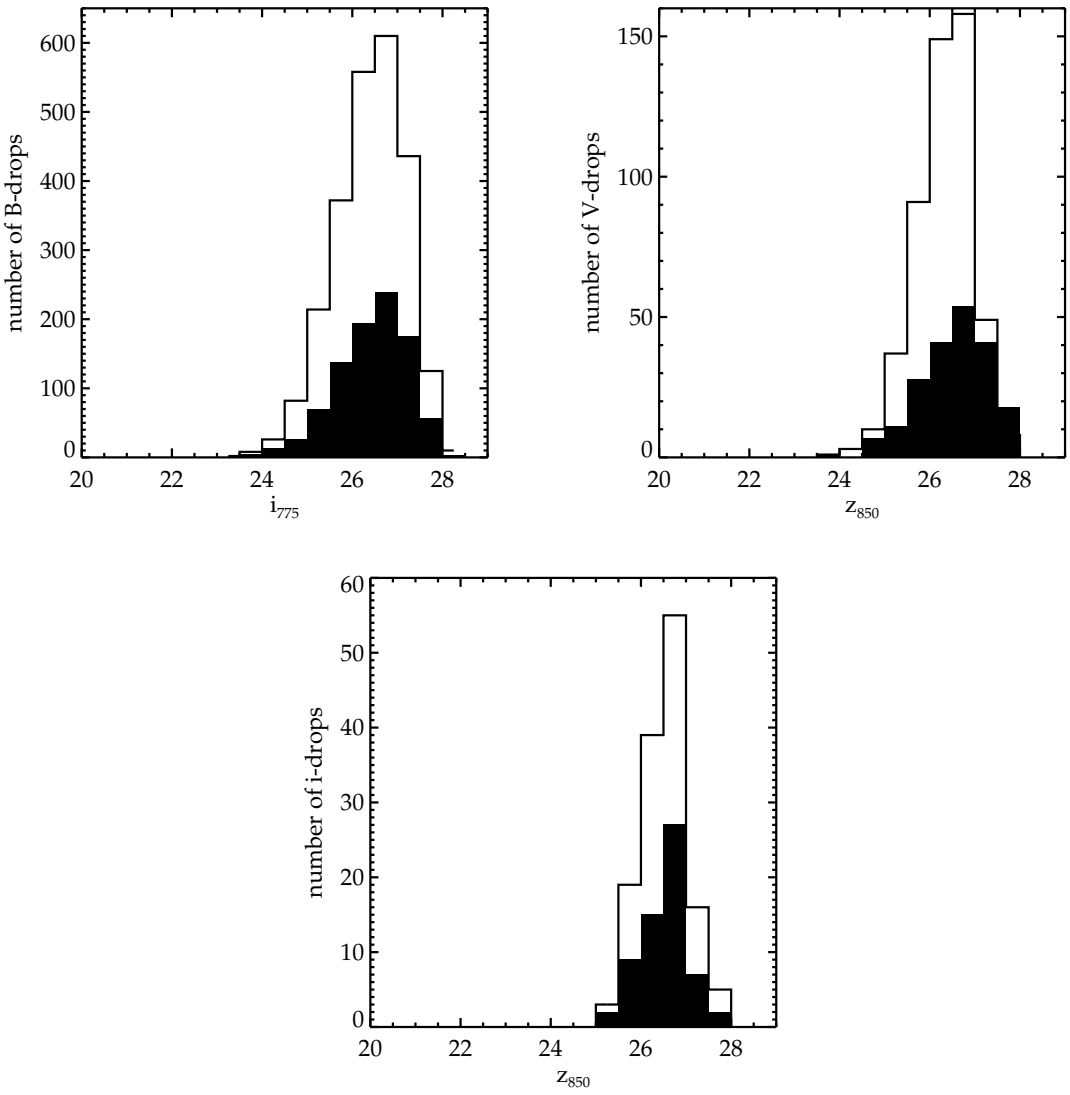

Figure 5.1 Histogram of z_{850} magnitudes for 2819 B-drops (upper left), 615 V-drops (upper right), and 166 i'-drops (bottom) in GOODS-S and GOODS-N. In each panel, the open histogram corresponds to the total sample of dropouts while the filled histogram corresponds to only those sources that are isolated in Spitzer (see §5.4.1).

5.3.2 Removal of Stellar and Low-z Contaminants

The Lyman-break selection is well known to include a variety of interlopers in addition to the desired high-redshift galaxies. Standard contaminants include cool stars and dusty or old galaxies at lower-redshifts (e.g., Stanway et al. 2004; Beckwith et al. 2006; Bouwens et al. 2006). We first seek to morphologically identify and excise stellar interlopers from the dropout catalogs. To assess the fraction of dropouts at low redshift, we first mine the existing spectroscopic surveys for known redshifts of our sample. We then proceed to compute photometric redshifts for all the remaining dropouts without spectroscopic redshifts and compute the uncertainty in the photometric redshifts.

We identify stellar contaminants by their morphology, removing all bright ($z_{850} < 26.0$) sources with SExtractor stellarity parameter greater than 0.80. We found that this value (very similar to those used in Bouwens et al.) was optimal in distinguishing between spectroscopically confirmed galaxies and stars. Applying this criteria removes 51 B-drops (20 in GOODS-S, 31 in GOODS-N), 23 V-drops (12 in GOODS-S, 11 in GOODS-N), and 8 i'-drops (3 in GOODS-S, 5 in GOODS-N) from our sample. Faintward of this limit, the S/N of the GOODS data is too low to reliably identify stars by their stellarity index. Following the approach taken in Bouwens et al. (2006), we estimate the number of faint stellar contaminants that remain in the GOODS dropout catalog by examining dropout samples in the Hubble Ultra Deep Field (HUDF); the exquisite data quality of the HUDF enables point sources to be identified with sufficient S/N for sources that would be located at the sensitivity limits of the GOODS data. Using the same dropout criteria as in GOODS, we select B, V, and i'-drops in the HUDF using publicly-available z_{850}-band source catalogs (Coe et al., 2006). We find that the fraction of dropouts with stellarity indices above 0.8 over the magnitude interval $26 < z_{850} < 28$ is very low for the B-drops (0/171), V-drops (0/35), and i'-drops (0/21). These results support the findings of previous studies (e.g. Bouwens et al. 2006; Bouwens et al. 2007) that stellar contaminants are most prevalent at relatively bright magnitudes (e.g., $z_{850} < 26$).

Dropouts in the GOODS fields have been observed spectroscopically with VLT/FORS2 (Vanzella et al., 2002, 2005, 2008) and Keck/DEIMOS (Stanway, 2004). The results of the VLT/FORS2 survey are made public in a large database of 1165 total spectroscopic redshifts in GOODS-S (Vanzella et al., 2008). We search the database (version 3.0) for each of the dropouts using an 0.5-arcsecond matching diameter. Thirty-seven B-drops have spectroscopic redshifts ranging between z=3.19 and 5.09 with a median redshift of 3.7. We remove the one B-drop with a low-redshift (z=1.54) identification from our sample. Twenty-four V-drops have spectroscopic redshifts at $z > 4$ with a median redshift of 4.81. Finally, 20 i'-drops have spectroscopic redshifts at $z > 5$, while one i'-drop (which we subsequently remove) has a low-z identification (z=1.32).

Photometric redshifts and their associated probabilities have been determined for each remaining dropout by fitting the observed SEDs against template galaxy SEDs of various ages, spectral types, and redshifts using the Bayesian Photometric Redshift (BPZ) software (Benítez, 2000). We fit the observed optical through near-IR SED against templates from Coleman et al. (1980) and the starburst templates from Kinney et al. (1996). BPZ outputs both a Bayesian and maximum-likelihood photometric redshift (and associated probability). We compute the root mean square difference in the photometric redshift estimates for those objects with known redshifts from FORS2. Using the maximum-likelihood photometric redshifts, the rms difference is 0.14, 0.39, and 0.14 for the B-drops, V-drops, and i'-drops, respectively, excluding one spectroscopically-confirmed source with an anomalously low photometric redshift. We find that the rms uncertainty in our BPZ photometric redshifts is similar to that from the GOODS MUSIC catalog (Grazian et al., 2006) for the subset of dropouts with spectroscopic redshifts.

We remove all sources with best-fit photometric solutions at low-redshift. Adopting a lower cutoff of z_{phot}=3, 4, and 5 for the B, V, and i'-drops, respectively, the BPZ photometric redshifts require the removal of 258, 47, and 14 (10, 8, and 9%) of the B, V, and i'-drop candidates from the catalogs, leaving a sample of 2443, 506, and 137 B, V, and i'-dropouts across both GOODS fields. In general, the excised sources are either marginally detected in the optical or very red in their $z_{850} - K$ colors, as

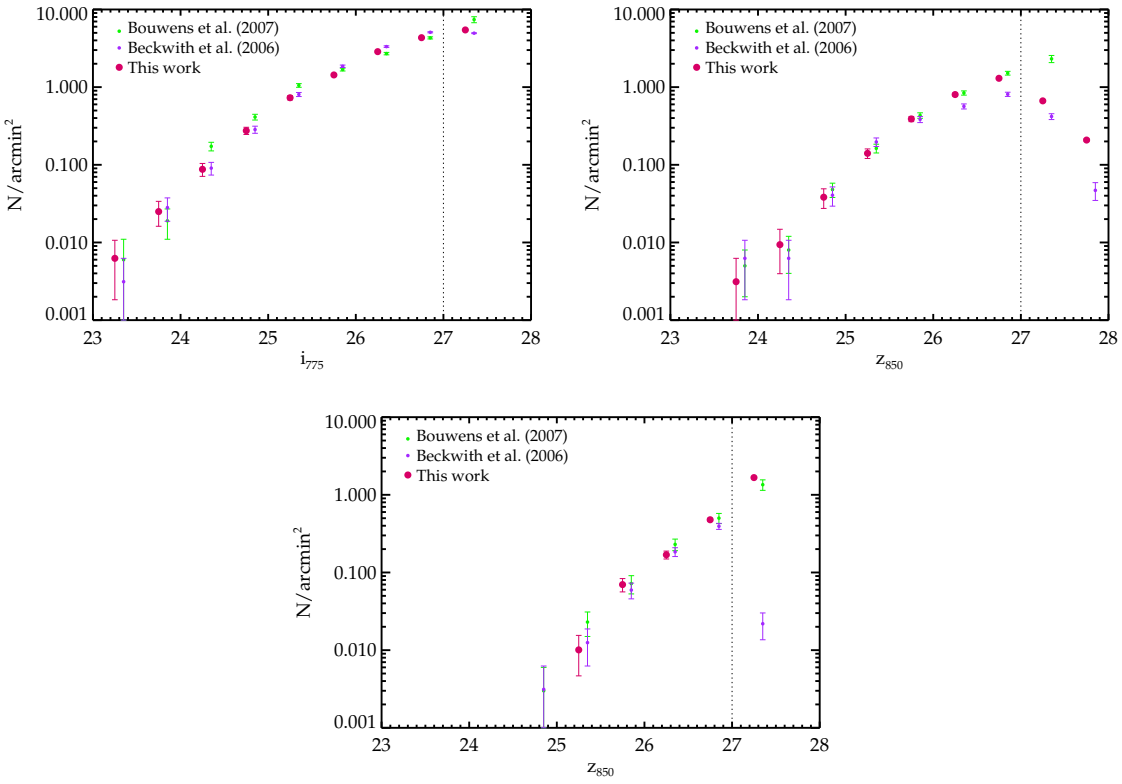

Figure 5.2 Surface densities of B-dropouts (upper left), V-dropouts (upper right), and i'-dropouts (bottom) samples. Stars, artifacts, and low-z galaxies have been removed from the initial sample as described in §5.3.2. We place the remaining sample in magnitude bins spanning 0.5 mags and adjust the measured densities for incompleteness (§5.3.3). Our samples are sufficiently complete brightward of 27th magnitude (vertical dotted lines) to enable reliable density measurements. The resulting surface densities are in excellent agreement with previous measurements.

would be expected for low-redshift sources which satisfy the dropout criteria. The median and standard deviation redshifts of the resulting B, V, and i'-drop samples are z_{phot}=3.96±0.30, 4.75±0.24, and 6.01±0.28 respectively.

5.3.3 Surface Densities and Effective Volume

The GOODS datasets allow sources to be detected down to an AB magnitude of 28.0 in i_{775} and z_{850} (our detection filters); however, as is apparent in Figure 5.1, the completeness begins to decline brightward of this limit. Hence, to compute the correct density of dropouts, we must account for this variation in completeness with

apparent magnitude.

To do this, we define a function $p(m, z)$ that represents the probability that a galaxy with apparent magnitude m and redshift z is recovered in our dataset. We compute this function for each of the three dropout samples by putting thousands of fake galaxies into the GOODS images and recreating a photometric catalog for the new image using the selection parameters described above. The apparent magnitudes of the fake galaxies span $i_{775} = 21 - 28$ (B-drops), $z'_{850} = 22 - 27.5$ (V-drops), $z'_{850} = 23 - 28$ (i'-drops) and their redshifts span the interval $3.0< z <4.9$ for the B-drops, $4.0\leq z \leq5.9$ for the V-drops, and $5.0< z <7.6$ for the i'-drops in steps of Δz=0.1. The sizes of the fake galaxies are chosen to be consistent with distribution of half-light radii derived for $z \simeq 4 - 6$ galaxies in Bouwens et al. (2004). The colors of the fake galaxies depend on the galaxy redshift and spectral energy distribution (SED). In order to compute these colors, we use the SED of a CB07 model with constant star formation history, an age of 100 Myr, and no dust as the intrinsic rest-frame SED of the fake galaxies. Allowing for a younger age or a selective extinction of E(B-V)=0.1 in the fake galaxies' SEDs alters the completeness by roughly 5%, which would not significantly change any of our results. The colors are computed at each redshift after applying the appropriate IGM absorption (e.g. Madau 1995) to the SED. The probability function, $p(m, z)$ is then given by the fraction of fake galaxies with apparent magnitude, m, and redshift, z, that satisfy the dropout color selection criteria defined in §5.2.4.

We next determine the volume observed as a function of apparent magnitude for each of the dropout samples following the approach of **?** using

$$V_{\rm eff}(m) = \int dz\, p(m, z)\, \frac{dV}{dz} \tag{A-14}$$

where $p(m, z)$ is the probability of detecting a galaxy at redshift z and apparent magnitude m, and $dz\, \frac{dV}{dz}$ is the comoving volume per unit solid angle in a slice dz over the redshift interval $3.0< z <4.9$ for the B-drops, $4.0\leq z \leq5.9$ for the V-drops, and $5.0< z <7.6$ for the i'-drops.

The effective volumes are subsequently computed as a function of apparent magnitude for the dropout samples following equation 15. In general, for the dropout samples in a single GOODS field, the effective volumes drop from 4-5$\times 10^5$ Mpc^3 at bright magnitudes (m_{AB}=23.5) to 0.6-2$\times$ 10^5 Mpc^3 at fainter magnitudes (m_{AB}=27). In Figure 5.2, we show the derived surface densities of our dropouts, corrected using the magnitude-dependent completeness $p(m)$ derived in equation above. The measured values are in excellent agreement (generally to within 1σ) with previous measurements (Bouwens et al., 2007) at AB magnitudes brighter than 27. Faintward of this limit, the completeness in the GOODS data is too low to enable reliable density measurements.

5.3.4 The Evolving Rest-Frame UV Slopes of High Redshift Galaxies

One of the most striking features of the i'-drop population is their rest-frame UV slopes, β, which are considerably bluer than those of star-forming galaxies studied at $z \simeq 3$ (Shapley et al., 2001). This discovery has led many to suggest that galaxies at $z \simeq 6$ are much less dusty than those at $z \simeq 3$ (Stanway et al., 2005; Bouwens et al., 2006; Bouwens et al., 2007). This finding would not be surprising if those objects at $z \simeq 3$ have been undergoing large-scale star formation for considerably longer than those at $z \simeq 6$. But care must taken to ensure that this redshift trend is not due to the fact that the HUDF photometric i'-drop samples actually probe fainter absolute magnitudes than the $z \simeq 3$ spectroscopic sample studied by Shapley et al. (2001). Indeed, if low luminosity galaxies are intrinsically less dusty than luminous systems (Reddy et al., 2006), then the blue colors of the i'-drops may partially result from the differing luminosity distributions of the samples. Disentangling these two effects is crucial for a reliable measurement of the evolving dust content of galaxies at high redshift. We thus consider the rest-UV slopes of LBGs at $z \gtrsim 4$ in some detail below.

As has been discussed in detail elsewhere (e.g., Bouwens et al. 2006), computation of the rest-UV slopes from broadband data at $z \gtrsim 4$ is complicated by a number of

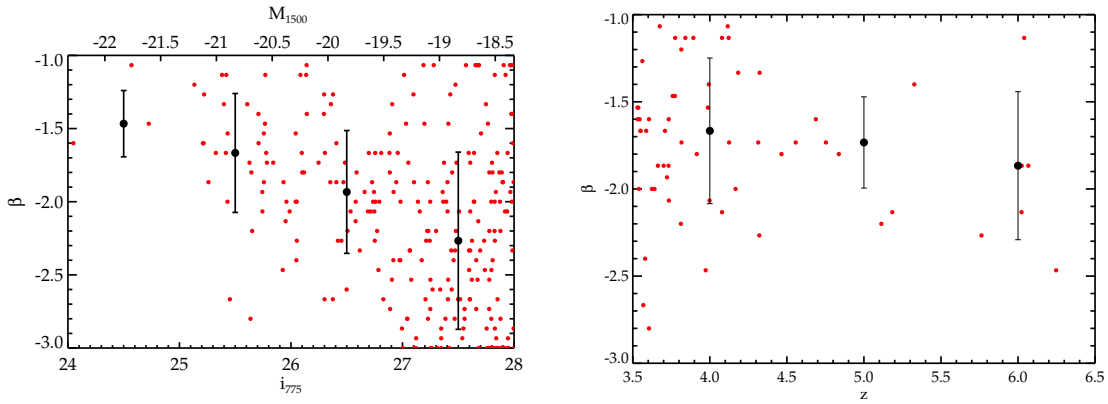

Figure 5.3 *Left* Relationship between rest-UV slope and i'_{775} magnitude for a sample of high S/N B-drops in the HUDF. Small red circles circles correspond to measurements of individual galaxies. Black circles show the median slope in each magnitude bin while the error bar gives the standard deviation. The data show that B-drops that are brighter in i'_{775} are on average redder in the rest-UV. *Right:* The evolution of rest-frame UV slope with redshift for dropouts brighter than $M_{1500} = -19.8$. The absolute magnitude limit was matched to the z_{850}-band magnitude limit of the i'-drop sample, ensuring that each dropout sample is complete. The data indicate that the rest UV colors do not vary as strongly with redshift as they do with magnitude.

factors, including the Lyman-α forest, strong Lyman- α emission, redshift errors, and of course, photometric uncertainty. Following previous efforts, we seek to minimize these errors by only using filters that lie redward of 1216 Å rest-frame ($i'_{775} - z'_{850}$ for the B-drops, $z'_{850} - J_{110}$ for the V-drops, and $J_{110} - H_{160}$ for the i'-drops) and only considering sources detected with high S/N. We deal with the latter requirement by making use of the dropouts in the HUDF, as these sources are detected with high S/N in the entire magnitude range probed in our GOODS samples. To compute colors of HUDF dropouts, we utilize the catalog presented in Coe et al. (2006) containing matched aperture optical and near-infrared photometry and photometric redshifts for each object selected in the original Beckwith et al. (2003) catalogs.

For each dropout in the HUDF (selected using the same criteria we used for our GOODS sample), we find the rest-frame UV slope, β, which produces colors closest to those observed, assuming the redshift is given by the best-fit photometric redshift. In Figure 5.3a, we present the inferred rest-UV slopes for the B-drops. While the data show significant scatter, the average rest-UV slope of the brightest sources ($\beta \simeq -1.5$)

is significantly redder than those at the magnitude limit of our survey ($\beta \simeq -2.3$), indicating that the brightest galaxies are, on average, significantly dustier than fainter systems.

The strong magnitude dependence of the rest-UV slopes requires that we adopt a fixed luminosity limit when examining the evolving rest-UV slopes of high redshift galaxies. In Figure 5.3b, we display the redshift evolution of the rest-UV slopes, limiting our analysis to dropouts with absolute magnitudes brighter than $M_{1500} < -19.8$, the absolute magnitude of our i'-drop sample. The data indicate that the rest-UV slopes change slightly over this redshift range, evolving from $\beta \simeq -1.7$ at $z \simeq 4$ to $\beta \simeq -1.9$ at $z \simeq 6$[2], indicating that the i'-drops are marginally bluer than the B-drops (although the statistics are admittedly poor at the high redshift end). Adopting the IRX-β relationship (Meurer et al., 1999), this implies that the rest-UV extinction, A_{1600}, varies by at most $\simeq 0.4$ magnitudes between $z \simeq 4$ and 6. Adopting a Calzetti dust law, this corresponds to median selective extinction of $E(B-V)=$ 0.10, 0.09, and 0.07 for the B, V, and i'-drops.

While the data do support previous claims that higher redshift galaxies are less dusty than those at slightly lower redshift, the differences are not large. In fact, our results indicate that at the high redshifts considered in this study, the luminosity of the present star formation episode plays a more significant role in determining the average dust content than does the galaxy's redshift. We will discuss the implications of this result in more detail in §5.6.

[2]It may seem curious that the median rest-UV slope of our i'-drop sample is redder than those quoted in previous studies (e.g., Stanway et al. 2005; Bouwens et al. 2006); however, considering the magnitude dependence of the rest-UV slopes (Figure 5.3a), it is clear that this difference arises merely because we have limited our analysis to much brighter sources. Indeed, if we adopt a fainter magnitude limit (e.g., $H_{160} = 27.7$ as in Bouwens et al. (2006), we find that the average rest-UV slope is $\beta = -2.0$, consistent with previous works.

5.4 Mid-infrared Properties of Dropouts

5.4.1 Construction of Spitzer-Isolated Subsample

Mid-infrared photometry is the crucial component for estimating the stellar populations of $z \gtrsim 4$ galaxies. However the low spatial resolution of *Spitzer* results in frequent blending between nearby sources, making accurate photometry of individual objects difficult. To ensure that objects in our sample were not contaminated by neighboring bright foreground sources, we examined each dropout by eye and flagged sources that are hopelessly confused with flux from bright, nearby sources.

Following Stark et al. (2007a), we only apply population synthesis models to those objects which are unconfused in the IRAC images, which we define as having no IRAC-bright sources within a $\simeq 2.5$ arcsecond radius around the position of interest. We find that $\simeq 35\%$ of the dropouts in our catalogs are sufficiently isolated to allow accurate photometry. In Figure 5.1, we show the distribution of i'_{775} and z_{850} magnitudes of the dropouts in our "Spitzer-isolated" subsample compared to the full dropout samples. The magnitude distribution of this subsample is very similar to that of the parent distribution albeit with a slightly greater proportion of UV bright sources. We correct for the small bias this introduces into the stellar mass functions in §5.7.

In Figure 5.4, we present the relationship between the IRAC 3.6μm magnitude and i_{775} or z_{850} magnitude for each of our dropout samples, foreshadowing the relationship between the assembled stellar mass and the current star formation rate (uncorrected for extinction). It is not necessarily obvious that the ongoing star formation in any galaxy should bear any relation to the past star formation history, yet immediately apparent is a correlation between the average optical and mid-infrared flux: sources that are brighter in the ACS bandpasses are, on average, brighter in IRAC. Also noticeable is that the median IRAC flux for a given i_{775} or z_{850} flux does not change significantly over the redshift range probed by the three dropout samples. We discuss the implications of these trends in more detail in §5.6.

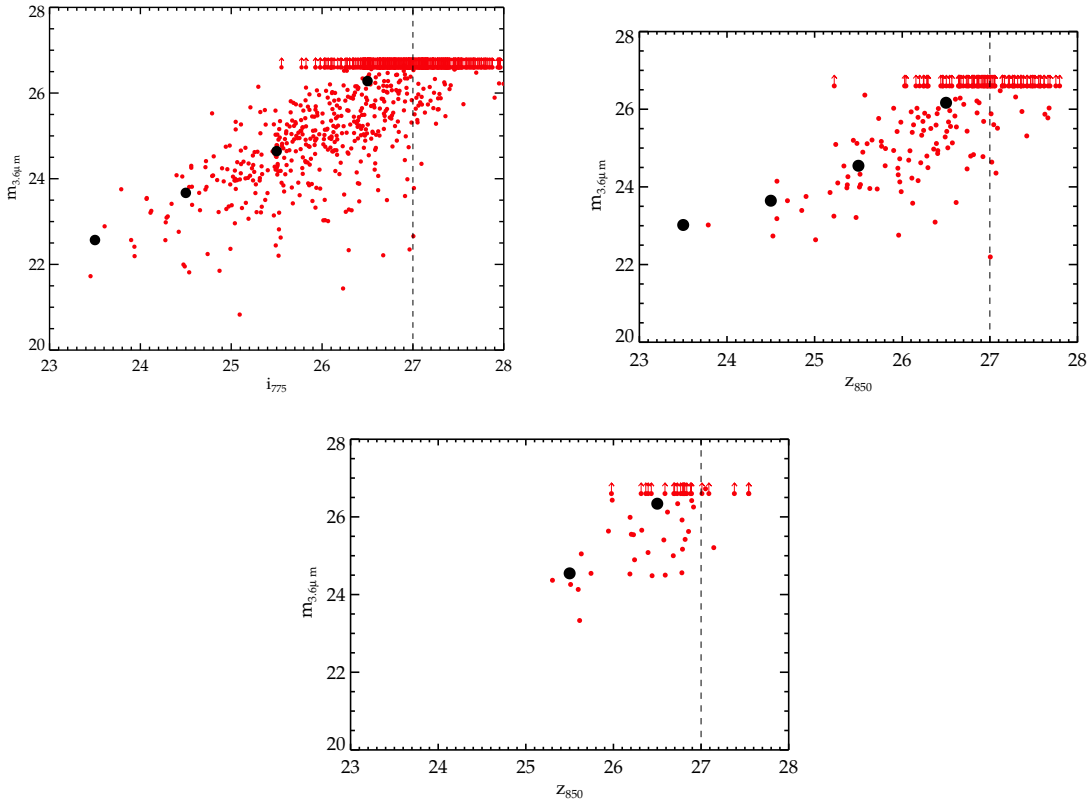

Figure 5.4 Mid-infrared vs. optical flux for the B (upper left panel), V (upper right panel), and i'-drops (bottom panel). Individual galaxies are shown as small red circles; the large black circles correspond to the median 3.6μm magnitude in bins of i_{775} or z_{850} magnitude. The dashed vertical lines correspond to our adopted completeness limit for each dropout sample. Those objects that are brighter in the optical are on average brighter in the mid-infrared. The relationship between mid-infrared and optical flux is very similar for each of the three different redshift ranges considered.

5.4.2 MIPS Detections

We have put considerable effort into removing low-redshift contaminants from our dataset. However, as is evident from Figure 5.4, the dropout samples still contain red objects, some of which are among the brightest sources detected in IRAC. Considering the fact that very massive sources (with bright IRAC fluxes) are likely much more common at $z \simeq 2$ than at $z \gtrsim 4$, it is clear that these sources require more scrutiny before proceeding.

We can gain some insight into the likely redshifts of this population from 24 μm imaging with the Multiband Imaging Photometer for Spitzer (MIPS) camera (Dickinson et al. in prep.; Chary et al. in prep.). At $z \simeq 2$, the MIPS imaging passband probes the bright rest-frame 7.7 μm feature from polycyclic aromatic hydrocarbons (PAHs). As a result, dusty star-forming galaxies at $z \simeq 2$ are commonly detected with MIPS (e.g., Reddy et al. 2006). Such PAH features are much less likely to be detected in sources over the redshift range our dropouts sample ($4 \lesssim z \lesssim 6$); hence if any of our sources are detected with MIPS, it very well may indicate that they lie at $z \simeq 2$.

In order to determine what fraction of our catalog is detected at 24μm, we visually examine the MIPS data of each dropout in the *Spitzer* isolated sample. The number of dropouts with MIPS detections is small (12/800 B-drops, 2/186 V-drops) but not negligible. As expected, each of the sources detected with MIPS is quite red ($z'_{850} - m_{3.6} \gtrsim 2$) in addition to being bright in the IRAC bandpasses.

We consider these sources as prime low redshift candidates; however, it is possible that some of these lie at $z \gtrsim 4$. Cross-correlating the 24μm-detected subset with our spectroscopic sample, we find that one of the MIPS-detected V-drops has a spectroscopically confirmed redshift of z=4.76. Since there are few strong PAH features that fall into the 24 μm filter at this redshift, we propose that the 24 μm emission most likely comes from a dusty AGN, a conclusion consistent with the point-like morphology in the observed optical-frame. Importantly, this establishes that not all 24μm-detected dropouts are foreground objects. The MIPS-detected subsample thus

places an upper limit (1.5% for the B-drops and 0.3% for the V-drops) on the number of dusty low-z interlopers remaining in our samples. In subsequent sections, we will derive the evolving stellar populations of our dropout sample both with and without the 24μm detected sources.

5.5 Derivation of Physical Properties

We infer stellar masses for the dropout sample by fitting the latest Charlot & Bruzual (2007, CB07 hereafter) stellar population synthesis models to the observed SEDs. These models include an improved treatment of the thermally pulsing asymptotic giant branch (TP-AGB) phase of stellar evolution, utilizing the Marigo & Girardi (2007) evolutionary tracks and the Westera et al. (2002) stellar library. In this section, we first describe the CB07 models and detail the fitting process that we use to infer the stellar masses and ages of the galaxies. We examine the effects of the TP-AGB stars on the inferred masses and ages of the dropouts by comparing the CB07 output to that from the Bruzual & Charlot (2003) population synthesis models (§5.5.2). We then comment on the uncertainties in the inferred properties of objects in our samples and stack the infrared photometry of the faintest sources to achieve a more reliable estimate of the average stellar populations of this subset.

5.5.1 CB07 Models

The CB07 models utilize 220 age steps from 10^5 to 2×10^{10} yr, approximately logarithmically spaced. For each source, we do not include age steps in excess of the age of the universe at $z \simeq 4,\ 5,$ and 6 for the B, V, and i'-drops, respectively. We also exclude age steps below the dynamical timescale for LBGs at high-redshift, which we take to be $\simeq$ 20 Myr adopting measurements of the mean half-light radii (Bouwens et al., 2004) and typical velocity dispersions (Erb et al., 2006b) of LBGs at high-redshift.

The CB07 models only include templates with the Chabrier (2003) and Salpeter (1955) initial mass functions (IMF). For consistency with previous efforts, we choose to focus on the Salpeter IMF in our analysis. The effects of utilizing a Chabrier IMF

have been discussed in detail elsewhere, including our previous work (Eyles et al., 2005; Stark et al., 2007a).

We use the high resolution (FWHM 3 Å) and 1 Å pixels evenly-spaced over the wavelength range of 3300 Å to 9500 Å (unevenly spaced outside this range). From the full range of metallicities offered by the code, we considered both solar and 0.2 $Z_\odot$ models. From several star formation histories available, we utilize the constant star formation history and exponentially decaying (τ) SFR models with e-folding decay timescales τ=100 and 300, Myr. We also utilize a model with a linearly increasing star formation rate, with a slope set to match the observed brightening in the UV LF between $z \simeq 6$ and 4 (0.74 mag at 1500 Å over $\simeq$ 620 Myr). The CB07 spectra are normalized to an SFR of $1\,M_\odot\,yr^{-1}$ for the continuous star formation model. For the exponential decay models, the galaxy mass is normalized to $M \longrightarrow 1\ M_\odot$ as $t \longrightarrow \infty$.

We also consider the effects of dust on the integrated SEDs, adopting the reddening model of Calzetti (1997)[3]. At each age step, the model SED was convolved with each of five different reddening curves corresponding to selective extinctions of E(B-V)=0.0, 0.03, 0.1, 0.3, 1.0.

For each of the galaxies in our sample, the model SEDs were interpolated onto each of the filters' wavelength scales after correcting the latter to the rest-frame wavelengths using the redshift appropriate for each object. In order to assess the uncertainty in the inferred parameters due to redshift error, we perform the SED fitting at three redshifts: $z = z_{\rm phot} - 0.15, z_{\rm phot}, z_{\rm phot}+0.15$. To account for Ly$\alpha$ forest absorption, we decrement the flux shortward of 1216 Å (rest-frame) by a factor of $\exp[-(1+z)^{3.46}]$ (Madau, 1995). We further assume the flux shortward of 912 Å (rest-frame) is zero due to Lyman-limit absorption.

The resulting template SEDs are convolved with each of the filter transmission curves to produce optical, near-IR, and mid-IR magnitudes for each model. Com-

[3]The Calzetti reddening is an empirical law given in terms of color excess E(B-V) = 0.44 E(B-V)$E_{\rm gas}$(B-V) with the wavelength dependence of the reddening expressed as:
$k(\lambda) = 2.656(-2.156 + 1.509\lambda^{-1} - 0.198\lambda^{-2} + 0.011\lambda^{-3}) + 4.88$ for $0.12\mu{\rm m} \leq \lambda \leq 0.63\mu{\rm m}$, and
$k(\lambda) = [(1.86 - 0.48\lambda^{-1})/\lambda - 0.1)]\lambda + 1.73$ for $0.63\mu{\rm m} \leq \lambda \leq 1.0\mu{\rm m}$ and the flux attenuation is given by:
$F_{\rm obs}(\lambda) = F_0(\lambda)10^{-0.4E(B-V)}k(\lambda)$.

paring the observed magnitudes and their associated errors[4] to the derived model magnitudes, we compute a reduced χ^2 value for each set of parameters (age, E(B-V), normalization). For individual sources, non-detections were set to the 1σ detection limit and the flux error was set at 100% (we also consider the average properties of this faint sample via a stacking analysis in §5.5.2)

The fitting routine returned the parameters for each model which were the best-fit to the broadband photometry (i.e., minimized the reduced χ^2). In addition to selecting those parameters which provide the best-fit, we also compute the range of ages, normalizations, and $E(B-V)$ values that result in an SED with reduced χ^2 values within $\Delta\chi^2$=1 of the minimum value; we take these as the 1-σ systemic uncertainties associated with each parameter. This normalization was then converted to the appropriate units and subsequently used to calculate the corresponding best-fit stellar and total mass (and the corresponding 1σ errors). The conversion factor between normalization and mass for a given age and star formation history is available in the '4color' files in the CB07 population synthesis output.

5.5.2 The Effect of TP-AGB stars on Inferred Properties at $z \gtrsim 4$

The TP-AGB stars contribute significantly to the integrated rest-frame near-infrared light. Maraston (2005) has shown that if the contribution from this phase of evolution is underestimated for galaxies at $z \simeq 2$, the stellar masses and ages inferred from models are typically overestimated. Note that this is not necessarily the case at $z \gtrsim 4$, since at these redshifts the first two IRAC channels only probe as far redward as the rest-frame optical, where the contribution from TP-AGB stars is less dominant than the rest-frame near-infrared. In this section, we investigate the effect of the TP-AGB stars on the inferred properties of the B, V, and i'-drops by comparing the model output of CB07 and BC03 models.

In Figure 5.5a, the stellar masses of the B, V, and i'-drop samples inferred from

[4]We increase the observed magnitude errors to 0.1 when they are less than this value to account for calibration uncertainties.

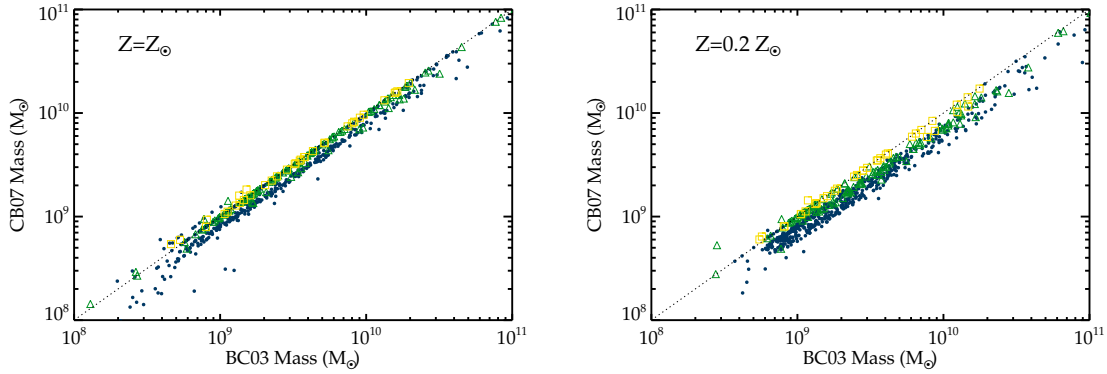

Figure 5.5 Comparison of the model output from Bruzual & Charlot (2003) (BC03) and the updated models presented in Bruzual 2007 (CB07) which now include the contribution of TP-AGB stars. The upper panel shows B-drops (blue circles), V-drops (green triangles), and i'-drops (yellow squares) for a solar metallicity τ=100 Myr exponential decay model. The lower panel is identical but with sub-solar (Z=0.2 $Z_{\odot}$) metallicity. The discrepancy between the BC03 and CB07 models increases at lower redshifts and lower metallicities.

BC03 and CB07 are plotted against one other for solar metallicity. In computing the masses and ages, we fix the redshift at the derived photometric redshift and the selective extinction is fixed to $E(B-V)$=0. In spite of the addition of TP-AGB stars, the inferred masses from BC03 and CB07 are in very good agreement. The median stellar mass of the BC03 i'-drops is less than 1% greater than that for the CB07 i'-drops. As expected the effect of TP-AGB is more pronounced at lower redshifts, but nevertheless we still find only a 9% difference between the median of the BC03 and CB07 B-drop samples.

At subsolar metallicity, the contribution from TP-AGB stars is significant ($\gtrsim$20-30% of luminosity for 1.3 Gyr instantaneous burst) in the rest-frame optical (Bruzual, 2007); hence, we expect the CB07 models to return lower masses than the BC03 models for the 0.2 $Z_{\odot}$ templates. Indeed, we find that in each dropout sample the variations between the two models is more extreme than in the solar metallicity case (Figure 5.5b). In the most discrepant case (the B-drops), the median mass inferred from the BC03 models is $\simeq$ 30% greater than that inferred from CB07.

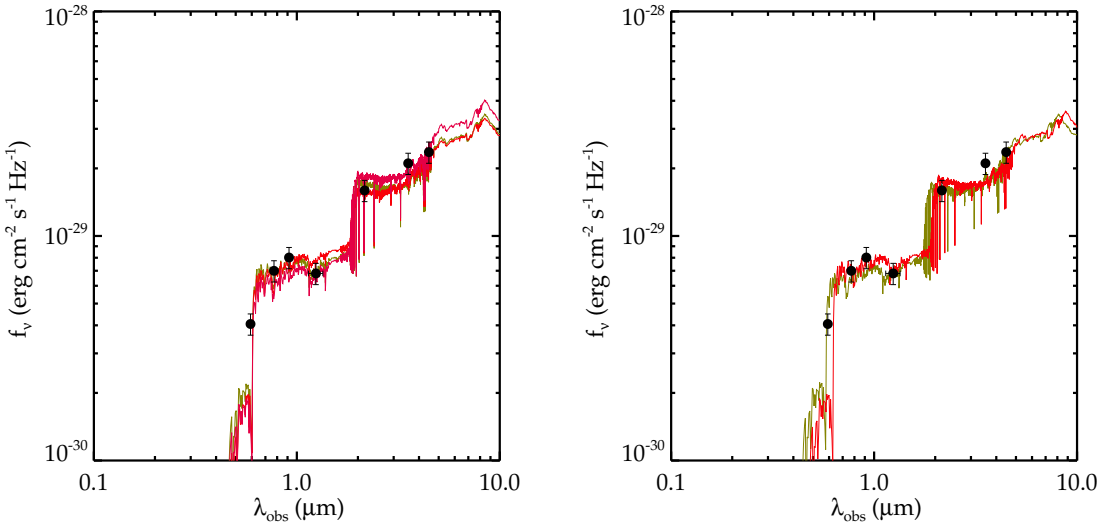

Figure 5.6 SED of a B-drop (typical of bright sources in our sample) compared with a range of CB07 model SEDs that fit the data. *Left:* Adopting a model with an exponentially decaying star formation history with τ=100 Myr, we find the SED is best fit by an age of 286 Myr and a stellar mass of 2.3×10^{10} $M_{\odot}$ with E(B-V)=0 (green curve). Allowing the dust content to vary, we find acceptable fits for stellar masses ranging between 2.0 and 2.8×10^{10} $M_{\odot}$ and ages between 180 and 321 Myr. The model with the lower mass and age is shown as the red curve (and has E(B-V)=0.1); the model that provides the upper bound to the mass and age is shown in purple (and has E(B-V)=0). *Right:* Perturbing the photometric redshift by Δ z=$\pm$0.2, we find that the higher redshift solution (red curve) provides a significantly less accurate fit to the data ($\Delta\chi^2$=2.16) then that provided by the Δz=-0.2 SED (green curve) and the SED derived using the best fit photo-z. The inferred stellar mass in the lower redshift model (2.2×10^{10} $M_{\odot}$) and age (286) are within 5% of those inferred using the photo-z.

5.5.3 Systematic Uncertainties in Derived Properties

Before examining the results in detail, we explore the reliability with which we can determine the stellar populations of $z \gtrsim 4$ galaxies. There is ample discussion of the systematic uncertainties inherent in population synthesis modeling in the literature (e.g., Papovich et al. 2001; Shapley et al. 2001; Yan et al. 2005; Eyles et al. 2005; Shapley et al. 2006). We direct the reader to these works for detailed discussion and focus our discussion below on the uncertainties in the inferred masses, ages, and extinction for our dropout samples.

The SED fitting procedure is most effective at fitting sources that are bright

enough to be detected with sufficiently high S/N ($\simeq$ 10) in the rest-UV and rest-optical. For the bright $z_{850} = 24.3$ dropout presented in Figure 5.6 (typical of bright B-drops in our sample), acceptable fits (within $\Delta\chi^2$=1 of the best-fit) are found for models with ages between 180 and 321 Myr, selective extinctions between E(B-V)=0.0 and 0.1, and stellar masses between 2.0 and 2.8×10^{10} $M_\odot$. If we allow the redshift to vary by $\pm$0.2, the inferred stellar masses and ages change by less than $\simeq$ 5%. Variations in the form of the star formation history do change the absolute values quoted above (see Shapley et al. 2005 for detailed discussion), with best fit stellar masses increasing by 35% and ages reaching 1.4 Gyr for a constant star formation model. Nevertheless the *relative* stellar masses and ages within our samples should be reasonably well determined for equally bright dropouts, unless the star formation history does not vary considerably within the sample.

Extracting robust information from the SEDs of faint dropouts is more difficult than for the bright sources discussed above, largely because the near and mid-infrared datasets are not deep enough to detect very faint objects. Sources that are undetected in IRAC have a median mass of 2×10^8 $M_\odot$ and of 80 Myr for the τ=100 Myr exponential decay model, but their SEDs have acceptable masses and ages spanning a factor of 10. In general, we find that in order to achieve reasonably reliable masses and ages (less than 50% uncertainty) for individual objects, we must limit our sample to those dropouts with $\gtrsim 10^{9.5}$ $M_\odot$.

To get a more robust estimate of the average properties of galaxies less massive than this limit, we perform a stacking analysis on the low S/N infrared data. For each of the three dropout samples, we select all sources that are undetected at 3.6 μm, amounting to 171 B-drops, 29 V-drops, and 17 i'-drops. For each of the dropout samples, the median z_{850}-band magnitude of this faint subset is $\simeq$ 26.7. Following the techniques discussed in Eyles et al. (2007), we stack the IRAC data of each of the undetected dropouts (excluding those with $\lesssim$ 65 ksec of exposure time) using a median combine with no weighting to reduce the effect of contamination by neighboring sources. In total, we stack 171 B-drops, 29 V-drops, and 17 i'-drops. We follow a very similar approach in stacking the near-IR data, limiting our sample to the objects in

Table 5.1. Photometry of Stacked Images

J	K_s	$m_{3.6\mu m}$	$m_{4.5\mu m}$
B-drops ($z \simeq 4$)			
27.03(0.15)	26.51(0.15)	26.79(0.31)	27.29 (0.17)
V-drops ($z \simeq 5$)			
26.7(0.34)	26.55(0.48)	26.89(0.21)	27.71(0.57)
i'-drops ($z \simeq 6$)			
26.69(0.32)	26.43(0.42)	27.23(0.33)	27.64(0.87)

GOODS-S given the slightly deeper images in that field.

The stacking procedure described above resulted in near and mid-IR detections for the B, V, and i'-drops (see Table 5.1 for photometry). The model fit to the composite faint B-drop subsample SED is displayed in Figure 5.7. For the exponential-decay ($\tau = 100$ Myr) model, the best-fit solar metallicity model has a stellar mass of 1.7×10^8 $M_\odot$ (acceptable fits range between 6.2×10^7 and 3.2×10^8 $M_\odot$) and age of 48 Myr. We find very similar best fitting models for the stacked V-drops (1.6×10^8 $M_\odot$ and 17 Myr) and i'-drops (1.4×10^8 $M_\odot$ and 10 Myr). In all cases, the SED is actually slightly better fit by a sub-solar metallicity model ($\Delta\chi^2 \simeq$ 0.4-0.6); however, the returned stellar masses and ages do not change significantly from those obtained using the solar metallicity models (Figure 5.7). Importantly, the inferred masses and ages of the stacked SEDs are consistent with what we would have obtained by merely taking the average of the masses and ages of the individual galaxies included in the stack, suggesting that in spite of the large uncertainties, we can still use the inferred properties of this faint subset and be confident that the average properties are robust.

5.6 New Insight into the History of High Redshift Star Formation

One of the most basic questions in the study of galaxy formation is how galaxies grow over cosmic time. Observations have now revealed vast populations of vigorously assembling galaxies at $z \gtrsim 4$, but it remains unclear how star formation proceeds in

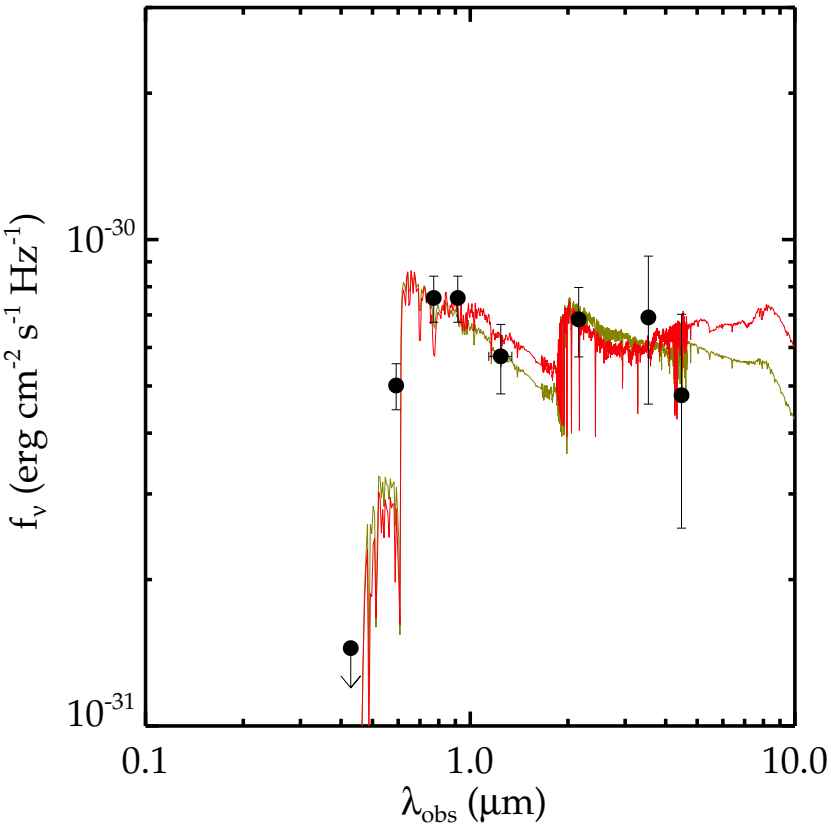

Figure 5.7 Fit to composite SED of faint B-drop stack. The best-fitting exponential decay τ=100 Myr model with solar metallicity (red SED) has a stellar mass of 1.7× 10^8 $M_\odot$ and age of $\simeq$ 50 Myr. Using a subsolar metallicity, Z=0.2$Z_\odot$, template (green SED), we find a marginally better fit to the data ($\Delta\chi^2$= 0.5) with similar inferred masses and ages (2.4×10^8 $M_\odot$ and $\simeq$ 70 Myr).

these objects. On one hand it is possible that $z \gtrsim 4$ LBGs assemble their mass at a constant rate, growing continuously between $z \simeq 6$ and 4. This "steady growth" scenario may be expected if high redshift galaxies are constantly fueled by cold gas which is in turn rapidly converted into stars. Alternatively, galaxies may undergo punctuated star formation episodes lasting only several hundred Myr, such that those LBGs seen at $z \simeq 5$ are not necessarily related to those seen at $z \simeq 4$ or 6. This "independent generations" scenario could arise if relatively rare events (e.g., major mergers, instabilities) are predominantly responsible for sparking luminous star formation at $z \gtrsim 4$.

Testing the validity of these scenarios has proven difficult with rest-UV observations alone, as these studies only probe recent star formation activity, revealing little about the physical properties of the galaxies being assembled. But it is the evolution of such properties (i.e., stellar mass, age, dust) which can potentially illuminate the relationship between galaxies at $z \simeq 4$ and $z \simeq 6$. If the LBGs seen at $z \simeq 4$ have been forming stars at a constant rate since $z \simeq 5-6$, then the higher redshift objects of a given luminosity should appear as "scaled-down" versions of those at $z \simeq 4$, with lower masses, ages, and reduced dust content. In contrast, if the LBG population at $z \simeq 4$ is dominated by galaxies which were either quiescent or forming stars less vigorously at $z \simeq 5$ and 6, then the stellar populations at fixed UV luminosity would not necessarily evolve significantly between the two different epochs.

In this section, we attempt to distinguish between these various scenarios by exploring the evolution of the relationship between the stellar mass and UV luminosity (hereafter the $M_\star$-M_{1500} relation). For a given galaxy, this diagnostic illuminates the ratio of the past and present star formation. At lower redshifts, this relationship has been used effectively to constrain stellar mass growth in galaxies (Noeske et al., 2007; Daddi et al., 2007). Studying the redshift evolution of this relation for a large sample of high redshift dropouts reveals whether the typical specific star formation rate (SFR/$M_\star$) and stellar mass of UV luminous galaxies changes significantly between $z \simeq 4$ and 6, allowing new constraints to be placed on the past star formation history.

In Figure 5.8, we present the inferred stellar masses of the B, V, and i'-drops

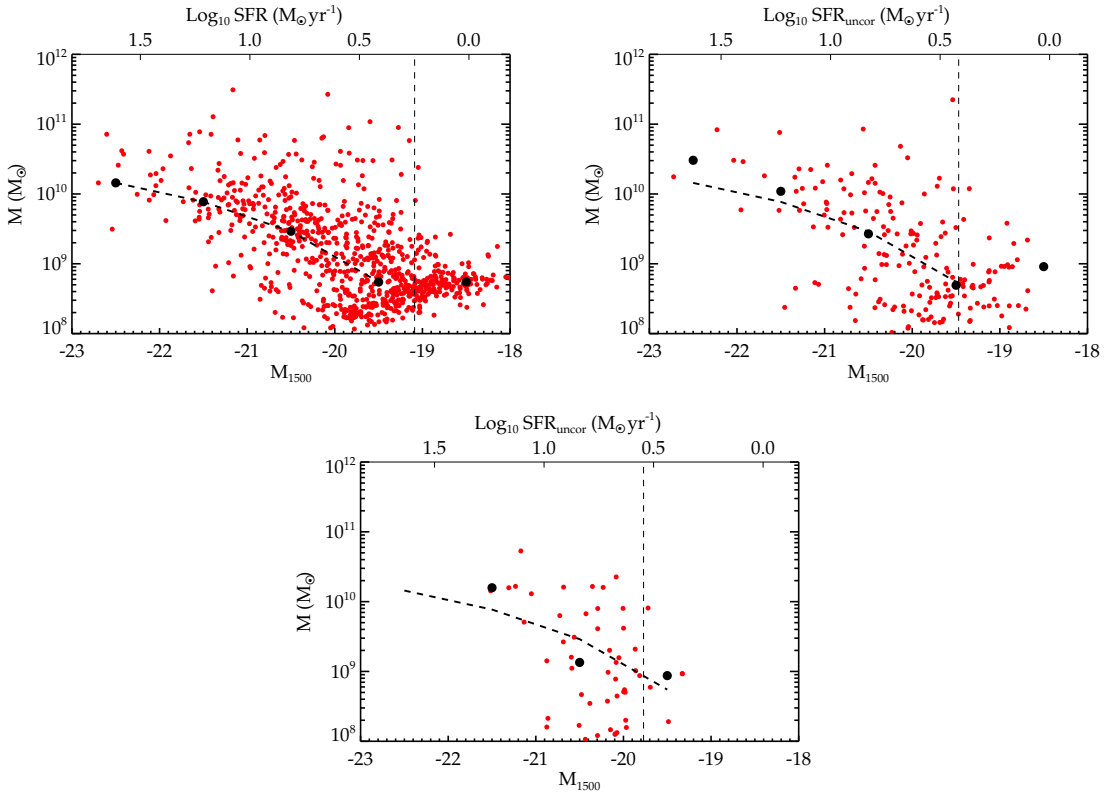

Figure 5.8 Stellar Mass vs. absolute magnitude at 1500Å (uncorrected for dust extinction) over $z \simeq 4-6$. Small red circles correspond to inferred masses and rest-UV absolute magnitudes for individual B-drops (upper left), V-drops (upper right) and i'-drops (bottom) assuming a $\tau = 100$ Myr exponential decay model. The dark solid circles are the median stellar mass in each magnitude bin. The relationship at $z \simeq 4$ is overlaid on the $z \simeq 5$ and $z \simeq 6$ as a black solid dashed line. The vertical solid lines represent the adopted completeness limits for each sample. The median stellar mass increases monontonically with M_{1500} in each dropout sample; however at a fixed M_{1500}, the median stellar mass does not vary significantly with redshift.

as a function of absolute magnitude at rest-frame 1500 Å (M_{1500}). We compute the absolute magnitude from the observed i'-band magnitudes for the B-drops, and the z'-band magnitudes for the V- and i'-drops using photometric redshifts where spectroscopic confirmation is not available. Ideally we would correct the absolute magnitudes for dust extinction, but doing so can introduce considerable error into the relation. For example, using the Meurer relation (see §5.3.4 for details) we find that the extinction at 1600 Å, A_{1600}, is related to the rest-UV color for dropouts at $z = 4$ by the following relation: A_{1600}=0.415 + 10.9(i'_{775}-z_{850}). This indicates that photometric uncertainties as small as 0.1 mags in the rest-UV color translate to more than 1 mag of uncertainty in the extinction correction. Further error arises from uncertainty in the redshifts and, to a lesser extent, the ages of the dropouts, both of which alter the relation between extinction and color derived above. Together, these sources of error would undoubtedly add significant random scatter to the $M_\star$-M_{1500} relation, quite possibly washing out any trends that may exist with luminosity or redshift. We thus limit our analysis to the relationship between stellar mass and emerging luminosity (i.e., the luminosity inferred from the flux that escapes the galaxy) and comment below on the specific effects that not correcting for dust extinction may have on our results.

For each of the dropout samples, we find that the median stellar mass increases monotonically with increasing emerging UV luminosity (forming a so-called "main-sequence"), albeit with very significant scatter in each magnitude bin. Similar relations are commonly seen at lower redshifts (e.g., Daddi et al. 2007) and are predicted to arise at high redshift in hydrodynamic simulations (e.g., Finlator et al. 2006). In the idealized scenario in which the bright dropout population emerges at $z \simeq 6.5$ and steadily grows in stellar mass via constant star formation (with no new galaxies emerging as luminous dropouts), we would expect the typical dropout stellar masses to increase by a factor of $\simeq 7$ in the time between $z \simeq 6$ and 4. Examining the top, middle, and bottom panels of Figure 5.8, we do not see such a systematic increase in the normalization of the $M_\star$-M_{1500} relation between (Table 5.2). While the lowest luminosity bin above our completeness limit may show some signs of marginal stellar

Table 5.2. Evolution of Galaxy Properties over $4 \lesssim z \lesssim 6$

M_{UV} (mag)	Num	$M_\star$ (τ=100) (10^8 $M_\odot$)	$M_\star$ (CSF) (10^8 $M_\odot$)	Age (Myr)
		B-drops ($z \simeq 4$)		
-22.5	15	144 (31-410)	223	180
-21.5	73	77 (24-380)	114	203
-20.5	227	29 (4.0-130)	38	181
-19.5	370	5.5 (2.0-42)	7.3	143
		V-drops ($z \simeq 5$)		
-22.5	3	304 (180-830)	520	286
-21.5	20	109 (5.4-234)	112	227
-20.5	67	27 (2.2-158)	36	181
-19.5	...	...	...	...
		i'-drops ($z \simeq 6$)		
-22.5	0	...	...	...
-21.5	8	160 (24-530)	226	286
-20.5	41	13 (1.3-90)	27	102
-19.5	...	...	...	...

Note. — The stellar masses and ages are inferred from models using a Salpeter IMF and solar metallicity. In column 3, we present the median stellar masses (and the range of masses spanned by the middle 80% of the distribution) determined from an exponentially-declining star formation history with τ=100 Myr. In column 5, we provide the median stellar masses inferred assuming a constant star formation history.

mass growth between $z \simeq 6$ and 5 (i.e., a $\times 1.3 - 2.0$ increase in the median stellar mass), this same bin shows no growth between $z \simeq 5$ and 4 in spite of the improved mass estimates and statistics. The most luminous bins actually show a slight decrease in the average stellar mass with cosmic time. As shown in Table 5.2, the absence of a systematic increase in the average stellar masses is not strongly dependent on the chosen star formation history. Overall these results seem to imply that the median stellar mass to emerging UV luminosity ratio of LBGs does not evolve significantly over $z = 4 - 6$. A galaxy with a given M_{1500} at $z \simeq 6$ will, on average, have the same assembled mass (to within a factor of $\simeq 2$) as a galaxy seen at $z \simeq 4$ with the same M_{1500}. This suggests that the specific star formation rate evolves weakly over $4 \lesssim z \lesssim 6$, indicating that the typical duration of past star formation for a galaxy of a given luminosity does not vary significantly between $z \simeq 6$ and 4.

While the inclusion of a dust correction would shift the $M_\star$-M_{1500} relation brightward (i.e., to the left in Figure 5.8), it would likely not lead to an increase in the normalization of the $M_\star$-M_{1500} relation over time. As we showed in §5.3.4, galaxies at $M_{1500} < -19.8$ do potentially become marginally dustier between $z \simeq 6$ and 4 which would cause the $z \simeq 4$ $M_\star$-M_{1500} relation to shift slightly more than the $z \simeq 5$ and 6 relations. Since a relative shift brightward is roughly the same as a shift toward lower stellar masses at fixed M_{1500}, this would actually have the effect of slightly decreasing the normalization of the $M_\star$-M_{1500} relation over the $4 \lesssim z \lesssim 6$ redshift range.

We now attempt to place the $M_\star$-M_{1500} relation presented in Figure 5.8 in the context of the steady growth scenario discussed at the outset of this section. To approximate this scenario, we assume a constant star formation history. Using solar metallicity templates and allowing the dust content to freely vary, we find that the typical star formation lifetimes of the B-drops are in excess of 700 Myr in the two brightest bins (Figure 5.9), implying that the precursors of the majority of B-drops would have been equally luminous in V and i'-drop samples. We therefore would have expected to see a steady decline in the typical stellar masses and ages of UV luminous galaxies at $z \simeq 5$ and 6. The fact that the $z \simeq 6$ LBGs are, on average, quite similar in mass and age to those of similar luminosity at $z \simeq 4$ suggests that the precursors

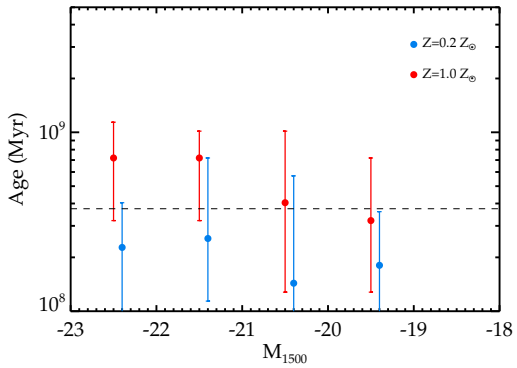

Figure 5.9 Ages inferred for B-dropout sample from constant star formation scenario as a function of absolute magnitude at 1500 Å (uncorrected for dust). The solid red circles give the median inferred age for CB07 models with solar metallicity while the blue circles give the median ages for models with 20% solar metallicity. The error bars on each datapoint correspond to the 25th (lower bar) and 75th (upper bar) percentile in the distribution of ages in each absolute magnitude bin. The horizontal dashed line denotes the amount of time spanned between $z \simeq 4$ and 5. Thus if the inferred ages are above the dashed line, it indicates a large fraction of the B-drops began forming stars beyond $z \simeq 5$, implying an abundant precursor population with scaled-down masses relative to those measured at $z \simeq 4$. The lack of evolution in the normalization of the $M_\star$-M_{1500} relationship over $z \simeq 4-6$ (Figure 8) casts doubt on this scenario.

of most of the $z \simeq 4$ LBGs were not at the same luminosity (or perhaps were even quiescent) at $z \simeq 6$. Similar arguments are arrived at by considering the observed UV luminosity function (UV LF) of the dropouts over this redshift interval (Bouwens et al., 2007). The large implied ages mentioned above suggest that the number density of galaxies at a given M_{1500} should not fall off significantly with increasing redshift, in sharp contrast to the observed trend. Indeed, the distribution of ages implied by this constant star formation scenario is such that the number density of galaxies at $M_{1500} < -21.5$ should not decrease by more than a factor of $\simeq 2$ over $4 \lesssim z \lesssim 6$, in marked contrast to the observed $\times 10$ decline in the bright end of the luminosity function at $M_{1500} \lesssim -21.5$ over this redshift interval (Bouwens et al., 2007).

We therefore argue that in order to explain the constancy in the $M_\star$-M_{1500} relationship and the decline in the UV luminosity function, a significant fraction of luminous galaxies at $z \gtrsim 4$ must have emerged at their present luminosity recently enough such that they would not have been visible as dropouts at the same luminosity just $\simeq 300$ Myr earlier. With a constantly increasing flux of newly luminous galaxies, the galaxy population at each epoch would be dominated by relatively young ($\lesssim 300$ Myr) objects. Hence the main sequence of the $M_\star$-M_{1500} relation would not necessarily grow significantly with cosmic time as one would expect in the steady growth scenario.

This requirement of a young population is not necessarily inconsistent with sustained star formation in galaxies. Indeed, if each of the $z \gtrsim 4$ dropout populations is dominated in number by newly emerged luminous galaxies, it is possible that systems which are UV luminous at $z \simeq 6$ remain luminous to $z \simeq 4$, but make up such a small fraction (by number) of the $z \simeq 4$ LBG population so as not to affect the main sequence of the $M_\star$-M_{1500} relation. The key problem with this picture, as hinted by our results above, is that constant star formation models struggle to produce young enough ages to be consistent with the need to have each epoch (i.e. $z \simeq 4$) dominated by systems that weren't present at the previous epoch (i.e. $z \simeq 5$). However, some caution in interpreting these results is surely warranted given the systematic uncertainties in using population synthesis modeling to infer properties at high redshift (§5.5.3). In particular, these inferences could be plagued by the degeneracy between

age and dust. If our dust estimates are systematically too low, then the ages quoted above are likely overestimates. In addition, if we adopt lower metallicity templates in our models (e.g., 0.2 $Z_{\odot}$) as may be appropriate for $z \gtrsim 4$, we find ages that are a factor of $\simeq 2$ lower than those in Table 5.2 (Figure 5.9). Thus while the relatively large ages implied by the constant star formation scenario do cause some tension with the observed evolution in the $M_{\star}$-M_{1500} relation and UV LF, there are steady growth scenarios that are consistent with the observations. Improved spectroscopic completeness and infrared photometry will soon enable us to lessen the uncertainty in the dust content and to provide estimates of the metallicities, both of which will help test the feasibility of these scenarios.

Another variant on the "steady growth" scenario is a situation where star formation grows increasingly vigorous as galaxies grow in mass at early times. While such star formation histories are not typically used in fitting high redshift galaxies, they are predicted in SPH simulations (Finlator et al., 2006) and have successfully been used to infer the properties of two $z \gtrsim 6$ galaxies (Finlator et al., 2007). In this case, galaxies would grow along the "main sequence" of the $M_{\star}$-M_{1500} relation of Figure 5.8, which results in little evolution of the normalization of the $M_{\star}$-M_{1500} relation over $4 \lesssim z \lesssim 6$, similar to the observed trend. This picture is also able to explain the observed luminosity function evolution. If galaxies in the luminosity range probed by our study steadily brighten by $\simeq 0.7$ mag at 1500 Å in the $\simeq 620$ Myr between $z \simeq 6$ and 4 (matching the evolution seen in the characteristic UV luminosity, $M^{\star}$), then this scenario would be fully consistent with the observed evolution in the UV luminosity function.

While this model can successfully reproduce the lack of evolution in the $M_{\star}$-M_{1500} relation and the decline in the UV LF, it has difficulty in explaining other observations. The first challenge stems from reproducing the diversity of SEDs seen in our dropout samples. Following the approach of Finlator et al. (2006), we approximated this star formation history as linearly increasing with time. We generally find reasonably acceptable fits for our dropout samples, except in the case of those objects with large rest-optical to rest-UV flux ratios. This problem arises because the linearly

increasing SFR ensures that a large fraction of the stellar mass assembly has occurred recently, increasing the time necessary to build up significant Balmer breaks. Models which have an upturn in their past star formation activity generally provide better fits to the data, perhaps implying star formation that the star formation histories of this subset of galaxies are slightly more complex then the simple model described above.

Importantly, a significant obstacle for each of the "steady growth" scenarios described above comes from observations of the clustering of dropouts at $z \gtrsim 4$ (Ouchi et al., 2004; Lee et al., 2006, 2008). By linking the dropouts of a given UV luminosity to a dark matter halo mass, constraints can be placed on the fraction of halos which are UV-bright, from which a star formation duty cycle can be determined. Using this approach, Lee et al. (2008) concluded that the typical duration of star formation activity in the dropouts at $z \simeq 4$ must last no longer than $\simeq 400$ Myr. Hence according to these results, those galaxies that are active at $z \simeq 6$ would no longer be active at $z \simeq 4$, in direct conflict with the sustained activity inherent to this picture.

Owing to the difficulties that the "steady growth" model faces in explaining the wide array of observations at $z \gtrsim 4$, we now consider the feasibility of the "independent generations" model mentioned at the outset of this section. In this picture, the galaxies we observe at $z \gtrsim 4$ undergo shorter timescale star formation episodes lasting no more than $\simeq$ 300-400 Myr. In order to achieve these relatively punctuated episodes of luminous activity, each star formation event must eventually decline. We model this behavior using the simple exponential decay models discussed in §5.5.3. The typical inferred ages for B-drops using solar metallicity models with decay constants of τ=100 (300) Myr range from 140 (230) to 200 (450) Myr at $M_{1500} < -19.5$, significantly lower than the constant star formation models discussed above. These ages are comparable to the time between $z \simeq 4$ and 5, indicating that with these assumptions the $z \simeq 4$ dropout population is dominated by sources which were not actively forming stars at $z \simeq 5$, as required based on our discussion above. Unless the cold gas reservoirs present in newly emerged galaxies at a given UV luminosity vary strongly between $z \simeq 4$ and 6, we would expect to see very little evolution in

$M_\star$-M_{1500} relation, similar to the observations presented in Figure 5.8.

Since the inferred ages of the dropouts in this episodic star formation scenario are typically small enough such that they would not have been active in higher redshift samples, there is no inconsistency with the observed decrease in the number density of luminous sources at $z \gtrsim 4$. The only requirement is that whatever process initiates the star formation activity must steadily produce more vigorous episodes over cosmic time. Given the expected growth in the underlying dark matter halos hosting the dropouts, this is not an unreasonable requirement.

Unlike the "steady growth" scenario discussed previously, the exponentially declining models predict that the dropouts will grow progressively fainter over time. Assuming models with decay constants of 100 Myr, the sources will fainten by 3 magnitudes in M_{1500} in just 300 Myr, and thus would almost certainly escape selection in future dropout samples with similar magnitude limits unless new star formation episodes have been initiated. The short ($\lesssim$ 500 Myr) star formation timescales implied by this scenario are clearly in much better agreement with those inferred from the clustering analysis previously discussed (Lee et al., 2008).

A potential drawback of the exponentially decaying models discussed above is that in order to reproduce the observed SEDs of the dropout populations in the required short timescales, we require the past UV luminosities to exceed those measured presently. For the τ=100 Myr models, we would expect the typical galaxy to have been a factor of $\simeq$ 3 brighter at 1500 Å just 150 Myr earlier (with this very luminous phase lasting for a duration of $\simeq$ 50 Myr). This implies an abundant, precursor population of very young, luminous objects, which are seemingly not present in sufficient number in the observed dropout sample. This problem could potentially be explained if this luminous phase is generally heavily extincted by dust. Indeed, Shapley et al. (2001) found that the most luminous $z \simeq 3$ LBGs tend to be very young and dusty. Further spectroscopy and higher S/N near-IR data will soon help test this possibility.

One prediction from this episodic star formation model is that there should be a significant repository of stellar mass in objects which underwent a UV luminous phase at an earlier epoch but are currently not actively forming stars. A careful

comparison of rest-UV and rest-optical selected samples at $z \simeq 4$ could thus yield significant insight into the mode of star formation that is dominant at $z \gtrsim 4$. By examining the range of star formation rates present in galaxies of fixed stellar mass, we should be able to distinguish between the steady growth and independent generations scenarios. The reliability of this test relies on having samples with secure redshifts and accurate extinction corrections, requiring both additional spectroscopy and improved IR photometry.

Before concluding, we must comment on several caveats of our discussion. The first is the possibility of an evolving initial mass function (Davé, 2008; van Dokkum, 2008) in which the characteristic stellar mass increases toward higher redshifts. As explained in detail in Davé (2008), this would alter the current star formation rates and the inferred stellar masses in such a way to decrease the normalization of the $M_\star$-M_{1500} relation at progressively earlier times. Clearly this does not help reconcile the observations with the steady growth picture. The second caveat is our neglect of the contribution of galaxy mergers to stellar mass growth. While mergers are expected to be very common at high redshift, they are likely to be gas-rich interactions which may not contribute significantly to the stellar mass growth. Indeed, simulations predict that galaxy growth is dominated by star formation and not mergers at the high redshifts we are considering (Kereš et al., 2005).

In summary, the episodic star formation model (approximated by a single component exponentially declining star formation history with luminous lifetimes of 300-500 Myr) appears to fare the best in explaining the evolution in the $M_\star$-M_{1500} relation, the UV LF, and the clustering properties at $z \gtrsim 4$. If this mode of star formation is dominant at $z \gtrsim 4$, it would signal a potential shift from the dominant mode of at $z \simeq 0.5 - 2$, where the lack of significant scatter in the dust-corrected SFRs of galaxies at fixed stellar mass (Noeske et al., 2007; Daddi et al., 2007) argues against the feasibility of star formation being dominated by short-timescale episodes (Davé, 2008). However, given the minimal spectroscopic completeness and low S/N of the IR data at $z \gtrsim 4$, it is too premature to rule out the sustained mode of star formation for $z \gtrsim 4$ galaxies. With new IR imaging and extensive spectroscopic surveys for high

redshift dropouts currently underway, it will soon be possible to improve the fidelity of the results presented here as well as to robustly test several of the additional predictions of the episodic star formation mode described above, both of which should lead to further progress in our understanding of the history of star formation at $z \gtrsim 4$.

5.7 Connecting the $z \gtrsim 4$ Mass Assembly History to Quiescent Galaxies at $z \simeq 2$

The assembly history of massive galaxies at high-redshift ($z \gtrsim 2$) has been a very active area of research in recent years. Near-infrared photometry of rest-UV selected objects at $z \simeq 2-3$ has revealed a significant population of massive galaxies at high redshift (Shapley et al., 2001, 2005). In addition, near-infrared color selected samples have proven very effective at isolating large samples of DRGs (e.g., Franx et al. 2003). The red colors of these objects likely arise from evolved stellar populations or dust (or some combination of the two). The addition of *Spitzer* photometry (e.g., Labbé et al. 2005; Webb et al. 2006; Papovich et al. 2006; Reddy et al. 2006) and very deep spectra (van Dokkum et al., 2004; Kriek et al., 2006) has enabled the passively evolving subset of DRGs to be separated from the dusty subset, providing more robust constraints on the physical properties and evolution of massive $\gtrsim 10^{11}$ $M_{\odot}$ galaxies at $z \gtrsim 2$. These studies have allowed much more accurate constraints to be placed on the epoch of formation of the population of massive galaxies at $z \simeq 2.3$. Kriek et al. (2006) find that the near-infrared spectra of a small sample of $z \gtrsim 2.3$ DRGs are best fit by ages of $\lesssim 1.3-1.4$ Gyr, suggesting that most of these systems started forming their stars between $z \simeq 3$ and 4.

While the formation epoch of the massive galaxies at high redshift is becoming increasingly better defined, it is still unclear what the precursors of these massive systems are. Sub-millimeter galaxies (Chapman et al., 2003; Smail et al., 1998; Capak et al., 2008) are convincing candidates since their intense star formation rates allow a substantial amount of mass to be assembled in a short period of time (see Cimatti

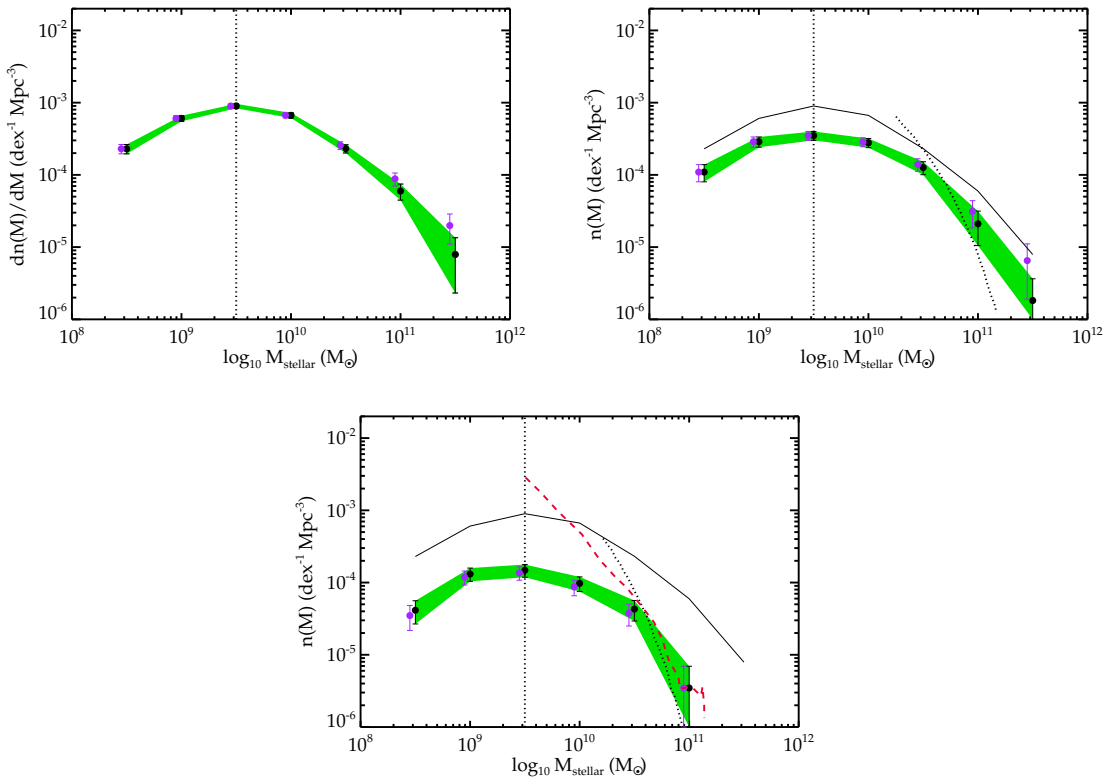

Figure 5.10 Stellar Mass Function of B-drops (upper panel), V-drops (middle panel), and i'-drops (bottom panel) with $M_{1500} < -20$. The green swath and associated solid black data points corresponds to the mass function determined from a large sample of dropouts in GOODS-S and GOODS-N. As discussed in §5.5.1, stellar masses are determined for individual galaxies by fitting the data against CB07 population synthesis models. This plot is constructed from models with exponentially-decaying star formation histories with τ=100 Myr, solar metallicity, and a Salpeter IMF. The purple datapoints (slightly offset from the central mass bin for clarity) correspond to the densities inferred if 24μm-detected sources are included. The vertical dotted lines represent the mass limit above which the inferred masses are reliable for individual galaxies. The black dotted lines overlaid on the V- and i'-dropout mass functions (upper right and bottom panels) correspond to the stellar mass function estimated in McLure et al. (2008) by multiplying the luminosity function by the average M/L ratio of the dropout population. The red dashed line overlaid on the i'-drop sample (bottom panel) corresponds to the predictions of the $z \simeq 6$ stellar mass function from the cosmological SPH simulations presented in Nagamine et al. (2008). The black solid curves overlaid in the upper right and bottom panel show the mass function determined in the B-drop sample (upper left panel).

et al. 2004; McCarthy et al. 2004). LBGs are also a viable candidate. Shapley et al. (2005) have shown that for reasonable assumptions the most massive objects in a $z \simeq 2$ rest-UV selected sample are likely to evolve into quiescent systems by $z \simeq 1.7$, with space densities that are virtually identical to those of the passive population at that redshift (Cimatti et al., 2004). Objects may of course spend portions of their assembly history in both a SMG and LBG phase. Our goal in this section is to extend the efforts of Shapley et al. (2005) to quantify the fraction of massive galaxies at $z \simeq 2-3$ that form a significant portion of their mass in an LBG phase at $z \gtrsim 3.5$.

We thus set forth to compute the number densities of massive objects in our B, V, and i'-drop samples. To derive the stellar mass functions, we group the dropouts by stellar mass in bins of $\Delta\log_{10}$M=1.0, spanning between $10^{7.5}$ and $10^{11.5}$ $M_{\odot}$ and then compute the number density of dropouts in each mass bin, accounting for the variation of the effective volume with apparent magnitude. We also apply a correction to account for the galaxies which are not included in the SED-fitting analysis due to being blended with foreground sources in the IRAC images. As we discussed in §5.5.1 (see also Figure 5.1), the fraction of sources that are blended varies with i'_{775} or z'_{850} apparent magnitude. We account for this slight bias by applying a magnitude-dependent correction: after computing the number density of galaxies in a given stellar mass and apparent magnitude bin, we correct this density by dividing by the fraction of high-redshift objects in that magnitude bin which were included in the SED-fitting analysis. In order to provide a consistent comparison of the mass function over $z = 4-6$, we impose an absolute magnitude limit of $M_{1500} = -20$ such that each dropout sample is complete enough to make a reliable measurement (see Figure 5.8).

The resulting mass functions are shown in Figure 5.10. Also shown on the plot (purple datapoints) are the inferred densities if we include sources detected at 24μm in the mass function analysis. As expected, the 24μm detections slightly increase the number densities of the B and V-drops in the most massive bins, but generally do not increase them by more than the Poisson uncertainties in that bin. As discussed in §5.4.2, the inferred stellar mass uncertainties for individual galaxies become consid-

erable for fainter sources with masses $\lesssim 10^{9.5}$ $M_\odot$. Although the average properties of sources less massive than this limit are reliable, we nevertheless choose to focus our analysis on the more robustly determined objects contained in bins $10^{9.5}$ $M_\odot$ and above.

The number densities derived here agree reasonably well with previous measurements. We plot the recent McLure et al. (2008) estimate of the $z \simeq 5$ and 6 LBG stellar mass functions over our curves in Figure 5.10 (after adjusting their masses to be consistent with a Salpeter IMF). In spite of their approximate way of determining the stellar mass function (the McLure et al. mass function is derived by scaling the luminosity function by the average stellar mass to light ratio), the two estimates agree to within a factor of 2 over the mass range probed, with our determination predicting a larger density of the most massive galaxies. The results also are in reasonable agreement with the massive end of the stellar mass function determined from the cosmological SPH simulations discussed in Nagamine et al. (2008). The observed mass function becomes shallower than the model predictions at $\lesssim 10^{10.0}$ $M_\odot$. This may be due, in part, to observational incompleteness at low mass limits. However a similar "knee" in the galaxy mass function is seen in the Drory et al. (2005) data suggesting that the simulations may be underpredicting low-mass galaxies, as suggested by Nagamine et al. (2008).

In contrast to the weakly evolving mass function at $z \lesssim 1$, the increase in stellar mass over $4 \lesssim z \lesssim 6$ occurs over the entire stellar mass range considered. Between $z \simeq 6$ and $z \simeq 4$, we find a factor of 5-6 increase in density for the bins ranging between $10^{9.5}$ and $10^{10.5}$ $M_\odot$. There is some evidence that the number density grows more rapidly for the most massive galaxies. While the uncertainties are significant, the mass functions suggest that the number density in the bin centered at 10^{11} $M_\odot$ increases by a factor of 17 between $z = 6$ and $z = 4$, nearly three times greater than the growth in less massive bins. It seems likely that we are witnessing a formative period of massive galaxy formation.

We finally turn to whether the observed number densities of massive LBGs at $z \gtrsim 2$ can account for a significant component of the largely quiescent population of

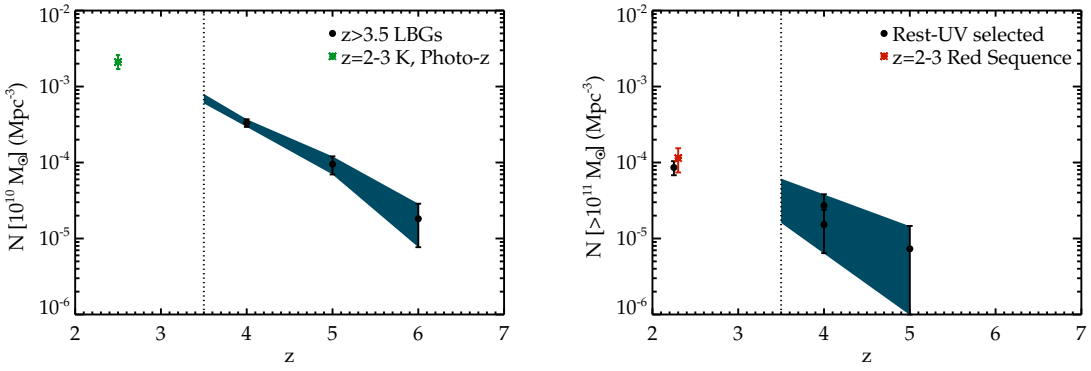

Figure 5.11 Evolving number density of massive galaxies at high redshift. *Top:* Solid black circles (and associated blue swath) show the evolution in the number density of actively forming galaxies more massive than 10^{10} $M_{\odot}$ derived in this paper. The green asterisk correspond to the total number density of galaxies more massive than 10^{10} $M_{\odot}$ at $z = 2.5$ identified in a K_s-band selected survey (Drory et al., 2005). The vertical dotted line demarcates the redshift range covered in this paper. *Bottom:* Same as top panel but for galaxies more massive than 10^{11} $M_{\odot}$. The black circles give the number density of rest-UV selected galaxies more massive than 10^{11} $M_{\odot}$; the upper datapoint at $z = 4$ corresponds to the number density inferred if the B-drops with 24μm detections are truly at high redshift. The red asterisk shows the number density of galaxies more massive than 10^{11} $M_{\odot}$ that are quiescent at $z = 2.3$ (Kriek et al., 2008).

DRGs at $z \simeq 2$. At $z \gtrsim 4$, we find that the number density of 10^{11} $M_{\odot}$ dropouts (excluding MIPS-detected sources) is $\simeq 2{\times}10^{-5}$ Mpc^{-3} (Figure 5.11). If these systems become quiescent on a timescale of less than 1 Gyr, then we would expect them to appear as red galaxies with little star formation at $z \simeq 2$. Indeed if we evolve the colors and rest-UV luminosities of these massive LBGs forward in time to $z \simeq 2$ assuming the simple exponential decay models considered in §5.6, we derive colors and optical apparent magnitudes that are consistent with the observed properties of DRGs (van Dokkum et al., 2006). Comparing the observed density of massive LBGs at $z \gtrsim 4$ to the number density of quiescent 10^{11} $M_{\odot}$ systems at $z \simeq 2-3$ ($1.1{\times}10^{-4}$ Mpc^{-3}, Kriek et al. 2008) indicates that at least $\simeq 20\%$ of the $z \simeq 2-3$ population of quiescent 10^{11} $M_{\odot}$ galaxies formed a large fraction of their stellar mass at $z \gtrsim 3.5$.

Given the expectation that dust-enshrouded "bursts" of star formation seen in the sub-mm are largely responsible for assembling massive galaxies by $z \simeq 2-3$ (Cimatti et al., 2004; McCarthy et al., 2004), it is interesting to extend our estimates of the number density of massive LBGs down to $z \simeq 2$ in order to compute the total fraction of massive galaxies that were formed (at least in part) in UV luminous episodes of star formation. Shapley et al. (2005) estimate that the number density of UV luminous galaxies at $z \simeq 2$ is $\simeq 10^{-4}$ $M_{\odot}$. We make our own estimate by selecting a sample of UV bright ($z' \lesssim 26.5$) galaxies in GOODS-S with photometric redshfits between $z = 2$ and 2.4 using redshifts and photometry from the GOODS-MUSIC z-band selected catalog (Grazian et al., 2006). Following the same procedures described earlier for computing stellar masses, completeness, and effective volumes, we derive a number density of $\simeq 9 \times 10^{-5}$ Mpc^{-3}, very close to the estimate from Shapley et al. (2005). These densities suggest that at $z \simeq 2$, the number density of UV-bright massive galaxies is roughly comparable to the density of systems that have already become quiescent.

Computing the contribution of UV luminous $z \gtrsim 2$ galaxies to the density of quiescent $z \simeq 2$ systems is non-trivial as it depends strongly on the timescale over which star formation is quenched in the LBGs. The shorter the timescale, the larger the implied number density of quiescent objects at $z \simeq 2$. If we assume that massive

LBGs join the red sequence over a period of 500 Myr, then we can estimate a quiescent number density by integrating over the growth in UV luminous massive galaxies over $2 \lesssim z \lesssim 6$ (Figure 5.11). Following this approach, we find that UV bright galaxies would produce a quiescent galaxy density of $7{\times}10^{-5}$ Mpc^3 by $z \simeq 2.5$, increasing to $2{\times}10^{-4}$ Mpc^{-3} at $z \simeq 2$. If the quenching timescale is longer (i.e., 1 Gyr), then the implied quiescent number density decreases to $\simeq 5 \times 10^{-5}$ Mpc^{-3} at $z \simeq 2$. Hence, these simple assumptions suggest that star formation in rest-UV selected $z \gtrsim 2$ galaxies accounts for the assembly of at least 50% of the total quiescent population of massive galaxies at $z \simeq 2$.

It thus appears reasonable that a significant fraction of the passively-evolving subset of $z \simeq 2-3$ galaxies with 10^{11} M$_\odot$ assembled their mass in *UV-luminous* star formation episodes at higher redshifts. While we cannot rule out that these rest-UV selected galaxies underwent short-duration sub-mm luminous bursts of star formation in their past (or perhaps will in their future as their dust content increases), these results indicate that sub-millimeter galaxies such as those presented in Capak et al. (2008) do not provide the only mode of assembling massive, quiescent galaxies by $z \simeq 2$.

5.8 Summary

We have studied the growth of galaxies over $4 \lesssim z \lesssim 6$ with the goal of improving our understanding of galaxy evolution in the first 2 billion years of cosmic history. Using the deep HST data available in the two GOODS fields, we compiled samples of 2819 B-dropouts, 615 V-dropouts, and 166 i'-dropouts. The superior quality of the multiwavelength data in GOODS (including optical data from HST spanning four filters, near-infrared data from the VLT and Subaru, and mid-infrared data from Spitzer) greatly helps identify foreground galaxies and stars which lurk in Lyman break dropout samples. Great care was taken to identify and remove these objects from our sample, using HST morphologies to excise point sources likely to be bright stellar contaminants and broadband SEDs spanning from the optical to the infrared

to remove low-redshift galaxies.

Our final high-redshift sample consists of 2443 B-dropouts, 506 V-dropouts, and 137 i'-dropouts. From this sample of galaxies, we constructed sub-samples of dropouts which are sufficiently unblended with nearby foreground objects in the deep Spitzer data to allow accurate photometry. In general, this corresponds to $\gtrsim 35\%$ of the total samples. We used the CB07 population synthesis models to estimate stellar masses and ages for this "Spitzer clean" subset. We compared the inferred properties to those derived from BC03 models, finding general agreement for solar metallicity models when the redshift is above 5. Below this redshift, the mid-IR data begin to probe the rest-frame near-infrared (which is affected by TP-AGB stars), and the CB07 models therefore return masses which are typically 10% lower than those from BC03 models.

Using this large database of stellar masses and rest-UV properties of B, V, and i'-dropouts, we examine the evolution of star-forming galaxies between $z \simeq 4$ and 6. We summarize our main results below.

1. We find that the typical stellar masses, ages, and dust content of galaxies of a fixed UV luminosity (uncorrected for dust extinction) do not evolve strongly between $z \simeq 6$, 5, and 4. This argues against the notion that the B-drops are made up of galaxies that have been steadily growing at fixed luminosity since $z \simeq 6$ (which we have termed the "steady growth" scenario). Instead, these data suggest that each successive epoch studied in this survey (e.g., $z \simeq 4$, 5, and 6) is likely dominated by galaxies that have only recently (within the last $\simeq 300$ Myr) emerged at their present luminosity.

2. We also considered two "hybrid" steady growth scenarios. In the first, we require that the dropouts assembled their stellar mass in a constant, sustained manner, but are sufficiently young so as to be consistent with the requirement that each epoch is dominated by systems which emerged recently. In the second scenario, star formation in individual systems becomes steadily more vigorous with cosmic time. Both of these scenarios can potentially explain the evolution in the $M_\star$-M_{1500} relation and the UV luminosity function, but both have difficulties explaining the full range of data

that exists at $z \gtrsim 4$. Most notably, both of these hybrid steady growth scenarios are inherently inconsistent with the short duty cycles implied by measurements of the clustering of $z \gtrsim 4$ LBGs (Lee et al., 2008).

3. Episodic star formation appears to provide a better fit to the wide range of observations. In this picture, each epoch is dominated by recently emerged sources, which remain luminous for no more than $\simeq$ 500 Myr on average. If the UV luminous periods become more intense with cosmic time between $z \simeq 6$ and 4, then this scenario could explain the evolution of the $M_\star$-M_{1500} relation and the UV LF. If this is the dominant mode of star formation at $z \gtrsim 4$, then there should be a significant population of relatively massive, quiescent sources that are in between star formation episodes. Future efforts at $z \simeq 4$ should help clarify whether this is the case.

4. The stellar mass function of UV luminous sources grows significantly over $4 \lesssim z \lesssim 6$, typically increasing by more than a factor of six in number density over the entire stellar mass range considered. There is some evidence that the growth in the most massive LBGs (Log_{10}=11$\pm$0.5) is a factor of three greater than in less massive systems, implying that this redshift range likely corresponds to the beginning of massive (10^{11} $M_\odot$) galaxy formation era.

5. The rapid growth in the assembly of massive galaxies at $z \gtrsim 4$ indicates that at least $\simeq$ 20% of the $z \simeq 2-3$ quiescent DRGs assembled their stellar mass at $z \gtrsim 3.5$. Fitting the increase in number density of UV luminous, massive galaxies between $z \simeq 6$ and 2, we estimate that it is feasible that more than 50% of quiescent $z \simeq 2-3$ DRGs were assembled in higher redshift LBGs. These results imply that rapid, dust-obscured bursts (seen as sub-mm galaxies) are not the only route toward assembling quiescent 10^{11} $M_\odot$ systems by $z \simeq 2-3$.

ACKNOWLEDGMENTS

We thank Chuck Steidel, Tommaso Treu, Niv Drory, Masami Ouchi, and Naveen Reddy for helpful conversations. DPS thanks the Department of Physics at the University of Oxford for its hospitality while much of this work was being conducted.

This paper is based on observations made with the NASA/ESA Hubble Space Telescope, obtained from the Data Archive at the Space Telescope Science Institute, which is operated by the Association of Universities for Research in Astronomy, Inc., under NASA contract NAS 5-26555. The *HST/ACS* observations are associated with proposals #9425 & 9583 (the GOODS public imaging survey).

Chapter 6

Resolving the Formation of the First Galactic Disks

One of the most important challenges of modern astrophysics is understanding the physical processes which produced the variety of present-day galaxies. In addition to detailed analyses of nearby examples, considerable progress has been made via the study of distant galaxies seen at large 'look back times (Shapley et al., 2003; Bouwens et al., 2007; Reddy et al., 2008). However since distant galaxies are both faint and small, only their integrated properties can usually be derived. Yet it is the internal properties of early galaxies, such as their dynamical state and the distribution of their star-forming regions, which provide key tests of galaxy formation models. Recent work has begun to focus on studying the internal dynamics of distant galaxies, seen as they were $\simeq$ 10 billion years ago (Genzel et al., 2006; Förster Schreiber et al., 2006; Nesvadba et al., 2006; Law et al., 2007). In this article we show how progress can be advanced by utilizing gravitational lensing, a phenomenon which enlarges both the apparent sizes and brightnesses, permitting studies which would otherwise require the increased resolution and light grasp of the next generation of telescopes, still a decade away. We have studied the highly-magnified Lyman Break galaxy (MACS J2135-0102,Smail et al. 2007), resolving the dynamics, star-formation and gas physics on scales of 150 parsecs. In this young galaxy (seen 2 billion years after the Big Bang), we find well-ordered rotation and infer that molecular gas, assembled via fragmentation, is being converted efficiently into stars. The remarkably detailed view enabled by

A version of this chapter was initially published in Stark et al., 2008, Nature, 455, 775

gravitational lensing suggests we are witnessing an early system destined to become a bulge-dominated galaxy. Whilst our study is based on a single object, ongoing imaging surveys are now yielding many more suitably-magnified distant galaxies. The technique exploited here will therefore become a very effective means of understanding how galaxies develop their eventual dynamical and morphological characteristics.

Resolved imaging spectroscopy provides a powerful route to probing the internal properties of young galaxies. Together with adaptive optics, which corrects for the effects of atmospheric motion on the image, maps of the internal velocity fields have been acquired for a small number of galaxies at redshifts of z=2-3 (2-3 billion years after the Big Bang) on scales of $\simeq 1$ kiloparsec (Genzel et al., 2006; Förster Schreiber et al., 2006; Law et al., 2007). These early results do not yet reveal a clear picture. The largest galaxies studied show evidence for systematic rotation, consistent with forming spiral disks (Genzel et al., 2006; Förster Schreiber et al., 2006). However, smaller more typical galaxies observed at the same epoch show chaotic velocity fields consistent with more primitive systemsLaw et al. (2007). The interpretation is still limited by poor spatial resolution: typical galaxies at redshifts z=2-3 have angular sizes of order 0.25 arcsec. Even with adaptive optics on the largest ground-based telescopes delivering 0.15 arcsec resolution (1.3 kpc at z=2), the velocity field in these galaxies can only be sampled at a few independent locations. Moreover, the emission lines used to trace the velocity field are not uniformly bright across the galaxy and co-adding pixels to improve the signal comes at the expense of a degradation in resolution.

An effective way to resolve these issues is to use gravitational lensing which magnifies the images of distant galaxies, both in their integrated brightness and angular size (Ellis et al., 2001; Kneib et al., 2004; Nesvadba et al., 2006; Swinbank et al., 2007) allowing a much more detailed view than otherwise possible. To demonstrate the advances possible, we have combined laser guide star adaptive optics with gravitational lensing to study a star-forming galaxy (MACS J2135-01028) at redshift 3.075 (seen 2.1 Gyr after the Big Bang). Detailed modelling of this system reveals that this galaxy is magnified in area 28 ± 3 times (and $\simeq 8$ times along its major axis) by the

combination of a foreground galaxy and galaxy cluster (Dye et al., 2007) and that its properties are typical of Lyman-break galaxies at this redshift.

To map the redshifted [OIII] 4959,5007 and Hβ 4861 Å emission lines, we employed the OSIRIS integral field spectrograph (Larkin et al., 2006) on the 10m Keck II telescope. J2135-0102 was observed for a total integration time of 15,000 seconds using a 3.6×6.4 arcsec field of view with 0.1 arcsec lenslets. Laser guide star adaptive optics correction was achieved via a R=14.2 'tip-tilt star 28 arcsec away from the source. The effective angular resolution of our data is 0.13 arcsec FWHM. Figure 6.1 shows a colour image of the target constructed from the optical Hubble Space Telescope image and the OSIRIS infrared spectroscopic data; clearly the two datasets are well-matched in resolution. Utilising adaptive optics, together with the gravitational magnification, $\simeq 0.13$ arcsec in the image plane translates to $\simeq 0.016$ arcsec in the source plane, corresponding to a physical scale of just $\simeq 120$ parsecs. Not only does this yield a $\simeq 5$ times improvement in linear resolution in sampling the velocity field compared to earlier work, but signal can be coadded in fainter regions whilst still maintaining an improved resolution compared to that achievable for unlensed sources.

In order to interpret our observations, we take into account the magnification caused by the foreground lens and reconstruct the resolved galaxy in the source plane, making use of the detailed mass model (Dye et al., 2007) which defines the mapping from each location in the image plane. Figure 6.2 shows the resulting intensity and velocity maps where binning has typically been undertaken with source plane pixels of 0.02 arcsec, corresponding to a sampling of 150 pc. The rest-frame UV continuum distribution reveals an elongated morphology with two components. Component 1 is the most highly magnified (a factor 28 ± 3 times) and gives rise to the ring-like structure in the image-plane. Component 2 extends just outside the caustic giving rise to a lower magnification (a factor 8.0 ± 0.9 times). These large magnifications enable us to study the internal properties of J2135-0102 in unprecedented detail. Fitting both the continuum and [O III] emission line distributions, we derive a half-light radius of 750 parsecs, a factor of five smaller than the large galaxies studied by

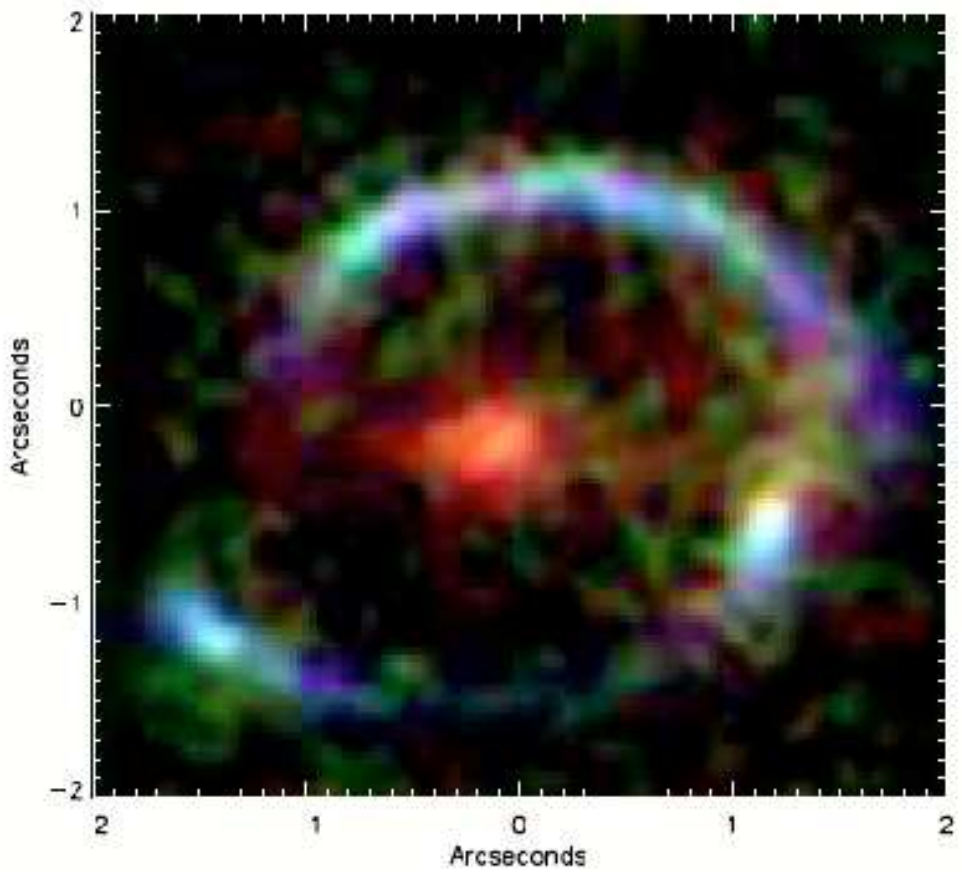

Figure 6.1 J2135-0102 a $z = 3.07$ galaxy magnified 28 ± 3 times into a near-complete Einstein ring. This color image combines a Hubble Space Telescope V606 image (blue) with Keck Laser Guide Star Adaptive Optics assisted near-infrared images in [O III] 5007 Å (green) and broad-band K (red). The foreground lensing galaxy at z=0.7 is the resolved red source at the center of the image. The large extent of the ring compared to the image plane resolution of our observations (0.13 arcsec) enables us to map the variation in spectral and dynamical properties of the background galaxy in fine detail.

many earlier workers (Genzel et al., 2006; Förster Schreiber et al., 2006) and much closer to the typical size of $z \simeq 3$ LBGs (Bouwens et al., 2004).

The most significant result revealed in Figure 6.2 is the well-sampled, regular, bi-symmetric velocity field revealed by the [O III] emission line measures which, together with the line widths which peak at the center of the galaxy, suggest a rotating system. But could the observed velocity pattern arise from a merging pair whose projected velocities are smoothed into an apparent rotation curve as a result of inadequate spatial resolution? This ambiguity, arising from the poorly-sampled data typically available at high-redshift, has plagued the interpretation of the first resolved data from distant galaxies (Genzel et al., 2006; Förster Schreiber et al., 2006; Law et al., 2007; Nesvadba et al., 2006), thereby precluding a robust test of the hypothesis that a large fraction of distant star-forming galaxies are undergoing major mergers (Abraham et al., 1996). With our considerably improved resolution, this ambiguity is greatly reduced. The well-sampled data for J2135-0102 reveals a velocity gradient spanning many independent resolution elements even internally with component 1. Moreover, the projected velocity of component 2 is consistent with an extrapolation of the gradient across component 1, which would be highly coincidental if the components were separate systems. We thus conclude that J2135-0102 it is much more likely to be a single system undergoing rotation.

Examining the velocity field in more detail, we extract a one-dimensional rotation curve along the major axis of the velocity field (at a position angle of 10° clockwise from the Δy-axis). Using an arctan function to model the shape of the rotation curve, the observations suggest a circular velocity of $v_C \sin i = 55 \pm 7$ km s^{-1} where i is the inclination angle. We estimate $i = 30° \pm 10$ from the surface photometry, implying a circular velocity of 109 km s^{-1}. As described above, component 2 shares the rotation, affecting only a minor 7 ± 3 km s^{-1} adjustment coincident with a 25 km s^{-1} rise in the line width. Using the rotation curve we derive a dynamical mass of $5{\times}10^9$ solar masses within a radius of 1.8 kpc. Thus, compared with the stellar mass of $6 \pm 2 \times 10^9$ solar masses (Coppin et al. 2007, assuming a Salpeter initial mass function), the central region appears to be baryon-dominated. While J2135-0102

certainly represents the most convincing example of a rotating galaxy, significant random motions are present. The central [O III] line width $\sigma_0 = 126 \pm 10$ km s^{-1} is comparable to the rotational velocity and the ratio v/$\sigma_0 = 0.87 \pm 0.10$ is consistent with previous, poorer-sampled, observations of similar-sized galaxies at this redshift (Law et al., 2007). Any disk present in J2135-0102 is thus most likely at an early stage of assembly (see Supplementary Information for further discussion).

Our OSIRIS data also yields the 2-D distribution of the nebular line Hβ, a valuable tracer of recent (< 20 Myr) star formation. The integrated star formation rate derived from the Hβ flux using the relations presented in Kennicutt (1998) is 40 ± 5 $M_\odot$ yr^{-1} (uncorrected for extinction), consistent with that derived from the 24μm flux (Coppin et al., 2007). The star formation rate density of 4.4 ± 0.5 solar masses yr^{-1} kpc^{-2} is typical of that derived for a larger sample of $z \simeq 2 - 3$ UV-selected galaxies (Erb et al., 2006c; Shapley et al., 2001) and comparable to that in local starbursts where activity is usually in compact, circumnuclear disks. The high star formation rates observed in these galaxies result in significant stellar winds and supernovae ejecta and as such vigorous galactic scale outflows have been observed in LBGs (Heckman, 2001). The blue-shifted UV-interstellar absorption lines (Δv = -400$\pm$100 km s^{-1}, Smail et al. 2007) are consistent with this interpretation.

Importantly, we also show that the Hβ velocity field confirms the overall rotation. However, both the Hβ and CO emission (Coppin et al., 2007) are not co-spatial with the center of the galaxy, but appear to peak within component 2. Moreover, the CO velocity and line width match those seen in [O III] for this component suggesting that almost all of the cold gas (which acts a reservoir for future star formation) resides in a region less than 1 kpc across. We utilize additional spatially-resolved ESO VLT SINFONI observations of [O II], [O III] and Hb (see Supplementary Information) to measure the R_{23} abundance index (Pettini & Pagel, 2004; Pilyugin & Thuan, 2005) finding a metallicity of $\simeq 0.9$ solar metallicity for both components.

These key findings allow us to determine the nature of J2135-0102. The interplay between the dynamics, star-formation and mass of the gas reservoir in high redshift star-forming galaxies is one of the primary science drivers for the next generation

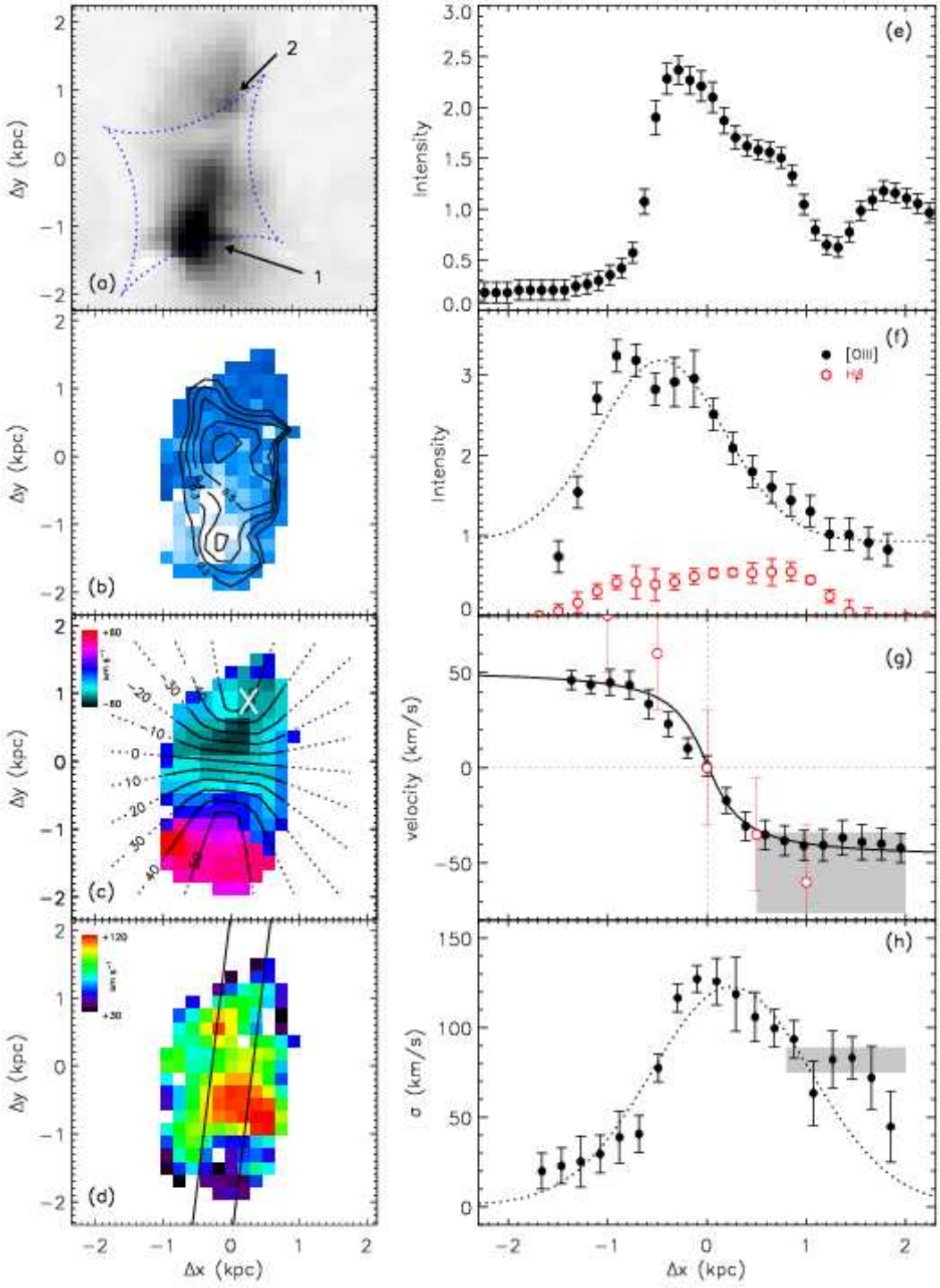
(a)
(b)
(c)
(d)
(e)
(f)
(g)
(h)
1
2
Δy (kpc)
Δx (kpc)
Intensity
[OIII]
Hβ
velocity (km/s)
σ (km/s)

Figure 6.2 Source plane properties of J2135-0102, reconstructed using the well-constrained lens model presented in Dye et al. (2007). Regions with the largest and smallest magnifications have source plane resolutions from 0.02 to 0.04, corresponding to physical scales of $\simeq$ 150-300 pc. For clarity we have resampled to a single pixel scale of 0.02. Each pixel thus represents a nearly independent measurement. Left (top to bottom): (a) Reconstructed HST V_{606} image of J2135-0102 showing the morphology of the rest-frame UV stellar continuum. Two major components within the galaxy are labelled as 1 and 2. The lens model caustic is overlaid (blue dashed line); regions close to the caustic have the highest magnification. (b) Distribution of [O III] 5007 Å emission (blue image) compared with that from Hβ (contours), which traces the star formation rate with contours varying linearly from 0.2 to 0.6 $M_\odot$/yr/pixel. (c) Velocity field derived from the [O III] emission. Overlaid contours indicate the best-fit disk model (see Supplementary Information). X marks the centre of the cold molecular gas16. (d) Distribution of the rest-frame [O III] emission line width (FWHM) showing a peak of 120 ± 20 km s^{-1} near the centre. Right (top to bottom): (e) V606 surface brightness profile. The extraction is performed along the long-axis of the galaxy (-10° from the Δy-axis) with Δx=0 corresponding to a location of (0,-0.2) on the left-hand side. (f) Spatial profiles of [O III] and Hβ. (g) Major axis rotation curve for [O III] (black points) verified with lower significance using Hβ (red points) with best-fitting disk model overlaid (solid line). (h) Profile of the [O III] emission line FWHM showing a maximum of $\sigma_0 = 126 \pm 10$ km s^{-1}. Shaded regions in panels (g) and (h) show the spatial and kinematic location of the molecular CO emission (Coppin et al., 2007) and the minor influence of component 2 on the overall dynamics.

facilities such as the Atacama Large Millimeter Array (ALMA). Since J2135-0102 is currently the only Lyman Break Galaxy for which high resolution kinematic and cold gas properties are available, we are uniquely able to dynamically constrain the gas mass and compare this with that implied using local calibrations, thereby testing whether star formation occurs in a mode similar to that seen in local spirals or appropriate to that in more extreme systems. The ratio α, between the molecular gas mass and the CO luminosity, has been used to distinguish the mode of star-formation (Solomon & Vanden Bout, 2005). For local spirals, $\alpha \simeq 5$, consistent with star formation occurring in discrete giant molecular clouds with 10^5-10^6 solar masses. In luminous infrared galaxies, where star formation occurs more vigorously in a single reservoir with 10^9 solar masses, α is close to unity (Solomon et al., 1997). α has yet to be measured at high redshift for all but the most extreme populations (Tacconi et al., 2008). By requiring that the gas mass must be less than the dynamical mass in J2135-0102 we find $\alpha < 0.8$. This implies that the gas lies in an extensive intercloud medium rather than in discrete, less massive, gravitationally-bound clouds (Solomon et al., 1997). The lower conversion factor identified here suggests that previous estimates of gas masses in $z \simeq 2$ UV-selected galaxies obtained using the "reverse" Kennicutt-Schmidt law (Erb et al., 2006b) may be a factor of $\simeq 5$ too large.

In summary, the enhanced star formation rate and compact gas repository together with the well-ordered velocity field strongly suggest we are witnessing the early assembly of a disk galaxy where the mode of star formation could soon produce a central spheroidal bulge. Our study of J2135-0102 demonstrates the remarkable level of detail in which UV- selected galaxies can be studied by combining spatially-resolved measurements of dynamics, star formation, metallicity, and molecular gas. The gain in resolution provided by gravitational lensing allows us to pursue these techniques a decade before such future facilities as the Thirty Meter Telescope and ALMA will make them commonplace.

6.1 Supplementary Information

6.1.1 Details of the Keck/OSIRIS Observations:

The strongly-lensed $z = 3.07$ galaxy, J2135-0102 (Smail et al., 2007) was observed with OSIRIS (Larkin et al., 2006) in conjunction with the Laser Guide Star Adaptive Optics system on the Keck II 10 metre telescope on UT September 4-5 2007 in photometric conditions and an optical seeing of 0.5 arcsec FWHM. The resulting Strehl is 25% and the encircled energy is 50% within a radius of 0.10 arcseconds. In order to map the nebular emission lines of [O III] $\lambda\lambda$4959, 5007 Å and Hβ 4861 Å , we used the narrow band Kn1 filter which provides a wavelength coverage from 1.955 to 2.055mm at a spectral resolution of $\lambda/\Delta\lambda \simeq 3400$. When deriving emission line widths, we subtract the instrumental profile, whose FWHM is 5.9×10^{-4} μm, in quadrature. As the target only partially fills the OSIRIS integral field unit (IFU) using the 0.1 arcsec lenslet scale, observations were conducted using a ABBA sequence with a 3.2 arcsec East-West chop onto adjacent sky, keeping the target within the field of view. The total integration time comprised 20 sub-exposures of 750 seconds. Individual exposures were reduced using the OSIRIS data reduction package. From each resulting datacube, a continuum image was constructed and the centroid of the foreground lensing galaxy measured. The final datacube was constructed by aligning the sub-exposures and combining using a 3σ clip to reject cosmic rays. Flux calibration was obtained by observing the R=14.2 'tip tilt star prior to each observation.

6.1.2 Gravitational Lens Modelling:

To interpret our data we must correct for the gravitational magnification and reconstruct the galaxy in the source plane. We first assign accurate world coordinates to each spectral pixel using the known coordinates of the foreground lens and the position angle of the IFU. The source plane is subsequently reconstructed with the lens model held fixed to the parameterization determined using the high signal/noise HST data (Dye et al., 2007) taking care to account for the PSF of the OSIRIS observations.

We note that the variable magnification across J2135-0102 leads to non-uniform resolution in the source plane; however we take this into consideration during the source-plane reconstruction of the data cube by utilizing an adaptive source plane grid (Dye & Warren, 2005). Regions in the image plane that are more highly magnified map to correspondingly smaller source plane pixels. The pixel size in each region of the source plane is selected by ray-tracing the image of the PSF into the source plane and ensuring that the derived resolution is finer than the pixel size. Hence each pixel in the source plane represents a nearly independent measurement of the intensity and velocity field. The pixel size ranges from 0.02 arcseconds in the regions of high magnification to 0.04 arcseconds in the regions of lower magnification, corresponding to physical scales of $\simeq$ 150 to 300 pc at z=3.07.

To evaluate the uncertainty on the magnification factor and on the image reconstruction, we also create a family of acceptable lens models. These models are constructed by varying the four main parameters of the lens model, namely the normalization of the dark matter halo density distribution of the lens galaxy, the elongation of the halo (the major / minor axis ratio), the orientation of the major axis, and the external shear provided by the cluster, such that the $\Delta\chi^2$ value from the best fit varies by $\pm 1\sigma$. Ray tracing each of these models and re-deriving the source-plane morphology and velocity field produces only minor changes in the dynamics, typically the various mappings produce a maximum shift of $\simeq$ 0.01 arcseconds compared to the best-fit solution and only a 10% uncertainty in the derived magnification (Supplementary Figure 1). All of the derived quantities in this paper include this uncertainty.

6.1.3 Analysis of Emission Line Maps:

The distribution of velocities and line widths across J2135-0102 was computed by fitting the [O III] λ5007 emission line in the spectral direction at each spatial location with a flat continuum plus Gaussian emission line profile using a χ^2 minimization procedure which takes into account the greater noise level close to atmospheric OH emission. We demanded a minimum signal to noise ratio of 5 to detect the emission

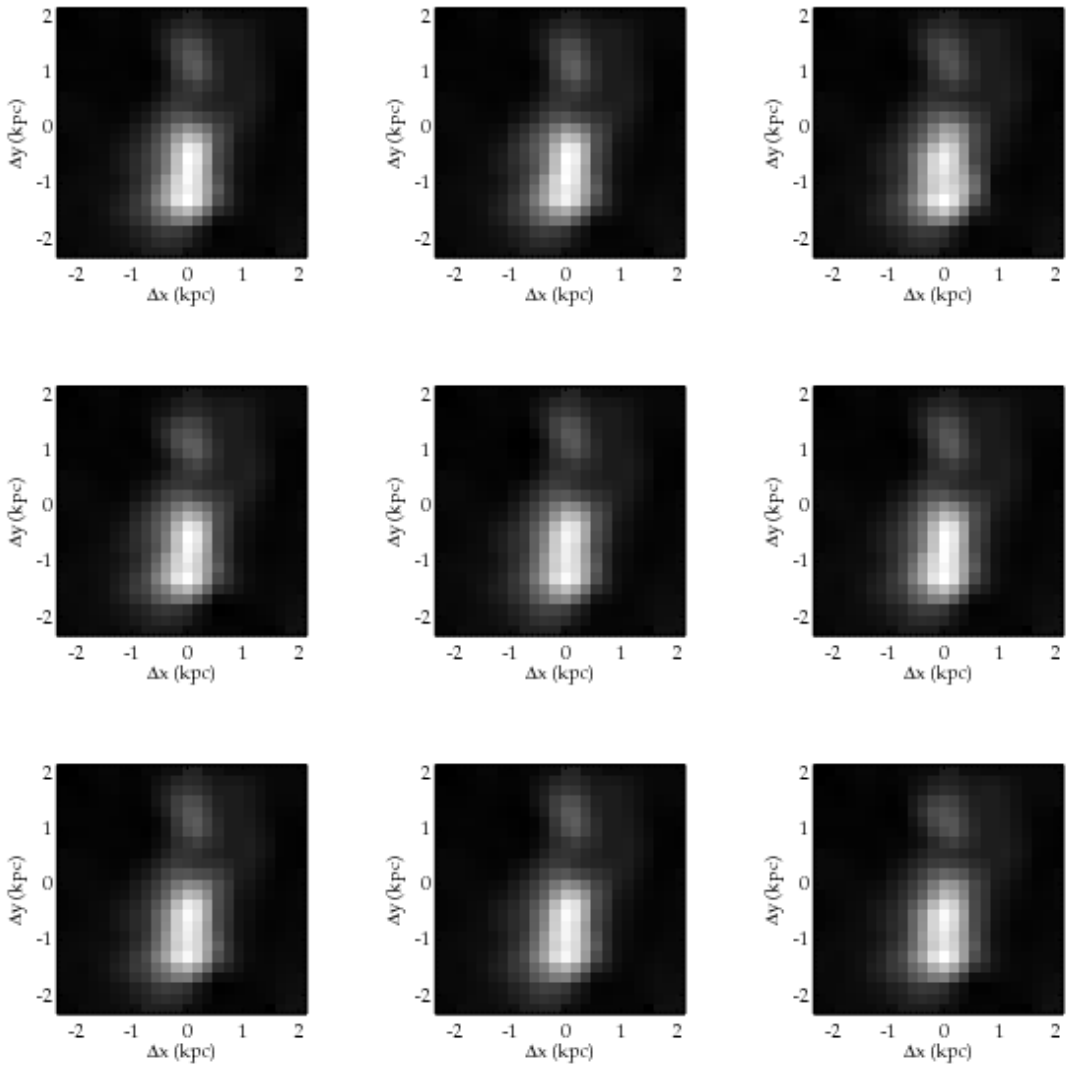

Figure 6.3 Uncertainties in source plane reconstruction. The nine different models are constructed by varying the normalization, elongation, orientation, and external cluster shear of the lens model (see text for details) by $\pm 1\sigma$ from their best-fit values. Ray tracing each of these models and re-deriving the source-plane morphology and velocity field produces only minor changes in the dynamics, typically the various mappings produce a maximum shift of $\simeq 0.01$ arcseconds compared to the best-fit solution and only a 10% uncertainty in the derived magnification. For consistency with Figure 6.2, the adaptive source plane grid (with pixel sizes varying between 0.02 and 0.04 arcseconds) is resampled onto a uniform grid with 0.02 arcsecond pixels.

line, and when this criterion is met, we determine the centroid, flux and line width of the best fit. In regions where the fit failed to detect a line, we average the surrounding 2×2 pixels and attempt the fit again. To derive error bars on each parameter we perturb the best fit such that the $\Delta\chi^2$ value from the best fit varies by $\pm 1\sigma$.

Star formation rates are derived from the Hβ line fluxes following the Kennicutt calibration (Kennicutt, 1998) which assumes a Salpeter IMF ranging from 0.1 to 100 solar masses and case B recombination. We rule out a significant contribution to the recombination flux from an active galactic nucleus (which would bias our star formation rate estimates) from the absence of bright CIV emission1 and bright mid-IR continuum (Coppin et al., 2007). The integrated Hβ line flux implies a star formation rate of 40 solar masses / year. This value likely underestimates the star formation rate of J2135-0102 since it does not account for dust. If we adopt an extinction correction of A(Hβ)$\simeq$ 1 mag, estimated by taking into account the reddening suggested from the broadband SED, the intrinsic star formation rate of J2135-0102 is closer to 100 solar masses / year. This is still consistent with the mid-infrared star formation rate (60 solar masses / year) and is identical to that predicted from the extinction corrected rest-UV continuum (Smail et al., 2007).

6.1.4 Rotation vs. Merger Interpretation:

Throughout the article, we argue that the most consistent explanation of our velocity and line width information (Figure 6.2) follows if the galaxy has well-ordered rotation. Here we discuss whether other interpretations are possible. In particular, are the data consistent with a merging system or a bipolar outflow?

Both observations and simulations have shown that gaseous disks are almost always completely destroyed in equal mass mergers (Barnes & Hernquist, 1996; Colina et al., 2005; Kronberger et al., 2007). Hence, if J2135-0102 is in the intermediate or late stages of a merger, we would expect the kinematics to be strongly disturbed. Instead, we see a relatively smooth rotation profile across the long axis of the galaxy with line widths peaking near the galaxy center, as predicted in simple models of

rotating disks. We note that simulations of equal mass mergers at high redshift suggest that with inadequate angular resolution ($\simeq$ 0.5-1.0 FWHM), the velocity distortions induced by a merger event may be smeared out giving the appearance of an undisturbed velocity field (Kronberger et al., 2007); however, on the $\simeq$ 150 pc scales probed by the OSIRIS observations of J2135-0102, the simulations suggest that such substructure should be readily apparent in the velocity field. Of course, the residual angular momentum from a galaxy merger can lead to the formation of a disk in as little as $\simeq$ 100 Myr (Robertson & Bullock, 2008), making it difficult to rule out the possibility that the ordered motions seen in J2135-0102 were initially generated in a major merger; however, the number of major mergers do not appear sufficient to account for all the star formation activity seen in LBGs (Dekel et al., 2008).

Alternatively, it is possible that the system is in the early stages of a merger. In this scenario, component 2 is seen in projection with a line-of-sight velocity coincident with the extrapolation of the rotation curve of component 1. Assuming that all velocity vectors are equally probable for the component 2, we derive a $< 1\%$ probability that the relative spatial position and radial velocity of the component would lie within 10 km s^{-1} from component 1 and $\pm$15 degrees from its location on the major axis defined in Figure 6.2. We therefore view this interpretation as unlikely.

We also consider whether the dynamics could be explained due to an outflow from the central source. While we do expect strong superwinds in J2135-0102, the outflow velocity suggested by the offset between the interstellar absorption features (400 ± 100 km s^{-1})1 is several times larger than the velocity gradient seen in [OIII] and Hβ ($\simeq$ 100 km s^{-1}). Furthermore, for a typical starburst galaxy in the local universe only 3-4% of the Ha luminosity arises from shock-heated gas (Calzetti et al., 2004). This emission also has a much lower surface brightness and is likely difficult to recover at high-redshift. Recalling that Hβ shows the same velocity structure as [O III], these observations suggest that the Hβ and [OIII] luminosity are dominated by radiative processes associated with star formation and not shocks generated in the outflow.

6.1.5 The Rotating Disk Model:

In order further evaluate the nature of the velocity field, we explore exponential disk models. We construct simplified two dimensional velocity fields assuming that the velocity follows an arctan function (Courteau, 1997). We allow the peak rotational velocity (v_c), turn-over radius (r_{peak}), inclination angle (i), and position angle (θ) to vary. For each disk model, we construct a datacube with the same pixel scale as our observations and add a Gaussian emission line with line centroid and width reflecting the local dynamics. At each pixel we also add noise appropriate for our data and then refit the velocity field using the same χ^2 minimization line fitting code. We find that the best fit model has a position angle +10° clockwise from the Δy-axis, v_c sin i = 54.7 km s^{-1}, r_{peak}=300 pc (Supplementary Figure 6.2). In Fig. 6.2c we show the two dimensional velocity field of J2135-0102 and overlay the contours from the best model fit. As can be seen, the model provides a reasonable fit to the data, with the contours tracing the global velocity field, as shown by the one dimensional extracted rotation curve (solid circles) and corresponding model (solid line). The velocity dispersion map and one-dimensional cut are also well-matched to the model (Fig. 6.2e).

While this simple disk model provides a reasonably good fit to the data, it is worth noting that we are not suggesting J2135-0102 is analogous to the cold, disk galaxies seen in the local universe. Indeed, there are numerous small-scale deviations from the model, most notably at the location of the gas-rich component (at Δx=1.5 kpc on the right-hand side of Fig. 6.2), where the extracted rotation curve shows an 8 km s^{-1} rise and the velocity dispersion shows evidence of a secondary peak. Such substructure might be explained via a disk instability which has led to rapid star formation in a subregion within J2135-0102 and thereby caused a disruption of the local dynamics. Disturbances to the velocity field and line widths are in fact predicted in simulations of unstable disks (Bournaud et al., 2007, 2008; Immeli et al., 2004). We also note that our simple disk model fails to explain the 500 pc offset in the peak of the line width distribution from our adopted galaxy center. This is perhaps not surprising considering that in the timescale required to assemble the observed stellar mass given

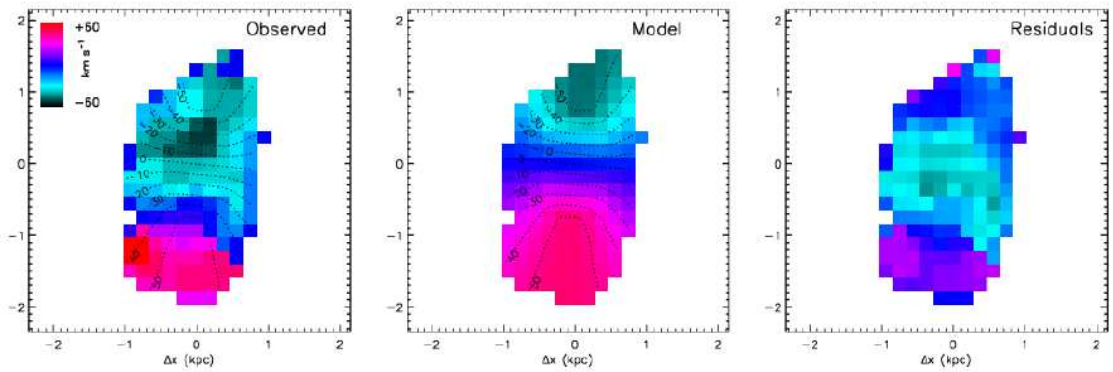

Figure 6.4 Best-fitting disk model and corresponding residuals. The data are fit using a simple arctan function11 allowing the peak rotational velocity, turn-over radius, inclination angle, and position angle to vary. The model that minimizes χ^2 has θ = +10° clockwise from the Δy-axis, v_c sin i = 54.7 km s^{-1}, i =30°, r_{peak}=300pc. The best-fitting disk model is able to reproduce the velocity shear with reasonably low residuals over most of the velocity field. Regions with larger residuals (<20 km s^{-1}) may potentially reflect substructure within disk, as predicted for unstable disks undergoing rapid star formation (Immeli et al., 2004; Bournaud et al., 2007, 2008).

a star formation rate of 60 solar masses yr^{-1} ($\simeq$ 100 Myr), a test particle at a radius of 1 kpc will have only completed $\simeq$ 1-2 orbits of the galaxy at the observed rotational velocity; hence it is likely still in a fairly unrelaxed state.

As discussed in the main paper, the line widths are comparable to the inclination-corrected rotational velocity of the galaxy (v_c / σ_0 = 0.87$\pm$0.10) suggesting considerable random motions. This could arise in two ways (Förster Schreiber et al., 2006). First, as gas is accreted, disk viscosity may convert gravitational potential energy into random motions. This heating may, however, inhibit the efficient dissipative processes necessary for the formation of the clumps seen in J2135-0102. Perhaps instead, random motions were generated after star formation was initiated as a result of the stellar winds and outflows present in this galaxy (Thompson et al., 2005). Which of these two scenarios plays the dominant heating role can be determined with knowledge of the relative distribution of stars and ionized gas. In the latter scenario, random motions are generated after the burst of star formation causing the ionized material to be extended relative to the distribution of stars. In the former case, the heating occurs before the star formation episode, leading to an equally extended dis-

tribution of stars and ionized gas. High-resolution near-infrared imaging will soon provide the necessary constraints on the stellar distribution of J2135-0102, enabling this test to be conducted.

6.1.6 Metallicity Constraints:

Additional data covering the redshifted [O II] 3727 Å emission line doublet was obtained using the SINFONI IFU and its associated Laser Guide Star Adaptive Optics system on the 8.2 metre ESO Very Large Telescope UT4 (Yepun). A 3,600 sec (on source) exposure was secured in photometric conditions in 0.6 arcsec seeing using the same tip-tilt reference star as in the OSIRIS observations. These data offer a 3.2 × 3.2 arcsec field with a sampling of 0.10 arcsec pixel^{-1}. The data have a lower spectral resolution ($\lambda/\Delta\lambda \simeq 1500$ at 1.5 μm) and (due to the shorter exposure time) poorer signal-to-noise than the OSIRIS data, but cover a wider wavelength range, λ = 1.4 2.4 μm. The observations were reduced in a similar manner to that described above using the ESOREX pipeline.

This data allows us to examine the chemical composition using the R_{23} index(Pettini & Pagel, 2004; Pilyugin & Thuan, 2005) derived from the ratio of [O II], [O III] and Hβ emission. Although each line comprising this index is clearly detected over the entire source, the signal-to-noise is insufficient for a measurement in each spatial pixel. However, the data do allow us to bin the spectra in component 1 and 2 separately for which we measure $R_{23} = 4.7 \pm 0.8$ and 3.8 ± 0.4, respectively.

In deriving metallicities from the R_{23} index, uncertainty arises from the double-valued nature of the calibration. We adopt the calibration based on the upper-branch of this relation, yielding 12 + log(O/H) = 8.6 for the entire galaxy, for two reasons. First, this gives a result that is closer to the median metallicity of a large sample of $z \simeq 2$ UV-selected galaxies measured using the [NII]6583/Hα calibration ($12+\log(O/H) \simeq 8.7$,Erb et al. 2006a) and a smaller sample of $z \simeq 3$ LBGs measured assuming the upper branch of the R_{23} calibration ($12+\log(O/H) \simeq 8.6$,Pettini et al. 2001). Secondly, our choice is also more consistent with the stellar mass metallicity

relation established for $z \simeq 2$ LBGs20 given the inferred stellar mass for J2135-0102(Smail et al., 2007). Adopting the upper branch calibration and estimating the excitation parameter via the ratio of [O III] and [O II], we find that the oxygen-phase abundance is $\simeq 0.9$ solar (12 + log(O/H)$\simeq$ 8.6) in both components. The lack of a pronounced metallicity gradient in J2135-0102 is consistent with the interpretation that the galaxy is still in a fairly unrelaxed state, having only been actively forming stars for little over a dynamical time.

Acknowledgements

We thank Jim Lyke for assistance with the Keck observators and acknowledge useful discussions with Richard Bower, Kristen Coppin, Matthew Lehnert, Reinhard Genzel, Dawn Erb, David Law, Alice Shapley, Adrian Jenkins, Paolo Salucci and Tom Theuns. The OSIRIS data were obtained at the W.M. Keck Observatory which is operated as a scientific partnership among the California Institute of Technology, the University of California and NASA. The observatory was made possible by the generous financial support of the W.M. Keck Foundation. The SINFONI data are based on observations made with the ESO Telescopes at the Paranal Observatories under programmes 079.B-0702 and 080.B-0035. AMS and IRS/RSE acknowledge financial support from STFC and the Royal Society respectively.

Chapter 7

Synthesis and Future Directions

In this section, I summarize our results and comment on ongoing work. I then revist the important question of whether galaxies are capable of reionizing hydrogen given current knowledge of galaxies at $z \gtrsim 6$. Finally, I highlight the prospects for improving observational constraints at high redshift in the near future.

7.1 Summary of Recent Progress

The observational study of the first two billion years of cosmic history has advanced significantly in recent years. Observers of this early era are now focused on the epoch of reionization, whereby intergalactic hydrogen transitioned from neutral to ionized. Determining the nature and redshift distribution of the sources resonsible for this transition represents the current frontier in studies of the first galactic systems.

Recent observations have begun to narrow the era during which reionization likely occurred. The WMAP EE spectrum (Dunkley et al., 2008) implies scattering of microwave photons by free electrons from ionizing sources at $z \simeq 11$ (and perhaps as early as $z \simeq 15 - 20$, see Figure 1.2). Meanwhile the upturn in the neutral hydrogen opacity beyond $z \simeq 5.5$, as probed by the most distant QSOs (Fan et al., 2006) may imply that reionization ended at $z \simeq 6 - 7$ (see also Becker et al. 2007). These results are indicative of significant star formation at $z \simeq 6 - 12$. However, early estimates of the abundance of luminous UV-emitting $i-$band dropouts at z$\simeq$6 reveal a deficit in the ionizing photons required for reionization (Bunker et al., 2004).

This points to a significant contribution from sources at higher redshifts or below the detection limits of current surveys. Detecting such sources has proved remarkably challenging for existing telescopes— currently, no galaxy has been identified with robust spectroscopic confirmation beyond $z \gtrsim 7$. Unless observational constraints are improved at $z \gtrsim 7$, the contribution of star-forming galaxies to reionization will remain unknown.

In Stark & Ellis (2006), we suggested an indirect method of constraining star formation activity at $z \gtrsim 7$. Motivated by the *Spitzer* discovery of massive galaxies with old stars at $z \gtrsim 6$ (Eyles et al., 2005), we proposed that the stellar mass density at $z \simeq 5-6$ could be used to robustly constrain the integrated star formation density at yet earlier times. Since it is incredibly challenging for current facilities to detect galaxies at $z \gtrsim 7$, this method may represent one of the most promising means of characterizing the role that star-forming galaxies play in reionization. In Chapter 2, I discussed efforts to constrain the amount of stellar mass that is locked in UV luminous galaxies at $z \simeq 5$ (Stark et al., 2007a). The large mass density derived in this study indicates that there must have been considerable star formation activity in the first billion years, implying that current surveys at $z \gtrsim 6$ may be missing a significant component of activity.

Comprehensive searches for galaxies over the redshift interval $6< z <12$ are thus key to progress. The first question that must be addressed is the luminosity distribution of the sources dominating the star formation rate density at these times. The variety of deep fields studied by HST and ground-based facilities in the past five years have provided robust constraints on the luminosity functions of B, V, i'-band dropouts, revealing that the mean UV-luminosity of galaxies decreases at earlier times (Figure 7.1, Bouwens et al. 2007; McLure et al. 2008). Efforts to extend these results to $z \simeq 7-10$ show that the prevalence of luminous galaxies continues to decline (Bouwens et al., 2008; Oesch et al., 2008). These observations imply that the sources which are likely to dominate reionization are low mass systems which form stars at a slow enough pace to lie faintward of the detection thresholds of current surveys at $z \gtrsim 7$.

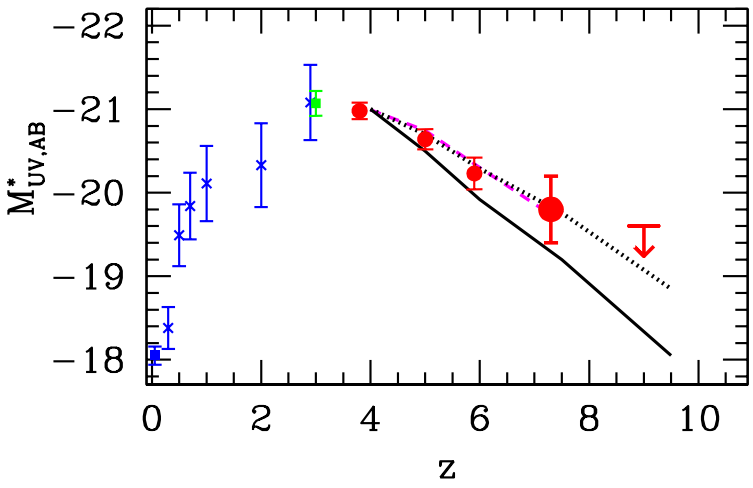

Figure 7.1 Redshift evolution of characteristic rest-frame UV luminosity taken from Bouwens et al. (2008). The data suggest that the mean UV luminosity of galaxies declines continuously between $z \simeq 3$ and $z \simeq 10$.

One means of achieving a glimpse of this feeble population in advance of next generation facilities is to make use of the natural magnification provided by the gravitational lensing of distant galaxies. In Chapter 3, I discussed a new, ambitious lensing survey to observe the critical lines of nine galaxy clusters for Lyman-α emission from low luminosity galaxies located at $8 \lesssim z \lesssim 10$ (Stark et al., 2007b). We identified six Lyα candidates and suggested that two appeared more promising than the others. If any of these sources lies at $z \gtrsim 8$, it would suggest that low luminosity galaxies indeed dominate the reionization process and furthermore as discussed in Chapter 4, may require a more top-heavy initial mass function in order to explain the observed counts (Stark et al., 2007c).

Given the importance of these results, we remain steadfast in our determination to confirm or otherwise reject the Lyα candidates and to extend this work to significantly larger areas. We now have two ongoing programs with this as their goal. Using the newly-developed multi-object spectrograph capability of MOIRCS on the Subaru telescope we have initiated a new lensing survey for Lyman-α emission from $z \gtrsim 7$ galaxies (PI: Egami). With the multiplexing advantage of MOIRCS, we are able to much more efficiently cover the critical lines of the clusters, enabling significant ($\times 5$) gains in survey area while simultaneously re-observing the candidates identified

in Stark et al. (2007b). In addition, we are pursuing a program using the integral field spectrograph SINFONI on the VLT to study the critical lines of galaxy clusters (PI: Kneib). We aim to use the large field of view of the SINFONI IFU to not only re-observe the candidates but also to search for their lensed counterimages. Image pairs are typically symmetrically located about the cluster critical line. Since the $z \simeq 9$ critical line is significantly offset from the critical line for sources at $z \lesssim 2$, the location of the lensed counterimage in the appropriate location would verify the $z \gtrsim 8$ interpretation for the line feature. Combined, these surveys should eventually enable us to determine the nature of our Lyman-α candidates and to significantly improve constraints on the abundance of low luminosity galaxies at $z \gtrsim 8$.

In the last year, additional evidence has emerged from our research group implying a vigorous population of faint galaxies at $z \gtrsim 7$. The results, presented in Richard et al. (2008), stem from a systematic search for gravitationally-lensed continuum dropouts beyond $z \simeq 7$ using very deep imaging through six foreground clusters with the Hubble and Spitzer Space Telescopes. The survey yielded 10 z-band dropouts to photometric limits of $J_{110} \simeq 26.2$ AB. Taking into account the magnification afforded by the clusters (1-4 magnitudes), we are able to place constraints on the UV luminosity function of dropouts to unlensed limits of $\mathrm{J}_{110} \simeq 30$ AB, fainter than those charted in the HUDF. We conduct a number of tests to evaluate the fidelity of our candidates and conclude that 60% are likely to lie at $z \gtrsim 7$. The large number density of faint galaxies implied by this survey lends further support the notion that low luminosity galaxies dominate the reionization process. We discuss future efforts to constrain the $z \gtrsim 7$ dropout population in §7.3.

As is clear from our discussion above, confirming galaxies in the reionization era ($z \gtrsim 7$) poses a significant challenge for current facilities. Those candidates that are identified at $z \gtrsim 7$ are generally too faint to extract anything more than an estimate of their current star formation rate. Whether these objects are low-mass, primordial systems in their first throes of star formation or mature, massive galaxies is thus hard to decipher. A more practical route toward revealing the nature of galaxies at the end of the reionization era is to study the detailed properties of galaxies located

at $z \simeq 4-6$. In this redshift range, it is possible to compile large, robust samples of objects that are sufficiently bright for reliable estimates of their assembled stellar mass and relative ages. By tracking the growth of galaxies throughout this redshift interval, we can gain significant insight into how galaxies are evolving as we look back to increasingly earlier epochs. Furthermore, we can begin to illuminate how the galaxies observed at the end of the reionization era relate to the well-studied populations observed at $z \simeq 2-3$.

With these goals, we conducted a survey of the evolution in the stellar populations of B, V, and i'-band continuum selected dropouts in the GOODS-S and GOODS-N fields (see Chapter 5 for dicussion). By tracking the growth in the stellar masses of dropouts between $z \simeq 4$ and 6, we concluded that $z \simeq 6$ objects do not appear to be simple scaled-down versions of those at $z \simeq 4$. At a given luminosity, the assembled stellar mass, age, and dust content of a $z \simeq 6$ galaxy appear quite similar to those of similarly luminous galaxies at $z \simeq 4$. We have argued that this implies a constant influx of newly luminous objects at each redshift, consistent with the observed growth in the UV luminous function. Moreover, we identified a fairly rapid increase in the number density of massive galaxies undergoing active star formation over $4 \lesssim z \lesssim 6$ and concluded that for nominal assumptions of the timescale required for star formation to cease, the growth of massive LBGs can account for a substantial fraction of the population of quiescent massive galaxies at $z \simeq 2-3$ (Kriek et al. 2008), suggesting that sub-mm galaxies are not the only route to forming at DRG at $z \simeq 2-3$.

While studies of the evolving stellar mass function over $4 \lesssim z \lesssim 6$ are effective at illuminating how mass assembly is occcuring, only by studying the internal structure of high redshift galaxies can we begin to understand the physical process driving the assembly. Such observations have the potential of addressing many important questions including the dynamical state of the recently discovered population of massive galaxies at $z \gtrsim 4$ the relationship between star formation, chemical abundance, and gas density (which relates to the modes of assembly), and most fundamentally, the likely path by which early systems mature into the regular galaxies we see today.

The resolved study of $z \gtrsim 2$ galaxies has benefited greatly from the development of laser guide star (LGS) AO-fed integral field units (Genzel et al., 2006; Law et al., 2007). However, even with the superb resolution offered by AO, representative high redshift galaxies can only be sampled with several independent resolution elements, precluding an unambiguous interpretation of the velocity field. Perhaps the only means of pursuing these questions in detail is via gravitational lensing which boosts the total flux of a source by $\times$10-30 and enlarges the apparent size by $\times$5-10, allowing $z \gtrsim 2$ galaxies to be sampled at a resolution that will not be possible until 20-40m telescopes become available.

We have recently initiated a program with OSIRIS, an LGS-AO IFU on Keck II, to study the internal properties of lensed galaxies at high redshift. In chapter 6, I present the first results from this program (Stark et al., 2008). I discuss the resolved kinematics, metallicity, star formation, and gas content of a strongly lensed galaxy at $z = 3.07$. Our analysis indicates an ordered velocity field is present. In conjunction with molecular gas dynamics from millimeter spectroscopy (Coppin et al., 2007), these data have provided unique information on a remakably compact (< 1 kpc) emission line source which would barely be resolved in the unlensed case. Although two components are evident, the gas-rich component barely perturbs the dynamical field suggesting it is already embedded in a young rotating structure. The next step in this pursuit is to extend this technique to a larger sample of sources covering a redshift range over $z \simeq 2$ to 5, enabling the study of luminosity and redshift dependent trends in the angular momentum content of high redshift galaxies. We discuss the prospects for doing so in §7.3.

7.2 The Contribution of Galaxies to Reionization

We now briefly return to one of the central questions of this thesis, whether galaxies capable of providing a sufficient number of ionizing photons for reionziation. We motivate our discussion with the recent results presented in Bolton & Haehnelt (2007). These authors considered three models for the variation in the ionizing emissivity at

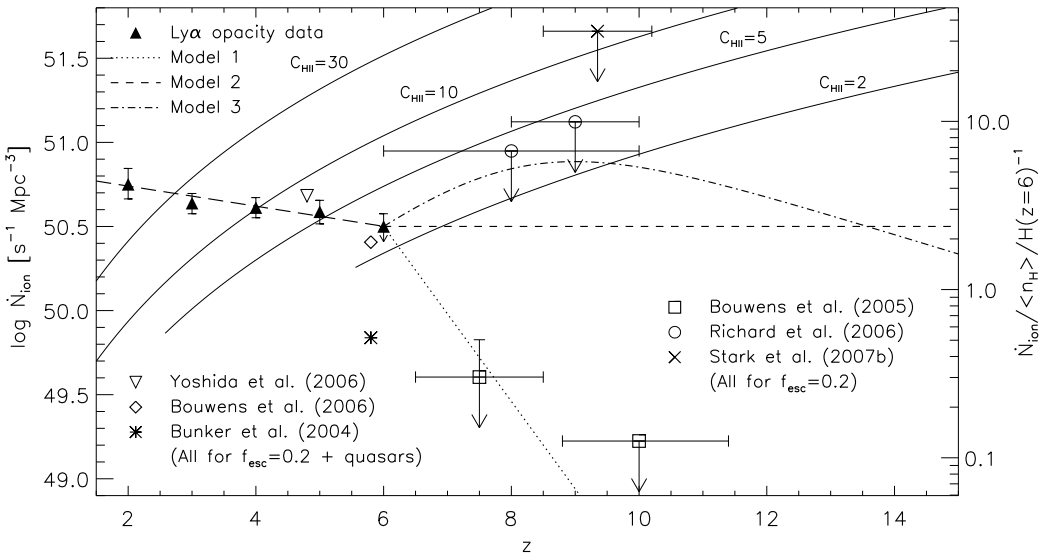

Figure 7.2 Observational constraints on the ionizing emissivity at high redshfit taken from Bolton & Haehnelt (2007). The solid curves show the emissivity required to keep the IGM ionized at a given redshift for four different IGM clumpiness parameters (C_{HII}=2,5,10,30). The dotted (model 1), dashed (model 2), and dotted-dashed (model 3) lines show three possible scenarios for the evolution of the ionizing background over $6 \lesssim z \lesssim 15$. The observational constraints from luminous dropouts (squares) indicate a sharp decline in the emissivity at $z \gtrsim 6$, consistent with model 1, while the constraints from lensing surveys suggest that it may be possible for the ionizing background to increase beyond its $z \simeq 6$ value, consistent with model 3. The ability of these sources to reionize the IGM are considered in Figure 7.2.

$z \gtrsim 6$ (Figure 7.2) and computed the evolution of the filling factor of ionized hydrogen in the IGM for each case. In model 1, the ionizing background sharply declines beyond $z \simeq 6$. In model 2, the ionizing background is assumed to remain constant at its value measured from Lyα opacity data at $z \simeq 6$. In the final model, the ionizing emissivity increases beyond what is observed at $z \simeq 6$ before eventually declining again toward $z \simeq 13$. Bolton & Haehnelt (2007) found that models 1 and 2 did not achieve reionization until $z = 4.16$ and 4.69, respectively (Figure 7.3). Moreover the integrated optical depths to electron scattering inferred from these models at $z \gtrsim 10$ is only $\tau = 0.033$ (model 1) and 0.055 (model 2), both values inconsistent (at the 3.2σ and 1.9σ levels) with the WMAP-5 value presented in Dunkley et al. 2008). In contrast, model 3 achieves reionization at $z = 6.22$ and produces an electron-scattering optical depth of 0.072, consistent with the WMAP5 estimate to within the 1σ uncertainties. Thus in order for the IGM to be reionized by $z \simeq 6$, the ionizing emissivity must *increase* beyond what is observed at $z \simeq 6$.

The first glimpse of the $z \gtrsim 7$ universe allows constraints to be placed on which of these models is most accurate. Studies of the evolving dropout population reveal a marked decline in the global star formation rate density over $6 \lesssim z \lesssim 10$ (Bouwens et al., 2008; Oesch et al., 2008), very similar to model 1 described above. While clearly there are many uncertainties involved in the computation (e.g. ionizing photon escape fraction, IGM clumpiness, etc.), it is very difficult to reconcile this observed decline with the requirements for reionization. If the dropout measurements of Bouwens et al. (2008) are correct, then for galaxies to reionize hydrogen, either their ionizing efficiency must be greater than assumed (Stiavelli et al., 2004) or there must be an unobserved feeble population of star forming galaxies in excess of that expected from extrapolation of the $z \simeq 7$ luminosity function. The tantalizing claim of a large density of candidate low luminosity star forming galaxies at $z \gtrsim 7$ (Stark et al., 2007b; Richard et al., 2008) indicates that a signficant population of faint sources may indeed be active beyond $z \simeq 7$, and that galaxies may thus produce enough ionizing photons for reionization. Although it may seem puzzling for there to be such an abundant population of efficiently-forming $z \gtrsim 8$ sources, this appears to be one

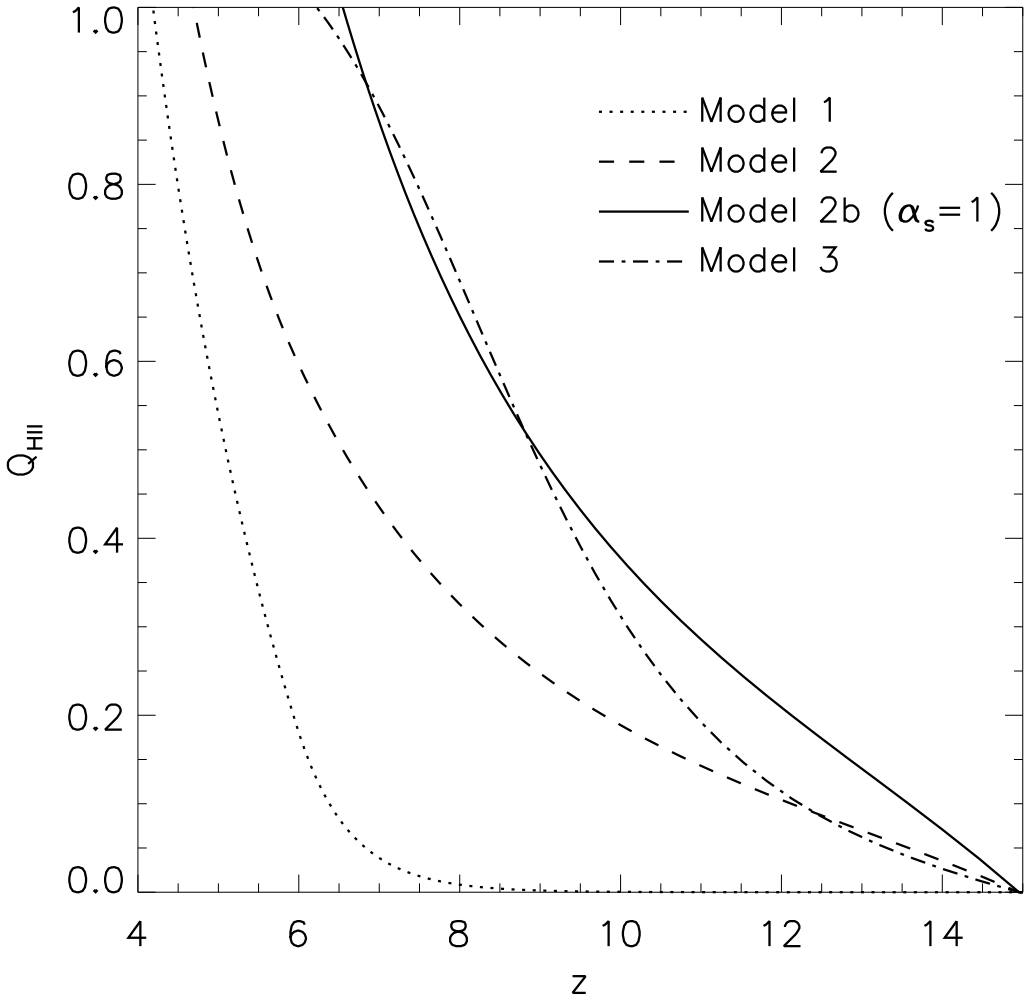

Figure 7.3 Predicted evolution of IGM filling factors for three separate scenarios for the redshift evolution of the ionizing emissivity (see Figure 1) taken from Bolton & Haehnelt (2007). While model 1 is most consistent with the observed decline in the number density of dropouts, it does not achieve reionization (defined as $Q_{HII} = 1$) until $z = 4.16$. Model 2 assumes a constant ionizing background between $z \simeq 6$ and 15 but it still does not achieve reionization until $z = 4.69$ unless a harder spectral index is assumed (model 2b). Model 3 requires an increase in the ionizing emissivity beyond $z \simeq 6$, consistent with implications from lensing surveys, and is able to achieve reionization by $z = 6.22$.

of the only means of achieving reionization by $z \simeq 6$ and satisfying the optical depth requirements of WMAP-5.

Clearly there is more work to be done in the quest to locate the nature and redshift distribution of sources responsible for reionization. The results described above suggests that future surveys must probe to much fainter limits if they are going to find a population capable of reionizing hydrogen. While this seems reasonable, it is important to remember that the initial observations comprise a handful of objects (none of which have been spectroscopically confirmed) detected in very small fields. The next step is thus to increase the areal coverage of blank field and lensing surveys in hopes of compiling much larger and more reliable samples. In the following section, we outline the most promising means of making progress in this pursuit.

7.3 Future Directions

We divide our discussion of future observational prospects into three separate sections. The first focuses on increasing samples of continuum dropouts over $7 \lesssim z \lesssim 11$. The second considers the ability of recently commissioned and upcoming narrow-band imagers and spectrographs to detect Lyman-α from star forming galaxies at $z \gtrsim 7$. Finally we discuss several opportunities of advancing our understanding of the physical processes governing galaxy assembly over $2 \lesssim z \lesssim 6$.

7.3.1 Continuum Dropouts at $z \gtrsim 7$

In the past five years, deep surveys with HST and ground-based facilities have uncovered hundreds of i'-dropout galaxies (Bouwens et al., 2006; Yoshida et al., 2006; McLure et al., 2008), allowing the $z \simeq 6$ luminosity function to be determined with good precision. Attempts to extend these measurements at $z \gtrsim 7$ have been frustratingly slow. Four z_{850} drop-outs at $z \simeq 7-8$ were initially claimed in the HUDF (Bouwens et al., 2004). Two of these were detected with Spitzer leading to improved photometric redshifts (Labbé et al., 2006), but the other two have since been removed from the high-redshift samples. Following a considerable investment by NICMOS and

ACS in various HUDF parallel fields, 8 luminous $z \gtrsim 7$ candidates are now claimed, but all except one have weak color constraints and none is yet spectroscopically confirmed (Bouwens et al., 2008). Likewise, three J_{110} dropout candidates (corresponding to $z \simeq 9 - 10$) were originally claimed (Bouwens et al., 2005) but it is now thought none of these is reliable (Bouwens et al., 2008). As we discussed in the previous section, all one can say is that the decline in luminous drop-outs observed with confidence over $3 \lesssim z \lesssim 6$ possibly continues to earlier times (Bouwens et al., 2007, 2008).

With the impending installation of the Wide Field Camera 3 (WFC3) on HST, a new survey is now poised to detect a large, robust, sample of LBGs at $z \simeq 7 - 8$ as well as provide the first constraints on an equivalent population to $z \simeq 10$ in the HUDF and associated parallel fields (PI: Illingworth). Coupled with constraints from fainter sources viewed through lensing clusters (PI: Kneib), these surveys will vastly improve our understanding of the contribution of star-forming sources to the process of reionization over $7 < z < 10$.

WFC3 offers a dramatic improvement over NICMOS in many respects. Most obvious are its 6.7× larger field and factor two improvement in sensitivity. However, of equal importance is its improved filter set. The restricted use of the two broad-band filters of NICMOS has led to many ambiguities in photometric selection and the implied source redshift (Figure 7.3). The latter problem is particularly troublesome given that both cool Galactic stars and dusty/quiescent $z \simeq 2$ galaxies are known contaminants (Stanway, 2004). The impending HUDF WFC3 survey will use three WFC3 filters (as opposed to two with NICMOS), which will significantly reduce foreground contamination for z-band drop-outs since two rest-frame UV colors will be available (Figure 7.4). Moreover, it will narrow the redshift range occupied by the z-band and Y-band dropouts ($z \simeq 7$ and 8, respectively), which as we will discuss in the next section is important for efforts to use LAEs to constrain the evolution of the IGM. Finally, it will allow the first comprehensive attempt to detect F125W-band dropouts ($z \simeq 10$) where the coaddition of all shorter wavelength data is an essential prerequisite.

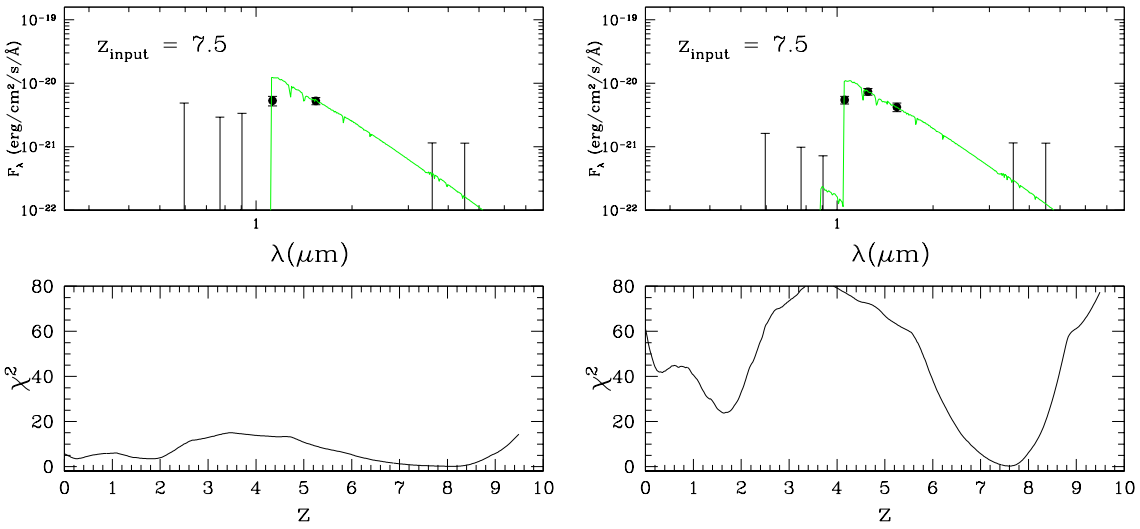

Figure 7.4 Combined advantage of deep z_{850} imaging and the use of 3 WFC3 filters for the robust selection and accurate redshift determination of galaxies at $z \gtrsim 7$. Panels show SED fits and χ^2 versus z for a simulated deep WFC3 exposure of a z=7.5, 30 Myr, galaxy at J=27.5 (AB). *Left:* A poorly- constrained solution resulting from 2 filters (F110W and F160W) and z_{850} data of just sufficient depth to select dropouts with $z - J > 0.8$, similar to that achieved in previous NICMOS campaigns. *Right:* The much more stringent solution resulting from combining ultra-deep ($z_{850} > 30$ (AB)) optical limits with the 3-filter strategy of the impending WFC3 survey.

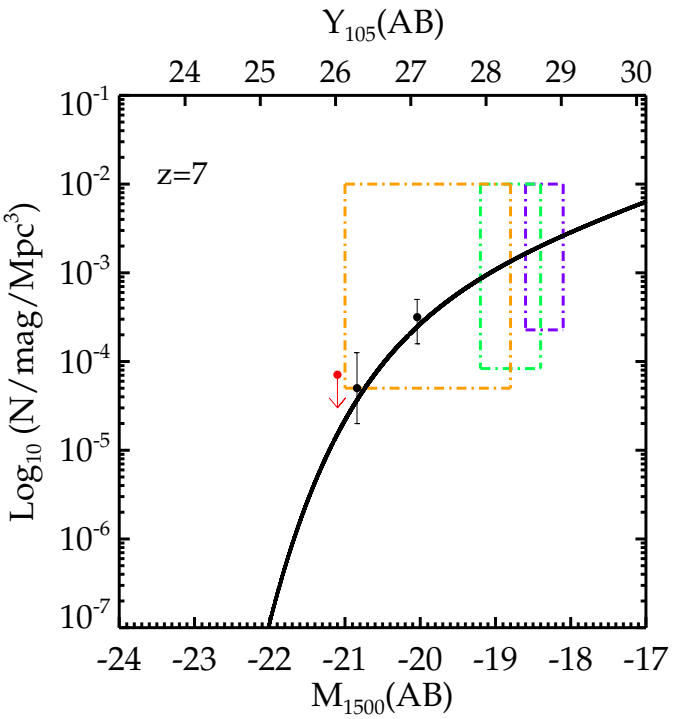

Figure 7.5 LF at $z \simeq 7$ consistent with current determinations. Datapoints are unconfirmed candidates from Bouwens et al. (2008). The hatched regions illustrate the predictions for a deep WFC3 survey of the HUDF and associated parallel fields. In total we expect $\simeq 85$ dropouts, a ten-fold improvement over the NICMOS samples.

Using the information gained from earlier z-drop campaigns (Bouwens et al., 2008) and our semi-analytical models normalized to the well-studied $z \simeq 6$ populations (Stark et al., 2007c), we can predict the likely yield of the new WFC3 campaign (Figure 7.5). Depending on the assumed parameters and their uncertainties, we expect to find 85±30 z-band drop-outs, 8±3 F105W dropouts and 1-3 F125W drop-outs. These z and F105W-band samples represent order of magnitude gains over present samples, quite apart from their improved fidelity.

7.3.2 Detecting Lyman-α at $z \gtrsim 7$

While the detection of large populations of $z-$ and J-band dropouts will certainly lead to significant progress, ultimately, we would like to spectroscopically confirm galaxies, whether they be LBGs or LAEs, at $z \gtrsim 7$. This venture is complicated by a number of issues. First is the resonant scattering of Lyman-α (the only strong emission line that is available through the optical or infrared atmospheric window) which is likely to decrease the observed Lyman-α flux. Second is the forest of bright OH emission lines from the atmosphere that fill the infrared spectral regime and the relatively poor sensitivity and small field of view achieved by longslit infrared spectrographs.

Many of the issues that have plagued previous searches for $z \gtrsim 7$ Lyman-α emission will soon be alleviated with the emergence of the next generation of near-IR narrow-band imagers and spectrographs. In the last year, large format near-IR imaging has become feasible on 8-10 meter telescopes with the development of MOIRCS on Subaru and HAWK-I on the VLT. The next major advance will be the commissioning of near-IR multi-object spectrographs on large ground based telescopes (MOSFIRE on Keck, Flamingos-II on Gemini, FMOS on Subaru, EMIR on the GTC) which will enable significant multiplexing capability and improve the sensitivity achieved in IR spectroscopic exposures. As we will discuss below, these developments will enable marked improvements in the quest to locate Lyman-α emission in distant galaxies.

The increased field of view of near-IR imagers on 8-10 meter telescopes will result in significant improvements in the efficiency of LAE surveys at $z \gtrsim 7$. A number of

efforts are currently underway to exploit the gains provided by these new instruments (e.g. Ouchi et al. 2007). Predicting the efficiency of these surveys is very difficult given the uncertainties in the galaxy luminosity function and the hydrogen content of the IGM. If the transmission of Lyα photons is not significantly lower than at $z \simeq 6$, our predictions from Chapter 4 suggest that samples of 10-20 $z \simeq 8$ LAEs could be uncovered in feasible time allocations. Pushing to $z \simeq 10$ may be significantly more difficult given the expected evolution in the underlying halo mass function.

Previous experience has taught us that the real challenge of $z \gtrsim 7$ LAE surveys is not identifying candidates but rather confirming them as LAEs. While archival broadband photometry can be used to reject selected foreground sources with optical detections (see Chapter 3), ultimately near-IR spectroscopy is necessary to identify Lyman-α and its asymmetric profile. The factor of $\simeq 2-3$ improved sensitivity of MOSFIRE combined with its ability to study 45 objects at once will significantly improve the efficiency of follow-up of LAE candidates. Likewise, MOSFIRE should be ideal for searching for Lyα from the brighter dropouts selected in the WFC3 survey discussed in the previous section. In our experience following up lensed dropouts at $J \simeq 26$ with NIRSPEC (Richard et al., 2008), we found that a 4 hr exposure set a useful limit of $W_\lambda < 5-20$ Å on the equivalent width of Lyman-α. Conducting similar measurements with very long MOSFIRE exposures (1-2 nights) should yield similar equivalent-width limits for candidate z-dropouts with $Y_{105} < 27.5-28$. If the fraction of sources with Lyman-α in excess of our equivalent width limit decreases significantly between $z \simeq 6$ and 7, this may indicate gradual evolution in the neutral hydrogen content of the IGM.

A similar test for IGM evolution can be achieved by studying the variation in the LAE luminosity function with redshift at $z \gtrsim 6$. As the neutral fraction increases with redshift, the LAE luminosity function should systematically shift to fainter fluxes (Malhotra & Rhoads, 2004; Shimasaku et al., 2006; Kashikawa et al., 2006). However such a signpost of reionization could also arise from gradual mass assembly (Ouchi et al., 2008). The existence of robust LBG samples spanning a narrow redshift range (see previous section) and LAE samples spanning from $z \simeq 6$ to 8 should allow the

LAE evolution to be modelled jointly with that of the continuum dropouts, enabling such degeneracies to be overcome.

7.3.3 Detailed Properties of Galaxies at $z \simeq 3-6$

The observations described above have focused on the prospect of extending the redshift frontiers by making use of newly-developed instrumentation on HST and ground-based facililities. Many of these same instruments, combined with the recent advances in adaptive optics fed IFUs, will also enable important advances in the detailed study of galaxy formation over $3 \lessapprox z \lessapprox 6$.

It is thought that in this era, massive 10^{11} $M_{\odot}$ galaxies emerge for the first time. How and when these galaxies first form and subsequently quench their star formation is still unclear. In Chapter 6, we showed how progress can be made by tracking the growth of LBGs from $z \simeq 6$ to $z \simeq 4$. The three primary limitations of efforts to track massive galaxy growth over this era are the lack of high S/N infared observations, the small sample sizes, and the lack of spectroscopic redshifts. Extension of this analysis to dropouts in the COSMOS field would greatly increase sample sizes and decrease cosmic variance. The addition of high S/N WFC3 imaging in some portion of GOODS or COSMOS will almost certainly emerge in the next several years, allowing much improved constraints on the stellar masses and ages of $z \gtrapprox 3$ galaxies. And finally, work is now underway to spectroscopically confirm the most massive galaxies at $z \simeq 4-5$ using DEIMOS (Stark et al. 2008, in prep). Combined, these improvements should yield a much improved census of the growth of massive galaxies at high redshift. Once equipped with a robust sample of massive galaxies at $z \gtrapprox 4$, we can begin to search for physical differences between those massive galaxies that are still actively forming stars and those with lower star formation rates in hopes of putting some basic constraints on the redshift and timescale over which the quenching of star formation begins to occur in these galaxies.

While the studies described above illuminate the global mass assembly history over $3 \lessapprox z \lessapprox 6$, in order to figure out why galaxies at this epoch are so effective at

forming stars, and to understand why rapid star formation is subsequently truncated, we need to study the internal structure of these early galaxies, observing their star formation regions, chemical abundance distributions, and dynamics on $\simeq$ 100 pc scales. This will allow us to establish how and why the properties at $z \gtrsim 3$ differ so much from those at the present day. In Chapter 5, we demonstrated the the potential of combining gravitational lensing and resolved spectroscopy in the study of high redshift LBGs.

Work is now underway to extend these measurements to a statistically-useful number of sources ($\simeq$ 10) spanning $z \simeq 2-5$ so we can begin to examine if the kinematical state varies as a function of galaxy properties (age, stellar mass, star formation rate) or redshift. A major gain for the lensed sources is the ability to bin up weaker diagnostic lines (e.g. Hβ, [NII]) while maintaing exquisite source plane resolution. With a sufficiently large sample, chemical abundance gradients, e.g. using the re-calibrated R_{23} index, can be used to test whether star formation occurs (i) via gas accretion (in which case accreted material should increase angular momentum and abundance gradients should be similar at all epochs) or (ii) following a rapid initial collapse (in which case enriched gas is transported inwards and abundance gradients should be weaker than today). By coordinating with CO studies secured from a parallel Plateau de Bure campaign, we can also infer the gas depletion timescale and test various star fomration - gas density laws (e.g. Kennicutt 1998) without making assumptions about how nebular emission relates to gas density.

In the next several years, imaging surveys such as PanSTARRS will find many more suitably-magnified $z \simeq 2-3$ systems. The development of multi-object integral field units (i.e. KMOS/VLT) will eventually enable significantly more efficient follow-up. The questions addressed in these surveys will be of great interest as we prepare for the era of Extremely Large Telescopes (ELTs) and the Atacama Large Millimeter Array (ALMA). The larger mirrors of the ELTs will offer $\simeq$ 3 times better resolution than is possible with the VLT or Keck while ALMA will be able to secure the molecular gas content for typical LBGs. The data obtained in these studies in the next several years will thus provide a unique glimpse as to what will be routinely

possible with these powerful, next generation facilities in the next decade.

Bibliography

Abel, T., Bryan, G. L., & Norman, M. L. 2000, ApJ, 540, 39

Abel, T., Bryan, G. L., & Norman, M. L. 2002, Science, 295, 93

Abraham, R. G., Tanvir, N. R., Santiago, B. X., Ellis, R. S., Glazebrook, K., & van den Bergh, S. 1996, MNRAS, 279, L47

Arnouts, S., et al. 2001, A&A, 379, 740

Babich, D., & Loeb, A. 2006, ApJ, 640, 1

Barger, A. J., Cowie, L. L., Sanders, D. B., Fulton, E., Taniguchi, Y., Sato, Y., Kawara, K., & Okuda, H. 1998, Nature, 394, 248

Barkana, R., & Loeb, A. 2000, ApJ, 531, 613

Barkana, R., & Loeb, A. 2006, MNRAS, 371, 395

Barkana, R., & Loeb, A. 2001, Phys. Rep., 349, 125

Barnes, J. E., & Hernquist, L. 1996, ApJ, 471, 115

Becker, R. H., et al. 2001, AJ, 122, 2850

Becker, G. D., Rauch, M., & Sargent, W. L. W. 2007, ApJ, 662, 72

Beckwith, S. V. W., et al. 2006, AJ, 132, 1729

Beckwith, S., Somerville, R., & Stiavelli, M. 2003, STScI Newsletter, Vol 20. Issue 04

Belokurov, V., et al. 2007, ApJ, 671, L9

Benítez, N. 2000, ApJ, 536, 571

Bertin, E., & Arnouts, S. 1996, A&AS, 117, 393

Bézecourt, J., Kneib, J. P., Soucail, G., & Ebbels, T. M. D. 1999, A&A, 347, 21

Birnboim, Y., & Dekel, A. 2003, MNRAS, 345, 349

Blumenthal, G. R., Faber, S. M., Primack, J. R., & Rees, M. J. 1984, Nature, 311, 517

Bolton, J. S., & Haehnelt, M. G. 2007, MNRAS, 382, 325

Borys, C., et al. 2004, MNRAS, 352, 759

Bournaud, F., Elmegreen, B. G., & Elmegreen, D. M. 2007, ApJ, 670, 237

Bournaud, F., et al. 2008, ArXiv e-prints, 803, arXiv:0803.3831

Bouwens, R. J., Illingworth, G. D., Blakeslee, J. P., Broadhurst, T. J., & Franx, M. 2004, ApJ, 611, L1

Bouwens, R. J., et al. 2004, ApJ, 616, L79

Bouwens, R. J., Illingworth, G. D., Blakeslee, J. P., Broadhurst, T. J., & Franx, M. 2004, ApJ, 611, L1

Bouwens, R. J., Illingworth, G. D., Thompson, R. I., & Franx, M. 2005, ApJ, 624, L5

Bouwens, R. J., Illingworth, G. D., Blakeslee, J. P., & Franx, M. 2006, ApJ, 653, 53

Bouwens, R. J., & Illingworth, G. D. 2006, Nature, 443, 189

Bouwens, R. J., Illingworth, G. D., Franx, M., & Ford, H. 2007, ApJ, 670, 928

Bouwens, R. J., Illingworth, G. D., Franx, M., & Ford, H. 2008, ArXiv e-prints, 803, arXiv:0803.0548

Bower, R. G., Benson, A. J., Malbon, R., Helly, J. C., Frenk, C. S., Baugh, C. M., Cole, S., & Lacey, C. G. 2006, MNRAS, 370, 645

Bradley, L. D., et al. 2008, ApJ, 678, 647

Bremer, M. N., Lehnert, M. D., Waddington, I., Hardcastle, M. J., Boyce, P. J., & Phillipps, S. 2004, MNRAS, 347, L7

Bremer, M. N., Jensen, J. B., Lehnert, M. D., Schreiber, N. M. F., & Douglas, L. 2004, ApJ, 615, L1

Broadhurst, T. J., Ellis, R. S., & Shanks, T. 1988, MNRAS, 235, 827

Broadhurst, T., et al. 2005, ApJ, 621, 53

Bromm, V., Coppi, P. S., & Larson, R. B. 1999, ApJ, 527, L5

Bromm, V., Kudritzki, R. P., & Loeb, A. 2001, ApJ, 552, 464

Bromm, V., Coppi, P. S., & Larson, R. B. 2002, ApJ, 564, 23

Bromm, V., & Larson, R. B. 2004, ARA&A, 42, 79

Bruzual, G., & Charlot, S. 2003, MNRAS, 344, 1000

Bruzual, G. 2007, ArXiv Astrophysics e-prints

Bundy, K., Ellis, R. S., & Conselice, C. J. 2005, ApJ, 625, 621

Bundy, K., Fukugita, M., Ellis, R. S., Targett, T. T., Belli, S., & Kodama, T. 2008, Submitted to ApJ

Bunker, A. J., Stanway, E. R., Ellis, R. S., & McMahon, R. G. 2004, MNRAS, 355, 374

Calzetti, D. 1997, AJ, 113, 162

Calzetti, D., Harris, J., Gallagher, J. S., III, Smith, D. A., Conselice, C. J., Homeier, N., & Kewley, L. 2004, AJ, 127, 1405

Capak, P., et al. 2004, AJ, 127, 180

Capak, P., et al. 2008, ApJ, 681, L53

Chabrier, G. 2003, PASP, 115, 763

Chambers, K. C., Miley, G. K., & van Breugel, W. J. M. 1990, ApJ, 363, 21

Chapman, S. C., Blain, A. W., Ivison, R. J., & Smail, I. R. 2003, Nature, 422, 695

Chapman, S. C., Blain, A. W., Smail, I., & Ivison, R. J. 2005, ApJ, 622, 772

Chary, R.-R., Stern, D., & Eisenhardt, P. 2005, ApJ, 635, L5

Cimatti, A., et al. 2004, Nature, 430, 184

Coe, D., Benítez, N., Sánchez, S. F., Jee, M., Bouwens, R., & Ford, H. 2006, AJ, 132, 926

Coleman, G. D., Wu, C.-C., & Weedman, D. W. 1980, ApJS, 43, 393

Colina, L., Arribas, S., & Monreal-Ibero, A. 2005, ApJ, 621, 725

Colless, M., Ellis, R. S., Taylor, K., & Hook, R. N. 1990, MNRAS, 244, 408

Coppin, K. E. K., et al. 2007, ApJ, 665, 936

Courteau, S. 1997, AJ, 114, 2402

Cowie, L. L. 1988, Post-Recombination Universe, 1

Cowie, L. L., & Hu, E. M. 1998, AJ, 115, 1319

Crampton, D., Cowley, A. P., & Hartwick, F. D. A. 1987, ApJ, 314, 129

Cuby, J. ., Hibon, P., Lidman, C., Le Fevre, O., Gilmozzi, R., Moorwood, A., & van der Werf, P. 2006, Accepted for publication in A&A, astro-ph/0611272

Daddi, E., et al. 2007, ApJ, 670, 156

Davé, R. 2008, MNRAS, 385, 147

Davis, M., & Wilkinson, D. T. 1974, ApJ, 192, 251

Dawson, S., McCrady, N., Stern, D., Eckart, M. E., Spinrad, H., Liu, M. C., & Graham, J. R. 2003, AJ, 125, 1236

De Breuck, C., et al. 2001, AJ, 121, 1241

Dekel, A., & Woo, J. 2003, MNRAS, 344, 1131

Dekel, A., et al. 2008, submitted to Nature

Dey, A., Spinrad, H., & Dickinson, M. 1995, ApJ, 440, 515

Dickinson, M., et al. 2004, ApJ, 600, L99

Dijkstra, M., Wyithe, S., & Haiman, Z. 2006, ArXiv Astrophysics e-prints

Djorgovski, S., & Thompson, D. J. 1992, The Stellar Populations of Galaxies, 149, 337

Djorgovski, S., Thompson, D., & Smith, J. D. 1993, First Light in the Universe. Stars or QSO's?, 67

Djorgovski, S. G., Castro, S., Stern, D., & Mahabal, A. A. 2001, ApJ, 560, L5

Drory, N., Salvato, M., Gabasch, A., Bender, R., Hopp, U., Feulner, G., & Pannella, M. 2005, ApJ, 619, L131

Dunkley, J., et al. 2008, ArXiv e-prints, 803, arXiv:0803.0586

Dunlop, J. S., Cirasuolo, M., & McLure, R. J. 2006, submitted to MNRAS, astro-ph/0606192

Dye, S., & Warren, S. J. 2005, ApJ, 623, 31

Dye, S., Smail, I., Swinbank, A. M., Ebeling, H., & Edge, A. C. 2007, MNRAS, 379, 308

Ebbels, T., Ellis, R., Kneib, J.-P., Leborgne, J.-F., Pello, R., Smail, I., & Sanahuja, B. 1998, MNRAS, 295, 75

Ebeling, H., Edge, A. C., & Henry, J. P. 2001, ApJ, 553, 668

Ebeling, H., Edge, A., Barrett, E., Donovan, D., van Speybroeck, L., Courtney, N., & Joy, M. 2003, The Cosmic Cauldron, 25th meeting of the IAU, Joint Discussion 10, 18 July 2003, Sydney, Australia, 10

Egami, E., et al. 2005, ApJ, 618, L5

Eggen, O. J., Lynden-Bell, D., & Sandage, A. R. 1962, ApJ, 136, 748

Ellis, R., Santos, M. R., Kneib, J.-P., & Kuijken, K. 2001, ApJ, 560, L119

Ellis, R. S. 2008, Observations of the High Redshift Universe (Saas-Fee Advanced Course 36: First Light In the Universe), 259

Erb, D. K., Shapley, A. E., Steidel, C. C., Pettini, M., Adelberger, K. L., Hunt, M. P., Moorwood, A. F. M., & Cuby, J.-G. 2003, ApJ, 591, 101

Erb, D. K., Shapley, A. E., Pettini, M., Steidel, C. C., Reddy, N. A., & Adelberger, K. L. 2006, ApJ, 644, 813

Erb, D. K., Steidel, C. C., Shapley, A. E., Pettini, M., Reddy, N. A., & Adelberger, K. L. 2006, ApJ, 646, 107

Erb, D. K., Steidel, C. C., Shapley, A. E., Pettini, M., Reddy, N. A., & Adelberger, K. L. 2006, ApJ, 647, 128

Eyles, L. P., Bunker, A. J., Ellis, R. S., Lacy, M., Stanway, E. R., Stark, D. P., & Chiu, K. 2007, MNRAS, 374, 910

Eyles, L. P., Bunker, A. J., Stanway, E. R., Lacy, M., Ellis, R. S., & Doherty, M. 2005, MNRAS, 364, 443

Fan, X., et al. 2006, AJ, 131, 1203

Fazio, G. G., et al. 2004, ApJS, 154, 10

Fernández-Soto, A., Lanzetta, K. M., & Chen, H.-W. 2003, MNRAS, 342, 1215

Finkelstein, S. L., Rhoads, J. E., Malhotra, S., Pirzkal, N., & Wang, J. 2006, Submitted to ApJ, astro-ph/0612511

Finlator, K., Davé, R., & Oppenheimer, B. D. 2007, MNRAS, 376, 1861

Finlator, K., Davé, R., Papovich, C., & Hernquist, L. 2006, ApJ, 639, 672

Ford, H. C., et al. 2003, in Future EUV/UV and Visible Space Astrophysics Missions and Instrumentation. Edited by J. Chris Blades, Oswald H. W. Siegmund. Proceedings of the SPIE, Volume 4854, pp. 81-94 (2003)., ed. J. C. Blades & O. H. W. Siegmund, 81

Förster Schreiber, N. M., et al. 2006, ApJ, 645, 1062

Franx, M., et al. 2003, ApJ, 587, L79

Frye, B. L., et al. 2007, ApJ, 665, 921

Fukugita, M., Hogan, C. J., & Peebles, P. J. E. 1998, ApJ, 503, 518

Furlanetto, S. R., Zaldarriaga, M., & Hernquist, L. 2004, ApJ, 613, 1

Furlanetto, S. R., Zaldarriaga, M., & Hernquist, L. 2006, MNRAS, 365, 1012

Gawiser, E., et al. 2006, ApJ, 642, L13

Genzel, R., et al. 2006, Nature, 442, 786

Giacconi, R., et al. 2002, ApJS, 139, 369

Giavalisco, M., Steidel, C. C., & Macchetto, F. D. 1996, ApJ, 470, 189

Giavalisco, M., et al. 2004a, ApJ, 600, L103

Giavalisco, M., et al. 2004b, ApJ, 600, L93

Gnedin, N. Y. 2000, ApJ, 542, 535

Grazian, A., Fontana, A., C., D., Nonino, M., Salimbeni, S., E., G., S., C., & S., G. 2006, A&A, accepted

Gunn, J. E., & Peterson, B. A. 1965, ApJ, 142, 1633

Haiman, Z., & Cen, R. 2005, ApJ, 623, 627

Hansen, M., & Oh, S. P. 2006, MNRAS, 367, 979

Heckman, T. M. 2001, Gas and Galaxy Evolution, 240, 345

Henry, A. L., Malkan, M. A., Colbert, J. W., Siana, B., Teplitz, H. I., McCarthy, P., & Yan, L. 2007, Accepted to ApJ Letters, astro-ph/0701045

Hopkins, A. M., & Beacom, J. F. 2006, ApJ, 651, 142

Horton, A., Parry, I., Bland-Hawthorn, J., Cianci, S., King, D., McMahon, R., & Medlen, S. 2004, in Ground-based Instrumentation for Astronomy. Edited by Alan F. M. Moorwood and Iye Masanori. Proceedings of the SPIE, Volume 5492, pp. 1022-1032 (2004)., ed. A. F. M. Moorwood & M. Iye, 1022

Hu, E. M., Cowie, L. L., & McMahon, R. G. 1998, ApJ, 502, L99

Hu, E. M., McMahon, R. G., & Cowie, L. L. 1999, ApJ, 522, L9

Hu, E. M., Cowie, L. L., Capak, P., & Kakazu, Y. 2005, in IAU Colloq. 199: Probing Galaxies through Quasar Absorption Lines, ed. P. Williams, C.-G. Shu, & B. Menard, 363

Hu, E. M., Cowie, L. L., Capak, P., McMahon, R. G., Hayashino, T., & Komiyama, Y. 2004, AJ, 127, 563

Hu, E. M., Cowie, L. L., & McMahon, R. G. 1998, ApJ, 502, L99

Hu, E. M., Cowie, L. L., McMahon, R. G., Capak, P., Iwamuro, F., Kneib, J.-P., Maihara, T., & Motohara, K. 2002, ApJ, 568, L75

Hughes, D. H., et al. 1998, Nature, 394, 241

Ichikawa, T., et al. 2006, in Society of Photo-Optical Instrumentation Engineers (SPIE) Conference Series, Vol. 6269, Society of Photo-Optical Instrumentation Engineers (SPIE) Conference Series

Immeli, A., Samland, M., Gerhard, O., & Westera, P. 2004, A&A, 413, 547

Iwata, I., Ohta, K., Tamura, N., Ando, M., Wada, S., Watanabe, C., Akiyama, M., & Aoki, K. 2003, PASJ, 55, 415

Iye, M., et al. 2006, Nature, 443, 186

Labbé, I., Bouwens, R., Illingworth, G. D., & Franx, M. 2006, ApJ, 649, L67

Larkin, J., et al. 2006, New Astronomy Review, 50, 362

Kaiser, N., & Peacock, J. A. 1991, ApJ, 379, 482

Kashikawa, N., et al. 2006, ApJ, 648, 7

Kayo, I., Taruya, A., & Suto, Y. 2001, ApJ, 561, 22

Kelson, D. D. 2003, PASP, 115, 688

Kennicutt, R. C., Jr. 1998, ARA&A, 36, 189

Kereš, D., Katz, N., Weinberg, D. H., & Davé, R. 2005, MNRAS, 363, 2

Kinney, A. L., Calzetti, D., Bohlin, R. C., McQuade, K., Storchi-Bergmann, T., & Schmitt, H. R. 1996, ApJ, 467, 38

Kneib, J.-P., Ellis, R. S., Santos, M. R., & Richard, J. 2004, ApJ, 607, 697

Kneib, J.-P., Ellis, R. S., Smail, I., Couch, W. J., & Sharples, R. M. 1996, ApJ, 471, 643

Kneib, J.-P., et al. 2003, ApJ, 598, 804

Knox, L., Scoccimarro, R., & Dodelson, S. 1998, Physical Review Letters, 81, 2004

Kohler, K., Gnedin, N. Y., & Hamilton, A. J. S. 2005, ArXiv Astrophysics e-prints, astro-ph/0511627

Koo, D. C. 1986, Spectral Evolution of Galaxies, 122, 419

Kraus, A. L., White, R. J., & Hillenbrand, L. A. 2006, ArXiv Astrophysics e-prints

Kriek, M., van der Wel, A., van Dokkum, P. G., Franx, M., & Illingworth, G. D. 2008, ArXiv e-prints, 804

Kriek, M., et al. 2006, ApJ, 645, 44

Kronberger, T., Kapferer, W., Schindler, S., & Ziegler, B. L. 2007, A&A, 473, 761

Labbé, I., et al. 2005, ApJ, 624, L81

Labbé, I., Bouwens, R., Illingworth, G. D., & Franx, M. 2006, ApJ, 649, L67

Lai, K., Huang, J.-S., Fazio, G., Cowie, L. L., Hu, E. M., & Kakazu, Y. 2007, ApJ, 655, 704

Larson, R. B. 1998, MNRAS, 301, 569

Law, D. R., Steidel, C. C., Erb, D. K., Larkin, J. E., Pettini, M., Shapley, A. E., & Wright, S. A. 2007, ApJ, 669, 929

Le Delliou, M., Lacey, C., Baugh, C. M., Guiderdoni, B., Bacon, R., Courtois, H., Sousbie, T., & Morris, S. L. 2005, MNRAS, 357, L11

Lee, K. ., Giavalisco, M., Conroy, C., Wechsler, R. H., Ferguson, H. C., Somerville, R. S., Dickinson, M. E., & Urry, C. M. 2008, ArXiv e-prints

Lee, K.-S., Giavalisco, M., Gnedin, O. Y., Somerville, R. S., Ferguson, H. C., Dickinson, M., & Ouchi, M. 2006, ApJ, 642, 63

Lilly, S. J. 1988, ApJ, 333, 161

Loeb, A., Barkana, R., & Hernquist, L. 2005, ApJ, 620, 553

Loeb, A. 2006, ecture notes for the SAAS-Fee Winter School, April 2006 (to be published by Springer Verlag), astro-ph/0603360

Lord, S. 1992, NASA Tech. Rep. 103957

Leggett, S. K., et al. 2002, ApJ, 564, 452

Larson, R. B. 1974, MNRAS, 166, 585

Madau, P. 1995, ApJ, 441, 18

Madau, P., Pozzetti, L., & Dickinson, M. 1998, ApJ, 498, 106

Madau, P., Haardt, F., & Rees, M. J. 1999, ApJ, 514, 648

Malhotra, S., & Rhoads, J. E. 2004, ApJ, 617, L5

Malhotra, S., & Rhoads, J. E. 2006, ApJ, 647, L95

Mao, J., Lapi, A., Granato, G. L., de Zotti, G., & Danese, L. 2006, Submitted to ApJ, astro-ph/0611799

Maraston, C. 2005, MNRAS, 362, 799

Marigo, P., & Girardi, L. 2007, A&A, 469, 239

Martin, C. L., Sawicki, M., Dressler, A., & McCarthy, P. J. 2006, New Astronomy Review, 50, 53

McCarthy, P. J., et al. 2004, ApJ, 614, L9

McLean, I. S., et al. 1998, in Proc. SPIE Vol. 3354, p. 566-578, Infrared Astronomical Instrumentation, Albert M. Fowler; Ed., ed. A. M. Fowler, 566

McLure, R. J., Cirasuolo, M., Dunlop, J. S., Foucaud, S., & Almaini, O. 2008, ArXiv e-prints, 805, arXiv:0805.1335

Meier, D. L. 1976, ApJ, 207, 343

Meurer, G. R., Heckman, T. M., & Calzetti, D. 1999, ApJ, 521, 64

Miralda-Escudé, J., Haehnelt, M., & Rees, M. J. 2000, ApJ, 530, 1

Miyazaki, S., et al. 2002, PASJ, 54, 833

Mobasher, B., et al. 2005, ApJ, 635, 832

Morales, M. F., & Hewitt, J. 2004, ApJ, 615, 7

Nagamine, K., Cen, R., Hernquist, L., Ostriker, J. P., & Springel, V. 2005, ApJ, 618, 23

Nagamine, K., Ouchi, M., Springel, V., & Hernquist, L. 2008, ArXiv e-prints, 802

Nakamura, F., & Umemura, M. 2001, ApJ, 548, 19

Nesvadba, N. P. H., et al. 2006, ApJ, 650, 661

Neufeld, D. A. 1991, ApJ, 370, L85

Noeske, K. G., et al. 2007, ApJ, 660, L47

Oesch, P. A., et al. 2008, ArXiv e-prints, 804, arXiv:0804.4874

Oke, J. B., & Gunn, J. E. 1983, ApJ, 266, 713

Omukai, K., & Yoshii, Y. 2003, ApJ, 599, 746

Ouchi, M., et al. 2004, ApJ, 611, 685

Ouchi, M., Tokoku, C., Shimasaku, K., & Ichikawa, T. 2007, Cosmic Frontiers, 379, 47

Ouchi, M., et al. 2008, ApJS, 176, 301

Overzier, R. A., Bouwens, R. J., Illingworth, G. D., & Franx, M. 2006, ApJ, 648, L5

Panagia, N., Fall, S. M., Mobasher, B., Dickinson, M., Ferguson, H. C., Giavalisco, M., Stern, D., & Wiklind, T. 2005, ApJ, 633, L1

Papovich, C., Dickinson, M., & Ferguson, H. C. 2001, ApJ, 559, 620

Papovich, C., Dickinson, M., Giavalisco, M., Conselice, C. J., & Ferguson, H. C. 2005, ApJ, 631, 101

Papovich, C., et al. 2006, ApJ, 640, 92

Partridge, R. B., & Peebles, P. J. E. 1967, ApJ, 147, 868

Partridge, R. B. 1974, ApJ, 192, 241

Pelló, R., Schaerer, D., Richard, J., Le Borgne, J.-F., & Kneib, J.-P. 2004, A&A, 416, L35

Peng, C. Y., Ho, L. C., Impey, C. D., & Rix, H.-W. 2002, AJ, 124, 266

Penzias, A. A., & Wilson, R. W. 1965, ApJ, 142, 419

Pettini, M., Steidel, C. C., Adelberger, K. L., Dickinson, M., & Giavalisco, M. 2000, ApJ, 528, 96

Pettini, M., Shapley, A. E., Steidel, C. C., Cuby, J.-G., Dickinson, M., Moorwood, A. F. M., Adelberger, K. L., & Giavalisco, M. 2001, ApJ, 554, 981

Pettini, M., & Pagel, B. E. J. 2004, MNRAS, 348, L59

Pilyugin, L. S., & Thuan, T. X. 2005, ApJ, 631, 231

Pirzkal, N., Malhotra, S., Rhoads, J. E., & Xu, C. 2006, ArXiv Astrophysics e-prints

Pritchet, C. J., & Hartwick, F. D. A. 1987, ApJ, 320, 464

Pritchet, C. J., & Hartwick, F. D. A. 1990, ApJ, 355, L11

Pritchet, C. J. 1994, PASP, 106, 1052

Reddy, N. A., Steidel, C. C., Fadda, D., Yan, L., Pettini, M., Shapley, A. E., Erb, D. K., & Adelberger, K. L. 2006, ApJ, 644, 792

Reddy, N. A., Steidel, C. C., Pettini, M., Adelberger, K. L., Shapley, A. E., Erb, D. K., & Dickinson, M. 2008, ApJS, 175, 48

Robertson, B. E., & Bullock, J. S. 2008, ApJ, 685, L27

Richard, J., Pelló, R., Schaerer, D., Le Borgne, J.-F., & Kneib, J.-P. 2006, A&A, 456, 861

Richard, J., Stark, D. P., Ellis, R. S., George, M. R., Egami, E., Kneib, J.-P., & Smith, G. P. 2008, ArXiv e-prints, 803, arXiv:0803.4391

Ricotti, M., & Shull, J. M. 2000, ApJ, 542, 548

Rowan-Robinson, M., et al. 1991, Nature, 351, 719

Ryan-Weber, E. V., Pettini, M., & Madau, P. 2006, MNRAS, 371, L78

Salpeter, E. E. 1955, ApJ, 121, 161

Samui, S., Srianand, R., & Subramanian, K. 2006, ArXiv Astrophysics e-prints

Santos, M. R., Ellis, R. S., Kneib, J.-P., Richard, J., & Kuijken, K. 2004, ApJ, 606, 683

Schaerer, D. 2003, A&A, 397, 527

Scheuer, P. A. G. 1965, Nature, 207, 963

Schlegel, D. J., Finkbeiner, D. P., & Davis, M. 1998, ApJ, 500, 525

Schmidt, M. 1965, ApJ, 141, 1295

Scott, A., et al. 2006, in Ground-based and Airborne Instrumentation for Astronomy. Edited by McLean, Ian S.; Iye, Masanori. Proceedings of the SPIE, Volume 6269, pp. 62695J (2006).

Shapley, A. E., Steidel, C. C., Adelberger, K. L., Dickinson, M., Giavalisco, M., & Pettini, M. 2001, ApJ, 562, 95

Shapley, A. E., Steidel, C. C., Pettini, M., & Adelberger, K. L. 2003, ApJ, 588, 65

Shapley, A. E., Steidel, C. C., Erb, D. K., Reddy, N. A., Adelberger, K. L., Pettini, M., Barmby, P., & Huang, J. 2005, ApJ, 626, 698

Shapley, A. E., Steidel, C. C., Pettini, M., Adelberger, K. L., & Erb, D. K. 2006, ApJ, 651, 688

Sheth, R. K., Mo, H. J., & Tormen, G. 2001, MNRAS, 323, 1

Shimasaku, K., et al. 2006, PASJ, 58, 313

Sirianni, M., et al. 2005, PASP, 117, 1049

Smail, I., Ivison, R. J., & Blain, A. W. 1997, ApJ, 490, L5

Smail, I., Ivison, R. J., Blain, A. W., & Kneib, J.-P. 1998, ApJ, 507, L21

Smail, I., et al. 2007, ApJ, 654, L33

Smith, R. E., et al. 2003, MNRAS, 341, 1311

Smith, G. P., Kneib, J.-P., Smail, I., Mazzotta, P., Ebeling, H., & Czoske, O. 2005, MNRAS, 359, 417

Smith, G. P., Sand, D. J., Egami, E., Stern, D., & Eisenhardt, P. R. 2006, ApJ, 636, 575

Smith, G. P., et al. 2002, MNRAS, 330, 1

Sokasian, A., Abel, T., Hernquist, L., & Springel, V. 2003, MNRAS, 344, 607

Sokasian, A., Yoshida, N., Abel, T., Hernquist, L., & Springel, V. 2004, MNRAS, 350, 47

Solomon, P. M., Downes, D., Radford, S. J. E., & Barrett, J. W. 1997, ApJ, 478, 144

Solomon, P. M., & Vanden Bout, P. A. 2005, ARA&A, 43, 677

Somerville, R. S., Lee, K., Ferguson, H. C., Gardner, J. P., Moustakas, L. A., & Giavalisco, M. 2004, ApJ, 600, L171

Spergel, D. N., et al. 2006, ApJ,submitted

Spergel, D. N., et al. 2003, ApJS, 148, 175

Stanway, E. 2004, PhD Thesis

Stanway, E. R., Bunker, A. J., & McMahon, R. G. 2003, MNRAS, 342, 439

Stanway, E. R., Bunker, A. J., McMahon, R. G., Ellis, R. S., Treu, T., & McCarthy, P. J. 2004, ApJ, 607, 704

Stanway, E. R., McMahon, R. G., & Bunker, A. J. 2005, MNRAS, 359, 1184

Stark, D. P., & Ellis, R. S. 2006, New Astronomy Review, 50, 46

Stark, D. P., Bunker, A. J., Ellis, R. S., Eyles, L. P., & Lacy, M. 2007, ApJ, 659, 84

Stark, D. P., Ellis, R. S., Richard, J., Kneib, J.-P., Smith, G. P., & Santos, M. R. 2007, ApJ, 663, 10

Stark, D. P., Loeb, A., & Ellis, R. S. 2007, ApJ, 668, 627

Stark, D. P., Swinbank, M., Ellis, R. S., Dye, S., Smail, I., Richard, J. 2008, accepted for publication in Nature

Steidel, C. C., & Hamilton, D. 1992, AJ, 104, 941

Steidel, C. C., & Hamilton, D. 1993, AJ, 105, 2017

Steidel, C. C., Pettini, M., & Hamilton, D. 1995, AJ, 110, 2519

Steidel, C. C., Giavalisco, M., Pettini, M., Dickinson, M., & Adelberger, K. L. 1996, ApJ, 462, L17

Steidel, C. C., Adelberger, K. L., Giavalisco, M., Dickinson, M., & Pettini, M. 1999, ApJ, 519, 1

Steidel, C. C., Pettini, M., & Adelberger, K. L. 2001, ApJ, 546, 665

Stern, D., Yost, S. A., Eckart, M. E., Harrison, F. A., Helfand, D. J., Djorgovski, S. G., Malhotra, S., & Rhoads, J. E. 2005, ApJ, 619, 12

Stiavelli, M., Fall, S. M., & Panagia, N. 2004, ApJ, 600, 508

Sunyaev, R. A., Tinsley, B. M., & Meier, D. L. 1978, Comments on Astrophysics, 7, 183

Swinbank, A. M., Bower, R. G., Smith, G. P., Smail, I., Kneib, J.-P., Ellis, R. S., Stark, D. P., & Bunker, A. J. 2006, MNRAS, 368, 1631

Swinbank, A. M., Bower, R. G., Smith, G. P., Wilman, R. J., Smail, I., Ellis, R. S., Morris, S. L., & Kneib, J.-P. 2007, MNRAS, 376, 479

Tacconi, L. J. et al. , 2008, ApJ, submitted

Thompson, T. A., Quataert, E., & Burrows, A. 2005, ApJ, 620, 861

Totani, T., Kawai, N., Kosugi, G., Aoki, K., Yamada, T., Iye, M., Ohta, K., & Hattori, T. 2006, PASJ, 58, 485

Tumlinson, J., Giroux, M. L., & Shull, J. M. 2001, ApJ, 550, L1

Tumlinson, J., & Shull, J. M. 2000, ApJ, 528, L65

Turner, E. L. 1991, AJ, 101, 5

van Dokkum, P. G., et al. 2004, ApJ, 611, 703

van Dokkum, P. G., et al. 2006, ApJ, 638, L59

van Dokkum, P. G. 2008, ApJ, 674, 29

Vanzella, E., et al. 2002, A&A, 396, 847

Vanzella, E., et al. 2005, A&A, 434, 53

Vanzella, E., et al. 2008, A&A, 478, 83

Verma, A., Lehnert, M. D., Förster Schreiber, N. M., Bremer, M. N., & Douglas, L. 2007, MNRAS, 377, 1024

Weatherley, S. J., Warren, S. J., & Babbedge, T. S. R. 2004, A&A, 428, L29

Webb, T. M. A., et al. 2006, ApJ, 636, L17

Westera, P., Lejeune, T., Buser, R., Cuisinier, F., & Bruzual, G. 2002, A&A, 381, 524

West, A. A., Walkowicz, L. M., & Hawley, S. L. 2005, PASP, 117, 706

White, S. D. M., & Rees, M. J. 1978, MNRAS, 183, 341

White, S. D. M., & Frenk, C. S. 1991, ApJ, 379, 52

Wilkins, S. M., Trentham, N., & Hopkins, A. M. 2008, MNRAS, 385, 687

Willis, J. P., & Courbin, F. 2005, MNRAS, 357, 1348

Wolfe, A. M. 1988, QSO Absorption Lines: Probing the Universe, 297

Wolfe, A. M., Lanzetta, K. M., Turnshek, D. A., & Oke, J. B. 1992, ApJ, 385, 151

Wyithe, J. S. B., & Loeb, A. 2005, ApJ, 625, 1

Wyithe, J. S. B., & Loeb, A. 2006, Nature, 441, 322

Yan, H., Dickinson, M., Giavalisco, M., Stern, D., Eisenhardt, P. R. M., & Ferguson, H. C. 2006, ArXiv Astrophysics e-prints

Yan, H., et al. 2005, ApJ, 634, 109

Yan, H., & Windhorst, R. A. 2004, ApJ, 600, L1

Yoshida, M., et al. 2006, ApJ, 653, 988